Torque Magnetometry Studies of High-Temperature Superconductors and Magnetic Materials

Dissertation

zur
Erlangung der naturwissenschaftlichen Doktorwürde
(Dr. sc. nat.)

vorgelegt der
Mathematisch-naturwissenschaftlichen Fakultät
der
Universität Zürich

von

Saskia Bosma
aus Frankreich

Promotionskomitee:

Prof. Dr. Hugo Keller (Vorsitz und Leitung der Dissertation)
Dr. Stephen Weyeneth
Prof. Dr. Roman Puzniak
Prof. Dr. Andreas Schilling

Zürich, 2013

Die vorliegende Arbeit wurde von der Mathematisch-naturwissenschaftlichen Fakultät der Universität Zürich auf Antrag von Prof. Dr. Hugo Keller als Dissertation angenommen.

dedicated to Raphaël

Abstract

The underlying mechanism of high-temperature superconductivity is still not fully understood, despite the 27 years elapsed since its discovery by Bednorz and Müller. The key of this mechanism is the interaction that allows electron pairs to flow without resistance in superconductors below a critical temperature. Superconductivity takes place in a wide variety of materials, differing for instance by crystal structure, non-superconducting parent compound, or thermodynamical parameters. Interestingly, all the high-temperature superconductors have a layered structure. Measuring the anisotropy parameter of those systems is therefore a privileged method to investigate their superconducting properties.

The most accurate technique to evaluate the anisotropy of a superconductor is torque magnetometry. The torque sensors and the experimental setup developed at the University of Zurich, and regularly improved over the years, allow us to reach unparalleled sensitivity. In order to extend the temperature and field domain accessible to our torque measurements, we built a new torque magnetometer that can be used in a 2 K cryostat equipped with a high-field superconducting magnet.

The anisotropy is related to the superconducting gap through the magnetic field penetration depth. The presence of multiple gaps has been proposed to explain the high critical temperatures of unconventional superconductors, and has also been linked to a temperature dependence of the anisotropy. Our anisotropy measurements on the cuprate high-temperature superconductor $YBa_2Cu_3O_{7-\delta}$ show a slight dependence on temperature, indicating the possible presence of several gaps. This dependence is carefully examined using not only the usual London model for the analysis, but also the more sophisticated Hao-Clem model. Accurate measurements are further enabled by the shaking technique, which consists in applying a small alternative magnetic field to shake the superconducting vortices into their thermodynamical equilibrium positions. The resulting gain in sensitivity allowed us to directly observe the lock-in of the vortices in the same $YBa_2Cu_3O_{7-\delta}$ crystal. The transition to the lock-in state happens when the superconducting coherence length becomes smaller than the distance between the superconducting layers. The behavior therefore changes from three dimensional to two dimensional. The lock-in is especially interesting because it is related to the dimensionality of the superconductor. The dimensionality is pertinent to the fundamental understanding of the material, but also to vortex pinning, a feature which is relevant for industrial applications.

Observing how superconductivity interacts with other ordered states can help to understand its basic principles. In many high-temperature superconductors, magnetic and superconductivity domains are separated in the phase diagram; the magnetic order has to be destroyed by doping for the electrons to condense into pairs. However, the intercalated iron selenides feature a coexistence of antiferromagnetic and superconducting phases at microscopic scales, as do some cuprates. In the iron-based high-temperature superconductor $Rb_xFe_{2-y}Se_2$, the anisotropy does not depend on temperature, but strongly depends on field, although the temperatures studied are too low to excite any change in the antiferromagnetic order. This points towards a role of the arrangement of the antiferromagnetic and superconducting domains, rather than an effect from changes in the magnetic moments configuration. Measurements of crystals annealed just at the onset of phase separation between antiferromagnetic and non-antiferromagnetic phases confirm that the degree of homogeneity seems to control the quality of the superconductor.

Even in materials in which magnetism and superconductivity do not closely coexist, it is interesting to observe how the proximity of strong magnetism influences the superconducting state. For example, in the iron-based superconductor $EuFe_{2-x}Co_xAs_2$, the superconductivity is reentrant (the resistivity does not completely vanish), due to the ordering of the large magnetic moments of the Eu atoms. Doping $EuFe_2As_2$ with cobalt on the iron site suppresses the low field, low temperature antiferromagnetic phase of the Eu moments. This shows that the superconducting iron-arsenic layer interacts with the Eu moments.

The results of this work point out the strong influence of competing or coexisting magnetic orders on superconductivity. They also show that a low anisotropy cuprate can develop 2D characteristics under certain conditions, and traces of multigap superconductivity were observed.

Zusammenfassung

Der zugrunde liegende Mechanismus der Hochtemperatursupraleitung ist noch nicht vollständig verstanden, trotz ihrer Entdeckung durch Bednorz und Müller vor schon 27 Jahren. Der Schlüssel dieses Mechanismus ist die Wechselwirkung zwischen Elektronen, durch welche die sich ergebenden Elektronenpaare unterhalb einer kritischen Temperatur ohne Widerstand fliessen können. Supraleitung tritt in vielen Materialien auf, die sich hinsichtlich Kristallstruktur, Ausgangsverbindung, oder thermodynamischer Parameter voneinander unterscheiden. Interessanterweise weisen alle Hochtemperatursupraleiter eine Schichtstruktur auf. Die Messung der Anisotropie Parameter dieser Systeme ist daher eine etablierte Methode um ihre supraleitenden Eigenschaften zu untersuchen.

Eine der präzisesten Techniken um die Anisotropie eines Supraleiters zu bestimmen, ist die Drehmoment-Magnetometrie. Der Versuchsaufbau und die Drehmomentsensoren, die an der Universität Zürich entwickelt und in den letzten Jahren weiter verbessert wurden, ermöglichen uns mit einzigartig hoher Empfindlichkeit zu messen. Um den vorhandenen Temperatur- und Magnetfeldmessbereich unserer Apparatur zu erweitern haben wir ein neues Drehmoment-Magnetometer konstruiert, das in einen standardmässigen 2 K Kryostaten mit supraleitendem Hochfeld-Magneten integriert werden kann.

Die Anisotropie ist über die magnetische Eindringtiefe mit der supraleitenden Bandlücke verknüpft. Um die hohen Sprungtemperaturen der unkonventionellen Supraleiter zu erklären, wurde das Konzept mehrerer Bandlücken entwickelt und ein Zusammenhang zur Temperaturabhängigkeit der Anisotropie hergestellt. Unsere Messungen der Anisotropie des Kuprat-Supraleiters $YBa_2Cu_3O_{7-\delta}$ zeigen eine geringe Abhängigkeit von der Temperatur, die auf das Vorhandensein mehrerer supraleitender Bandlücken oder des Pseudobandlücken-Effekts hinweisen. Diese Abhängigkeit wurde tiefgründig untersucht, indem nicht nur das übliche London Modell für die Analyse genutzt wurde, sondern auch das anspruchsvollere Hao-Clem Modell. Eine höhere Genauigkeit der Messung wird durch die 'Schüttel Technik' erzielt, die beim Anlegen eines kleinen zusätzlichen Magnetfeldes die magnetischen Flusswirbel in ihre thermodynamische Gleichgewichtsposition bringt. Durch die daraus resultierende Erhöhung der Empfindlichkeit konnten wir den Lock-in-Effekt der Flusswirbel im gleichen $YBa_2Cu_3O_{7-\delta}$ Kristall direkt beobachten. Der Übergang in den Lock-in-Zustand tritt auf, wenn die supraleitende Kohärenzlänge kleiner wird als der Abstand zwischen den supraleitenden Schichten. Das Verhalten ändert sich dann von dreidimensional zu zweidimensional. Der Lock-in-Effekt ist besonders interessant, da er mit der Dimensionalität des Supraleiters in Beziehung steht. Die Dimensionalität ist von Bedeutung für das grundlegende Verständnis des Materials und für das Pinning der Flusswirbel (eine Eigenschaft, die für industrielle Anwendungen interessant ist).

Untersuchungen der Interaktion von Supraleitung mit anderen geordneten Zuständen können helfen die grundlegenden Prinzipien zu verstehen. Bei vielen Hochtemperatursupraleitern werden im Phasendiagramm magnetische von supraleitenden Domänen getrennt, da davon ausgegangen wird, dass erst magnetische Ordnung zerstört werden muss damit die Elektronen in Paare kondensieren können. Selenide mit eingelagertem Eisen weisen allerdings eine Koexistenz von Antiferromagnetimus und Supraleitung bis auf mikroskopischer Skala auf, wie auch einige Kupfer basierte Verbindungen. Im eisen-basierten Hochtemperatursupraleiter $Rb_xFe_{2-y}Se_2$ ist die Anisotropie nicht von der Temperatur abhängig. Sie ist stattdessen stark feldabhängig, obwohl die untersuchten Temperaturen zu niedrig sind um Änderungen der antiferromagnetischen Ordnung anzuregen. Dies deutet daraufhin, dass eher die Anordnung der antiferromagnetischen und supraleitenden Domänen eine Rolle spielt, anstelle eines Effekts resultierend aus der Konfiguration der magnetischen Mo-

mente. Messungen von Kristallen, die genau beim Einsetzen der Phasentrennung zwischen Antiferromagnetismus und Nicht-Antiferromagnetismus getempert wurden, bestätigen, dass der Grad der Homogenität die Qualität des Supraleiters zu steuern scheint.

Auch in Materialien, in denen Magnetismus und Supraleitung nicht eng koexistieren, ist es interessant zu beobachten, wie die Nähe von starken Magnetfeldern den supraleitenden Zustand beeinflusst. Im eisen-basierten Hochtemperatursupraleiter $\mathrm{EuFe}_{2-x}\mathrm{Co}_x\mathrm{As}_2$ beispielsweise ist die Supraleitung wiedereintretend (der spezifische Widerstand verschwindet nicht vollständig), aufgrund der Ordnung der hohen magnetischen Momente der Eu Atome. Wird $\mathrm{EuFe}_2\mathrm{As}_2$ mit Kobalt an der Eisenposition dotiert werden das niedrige Magnetfeld und der Tieftemperatur Antiferromagnetismus der Eu Momente unterdrückt. Dies zeigt, dass die supraleitende Eisen-Arsen-Schicht mit den magnetischen Eu Momenten interagiert.

Die Ergebnisse dieser Dissertation weisen auf einen starken Einfluss von konkurrierenden oder koexistierenden magnetischen Ordnungen auf die Supraleitung hin. Sie zeigen auch, dass unter bestimmten Bedingungen Kuprate mit kleiner Anisotropie 2D-Eigenschaften entwickeln können, und Spuren von mehreren supraleitenden Bandlücken beobachtet werden können.

Contents

Introduction

The first manifestation of superconductivity was observed in 1911 [1], as a drop in the resistivity of mercury at 4.2 K. This zero-resistance state below a critical temperature T_c was subsequently discovered in many other compounds, but the critical temperatures were quite low, sometimes of the order of the millikelvin.

A further historical step was the discovery of the Meissner-Ochsenfeld effect in 1933 [2]. It consists in the expulsion of magnetic field lines from the bulk of a superconductor (*i.e.* perfect diamagnetism) when it is cooled below T_c. This observation led to the London theory (1935) [3], which explains the drop in resistivity and flux expulsion from fundamental electrodynamic equations. The underlying mechanism was however still unknown.

The conventional low-temperature superconductors were successfully explained by Bardeen, Cooper and Schrieffer in 1957 [4], through the so-called BCS theory. The carriers of the superconducting currents in the BCS theory are electrons paired by an electron-phonon interaction. One of the main experimental bases of this theory is the isotope effect [5, 6]: increasing the mass of the lattice ions decreases T_c, evidencing the ions role on superconductivity. The pairing allows the resulting two-electron bosonic quasiparticles to condense in the superconducting ground state, in a phase-coherent way, and to flow without the interferences which give rise to resistance in normal conductors.

Superconductivity at much higher temperatures was then discovered by Bednorz and Müller in LaBaCuO in 1986 [7], with $T_\mathrm{c} = 35$ K. In the following years many compounds of the layered cuprate family were synthesized, with a record critical temperature at atmospheric pressure of 133 K in $\mathrm{HgBa_2Ca_2Cu_3O_{8+\delta}}$ [8]. Although the carriers are still electron pairs in high-temperature superconductors, the pairing interaction is the object of debate since their discovery.

Recently, iron-based superconductors were discovered by Kamihara *et al.* [9]. Although the maximal T_c of this new class is 56 K, these materials are especially interesting due to the interplay between magnetism and superconductivity; in some extreme cases, there is even coexistence between those two phases similar to the cuprates. Like the cuprates, iron-based superconductors are layered compounds, but superconductivity is supported by Fe-Se or Fe-As planes instead of $\mathrm{CuO_2}$ planes.

Over the years, several different families of materials superconducting at various temperatures were found: A15 compounds up to 23 K in 1953 [10, 11], heavy fermions around up to 2.3 K in 1978 [12, 13], low dimensional organic superconductors at a few Kelvins in 1981 [14], fullerenes up to 33 K in 1991 [15, 16], $\mathrm{MgB_2}$ at 39 K in 2001 [17], and carbon nanotubes around 15 K in 2001 [18]. This great variability in superconducting materials shows that superconductivity is a many-faceted phenomenon.

Even if there is no complete theory of high-temperature superconductors, the phenomenological Ginzburg-Landau theory [19] describes many features of these superconductors. The superconducting state is modeled within the framework of the Landau theory of phase transitions, and the order parameter is assumed to be the wave function of the superconducting carrier density. The Ginzburg-Landau theory is especially useful to explain the properties of the mixed state, in which the field partially penetrates the superconductor in the form of vortices. The vortex state has a rich phase diagram, and vortex physics is a manifestation of the underlying superconducting fluid behavior. The Ginzburg-Landau theory was actually shown by Gor'kov [20] to be a limit case of the BCS theory.

Since the diamagnetic behavior of superconductors is intimately linked to the superconducting currents circulating in the material, magnetometry is a privileged investigating tool for superconductivity, especially since high-temperature superconductors exhibit many magnetic properties in addition to superconductivity.

The theoretical background from which our data analysis methods are derived is introduced in Chapter 1. Chapter 2 presents the torque magnetometry technique and the new setup designed during this Ph.D. work. The dependence of the anisotropy of $YBa_2Cu_3O_{7-\delta}$ on temperature, field, and modelisation is studied in Chapter 3, together with a detailed examination of the lock-in effect. The anisotropy of $Rb_xFe_{2-y}Se_2$, in which magnetism and superconductivity coexist, is reported in Chapter 4. In Chapter 5, the different magnetic configurations of Eu ions in the superconducting parent compound $EuFe_2As_2$ (and in $EuFe_{2-x}Co_xAs_2$) are detected by torque, confirming SQUID observations on the same samples.

Chapter 1

General properties of superconductors

Although no microscopic theory comparable to BCS was derived for high-temperature superconductors, the phenomenological Ginzburg-Landau theory can successfully describe many properties of these materials. The Ginzburg-Landau theory describes the behavior of anisotropic superconductors in a magnetic field, but does not explain the origin of pairing (superconductivity is assumed to exist).

This Chapter exposes the Ginzburg-Landau expression of the free energy, and how a working expression of the magnetic torque can be derived in the London approximation.

1.1 The Ginzburg-Landau theory

According to the Landau theory of phase transitions [21], the free energy of a system approaching a phase transition can be written as a functional of the order parameter. This parameter is a quantity characterizing the order that forms below the critical temperature T_c. For example, in the case of phase transitions resulting in ferromagnetically ordered magnetic moments, the order parameter is the magnetization; it is zero above the critical temperature, and non-zero below. A phenomenological expression of the free energy for superconductors was derived by Ginzburg and Landau [19], based on the Landau theory :

$$f(\vec{H}) = f_{\mathrm{n}0}(0) + \alpha|\psi|^2 + \frac{\beta}{2}|\psi|^4 + \frac{1}{2m^*}\left|\left(\frac{\hbar}{i}\vec{\nabla} - e^*\vec{A}\right)\psi\right|^2 + \frac{\mu_0\vec{H}^2}{2}, \tag{1.1}$$

where $f_{\mathrm{n}0}(0)$ is the free energy in the non-superconducting (disordered) state without any magnetic field $\vec{H}$ applied, $\vec{A}$ is the vector potential, μ_0 is the magnetic permeability of vacuum, α and β are phenomenological parameters, and ψ is the order parameter. ψ is the wave function of a superconducting carrier quasiparticle of mass m^* and charge e^*.

A variational minimization of the corresponding Gibbs energy with regards to ψ and $\vec{A}$ yields the two Ginzburg-Landau (GL) equations:

$$\alpha|\psi| + \beta|\psi|^2\psi + \frac{1}{2m^*}\left(\frac{\hbar}{i}\vec{\nabla} - e^*\vec{A}\right)^2\psi = 0, \tag{1.2}$$

$$\vec{j}_\mathrm{s} = \frac{e^*}{m^*}|\psi|^2\left(\hbar\vec{\nabla}\psi - e^*\vec{A}\right). \tag{1.3}$$

By solving Eq. (1.2) at zero field, and Eq. (1.3) at constant ψ, natural scales for the variations of respectively the order parameter and the field inside the superconductor are obtained:

$$\xi = \sqrt{\frac{\hbar^2}{2m^*\,|\alpha|}}, \tag{1.4}$$

$$\lambda = \sqrt{\frac{m^*}{\mu_0 n_\mathrm{s}^* e^{*2}}}. \tag{1.5}$$

The superconducting carrier density is denoted as $n_s^* = |\psi|^2$, m^* is the carrier effective mass, and e^* is the carrier charge. The variables n_s^*, m^*, and e^* are a priori different from respectively the electron density, the free electron mass, and the electron charge. The BCS theory and many experiments indicate that the superconducting carriers are electron pairs. The values of e^* and m^* are therefore $2e$ and $2m_\mathrm{e}$, where e and m_e are the electron charge and mass, respectively. ξ is the coherence length, *i.e.* the typical distance on which the order parameter can go down to zero at an interface between the superconductor and a normal material. λ is the magnetic field penetration depth; the field vanishes exponentially inside the superconductor on a characteristic length λ. Both parameters depend on temperature via $|\alpha|$ and n_s^*. Their ratio determines whether the superconductor is of type I ($\kappa = \lambda/\xi < 1/\sqrt{2}$) or type II ($\kappa > 1/\sqrt{2}$). Type I superconductors feature only one critical field H_c above which superconductivity and perfect Meissner screening disappear (Fig. 1.1a). Type II superconductors display a mixed state at fields between the lower critical field H_c1, at which the Meissner screening stops, and the upper critical field H_c2, at which superconductivity vanishes. In the mixed state, the field partially penetrates the bulk of the superconductor in the form of vortices (Fig. 1.1b). These vortices each carry the same quantity of magnetic flux: one flux quantum $\Phi_0 = hc/e^*$. When the material is type II, the field can penetrate on a large length and the order parameter can go to zero on a short length, so the apparition of interfaces between superconducting and normal state saves energy. The energy lost in turning off superconductivity in the vortex is compensated by the magnetic energy gained by allowing some field to penetrate. The typical size of the vortex normal state core is ξ, and the magnetic field penetration depth around the core is λ.

Type I superconductors have such a low critical field that they are useless for applications where magnetic fields are involved. In type II superconductors, H_c1 is related to the penetration of the field, and H_c2 is related to the coherence length [22] (neglecting vortex lattice corrections):

$$H_\mathrm{c1} = \frac{\Phi_0}{4\pi\mu_0\lambda^2}\ln(\kappa), \tag{1.6}$$

$$H_\mathrm{c2} = \frac{\Phi_0}{2\pi\mu_0\xi^2}. \tag{1.7}$$

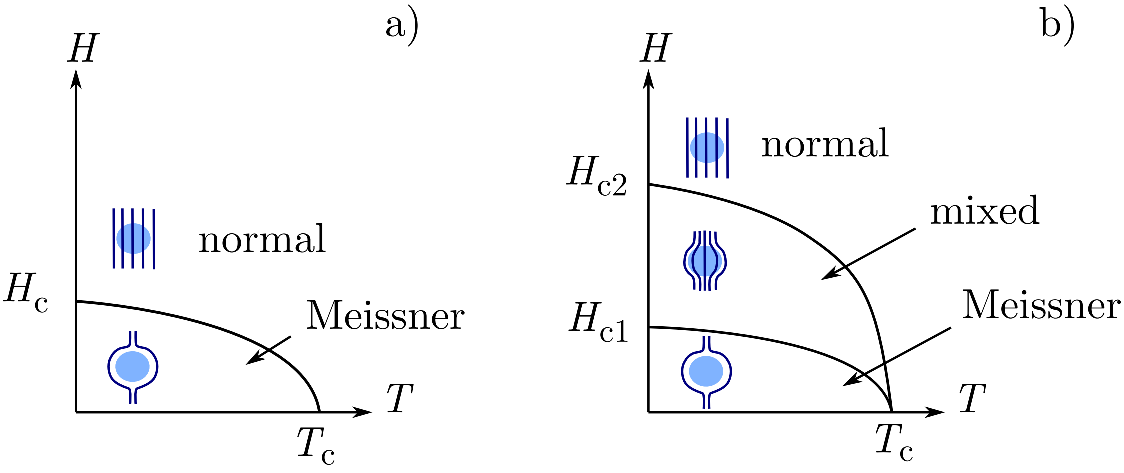

Figure 1.1: a) Generic phase diagram of a type I superconductor. The light blue sphere represents the superconductor, the dark blue lines are the field lines. The field is expelled in the Meissner state, and undisturbed in the normal state. b) Phase diagram of a type II superconductor. In the mixed state, the field penetrates partially into the bulk of the superconductor.

1.2 Magnetization in the London approximation

All high-temperature superconductors are type II. For extreme type II superconductors ($\kappa >> 1$), the size of the vortex core is negligible compared to the size of the region around it where the field penetrates. The order parameter can be considered constant in most of the superconductor, which then behaves according to the electromagnetic London equations [3]. This London approximation is valid when the applied field H verifies $H << H_{c2}$. When $H \simeq H_{c2}$, the coherence length is diverging, so the core size would not be negligible.

In an anisotropic superconductor, the effective mass is replaced by a tensor having its principal directions along the crystallographic axes a, b, and c. The free energy (per unit length in the vortex direction) is [23]:

$$F = 2\pi V \int \left(H^2 + \lambda^2 \sum_{i,k \ \text{in}(a,b,c)} m_{ik} \vec{\nabla}_i \times \vec{H} \cdot \vec{\nabla}_k \times \vec{H} \right) dxdy, \tag{1.8}$$

where V is the volume of the sample, $\lambda = (\lambda_a \lambda_b \lambda_c)^{1/3}$ (λ_i is the penetration depth along the i-axis), and the m_ik are the effective mass tensor coefficients. If $H_{c1} << H$, Eq. (1.8) reduces to [24]:

$$F = \frac{\mu_0 V H^2}{2} + \frac{\Phi_0 H V}{8\pi\lambda^2} \ln\left(\frac{\upsilon H_{c2}}{H}\right). \tag{1.9}$$

The factor υ is a dimensionless constant stemming from an integral cutoff in the free energy derivation depending on the vortex lattice structure. The present work mainly makes use of torque measurements. A magnetic moment $\vec{m}$ in a magnetic field $\vec{H}$ undergoes a torque defined magnetostatically as $\vec{\tau} = \mu_0 \left(\vec{m} \times \vec{H}\right)$. The free energy represents the maximal quantity of work that can be extracted from a system. In the case of a sample rotating under a torque τ, the elementary work is $\partial W = \tau \partial\theta$, where $\partial\theta$ is the elementary angular displacement. The torque can therefore be defined thermodynamically as:

$$\tau = -\frac{\partial F}{\partial \theta} \tag{1.10}$$

In a layered tetragonal superconductor ($\lambda_a = \lambda_b = \lambda_{ab}$) in the London approximation, the expression for the torque can therefore be derived from Eq. (1.9), yielding

$$\tau(\theta) = -\frac{V\Phi_0 H}{16\pi\lambda_{ab}^2}\left(1 - \frac{1}{\gamma^2}\right)\frac{\sin(2\theta)}{\epsilon(\theta)} \ln\left(\frac{\eta H_{c2}^{||c}}{\epsilon(\theta) H}\right), \tag{1.11}$$

where θ is the angle between the field and the crystallographic c-axis, $\epsilon(\theta) = \sqrt{\cos(\theta)^2 + \sin(\theta)^2/\gamma^2}$ is the angular scaling function, $\gamma = \lambda_c/\lambda_{ab}$ is the anisotropy parameter, and η is a dimensionless parameter related to υ. In the GL theory for a one gap superconductor, $\gamma = \sqrt{m_{ab}^*/m_c^*} = \lambda_c/\lambda_{ab} = \xi_c/\xi_{ab}$. η can in most cases be fixed around 1; a more detailed account of this approximation is described in Section 3.1.

The original source [24] for this derivation mentions that the angular dependence of H_{c2} should not be taken into account in order to stay within the London approximation. However, subsequent theoretical work (for example [25]) introduce this angular dependence via the $\epsilon(\theta)$ factor, and the torque expression (1.11) is widely used in experimental works (see for example Refs. [26, 27, 28, 29, 30, 31]). The angle dependence changes $H_{c2}(\theta) = H_{c2}^{||c}/\epsilon(\theta)$ by at most a γ factor, and at least a factor one. Since H_{c2} enters Eq. (1.11) only in the logarithmic term, it is reasonable to assume that using an angle dependent H_{c2} does not overstep the London approximation for moderately anisotropic superconductors.

CHAPTER 2

Probing the magnetic properties of high-temperature superconductors

---

The properties of the superconducting state can be studied by magnetometric techniques, since the screening of the magnetic field makes the materials diamagnetic. The magnetic behavior of a superconductor can provide insights into its superconducting behavior. Besides, many superconductors exhibit magnetic orders independently of superconducting diamagnetism, which may influence superconductivity or compete with it. For example, in cuprates the Cu moments in the superconducting planes order antiferromagnetically at low oxygen doping, and many superconductors feature coexisting antiferromagnetism and superconductivity.

In this chapter, different magnetometry techniques are compared, and the specificities of the torque technique are underlined. Torque magnetometry is then described in detail. Finally, the new high-field, low-temperature torque setup developed for this Ph.D. project is presented.

2.1 Experimental techniques overview

There are many ways to measure the magnetic properties of superconductors. One of the most commercially successful is the SQUID (Superconducting QUantum Interference Device) [32]. The bulk average magnetic moment of a sample is measured by sweeping it through superconducting half loops connected via Josephson junctions. These loops pick-up the voltage difference due to the magnetic flux variation resulting from the movement. Another method used in this work to study magnetization is Muon Spin Rotation-Relaxation (μSR). It is a particle implantation method, which yields the distribution of the internal field inside a material.

Torque magnetometry measures the bulk magnetization. It has the advantage of being more sensitive than a SQUID at high fields and of not having crystal orientation issues, since a typical measurement consists in sweeping the direction of an applied magnetic field. Torque magnetometry provides a direct method to study the anisotropic magnetic properties of superconductors, contrary to methods measuring physical quantities separately along different crystallographic directions in order to determine the anisotropy parameter. A determination of the anisotropy from the ratio of the penetration depths requires a careful measurement of λ_c and λ_{ab}. Any misalignment of the sample with the applied magnetic field results in an underestimation of λ_c and the deduced γ. In torque measurements, however, the anisotropy is extracted from a fit to the data, without orientation issues since the model used for the analysis [Eq. (1.11)] describes the torque in the full angular range. Torque methods probe directly the component of the magnetization which is orthogonal to the field.

2.2 Torque magnetometry

A magnetic moment $\vec{m}$ in a magnetic field $\vec{H}$ is subjected to a torque

$$\vec{\tau} = \mu_0 \left(\vec{m} \times \vec{H} \right) . \tag{2.1}$$

Bulk magnetometry techniques give access to the magnetization $M = m/V$, where V is the volume of the sample. In anisotropic superconductors, the diamagnetic moment is not aligned with the field, because the supercurrents giving rise to the diamagnetism flow more easily in the superconducting planes, and not necessarily orthogonally to the field lines (see Fig. 2.1). Therefore, the vector product of M and H is not zero if the field is not along the principal axes, and it is possible to access magnetization information from torque measurements. The torque only yields the component $M_{\perp H}$ of the magnetization which is perpendicular to the field, so the analysis is usually done with models deriving directly the torque from the free energy, rather than with models calculating $M_{\perp H}$.

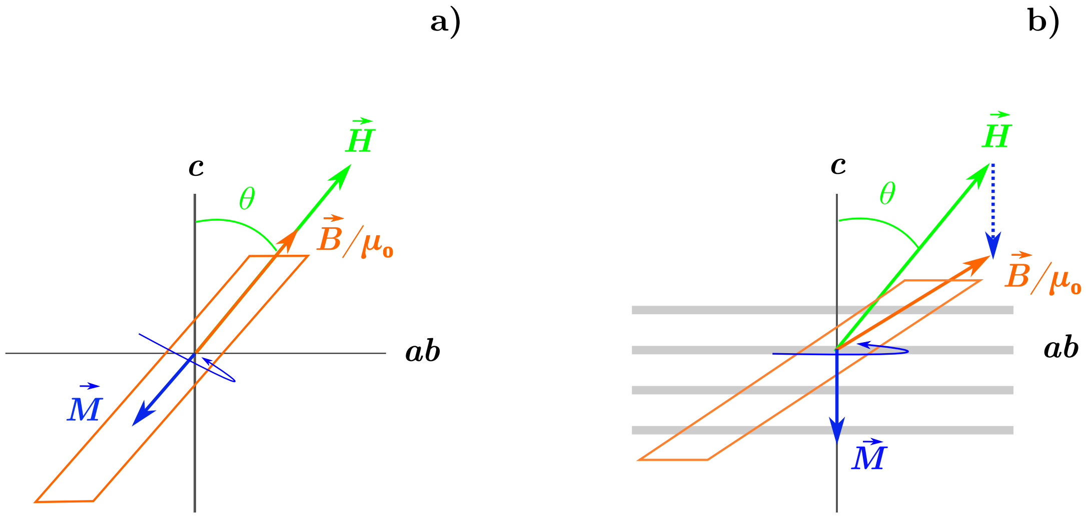

Figure 2.1: Field and magnetization vectors configuration in the vortex state. The curly arrow shows the direction of the superconducting currents flowing around the vortex and shielding the rest of the superconductor from the magnetic field. a, b, and c are the crystallographic axes. a) Isotropic superconductor. b) Anisotropic layered superconductor.

Torque measurements typically consist in sweeping the magnetic field direction from the c-axis through the ab-plane and to the opposite direction of the c-axis (clockwise), then back again (counterclockwise) as shown on Fig. 2.2a. Such a measurement yields the torque τ as a function of the angle θ between the applied field H and the c-axis. The resulting function $\tau(\theta)$ can be fitted with Eq. (1.11) if the London approximation is valid. As the field direction is approaching the ab-plane, the screening currents start to flow not only in plane, but also out of plane, which makes the torque depend strongly on both λ_{ab} and λ_c in this angular region. The temperature and field effect on the anisotropy γ_λ are consequently visible on angular torque data taken around the ab-plane at various fields and temperatures, independently of the strict validity of Eq. (1.11) or the fit quality.

The first torque setup used in our measurements consists of a rotating resistive 1.4 T magnet, a cryostat cooling down to 12 K, a shaking coil producing a few mT of AC field at 200 Hz, and piezoresistive torque sensors designed by S. Kohout [33]. The sensor is a platform connected to piezoresistive legs which are bent when the sample mounted on the platform undergoes a torque (Fig. 2.2b). The resulting resistance change in the piezoresistors is detected by a Wheatstone bridge, and the read-out voltage is proportional to the torque magnitude. The small dimensions needed for the sample - typically less than 100 μm - allow the study of high-quality single crystals. This is especially useful in the case of newly discovered materials, for which it is not possible to grow large single crystals of sufficient quality.

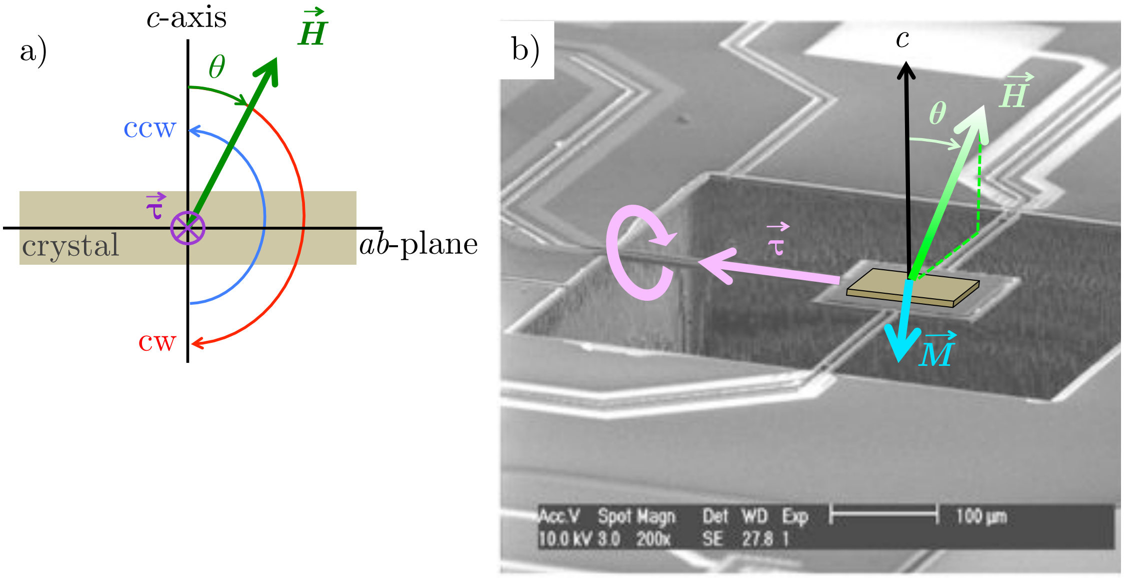

Figure 2.2: a) Visualization of the vectors during a typical measurement. The field direction is swept clockwise (CW), then counterclockwise (CCW). The measurement is reversible when there is no pinning; the signal corespond to a thermodynamic equilibrium state. The torque is then identical in both field sweep directions. b) Electron microscope picture of the torque sensor. The superconducting crystal (brown) is mounted on the platform, and a magnetic field H (green) with angle θ varying with regards to the crystallographic c-axis is applied. The diamagnetic moment and the misalignment due to the crystal anisotropy result in a torque τ (violet). When the field is swept in the plane containing the c-axis and the piezoresistive legs, the torque is perpendicular to the legs, resulting in a symmetric deformation of the piezoresistors.

There is an irreversibility between the clockwise (CW) and counterclockwise (CCW) measurements, due to pinning of the vortices on defects in the crystal. In order to get reversible measurements that can be compared to thermodynamic models, a vortex shaking technique [27, 34] is used. It consists in applying a small AC magnetic field perpendicular to the main field. The oscillating Lorentz force thus applied tears the vortices away from their pinning centers and allows for measurements at thermodynamic equilibrium (Fig. 2.3 and 2.4). Measurements without shaking tend to overestimate the anisotropy [35, 36, 37].

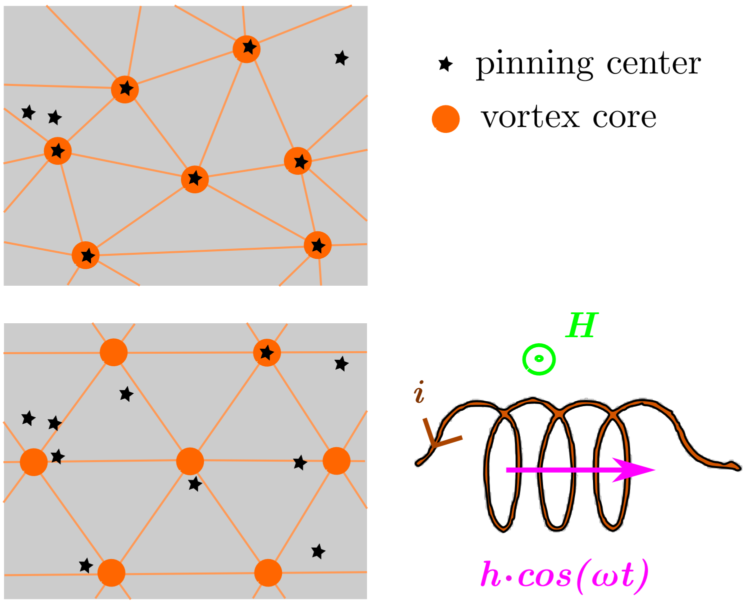

Figure 2.3: Visualization of the shaking effect. On the top, a superconductor (grey) with vortices (orange spots) pinned on defects (black stars), viewed along the field direction. On the bottom, after shaking with the AC field $h\cos(\omega t)$, the vortex lattice is in the equilibrium triangular configuration.

When using Eq. (1.11) to analyze angular torque data, the free fit parameters are γ, λ_{ab}, η, and H_{c2}. In order to reduce the number of fit parameters, H_{c2} is usually fixed with the Werthamer-Helfand-Hohenberg (WHH) temperature dependence [38]:

$$\mu_0 H_{c2}^{||c} \simeq \left.\frac{dH_{c2}}{dT}\right|_{T=T_c} \cdot (T-T_c). \tag{2.2}$$

H_{c2} can therefore be estimated from resistivity measurements around T_c. Small variations in H_{c2} do not affect the results of the analysis, since H_{c2} contributes only logarithmically in Eq. (1.11) and has very little weight in the determination of the anisotropy and the penetration depth in low magnetic fields [39].

In addition to the superconducting magnetization signal, a paramagnetic background due to impurities can be present. The general shape of such a signal is proportional to $\chi(VH^2/2)\sin(2\theta)$, where $\chi = M/H$ is the magnetic susceptibility (see Appendix B). It can be subtracted from the data by analyzing $\tau(\theta) + \tau(\theta + 90°)$ instead of $\tau(\theta)$, or by including an additional sinusoid in the fitting. Unless otherwise specified, the results are independent of the background subtraction procedure [39].

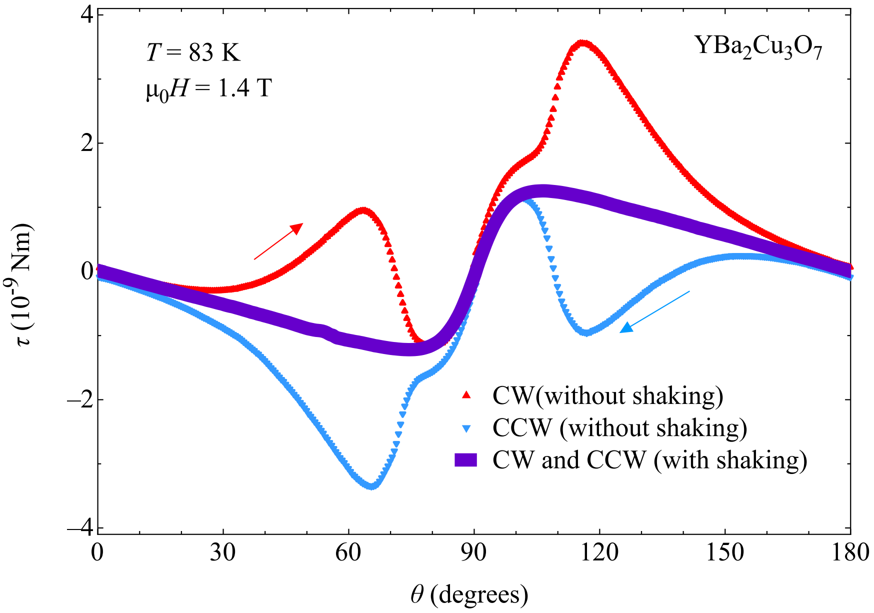

Figure 2.4: Example of the shaking effect on a $YBa_2Cu_3O_{7-\delta}$ single crystal (1.4 T torque setup). The irreversibility between CW and CCW directions is completely removed. Note that the final signal does not exactly coincide with the average of the CW and CCW data.

2.3 A new torque setup for high-field, low temperature measurements

In order to reach higher fields and lower temperatures in torque experiments, we conceived a new design for the torque magnetometry setup. It consists of a rod inset compatible with the general purpose *Quantum Design* PPMS (Physical Properties Measurement System). We use the same piezoresistive torque sensors as the 1.4 T station, and introduce shaking coils inside the cryostat. There is a commercial torque option to the PPMS, inspired by the first designs made at the University of Zurich and IBM Rüschlikon [40]. However, its resolution is much lower than what we can achieve, because the sensor size of this device is much bigger and less accurate, and only larger crystals of lesser quality can be measured. There is no shaking option either.

The main challenge is to achieve sufficient shaking power with very small coils, since the space inside the cryostat is quite reduced (approximately 2.5 cm of useful diameter). Figure 2.5 shows a simplified outline of the assembly part which performs the magnetometry measurements inside the cryostat. The field direction is fixed, so the sensor has to be rotatable in order to do angle dependent measurements. Besides, the Lorentz force due to the main field induces vibrations in the current-carrying coil, which necessitates a large contact gap tolerance between objects, further reducing the available space. Since space is limited, the number of windings on the coils at a given wire diameter is also limited, putting an upper limit on the shaking field at a given current. The Joule heating of the coils can also introduce noise due to the changes in temperature at the sample site.

2.3.1 Shaking coils

The new coil size is a compromise between shaking field strength, cryostat size, and sensor holder size. There are two shaking coils on either side of the sample location, in a Helmholtz configuration. They are wound between plastic holders (transparent parts in Fig. 2.5). The sample (grey

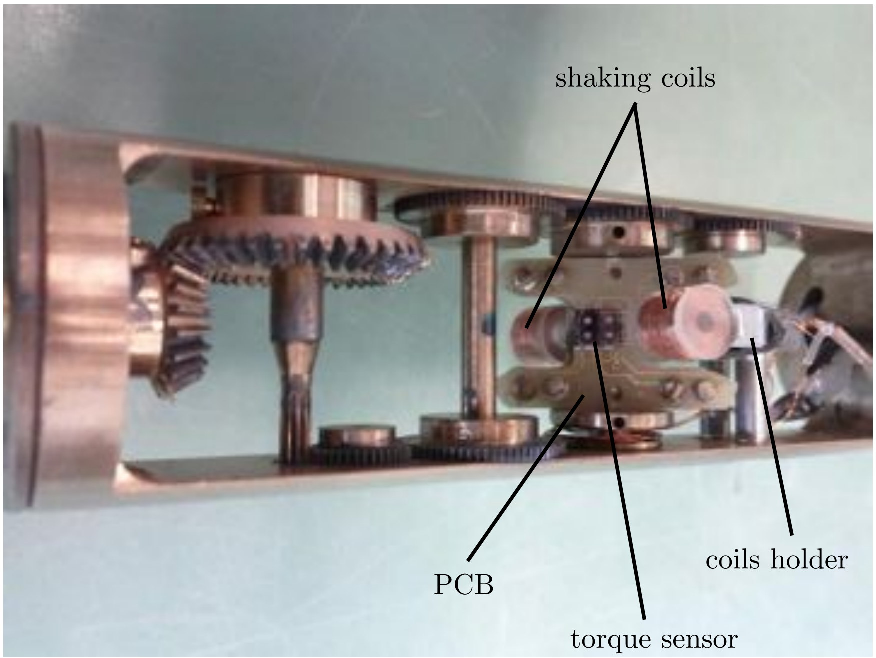

Figure 2.5: Cryostat part of the new torque magnetometer inset. The casing (metallic orange) is made of beryllium copper. The green plates are the sensor holder and the sensor printed circuit board (PCB). The black rectangle on the PCB is the piezoresistive sensor. The aluminum part is the shaking coils holder. The transparent plastic part is the coil support. The copper coil wire is wound around the plastic cylinder, and held in place by the two transparent discs.

rectangle) is located on the torque sensor (black rectangle). An estimation of the shaking field was calculated numerically by adding the fields created by simple current loops covering the volume of the coils. The coils can be considered as circular current loops in series stacked concentrically and horizontally (see Fig. 2.6a). This estimation (calculated in Python [41]) yields 0.32 mT at the sample position for a 300 mA current (the maximal current in the coil windings at room temperature, which is given by the melting temperature of copper via Joule heating). The setup maximal current of 1.8 A yields a 1.97 mT field. For comparison, the previous torque setup in a resistive 1.4 T magnet used a large copper shaking coil outside the cryostat, allowing a maximal shaking field of 7 mT at 200 Hz on the whole volume of the measured sample.

A COMSOL simulation was made to estimate the field at the sample position, but also at positions slightly off the axis, for which it is difficult to get a simple expression for the magnetic field. This simulation uses the optimized dimensions shown in Fig. 2.6a. COMSOL [42] is a finite elements simulation software which allows the simultaneous solving of different physical equations. The modeling is quite simple; it consists of Ampere's law applied to two copper cylinders in air with a radial current circulating over their whole volume. In the actual coils, the windings do not cover a perfectly cylindrical volume, since the wires have a circular section and are stacked in a rectangular area A (see Fig. 2.6a). The simulation yields a field ≈ 0.3 mT at the position of the torque sensor at 300 mA. With a 1.8 A current, the field at the center is 1.5 mT (see Fig. 2.6b). These values are consistent with the simple Python model used for the first calculation.

Prototype coils of this size where made and tested in air at 293 K. The field measured then was analogous to the one from the simulation and the calculation, ≈ 0.5 mT at 300 mA. The inductance of the coil is measured at $L = 1.13$ mH, and its resistance is measured at 30 Ω at 300 K, and 5.5 Ω at 5 K. The AC current rise time L/R is thus always smaller than the 5 ms

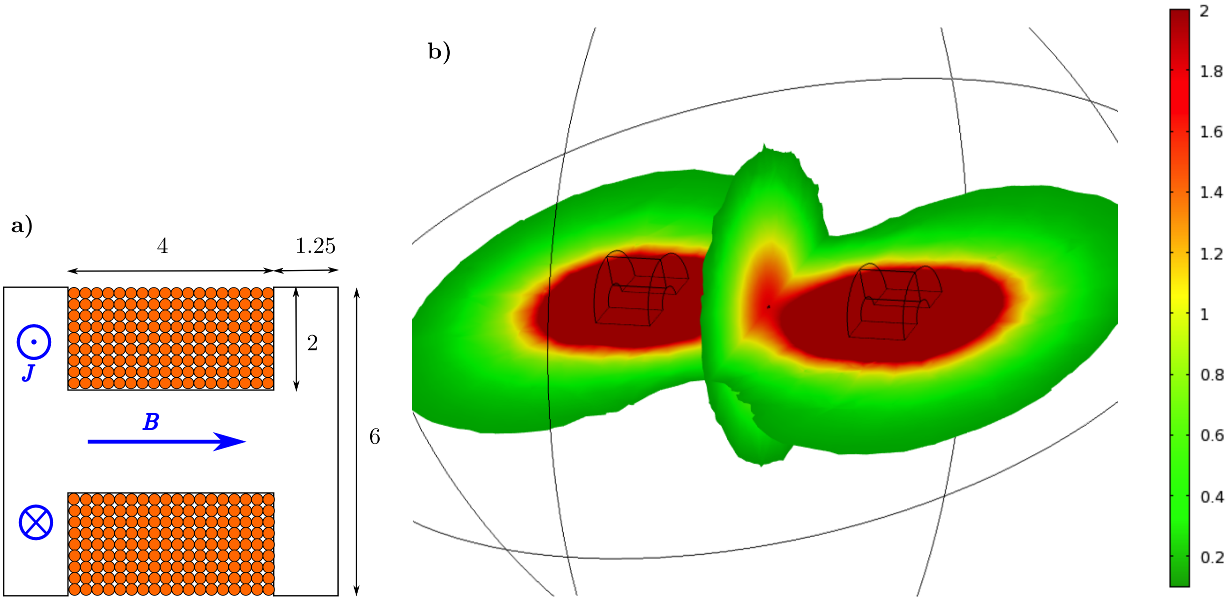

Figure 2.6: a) Side cut view of a shaking coil. All dimensions are in millimeters. The coil wire diameter is 0.2 mm. b) COMSOL simulation of the magnetic field amplitude created by the shaking coils. The color scale is in mT, the maximum shown is 2 mT (red), the minimum shown is 0.1 mT (green). The current density in the coil volume coresponds to a 1.8 A current in the 150 windings.

(200 Hz) period of the shaking excitation. A current larger than the 300 K limit may be used in operation in the cryostat, since the melting risk is suppressed at low temperatures. However, the heating of the coil can disturb the temperature of the measured sample, introducing noise in the physical measurements.

There are current limitations to avoid heating of components nearby the current carrying wire inside the *Quantum Design* device, and to avoid sparks between metallic pins in the cryostat. As per specifications of the PPMS, shaking currents above 100 mA have to be used with caution if the shaking current is carried via the internal all-purpose wires. In order to avoid this limitation, we bring the shaking current via the top of the inset, independently of the PPMS internal wiring.

2.3.2 Mechanical design

Figure 2.7 shows the complete assembly of the new PPMS inset. The global shape of the new inset casing is inspired from the commercial *Quantum Design* torque option. Since the direction of the external field is fixed, the sample has to be rotated in order to get angular dependent torque measurements. The rotation is ensured by a stepper motor (see Section 2.3.4) mounted on top of the inset, outside the cryostat. The movement is transmitted via a rod to the bottom of the assembly (shown in Fig. 2.8). The gears ensure the rotation of the sensor holder, the printed circuit board (PCB) clipped to it, and the sensor itself, glued to the PCB (see Section 2.3.3).

The goal of the sensor holder/PCB clipping is to enable the user to easily remove the sensor from the assembly in order to mount and dismount samples, or to change the piezoresistive sensor. The input and output of the sensor go through the PCB pins to the sensor holder, which is connected to the bottom puck of the PPMS via copper wires. Data acquisition devices outside the PPMS are connected through this puck to the sensor and to an additional Cernox thermometer in the sample chamber (not represented on the drawings for clarity). The coil current feed comes through the top of the PPMS to bypass current limitations. The contact between sensor holder and PCB is done by pins clipping into receptacles. If the pin and the receptacle are perfectly straight, the contact can be weak; if the pins are slightly skewed to insure better contact, fitting into the receptacles can then be compromised.

2.3.3 Wheatstone bridge sensor readout

The torque sensor is glued with silver paint on the printed circuit board (PCB), on which the Wheatstone bridge tracks are patterned in gold. The outputs lithographied on the sensor are bonded to the PCB tracks with aluminum wires. The readout of the changes in the piezoresistive legs resistance is made via the Wheatstone bridge. When it is well balanced, *i.e.* $R1 = R3 = R$ and $R2 = R + \Delta R$, $R4 = R - \Delta R$ (see Fig. 2.9), the output voltage V_{out} which is read is expressed easily as a function of the excitation voltage V_{in}:

$$V_{\text{out}} = -\frac{\Delta R}{2R} V_{\text{in}} \tag{2.3}$$

2.3.4 Motor assembly

The rotation of the angle between the field and the crystallographic axes of the investigated single crystal is ensured by a stepper motor (Fig. 2.10). A potentiometer is mounted on the motor shaft to provide basic feedback on the angle between the PCB and the vertical (which is the PPMS static field direction), as the motor controller does not provide it. This feedback is not accurate enough to be used in an angle correction loop for example, but it is useful to know roughly the position of the PCB. If there is a power or program failure, the position of the PCB (readout from the motor controller) can be erroneous, and since the whole inset is in a closed cryostat, it is not possible to determine the position visually. In that case, a direct readout of the potentiometer resistance can give an idea of the position without dismounting the inset from the cryostat, which necessitates a long warm up to room temperature. Knowing roughly the position of the motor is especially important because the torque sensor input/output wires soldered on the sensor holder wrap around the holder rotation shaft during a rotation of the PCB. If there is a mistake in the chosen rotation parameters, the resulting tight wire wrapping can result in ripping of soldering.

There is a small position hysteresis between the clockwise and counterclockwise directions of the motor, which has to be taken into account in the data analysis. It is possible to configure the motor to always reach an angle from the same direction (for example, increasing angles), by making it reach first a slightly lower angle in the case of a downwards movement, then up to the target angle. This method makes the whole downwards movement more noisy; since the hysteresis is constant, it is better to correct it by a post-treatment of the data than to suppress it at the cost of data quality.

The motor controller has to be manually configured, because the automatic configuration sends a large current to the motor coils (useful only in applications driving a heavy load, which is not the case here). This current can heat up the motor, which is problematic for the assembly thermal stability. Besides, the automatic stall detection is faulty (the controller is supposed to stop when it detects a 'stall', *i.e.* when a motor step has been lost), and this stall detector is systematically blocking the motor after a few degrees of rotation. We can be confident that this blocking is not due to an actual stalling issue, since stalling is usually due to a large load which is too heavy for the stepper motor, thus preventing it from completing a step and ending up in a stall state. Details on the motor command devices can be found in Appendix A.

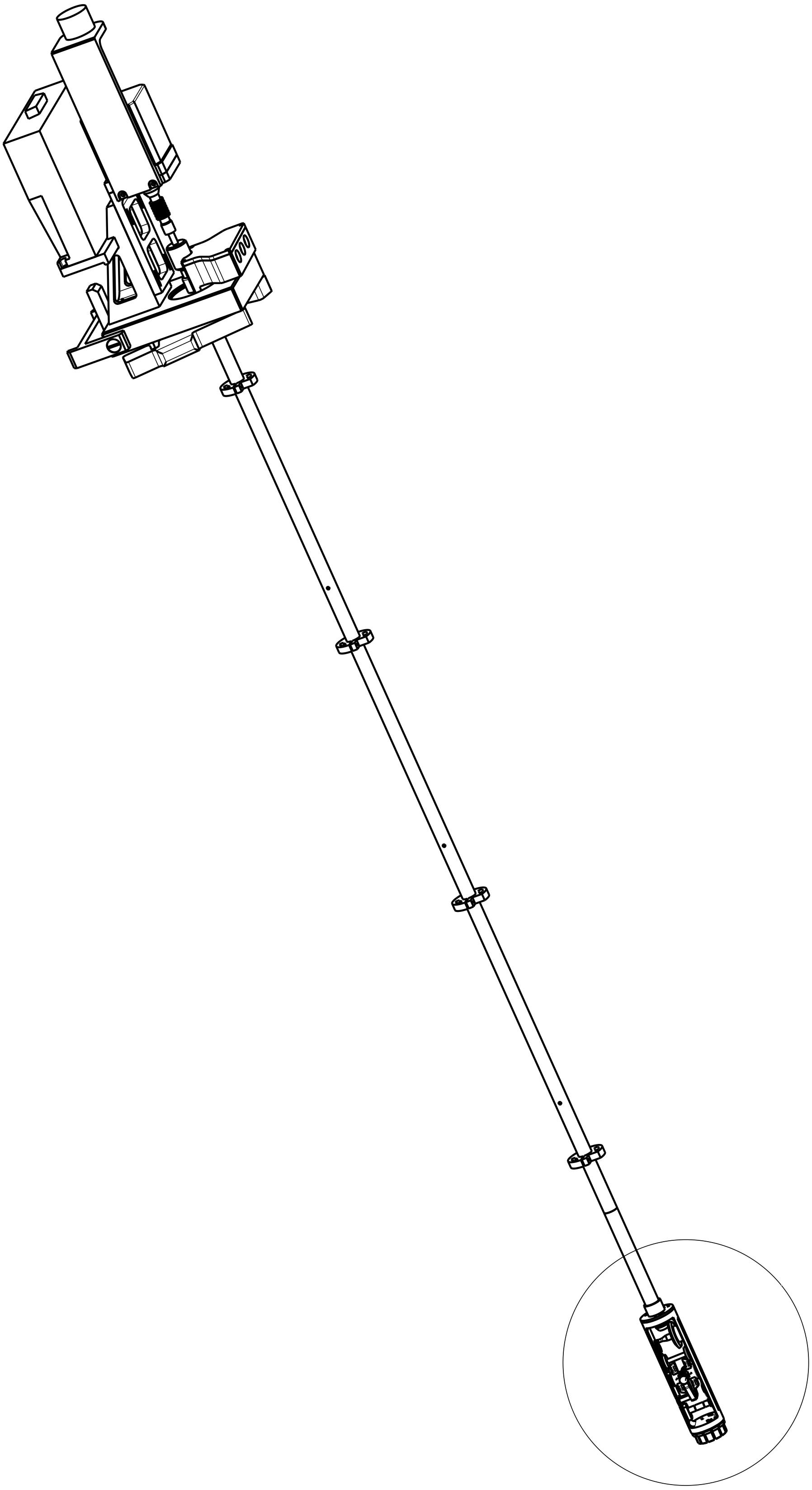

Figure 2.7: Global view of the new torque assembly. The motor and its controller are on the top of the rod, outside the cryostat. The circled part is shown in detail in Fig. 2.8.

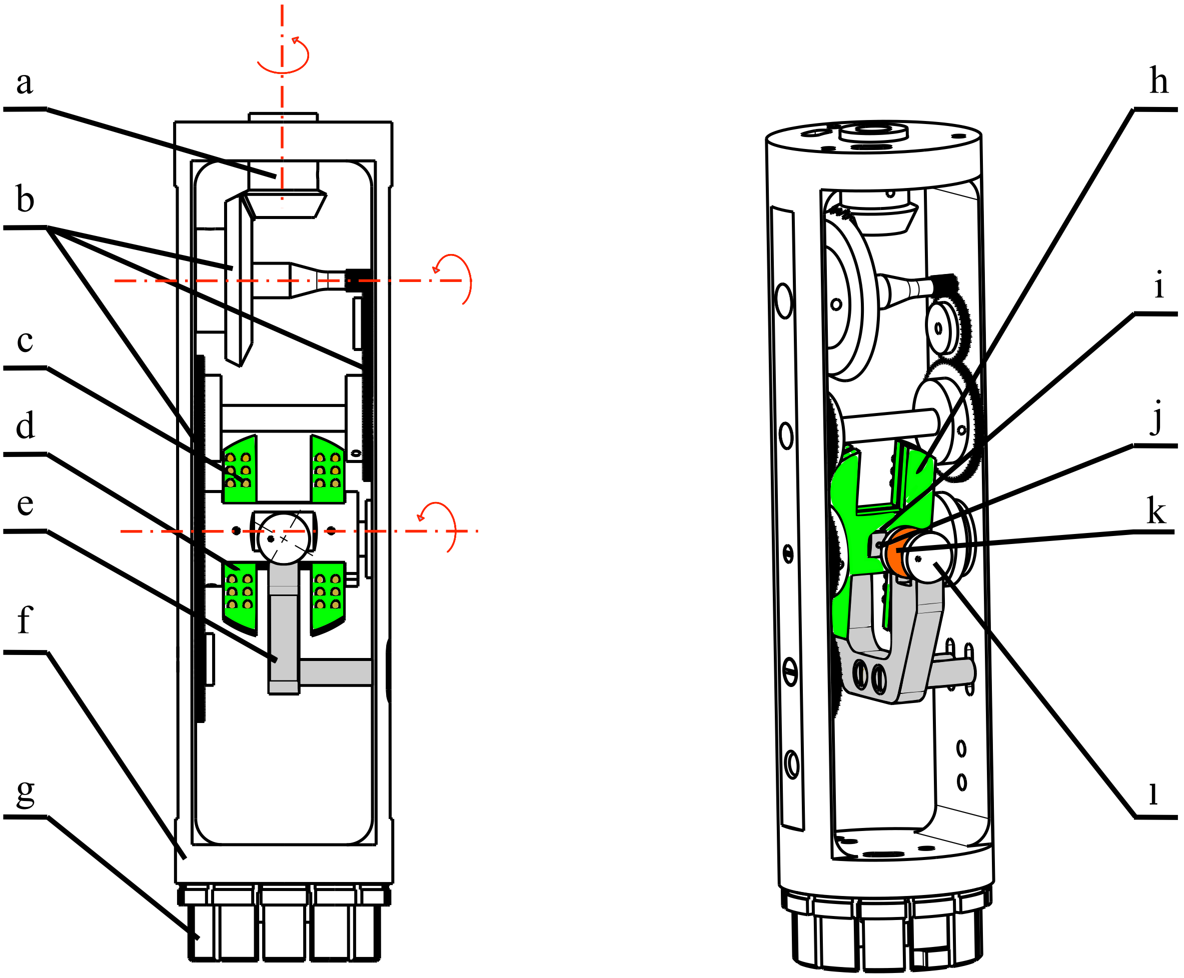

Figure 2.8: Side view and isometric view of the bottom magnetometer assembly placed at the bottom of the cryostat. The rotation axes are shown in red. a) Transmission axis. b) Gears bringing rotation to the sensor holder. The gear ratio is 1:14. c) Pin receptacles ensuring contact between the sensor holder and the sensor PCB. d) Sensor holder, fixed on the rotating axis. e) Shaking coils holder. f) Casing. g) Contact puck to the user bridge ports at the bottom of the cryostat. The contacts map is detailed in Fig. A.1. h) Sensor PCB, on which the torque sensor is glued and the Wheatstone bridge electrical tracks are patterned. i) Torque sensor. j) Measured sample. k) Shaking coil copper wire windings. l) Plastic coil support.

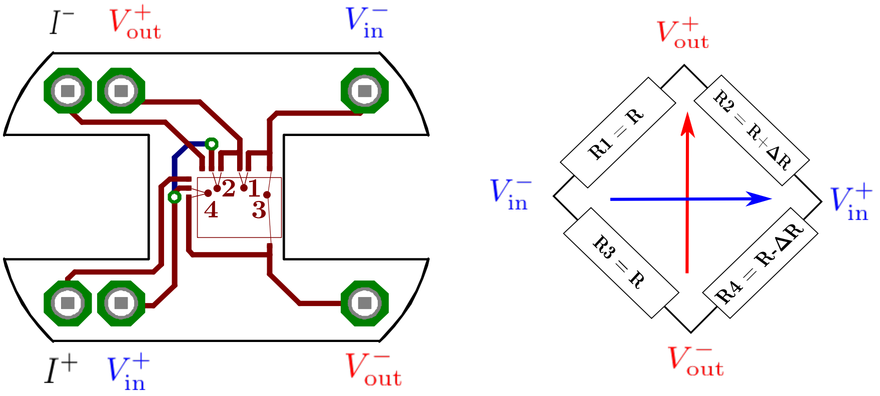

Figure 2.9: Schematic view of the sensor PCB implementing the Wheatstone bridge. The gold tracks are in red, the blue track is patterned on the other side of the PCB. R1, R2, R3, and R4 are the resistances of the four legs on the two sensors used in the measurement. One of the sensors is empty and used as reference (R1 and R3). The other holds the sample and has deviating resistances (R2 and R4). It is assumed that at rest (no torque is present) R1 = R2 = R3 = R4. This is experimentally valid within 1% accuracy. The calibration loop current is brought via the I^+ and I^- contacts.

2.3.5 Computer control

The experiment control is done with purpose-built Labview programs. Labview [43] is a graphical programming language which enables to easily create Virtual Instruments (VIs) with graphical user interfaces. Most laboratory devices come with Labview drivers, which is especially useful in the case of a motor control chain as the one used in our setup. An overview of the dependencies between the main Labview VIs is given in Fig. 2.11. Figure 2.12 shows a schematic representation of the experimental setup, while Fig. 2.13 show the main graphical user interfaces. TorqueControl.vi is the main input for the measuring sequence and the measurement parameters, while the other VIs principally display setup readings. The Labview version used in this work is 8.2.

2.3.6 Performance

The calibration of the sensors in the new setup yielded results consistent with the behavior of the sensors in the previous setup. As expected, the torque signal from a constant magnetic moment (from the calibration current loop integrated on the sensor platform) is a sine, with an amplitude increasing with increasing temperature.

The PPMS setup was tested with systems also investigated with the previous setup: $\mathrm{EuFe_2As_2}$ and $\mathrm{Rb_xFe_{2-y}Se_2}$. Figure 2.14 shows some typical torque measurements side by side for the 1.4 T and PPMS setups (without shaking). Due to crystal degradation, the tests could not be performed with the same samples that were measured in the 1.4 T setup. However, there is no difference in the noise level on the torque signal and the angle θ between both setups.

In order to test the efficiency of the vortex shaking coils, $\mathrm{YBa_2Cu_3O_{7-\delta}}$ crystals were measured at 0.94 T_c (Fig. 2.15). The shaken data appears more reversible; however, it is possible that this is actually an effect of the rise in temperature due to the coils Joule heating. A thermometer placed at a few centimeters of the samples and coils shows that there are small variations of temperature, which correlate exactly with the noise on the torque. The same thermometer, glued directly on the coils, shows very large temperature bursts, as high as 15 K, during shaking at maximal power. These can have a duration between a few seconds and half an hour. The previous shaking setup used sinusoidal shaking currents. In order to try to reduce the power dissipated in the coils when shaking, we tested a rectangular 200Hz AC current featuring short spikes instead of values changing between +A and -A. The success of shaking with this current profile would mean that vortices can be teared away from pinning centers by a short, large force just as well as by a continuous, weaker force. The duration of the spikes should stay above 1 ms, to avoid the inductance cutoff. However, this strategy did not yield significantly better stability. The temperature on the sample itself is likely not varying as much as the coil temperature, but one cannot exclude that the observed decrease in irreversibility is not due to vortex shaking, but to a higher sample temperature.

A possible way to enhance the temperature stability would be to use a thermometer placed near the sample as input for the PPMS temperature control. The PPMS thermometer is too far from the source of heat to register the temperature fluctuations, and therefore the PPMS feedback loop does not try to compensate the heat disturbances.

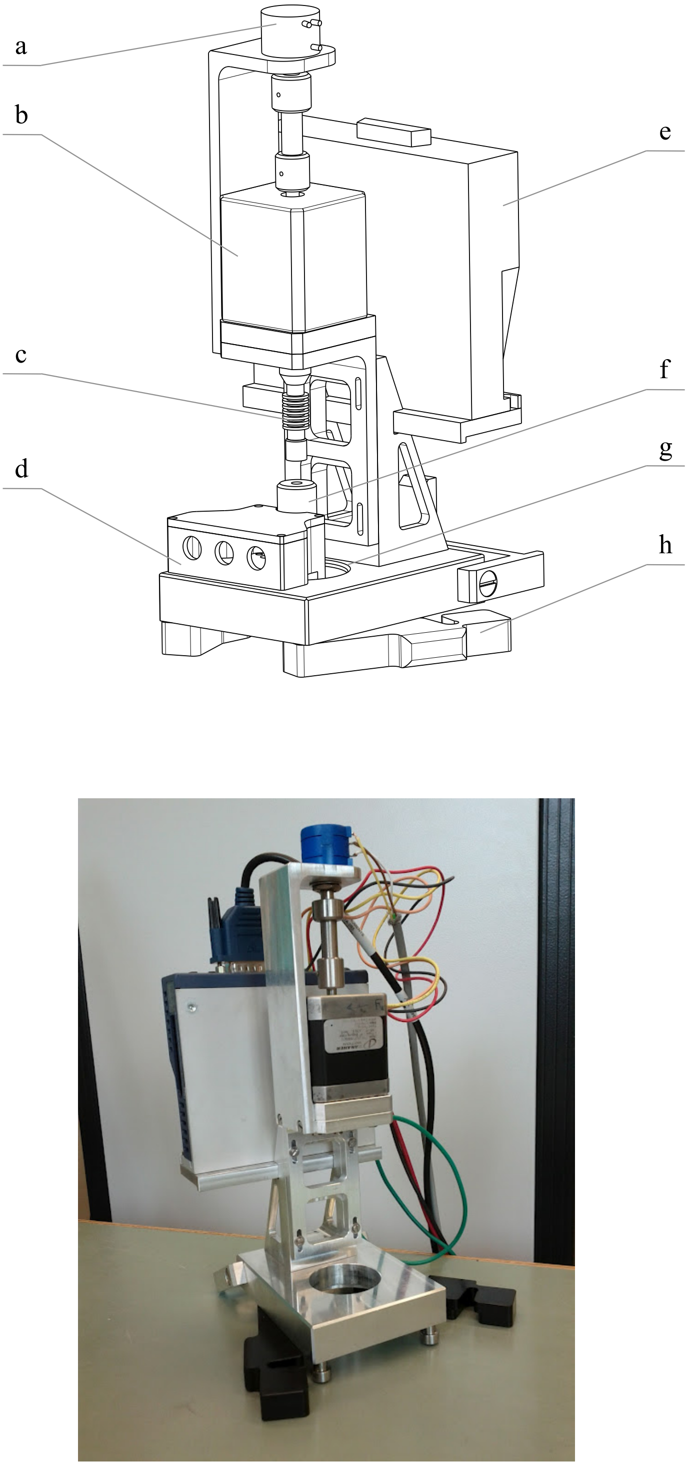

Figure 2.10: Isometric view and photograph of the motor assembly. a) Potentiometer for position feedback. b) Stepper motor. c) Connection between the motor shaft and the inset rod. The belows allow for some height tolerance. d) Connection box for supplementary wires running down to the sensors (if the pins at the bottom of the cryostat cannot be used). One of the connections is used for shaking current feed through. e) Motor driver. f) Top of the inset rod. g) O-ring sealing the cryostat when this motor motor assembly is in place. h) Clamps holding the assembly on the top of the PPMS.

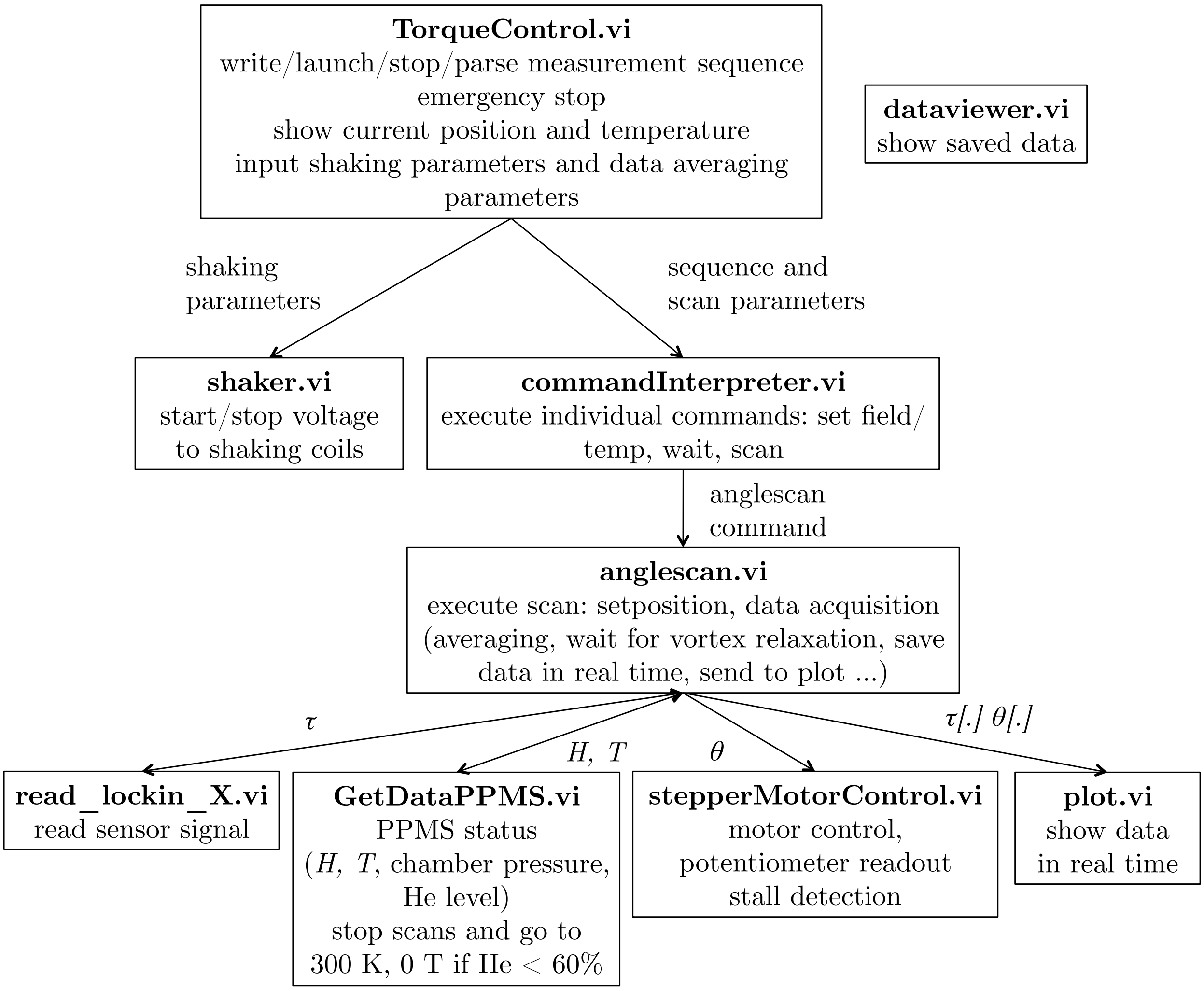

Figure 2.11: Schematic architecture of the main programs functions and dependencies. The arrows denote which data is passed on between programs and their subprograms. The main graphical user interface is TorqueControl.vi (Fig. 2.13).

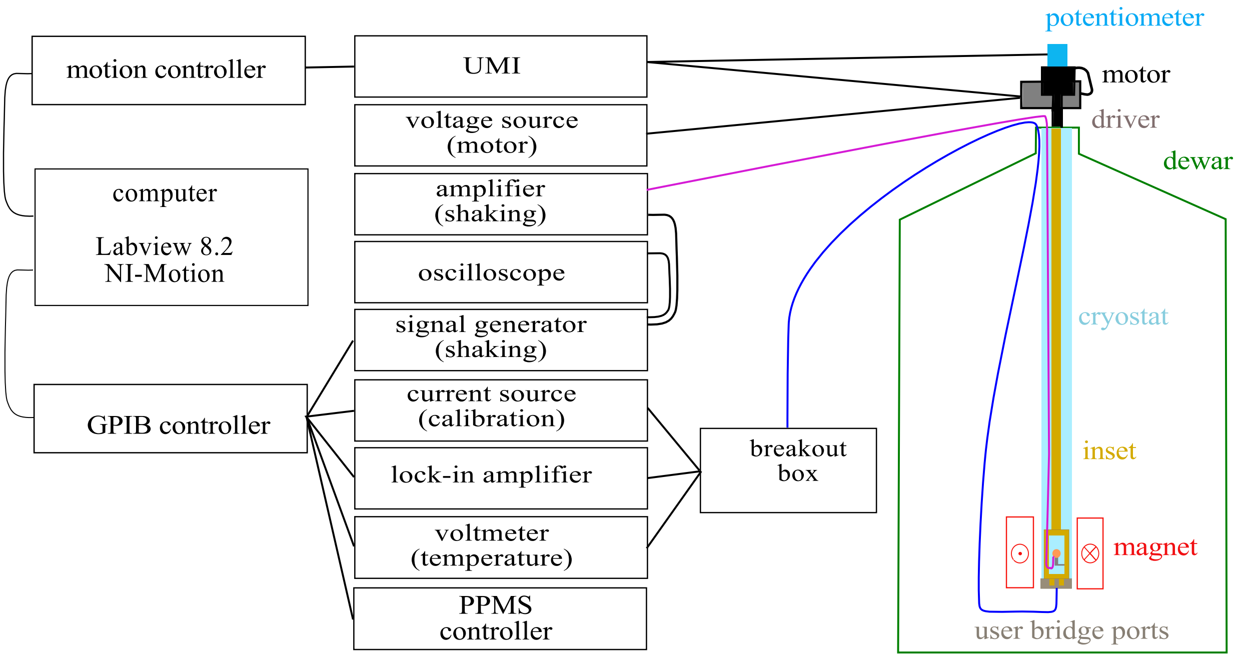

Figure 2.12: Schematic representation of the experimental setup. The breakout box routes the user bridge connections from the PPMS to ad-hoc devices.

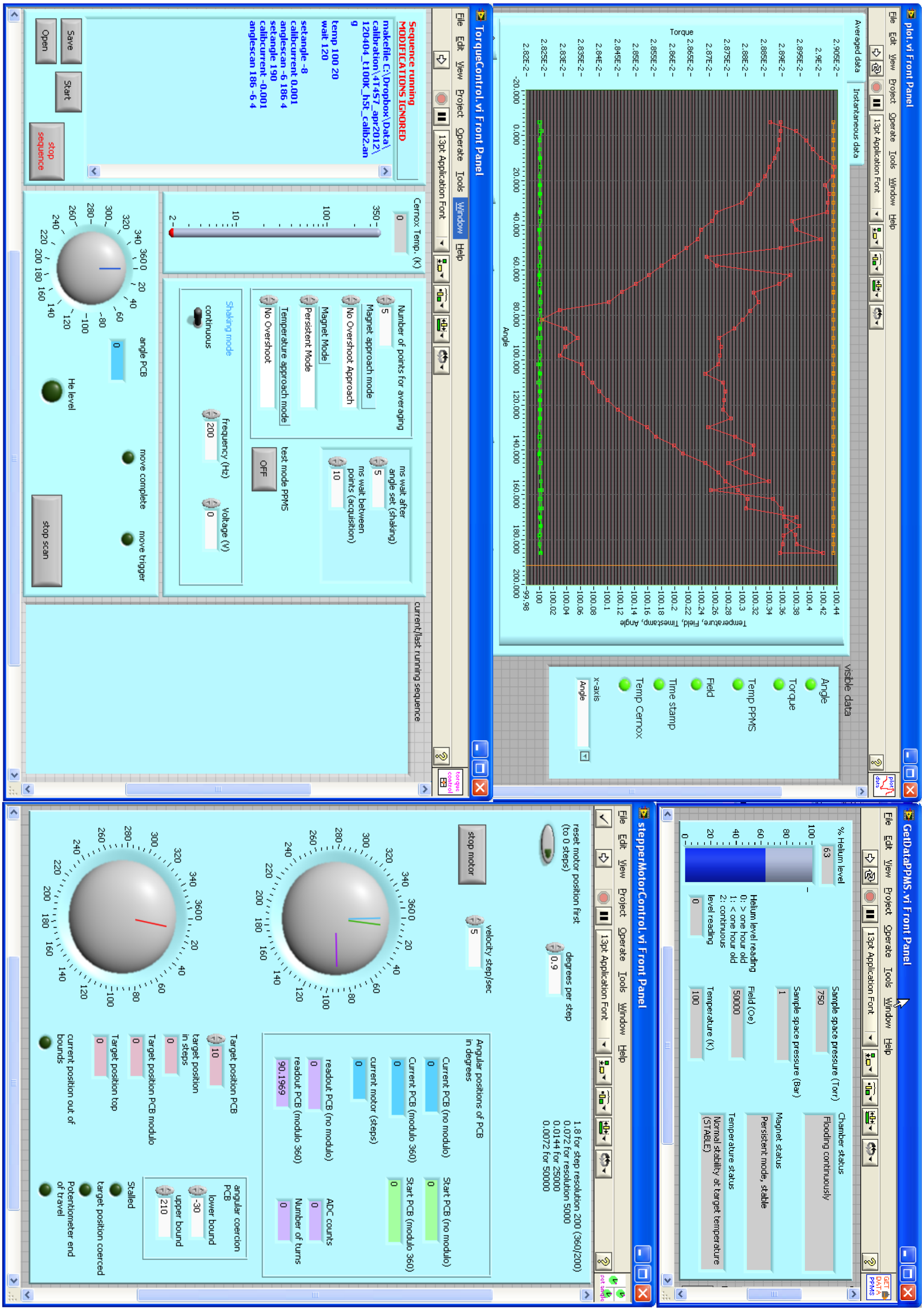

```
Sequence running
MODIFICATIONS IGNORED
makefile C:\Dropbox\Data\calibration\4T457_apr2012\120404_t100K_h5t_calib2.ang
temp 100 20
wait 120
setangle -8
calibcurrent 0.001
anglescan -6 186 4
setangle 190
calibcurrent -0.001
anglescan 186 -6 4
```

Cernox Temp. (K): 0

Number of points for averaging: 5

Magnet approach mode: No Overshoot Approach

Magnet Mode: Persistent Mode

Temperature approach mode: No Overshoot

ms wait after angle set (shaking): 5

ms wait between points (acquisition): 10

test mode PPMS: OFF

Shaking mode: continuous

frequency (Hz): 200

Voltage (V): 0

angle PCB: 0

visible data: Angle, Torque, Temp PPMS, Field, Time stamp, Temp Cernox

x-axis: Angle

% Helium level: 63

Helium level reading 0: > one hour old 1: < one hour old 2: continuous level reading: 0

Sample space pressure (Torr): 750

Sample space pressure (Bar): 1

Field (Oe): 50000

Temperature (K): 100

Chamber status: Flooding continuously

Magnet status: Persistent mode, stable

Temperature status: Normal stability at target temperature (STABLE)

reset motor position first (to 0 steps)

degrees per step: 0.9

velocity step/sec: 5

1.8 for step resolution 200 (360/200)
0.072 for resolution 5000
0.0144 for 25000
0.0072 for 50000

Angular positions of PCB in degrees

Current PCB (no modulo): 0

Current PCB (modulo 360): 0

current motor (steps): 0

readout PCB (no modulo): 0

readout PCB (modulo 360): 90.1969

Start PCB (no modulo): 0

Start PCB (modulo 360): 0

ADC counts: 0

Number of turns: 0

Target position PCB: 10

target position in steps: 0

Target position PCB modulo: 0

Target position top: 0

angular coercion PCB lower bound: -30

upper bound: 210

Figure 2.13: Main graphical user interfaces TorqueControl.vi, plot.vi, GetDataPPMS.vi, and stepperMotorControl.vi.

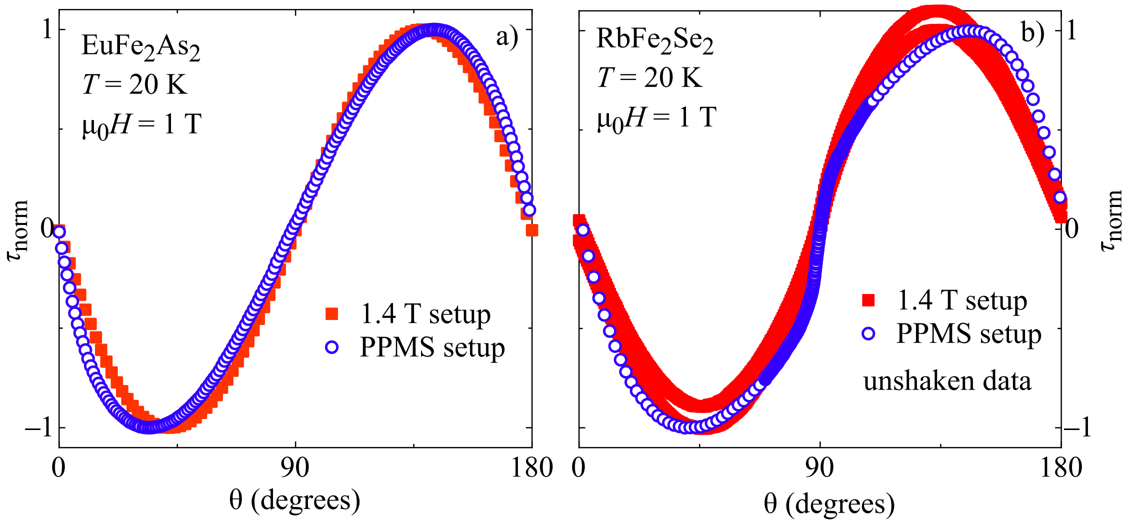

Figure 2.14: a) Comparison of the normalized angular torque from EuFe$_2$As$_2$ in the 1.4 T and PPMS setups at 20 K and 1 T. b) Comparison of the normalized angular torque from Rb$_x$Fe$_{2-y}$Se$_2$ in the 1.4 T and PPMS setups at 20 K and 1 T. In both cases, the measurements were done with crystals from different batches, resulting in difference of the torque shape. The newer samples (measured in the PPMS) have larger impurity phases.

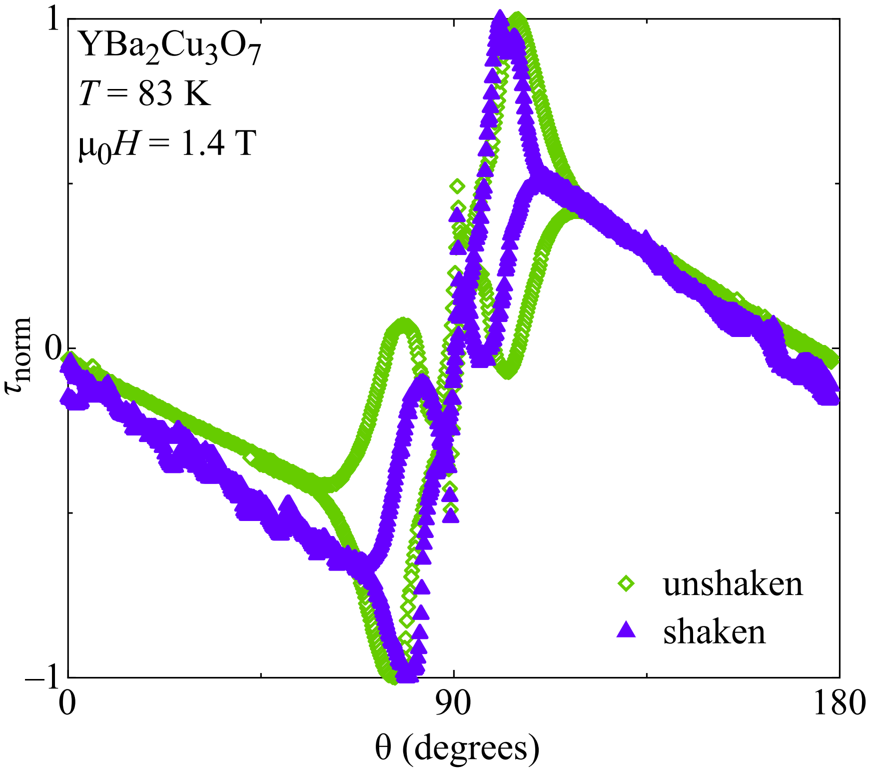

Figure 2.15: Shaken and unshaken torque on single crystal YBa$_2$Cu$_3$O$_{7-\delta}$ at 83 K and 1.4 T in the PPMS setup. The temperature fluctuations of the coils due to Joule heating can reach 15 K.

CHAPTER 3

Anisotropic behavior of $YBa_2Cu_3O_{7-\delta}$

$YBa_2Cu_3O_{7-\delta}$ was the first high-temperature superconductor with a critical temperature above the boiling point of nitrogen [44]. It belongs to the family of layered cuprates, in which superconductivity is supported by the CuO_2 planes. The crystal structure of $YBa_2Cu_3O_{7-\delta}$ is represented in Fig. 3.1. Since its discovery growth techniques have been substantially improved, yielding high-quality single crystals [45]. The high T_c, high crystal quality, and an anisotropy that is relatively low among cuprate superconductors make $YBa_2Cu_3O_{7-\delta}$ a well-balanced compound to test the limits of the London approximation.

For simplicity, the London approximation of the anisotropic Ginzburg-Landau theory (AGLT) [19, 22] is often used for analyzing experimental data. It consists in neglecting the effects of the vortex cores. However, as pointed out by Hao and Clem, this approximation may not necessarily be adapted to the interpretation of magnetization measurements like torque magnetometry [46, 47, 48]. A comparison of those two models is provided in the first section of this Chapter. The London model is 3-dimensional (3D). Although $YBa_2Cu_3O_{7-\delta}$ has a low anisotropy, there are indications [26, 49, 50, 51, 52] that it displays lock-in effects [53]. This is typical of 2-dimensional (2D) systems, and therefore is a deviation from the London model. The second section of this Chapter describes lock-in effects observed in $YBa_2Cu_3O_{7-\delta}$.

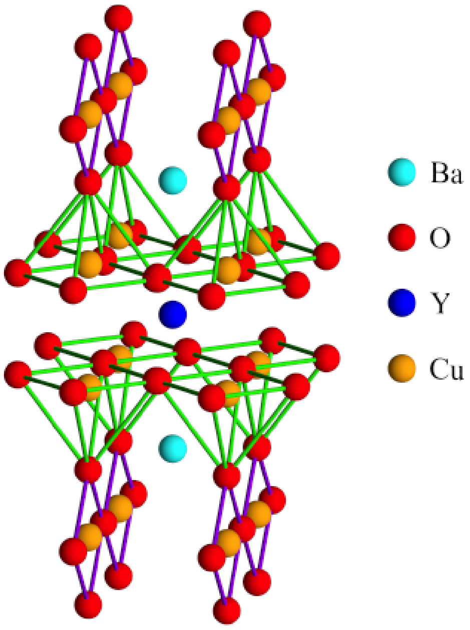

Figure 3.1: Crystal structure of $YBa_2Cu_3O_{7-\delta}$, underlining the superconducting CuO_2 planes, the pyramid configuration of the oxygen atoms around the Cu in the planes, and the Cu-O chains.

3.1 The London and the Hao-Clem model

The magnetic torque is thermodynamically defined as (see Chap.1):

$$\tau(\theta) = -\frac{\partial F}{\partial \theta}. \tag{3.1}$$

The free energy F depends on the distribution of vortices inside the superconductor. There are various ways of modeling these vortices in order to get an analytical expression for F. In the London model, the finite vortex core size is neglected. This is valid if the vortex core size is small compared to the vortex itself, *i.e.* the penetration depth is much larger than the coherence length.

The torque τ in the London model is given by Eq. (1.11):

$$\tau_{\mathrm{L}}(\theta, H) = -\frac{V\Phi_0 H}{16\pi\lambda_{ab}^2}\left(1-\frac{1}{\gamma^2}\right)\cdot\frac{\sin(2\theta)}{\epsilon(\theta)}\ln\left(\frac{\eta H_{\mathrm{c2}}^{||c}}{\epsilon(\theta)H}\right). \tag{3.2}$$

In a tetragonal crystal, the anisotropy of interest is $\gamma = \lambda_c/\lambda_{ab}$ (where $\lambda_{ab} = \sqrt{\lambda_a\lambda_b}$). The parameter η accounts for uncertainties due to the approximation of the London limit. It stems from a cutoff in the integration of a Fourier expression of the free energy.

Hao and Clem [46] showed that the parameter η cannot be field-independent in the entire vortex state ($H_{\mathrm{c1}} < H < H_{\mathrm{c2}}$). Their derivation of F includes the vortex core contribution to the free energy functional [46, 47, 48]. The empirical functions $\alpha(h)$ and $\beta(h)$, where h denotes the reduced field $H/H_{\mathrm{c2}}(\theta)$, are added in the expression for the magnetization M and torque τ. Their generalization yields a refined formula for the magnetization [46]

$$M_{\mathrm{HC}}(\theta, H) = -\alpha(h(\theta))\frac{\Phi_0\epsilon(\theta)}{8\pi\mu_0\lambda_{ab}^2}\ln\left(\frac{\beta(h(\theta))}{h(\theta)}\right), \tag{3.3}$$

resulting with Eq. (3.1) in the torque:

$$\tau_{\mathrm{HC}}(\theta, H) = -\alpha(h(\theta))\frac{V\Phi_0 H}{16\pi\lambda_{ab}^2}\left(1-\frac{1}{\gamma^2}\right)\cdot\frac{\sin(2\theta)}{\epsilon(\theta)}\ln\left(\frac{\beta(h(\theta))}{h(\theta)}\right). \tag{3.4}$$

The functions $\alpha(h)$ and $\beta(h)$ refine the in-plane magnetic penetration depth λ_{ab} and the c-axis upper critical field $H_{\mathrm{c2}}^{||c}$, respectively. For $\alpha(h) = 1$ and $\beta(h) = \eta$, Eq. (3.4) reduces to the London limit Eq. (3.2). The original Hao-Clem (HC) model for the free energy does not make use of the phenomenological functions $\alpha(h)$ and $\beta(h)$.

The field dependence of the reduced magnetization $M_{\mathrm{HC}}(h)/H_{\mathrm{c2}}$ (Fig. 3.2a) can be numerically calculated and compared with Eq. (3.3) in order to extract $\alpha(h)$ and $\beta(h)$. This calculation of M_{HC} consists in solving the implicit equation of B as a function of H defined in [47] [Eq. (20)]; the assumption that $\kappa > 10$ is necessary. Since Eq. (3.3) can be written as $\alpha(h)A\log(H)+\log(\beta(h))B$, where A and B are known parameters, a local linear regression of the numerical $M_{\mathrm{HC}}(h)$ at each point h yields the value of $\alpha(h)$ and $\beta(h)$.

For $\kappa > 50$, the functions $\alpha(h)$ (Fig. 3.2b) and $\beta(h)$ (Fig. 3.2c) become essentially independent of κ, even when taking into account the angle dependence of κ resulting from the crystal anisotropy. The functions $\alpha(h)$ and $\beta(h)$ thus derived are in good agreement with the particular values estimated by Hao and Clem [46].

3.2 Temperature dependence of the anisotropy

All high-temperature superconductors, whether cuprates or iron-based, have a layered structure. Anisotropic behavior is thus expected from superconducting parameters like the magnetic field

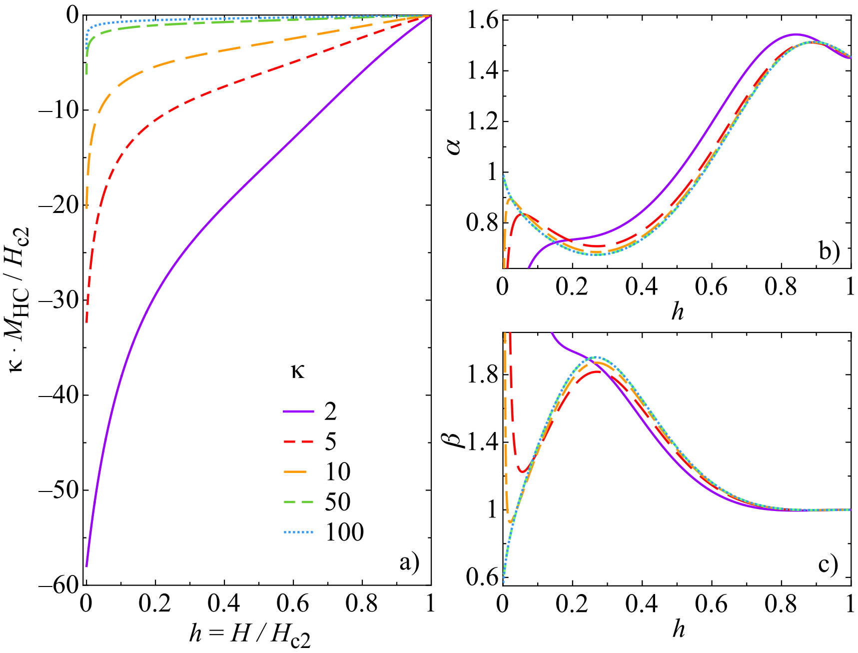

Figure 3.2: a) $\kappa M_{\mathrm{HC}}(h)/H_{\mathrm{c2}}$ for various values of κ calculated using the HC model. For better curve separation, $\kappa M_{\mathrm{HC}}(h)/H_{\mathrm{c2}}$ is shown instead of $M_{\mathrm{HC}}(h)/H_{\mathrm{c2}}$. b) Empirical parameter $\alpha(h)$ extracted from $M_{\mathrm{HC}}(h)/H_{\mathrm{c2}}$. c) Empirical parameter $\beta(h)$ extracted in the same way as $\alpha(h)$ in panel b).

penetration depth, the upper critical fields, and the energy gap. In the AGLT, the anisotropy $\gamma = \lambda_i/\lambda_j = \sqrt{m_i^*/m_j^*} = H_{\mathrm{c2}}^{||j}/H_{\mathrm{c2}}^{||i}$ is temperature independent. However, a temperature dependence, and even sometimes a field dependence of γ is observed in $\mathrm{MgB_2}$ and iron-based superconductors, which are known to be multigap superconductors. This dependence may thus be linked to multigap superconductivity [54], as also suggested in [55]. Since this temperature dependence seems more common than expected, it is interesting to know if the anisotropy of layered high-temperature superconductors are systematically temperature dependent, and what the shape of this dependence is. For example, the anisotropy of underdoped $\mathrm{SmBa_2Cu_3O_{7-\delta}}$ is temperature dependent [56]. This compound features a well developed pseudogap, *i.e.* an additional energy scale which may play a similar role in the development of the temperature dependence of the anisotropy as the multigap structure. We thus extended the anisotropy studies to the overdoped cuprate $\mathrm{YBa_2Cu_3O_{7-\delta}}$, in which we expect no pseudogap effects.

The torque data (Fig. 3.3) of single crystal $\mathrm{YBa_2Cu_3O_{7-\delta}}$ are analyzed with the Hao-Clem [Eq. (3.4)] and with the Kogan model [Eq. (3.2)]. Both models yield similar values for γ_{cb} within 2% accuracy (Fig. 3.4a). Moreover, the results depend only weakly on the value taken for $H_{\mathrm{c2}}^{||c}$ (Fig. 3.4b) and on the external field (Figs. 3.4c and 3.4d). The errors of the fit parameters γ_{ij} and λ_{ab} were estimated with a bootstrapping method: different fits were performed for randomly sampled points within the experimental error of the measured data points. The final values of the parameters γ and λ were taken as the average values obtained by this procedure, and their errors were defined as twice the standard deviation of these results. The estimated error bars are smaller than the size of the data points.

Over the temperature range studied, γ_{ca} as well as γ_{cb} slightly increase with decreasing temperature (Fig. 3.5a), whereas the in-plane anisotropy parameter γ_{ab} is temperature independent. The torque data were analyzed here under the assumption that the field and penetration depth

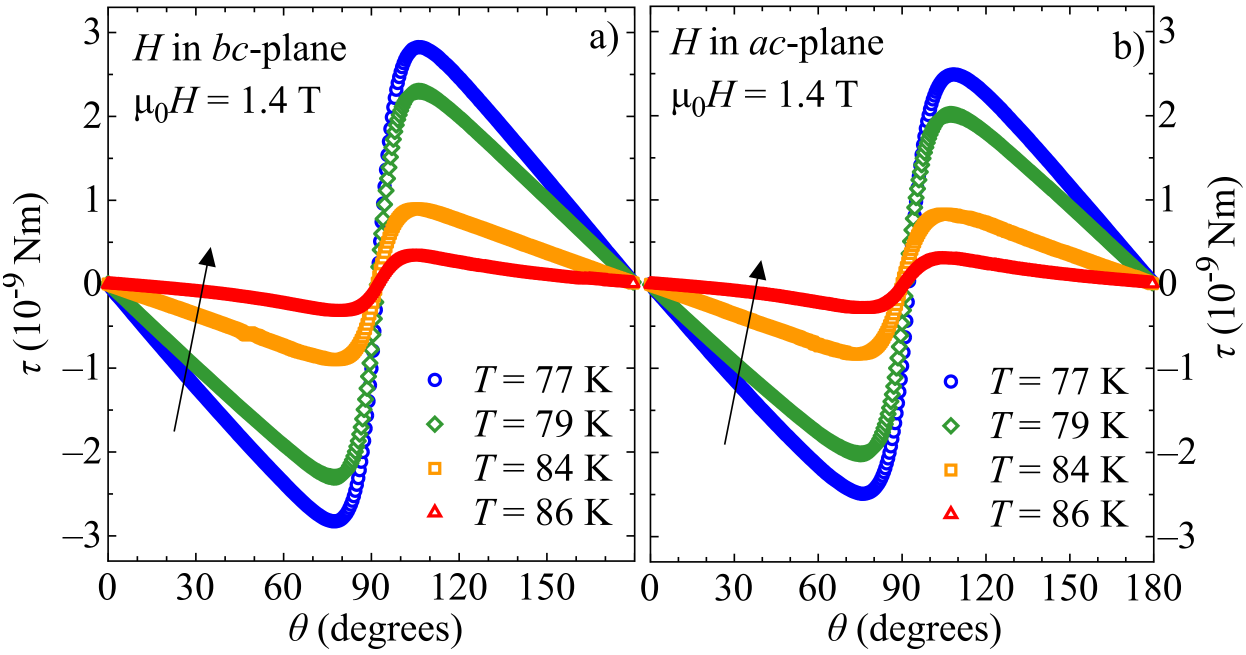

Figure 3.3: Angular dependent torque measurements of a single crystal $YBa_2Cu_3O_{7-\delta}$ taken in the temperature range between 77 K and T_c = 88 K at 1.4 T. The temperature range of the angular measurements was chosen such as to avoid the lock-in effect (see Section 3.3) [57], which influences the torque in a way not accounted for in Eq. (3.4). The upper temperature bound was chosen such as to stay below the fluctuation regime close to T_c. Fluctuation effects [58] are not taken into account in the mean-field approximation of the AGLT. As $YBa_2Cu_3O_{7-\delta}$ has an orthorhombic structure, measurements as a function of angle need to be performed in both the *bc*-plane and *ac*-plane in order to confirm that the uniaxial approximation [59] is correct. The arrows indicate increasing temperature. These raw data include a sinusoidal paramagnetic background. a) Measurements with *H* in the *bc*-plane. b) Measurements with *H* in the *ac*-plane.

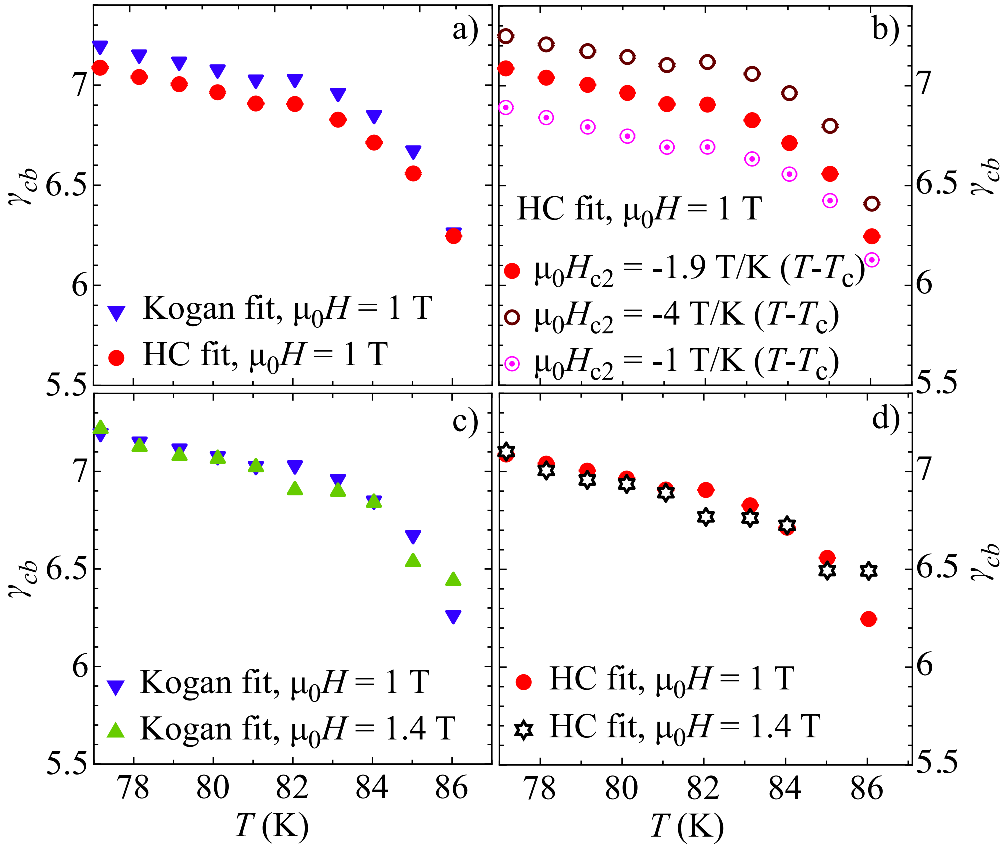

Figure 3.4: Overview of the results of the angular dependent magnetic torque measurements of single crystal $YBa_2Cu_3O_{7-\delta}$ for various temperatures and fields. a) Comparison of γ_{cb} for the HC and Kogan model at fixed $\mu_0 H = 1$ T and fixed upper critical field ($\mu_0 dH_{c2}^{||c}/dT = -1.9$ T/K). The Kogan model yields a slightly larger anisotropy parameter than the HC model. b) γ_{cb} for the HC model at $\mu_0 H = 1$ T and various upper critical fields. The parameter $\mu_0 dH_{c2}^{||c}/dT$ does not change the shape of $\gamma(T)$. c) γ_{cb} for the Kogan model at $\mu_0 H = 1$ T and $\mu_0 H = 1.4$ T and fixed upper critical field ($\mu_0 dH_{c2}^{||c}/dT = -1.9$ T/K). d) γ_{cb} for the HC model, same conditions as in panel c). Panels c) and d) show that the field dependence of γ is only marginal; the final γ is taken as the average of the values for both fields.

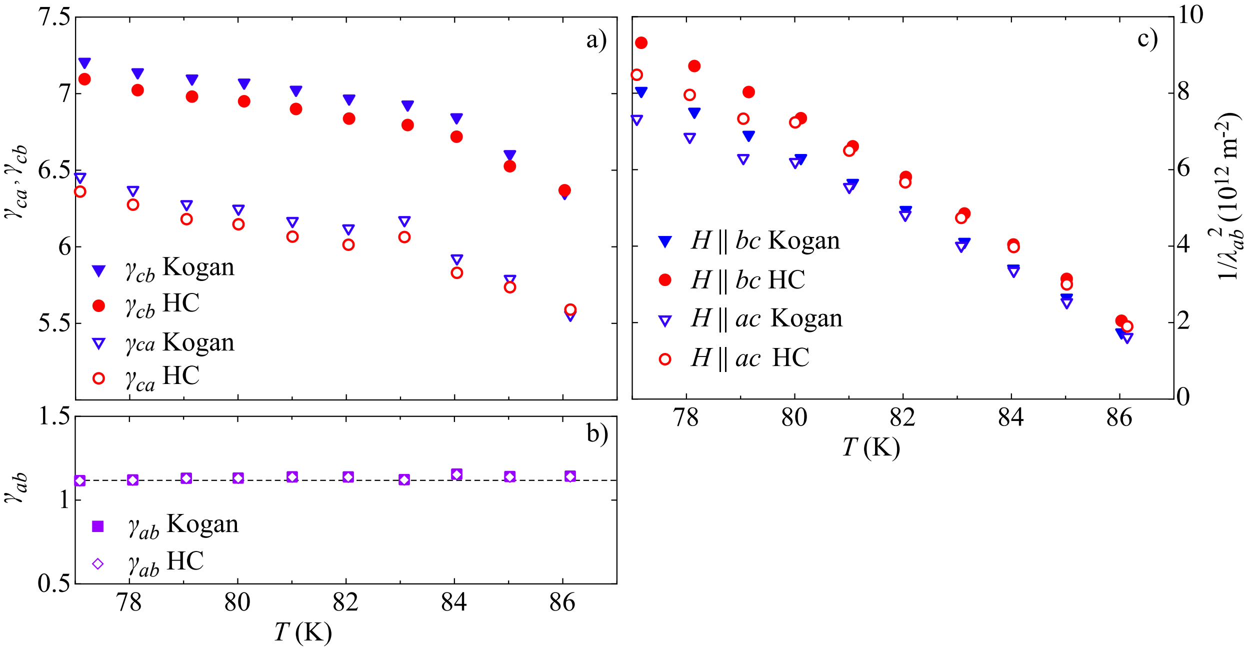

Figure 3.5: a) Temperature dependence of the anisotropy parameters γ_{ca} and γ_{cb} for single crystal $YBa_2Cu_3O_7$. b) Temperature dependence of the in-plane anisotropy parameter γ_{ab}. The dotted line is the average $\gamma_{ab} = 1.12(5)$. c) Temperature dependence of $1/\lambda_{ab}^2$ for measurements with H parallel to the ac- and bc- planes.

anisotropy parameters are equal. It is possible to generalize this analysis to the multigap case, where these parameters are not equal [25]. Such an analysis of the present torque data would not provide reliable results due to the excessive number of fit parameters. However, we expect any multiband effects in $YBa_2Cu_3O_{7-\delta}$ to be rather weak, allowing to take the field and penetration depth anisotropy parameters as equal.

The anisotropy of Pr-doped $YBa_2Cu_3O_{7-\delta}$ [52] and $HgBa_2Ca_3Cu_4O_{10}$ [60] was found to be temperature independent, but was studied over narrow temperature ranges only. A temperature dependent anisotropy parameter was seen in MgB_2 [36] and later in iron-based superconductors [61, 39], and was consistently described in the framework of two-gap superconductivity. This may suggest that our $YBa_2Cu_3O_{7-\delta}$ results are a signature of two-gap superconductivity, as proposed in Ref. [62]. However, the well pronounced temperature dependence of the anisotropy for strongly underdoped samples [56] becomes weak in our overdoped $YBa_2Cu_3O_{7-\delta}$. This may be related to the evolution of the pseudogap with oxygen doping in $YBa_2Cu_3O_{7-\delta}$. It suggests that an additional energy scale to the system's superconducting energy gap is necessary to get a temperature dependent out-of-plane anisotropy parameter in layered superconductors. Such an energy scale may originate from the multigap nature of superconductivity and/or from the appearance of the pseudogap.

3.3 The lock-in transition

In highly anisotropic superconductors ($\gamma > 50$), the superconducting planes are in general almost decoupled, and physical phenomena are quasi two-dimensional. This behavior can be described by the Lawrence-Doniach model [63], in which the planes are treated within the GL model, and are

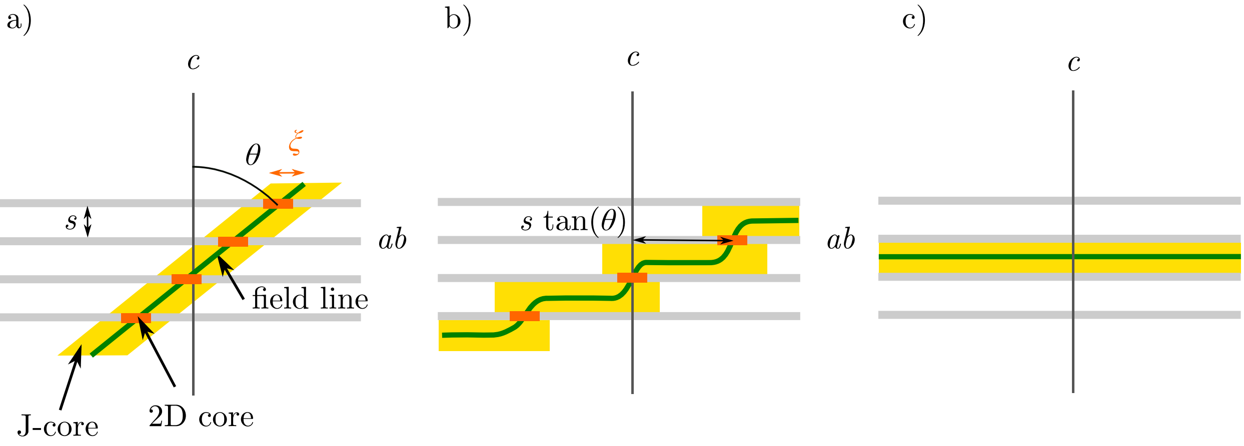

Figure 3.6: Vortex profile in an anisotropic superconductor below the dimensional crossover temperature T_{cr} for different applied field directions. The gray lines represent the superconducting layers, the orange zone is the vortex core, the yellow area is the vortex 'nucleus', and the green line is a magnetic field line. a) $\tan(\theta) < \gamma$: straight vortex, the superconducting cores are confined in the layers, and linked by Josephson nuclei. b) $\tan(\theta) > \gamma$: the distance between two superconducting cores is larger than the Josephson length γs, resulting in a staircase shape. c) $\theta \simeq 90°$: the vortex is locked between the superconducting layers.

coupled to each other by Josephson currents [64].

Even in lower anisotropy systems like $\mathrm{YBa_2Cu_3O_{7-\delta}}$ ($\gamma \approx 7$), a 3D to 2D crossover can take place when the superconducting coherence length along the c-axis ξ_c becomes smaller than the distance s between the planes supporting superconductivity [65]. Since $\xi_c(T) = \xi_{c,0}/\sqrt{1 - T/T_c}$ (where $\xi_{c,0} = \xi_c(T = 0\ \mathrm{K})$), the crossover temperature T_{cr} may eventually be such that $\xi_c(T_{\mathrm{cr}}) = s$. For $\mathrm{YBa_2Cu_3O_{7-\delta}}$, $s \simeq 0.8$ nm [49], $\xi_{c,0} \simeq 0.3$ nm [66], and $T_c \approx 88$ K [67], so $T_{\mathrm{cr}} \simeq 76$ K. Note that the interplane distance s in $\mathrm{YBa_2Cu_3O_{7-\delta}}$ corresponds to the distance between a 'top' plane and the next 'bottom' plane (see Fig. 3.1), and not to the size of the unit cell along the c-axis.

In the vortex state below T_{cr}, for large inclinations of the applied magnetic field, *i.e.* $\tan(\theta) < \gamma$ (where θ is the angle between the applied field and the c-axis and γ is the anisotropy), the vortex lines are not straight anymore (see Fig. 3.6a and b). The condition $\tan(\theta) < \gamma$ means that the Josephson coherence length $\lambda_J = s\gamma$ is smaller than the distance between two consecutive vortex cores (Fig. 3.6b). This corresponds to a staircase configuration [57]. The order parameter inside the vortex center is not suppressed between the layers, because the circulating currents are Josephson currents and not superconducting currents (yellow zone in Fig. 3.6b). This Josephson-type core is sometimes called 'nucleus'. The order parameter is only suppressed within the superconducting layers (orange zone in Fig. 3.6b). The vortex consists of 2D cores in the layers, linked by Josephson nuclei between the layers. The physics remains 3D on large scales: corrections to the London model only concern the vortex core contribution, but the free energy still deviates from the 3D London model [68].

When the applied magnetic field direction is nearly parallel to the ab-plane, a lock-in transition of the vortices may take place [53]. In this case, the vortex is confined between the superconducting layers, even though the field is not aligned with these layers (see Fig. 3.6c). This minimizes superconducting condensation energy at the cost of magnetic energy coming from the misalignment of vortices and field, since the cores do not cross the layers anymore. This is also known as intrinsic pinning, since it immobilizes the vortices independently of impurities (which are extrinsic to the crystal). It was observed mainly in high anisotropy materials (mainly TlBaCuO [69, 70, 71],

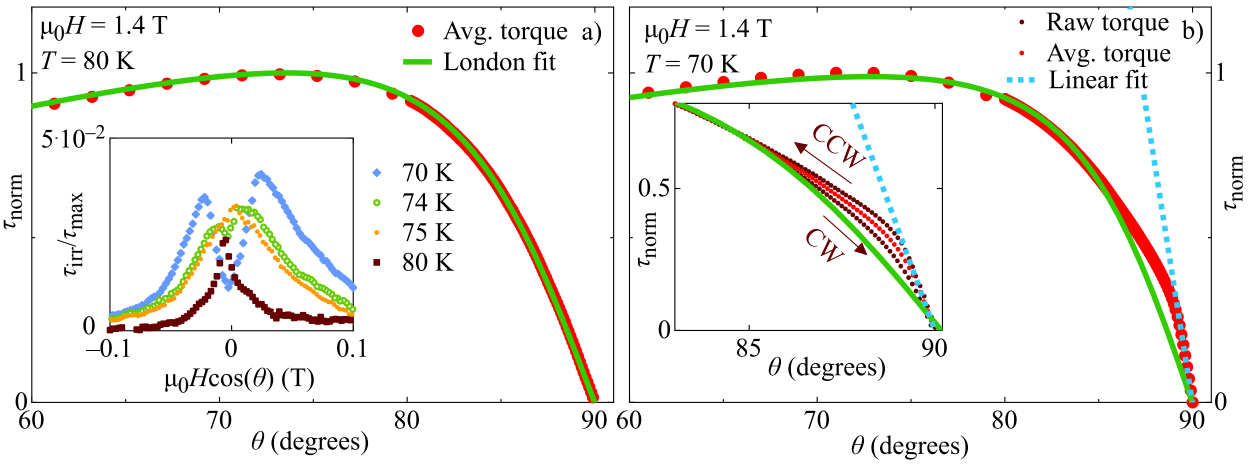

Figure 3.7: a) Normalized torque τ_{norm} of detwinned single crystal $YBa_2Cu_3O_{7-\delta}$ as a function of angle θ at 80 K and 1.4 T. The torque follows the London dependence at all angles. The green line is a fit of Eq. (1.11) to the data. The light red points represent an average of the CW and CCW angle measurements. Inset: Irreversible component of the torque $\tau_{\text{irr}} = (\tau_{\text{CW}} - \tau_{\text{CCW}})/2$ normalized to the maximum of the averaged torque at various temperatures at 1.4 T. b) Normalized torque τ_{norm} as a function of angle at 70 K and 1.4 T. The dotted blue line is a linear fit of the lock-in region. Inset: Close-up around the *ab*-plane. The two dark red curves (CW and CCW) are the raw torque. The arrows indicate the field sweep direction for each branch.

BSCO [72], and HgBaCuO [73]), but also in $YBa_2Cu_3O_{7-\delta}$ ([26, 49, 50, 51, 52]) and other layered superconductors (for example Nb/Cu multilayers [74], organic superconductors [75], LSCO [76, 77, 78], and ErBaCuO [79]). $YBa_2Cu_3O_{7-\delta}$ is of particular interest for lock-in studies, since its low anisotropy allows one to observe the onset of lock-in far from T_c, where critical fluctuations makes the analysis more difficult. Many theoretical models of the lock-in have been proposed [65]. The models most relevant to this work are presented in [80] and [57].

As seen on Fig. 3.7, the torque measured in $YBa_2Cu_3O_{7-\delta}$ deviates from the London model at low temperatures. This shape of the torque graph is the same as predicted in [57] (Fig. 3.8). Interestingly, this model was originally developed for quasi-2D superconductors, with $\gamma \approx 50$, and not $\gamma \approx 7$ like $YBa_2Cu_3O_{7-\delta}$. The first deviation from the London model corresponds to the staircase state, the second deviation (slope change of the torque, which becomes linear) corresponds to the lock-in transition. The field range is in the London regime $H_{c1} << H << H_{c2}$, which excludes interfering effects due to vortex lattice melting or glass behavior.

Torque data often present an angular irreversibility between the clockwise (CW) and counter-clockwise (CCW) branches, which is usually due to pinning and can be reduced by the shaking technique (see Section 2.2 for details). The shape of the normalized irreversible torque $\tau_{\text{irr}} = (\tau_{\text{CW}} - \tau_{\text{CCW}})/(2\tau_{\text{max}})$ (shown in the inset of Fig. 3.7a) changes when the lock-in appears. Double peaks in τ_{irr} have been observed and linked to the lock-in state [81]. The difference between the London fit and the averaged torque is too large to be an artifact of irreversibility (Fig. 3.7b inset). The irreversibility that appears with the lock-in can be decreased by shaking, but not completely, depending on the field and temperature. We consider that the lock-in properties are reliably measured if increasing the shaking power does not change the shape of the averaged torque; at low temperature and high fields, the shaking is not sufficient to ensure completely reliable measurements. The shaking efficiency limit is reached when a small peak appears at the

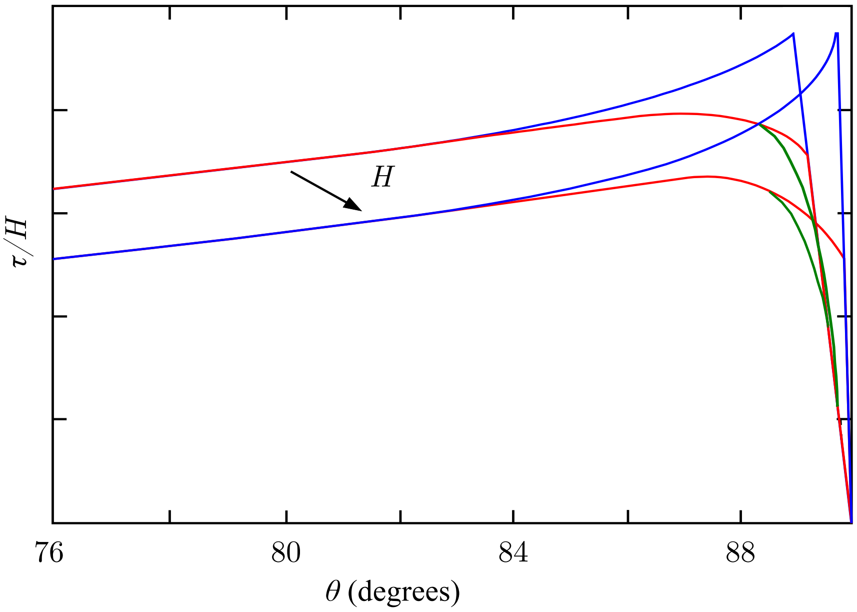

Figure 3.8: Angular torque divided by field τ/H as derived in [57]. Red line: quasi-2D model. Blue line: 2D model. Dotted green line: 3D London model. This profile corresponds to $\gamma \simeq 50$, $H/H_{c2} = 0.005, 0.02$. (Picture adapted from [57]).

limit of the lock-in domain (Fig. 3.11a). The peak feature in the CCW branch of the torque is characteristic of lock-in observed in conjunction with extrinsic pinning [82, 83, 52], although such a peak can also be observed in purely 3D-regime crystals like MgB_2 [37] (it may result from stacking faults). This usually masks the lock-in effect in lower quality crystals, as mentioned in [81].

There are several ways to define the lock-in angle θ_{lock}. Theoretically, the lock-in should happen when the perpendicular component of the field $H^{||c}$ goes below $H_{\mathrm{c1}}^{||c}$. Field penetration across the layers is then impossible, thus locking the vortices between the planes. In this model, $\cos(\theta_{\mathrm{lock}}) = H_{\mathrm{c1}}^{||c}/H$ (Fig. 3.9). As a result, the lock-in angle is closer to 90° when H increases, as observed in high-anisotropy cuprates [73]. A similar field dependence was derived for $YBa_2Cu_3O_{7-\delta}$ [53, 80] but was not experimentally confirmed. However, at the lock-in angle in $La_{2-x}Sr_xCuO_4$ ($x = 0.075$), $H^{||c} \neq H_{\mathrm{c1}}^{||c}$ [84]. It is thus possible that this simple model holds only for high-anisotropy superconductors.

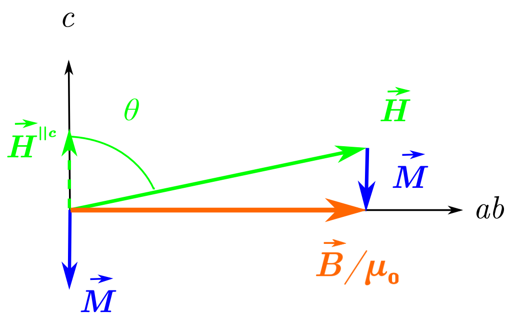

Figure 3.9: Schematic representation of the magnetic field $\vec{H}$, magnetic induction $\vec{B}$, and magnetization $\vec{M}$ in the lock-in state. Since $\vec{B}$ is aligned with the ab-planes, it can be approximated as $\mu_0 H^{||ab}$. $|\vec{M}|$ can therefore be approximated as $|H^{||c}|$.

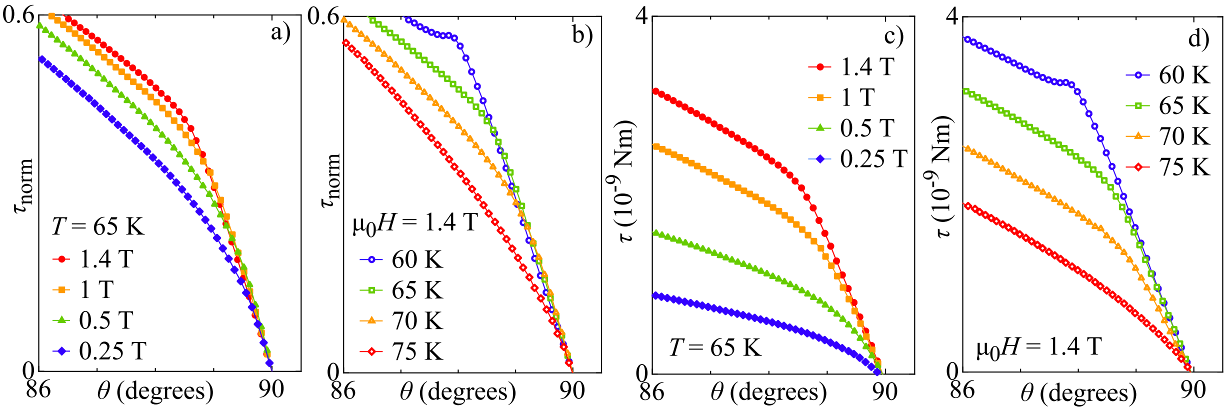

Figure 3.10: a) Normalized torque τ_{norm} of detwinned single crystal $YBa_2Cu_3O_{7-\delta}$ as a function of angle at 65 K for various fields. The lock-in angular domain and the lock-in amplitude are smaller at low fields. b) Normalized torque τ_{norm} as a function of angle at 1.4 T for various temperatures. The lock-in angular domain and the lock-in amplitude are larger at high temperatures. c) Torque τ as a function of angle at 65 K for various fields. d) Torque as a function of angle at 1.4 T for various temperatures.

The vortex direction is along the magnetic induction $\vec{B}$; $\vec{B}$ is therefore aligned with the planes in the lock-in state (but $\vec{H}$ is not). Since $\vec{B} = \mu_0(\vec{H} + \vec{M})$ and M is small compared to H, B can be approximated as the parallel component of H (see Fig. 3.9); then $M = H^{||c} = H\cos(\theta)$. In that case, the torque $|\vec{\tau}| = |V\vec{M} \times \mu_0\vec{H}| = V\mu_0 HM\sin(\theta)$ becomes:

$$\tau_{\text{lock}} = V\mu_0 H^2 \sin(\theta)\cos(\theta). \tag{3.5}$$

The lock-in angle θ_{lock} can also be defined empirically as the angle where the torque slope changes, *i.e.* the torque is not linear as described by Eq. (3.5) anymore. In our measurement, θ_{lock} increases at low temperatures, but also at high fields (Fig. 3.10). This could be due to the fact that θ_{lock} becomes more difficult to identify at higher temperatures and lower fields. Figure 3.11 shows how the staircase region and the broad transition (red color gradient) hide θ_{lock}. It is thus possible that the observed unconventional increase of θ_{lock} at high fields is biased; since the transition is smoother at low fields, the field dependence of θ_{lock} might be drowned in the large transition.

Figure 3.10c and d show the non normalized torque in the lock-in region; even though all curves merge around the *ab*-plane, the torque slope in the linear region depends slightly on temperature, contrary to the prediction of Eq. (3.5). Since the lock-in transition is not sharp at higher temperatures, the curvature of the torque that accompanies this transition may extend into the linear region and change the slope dependence given by Eq. (3.5). The observed temperature dependence of the slope might therefore be an artifact of the broad transition.

To conclude, the anisotropy of $YBa_2Cu_3O_{7-\delta}$ slightly depends on temperature, independently of the model used for the analysis. This could be a consequence of multigap superconductivity, or a pseudogap effect. A lock-in effect was observed at the 2D to 3D crossover temperature. The lock-in predictably increases at low temperature, but surprisingly also increases at higher fields, in contrast to previous cuprate experiments and theoretical models.

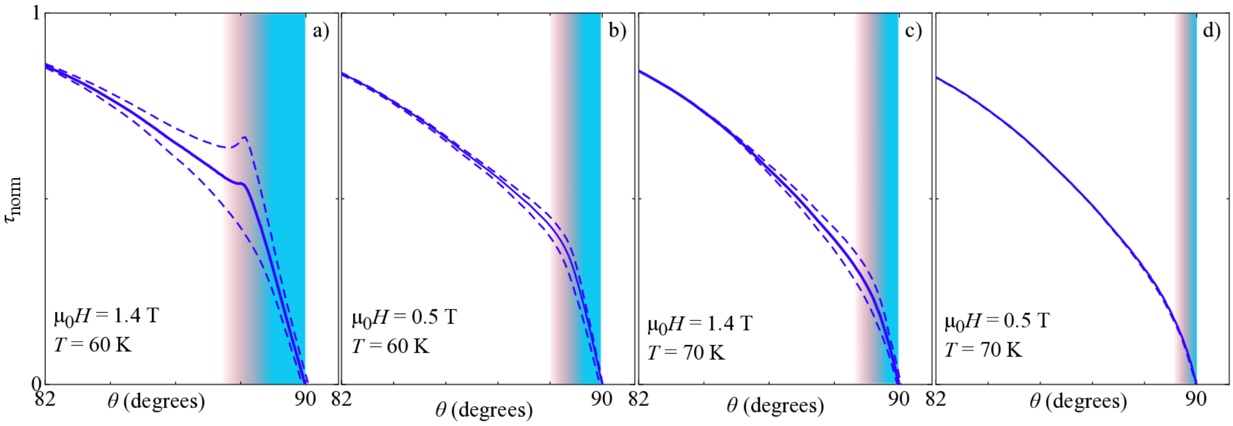

Figure 3.11: Normalized torque τ_{norm} of detwinned single crystal $\mathrm{YBa_2Cu_3O_{7-\delta}}$ as a function of angle θ. The dashed lines represent the raw irreversible data and the solid lines the average between the CW and CCW measurements. The irreversibility is limited to the angle range where the torque does not follow the London model above 80°. The color gradients underline the lock-in region (blue) and the angular transition (red). The lock-in transition is not sharp at low fields and high temperatures. a) 1.4 T and 60 K. At these low temperature, the torque does not follow the shape described in [57] b) 0.5 T and 60 K. This shape is predicted in [57]. c) 1.4 T and 70 K. d) 0.5 T and 70 K. The shaking is optimal: the signal is fully reversible.

3.4 Publications related to Chapter 3

- *Magnetic torque study of the temperature-dependent anisotropy parameter in overdoped superconducting single-crystal* $YBa_2Cu_3O_{7-\delta}$
  S. Bosma, S. Weyeneth, R. Puzniak, A. Erb, A. Schilling, and H. Keller
  Physical Review B **84**, 024514 (2011)
  DOI: 10.1103/PhysRevB.84.024514

  e-prints:
  `http://arxiv.org/abs/1102.2990`
  `http://www.zora.uzh.ch/50121/`
  `http://prb.aps.org/abstract/PRB/v84/i2/e024514`

- *Vortex lock-in transition coinciding with the 3D to 2D crossover in* $YBa_2Cu_3O_{7-\delta}$
  S. Bosma, S. Weyeneth, R. Puzniak, A. Erb, and H. Keller
  Physical Review B **86**, 174502 (2012)
  DOI: 10.1103/PhysRevB.86.174502

  e-prints:
  `http://arxiv.org/abs/1208.3062`
  `http://www.zora.uzh.ch/67294/`
  `http://prb.aps.org/abstract/PRB/v86/i17/e174502`

PHYSICAL REVIEW B **84**, 024514 (2011)

Magnetic torque study of the temperature-dependent anisotropy parameter in overdoped superconducting single-crystal $YBa_2Cu_3O_7$

S. Bosma,[1,*] S. Weyeneth,[1] R. Puzniak,[2] A. Erb,[3] A. Schilling,[1] and H. Keller[1]
[1]*Physik-Institut der Universität Zürich, Winterthurerstrasse 190, CH-8057 Zürich, Switzerland*
[2]*Institute of Physics, Polish Academy of Sciences, Aleja Lotników 32/46, PL-02-668 Warsaw, Poland*
[3]*Walther Meissner Institut, Bayerische Akademie der Wissenschaften, D-85748 Garching, Germany*
(Received 14 February 2011; revised manuscript received 3 May 2011; published 12 July 2011)

An overdoped $YBa_2Cu_3O_7$ single crystal was studied by SQUID and torque magnetometry in order to investigate the temperature dependence of the anisotropy parameter close to the transition temperature T_c ($0.87T_c < T < T_c$). Angle-dependent torque measurements were performed and analyzed with the widely used Kogan model [Phys. Rev. B **38**, 7049 (1988)] as well as with an extended model by Hao and Clem [Phys. Rev. Lett. **67**, 2371 (1991)], taking into account the influence of the vortex cores on the magnetization. Both approaches yield similar results, with an out-of-plane anisotropy parameter around 6.5 which slightly increases with decreasing temperature, and a temperature independent in-plane anisotropy parameter $\gamma_{ab} = 1.12(5)$.

DOI: 10.1103/PhysRevB.84.024514 PACS number(s): 74.20.De, 74.25.Ha, 74.72.−h

I. INTRODUCTION

Since the discovery of high-temperature superconductivity in the cuprates,[1] the anisotropic magnetic properties of layered superconductors were extensively studied (see, e.g., Refs. 2–9). All superconductors with a transition temperature $T_c > 30$ K have a layered structure. In particular, the superconducting gap of cuprates was found to be strongly anisotropic due to the crystal structure consisting of weakly coupled superconducting CuO_2 planes.[10] It is interesting to investigate how the anisotropic properties change as a function of thermodynamic parameters and doping within a particular family of cuprates, and to explore their common features by comparing various families.

The gap structure can be probed directly by exciting superconducting carriers. Importantly, the energy needed for this, i.e., the energy gap, may be accessed by probing the magnetic penetration depth λ.[11] In a layered superconductor, the gap structure is strongly anisotropic, thus λ is anisotropic as well. The magnetic penetration depth related to a supercurrent flowing along the i-axis ($i = a,b,c$) is denoted as λ_i, and the penetration depth anisotropy between two crystallographic directions i and j is $\gamma_{ij} = \lambda_i/\lambda_j$.

In the anisotropic Ginzburg-Landau theory, which is the most commonly applied phenomenological description of layered superconductors, the anisotropy is described by the temperature-independent effective mass anisotropy [assuming $\lambda_i/\lambda_j = (m_i^*/m_j^*)^{1/2} = H_{c2}^{\|j}/H_{c2}^{\|i}$, where $H_{c2}^{\|k}$ is the upper critical field along the k-axis]. However, a temperature-dependent anisotropy was observed in various superconductors, especially in the two-gap superconductor MgB_2 (see Refs. 7 and 12), and was explained as a consequence of the presence of two superconducting gaps. A similar temperature dependence was also observed in iron-based superconductors,[13] in which evidence for two-band superconductivity was provided by several experiments, including point contact spectroscopy[14,15] and angle resolved photoemission spectroscopy (ARPES).[16,17] Multigap superconductivity seems to be more common than first expected, as indications of it were also observed in cuprates.[18–20] It may be related to the temperature dependence of the anisotropy,[21] as in the case of MgB_2 (Ref. 7) and the iron-based superconductors.[13] However, there may be other reasons for this temperature dependence: the anisotropy of the gap,[11,22] the anisotropy of the Fermi surface,[23] or strong coupling.[24] A temperature-dependent anisotropy parameter was also observed in cuprates (see, e.g., Refs. 9, 18, 25, and 26). This rises the question whether the temperature dependence of the anisotropy is a common property of all layered high-T_c superconductors, and how it is linked to the gap structure.

A recent study of the cuprate superconductor $SmBa_2Cu_3O_{7-\delta}$ facing this question was limited to the underdoped region only.[9] It was shown that the temperature dependence of the anisotropy is more pronounced for samples with lower oxygen content. Such samples are characterized by a well-developed pseudogap, i.e., an additional energy scale which may play a similar role in the development of the temperature dependence of the anisotropy as the multigap structure in MgB_2 and iron-based superconductors. Therefore, it is very important to perform reliable studies of the temperature dependence of the penetration depth anisotropy for optimally doped and overdoped cuprates. In this doping range, the pseudogap vanishes or eventually overlaps with the superconducting gap.

Taking all of the above into account, we decided to study the temperature dependence of the anisotropy of a detwinned, almost fully oxygenated, overdoped single crystal of $YBa_2Cu_3O_{7-\delta}$. This system exhibits an anisotropic energy gap,[27] and several experiments indicate an order parameter of $s + d$ wave symmetry.[18,28]

Here, we report on torque measurements of the anisotropy parameter of an overdoped $YBa_2Cu_3O_7$ single crystal. Torque magnetometry provides a direct method to study the anisotropic magnetic properties of superconductors, contrary to methods measuring physical quantities separately along different crystallographic directions from which the anisotropy parameter is determined. An analytical approach for the analysis of experimental data based on the solution of the Hao-Clem (HC) functional[29] is applied, which allows to investigate anisotropic extreme type-II superconductors beyond the London approximation. For simplicity, the London approximation of the anisotropic Ginzburg-Landau theory (AGLT),[30,31] in which simplifications of the geometry of the vortex structure are made, is often used for analyzing experimental data. However, as discussed by Hao and Clem,[29] this approximation may not necessarily be adapted to the interpretation of magnetization measurements, and thus both approaches are compared in this work.

Section II gives a brief review of the London and of the Hao-Clem models in connection with the torque magnetometry technique used in this work. The experimental details are described in Sec. III. The results and the discussion are presented in Sec. IV, followed by the conclusions in Sec. V.

II. LONDON AND HAO-CLEM MODELS

The angular-dependent magnetization $\vec{M}$ of a sample with volume V and magnetic moment $\vec{m}$ is derived from the free energy F of an anisotropic superconductor in the mixed state[32]

$$\vec{M}(\theta,H) = \frac{\vec{m}(\theta,H)}{V} = -\frac{1}{V}\vec{\nabla}_B F. \tag{1}$$

The magnetic torque

$$\vec{\tau} = -\vec{\nabla}_\theta F = \mu_0 V(\vec{M} \times \vec{H}) \tag{2}$$

is related to $\vec{M}$ and the angle θ between $\vec{H}$ and the crystallographic c-axis.

A direct calculation of F within AGLT is not trivial, since F depends on the exact distribution of vortices and thus on the local magnetic induction $B(H)$ inside the superconductor. However, F can be expressed within the so-called London limit, assuming that the influence of the finite vortex core size can be neglected. This is valid if the vortex core size is very small compared to the vortex itself, i.e., the penetration depth is much larger than the coherence length. Anisotropic superconductors exhibit distinct magnetic properties along the principal axes a, b, and c. In layered superconductors, the largest anisotropy is observed between the c-axis and the layers (ab-plane). Therefore, we may approximate the orthorhombic structure of $YBa_2Cu_3O_7$ by a tetragonal one,[33] introducing the anisotropy parameter

$$\gamma = \frac{\lambda_c}{\lambda_{ab}}, \tag{3}$$

where the in-plane magnetic penetration depth $\lambda_{ab} = \sqrt{\lambda_a\lambda_b}$. The magnetization M and the torque τ are derived in the so-called Kogan model[32] as

$$M_L(\theta,H) = -\frac{\Phi_0\epsilon(\theta)}{8\pi\mu_0\lambda_{ab}^2}\ln\left(\frac{\eta H_{c2}^{||c}}{\epsilon(\theta)H}\right) \tag{4}$$

and

$$\tau_L(\theta,H) = -\frac{V\Phi_0 H}{16\pi\lambda_{ab}^2}\left(1-\frac{1}{\gamma^2}\right)\frac{\sin(2\theta)}{\epsilon(\theta)}\ln\left(\frac{\eta H_{c2}^{||c}}{\epsilon(\theta)H}\right). \tag{5}$$

Here, the index L indicates the London approach, Φ_0 is the magnetic flux quantum, and $\epsilon(\theta)$ is the angular scaling function

$$\epsilon(\theta) = \sqrt{\cos^2(\theta) + \frac{1}{\gamma^2}\sin^2(\theta)}. \tag{6}$$

The parameter η accounts for uncertainties due to the approximation of the London limit (e.g., the neglected suppression of the order parameter inside the vortex cores).

Hao and Clem[29] showed by analyzing the free energy within AGLT that the parameter η cannot be constant in the entire magnetic field range $H_{c1} < H < H_{c2}$, which is also evident from more recent theoretical work[34] beyond the Hao-Clem model. The more general functional form of F by Hao and Clem[29,35,36] incorporates in the expression for M and τ the empirical functions $\alpha(h)$ and $\beta(h)$, where h denotes the reduced field

$$h(\theta) = \frac{H}{H_{c2}(\theta)}. \tag{7}$$

Their generalized treatment of the mixed state of a superconductor, which includes the vortex core contribution to the free energy functional, yields a more realistic formula for the magnetization[29]

$$M_{HC}(\theta,H) = -\alpha(h(\theta))\frac{\Phi_0\epsilon(\theta)}{8\pi\mu_0\lambda_{ab}^2}\ln\left(\frac{\beta(h(\theta))}{h(\theta)}\right), \tag{8}$$

where the index HC indicates the Hao-Clem model. According to Eq. (2), the torque is written as

$$\tau_{HC}(\theta,H) = -\alpha(h(\theta))\frac{V\Phi_0 H}{16\pi\lambda_{ab}^2}\left(1-\frac{1}{\gamma^2}\right) \times \frac{\sin(2\theta)}{\epsilon(\theta)}\ln\left(\frac{\beta(h(\theta))}{h(\theta)}\right). \tag{9}$$

Here, taking into account the suppression of the order parameter in the vortex core leads to a modification of Eqs. (4) and (5) by including the functions $\alpha(h)$ and $\beta(h)$. These functions account for the correction of the in-plane magnetic penetration depth λ_{ab} and the c-axis upper critical field $H_{c2}^{||c}$, respectively. For $\alpha(h) = 1$ and $\beta(h) = \eta$, Eqs. (8) and (9) reduce to Eqs. (4) and (5) of the London limit. Within the HC treatment, no analytical formulas for $\alpha(h)$ and $\beta(h)$ can be derived easily. However, for a Ginzburg-Landau parameter $\kappa \gg 1$, the following values for α and β are found[29]

$$0.02 \lesssim h \lesssim 0.1 : \alpha(h) \simeq 0.84,\ \beta(h) \simeq 1.08, \tag{10}$$

$$0.1 \lesssim h \lesssim 0.3 : \alpha(h) \simeq 0.70,\ \beta(h) \simeq 1.74. \tag{11}$$

It is clear that although α and β are assumed to be constant in the London limit, they are field dependent and may vary considerably with magnetic field (α and β are fully determined by the reduced field h).[29]

In Fig. 1, we present the numerically calculated field dependence of the reduced magnetization $M_{HC}(h)/H_{c2}$ and compare it with the empirical Eq. (8) in order to extract $\alpha(h)$ and $\beta(h)$. The quantity $\kappa M_{HC}(h)/H_{c2}$ for $2 < \kappa < 200$ is presented in Fig. 1(a) (for clarity, $\kappa M_{HC}(h)/H_{c2}$ is shown instead of $M_{HC}(h)/H_{c2}$). Obviously, $M_{HC}(h)/H_{c2}$ strongly depends on κ. The functions $\alpha(h)$ and $\beta(h)$ are presented in panels (b) and (c), respectively. For $\kappa > 50$, the functions $\alpha(h)$ and $\beta(h)$ become essentially independent of κ. The derived $\alpha(h)$ and $\beta(h)$ are in good agreement with the values estimated by Hao and Clem[29] given in Eq. (10).

Analyzing magnetic torque experiments by means of the above-described theoretical model by Hao and Clem, one

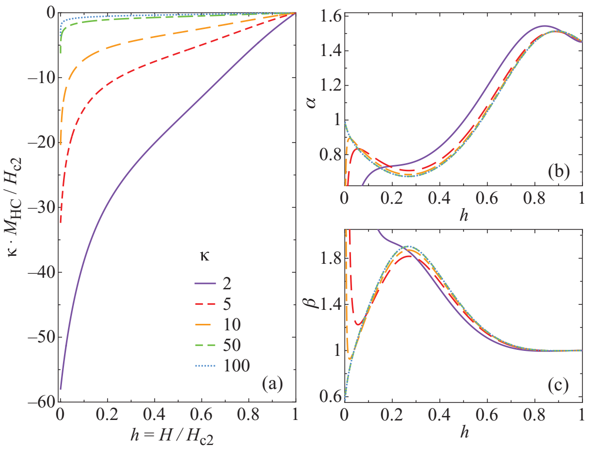

FIG. 1. (Color online) (a) $\kappa M_{HC}(h)/H_{c2}$ for various values of κ calculated using the HC model. (b) Empirical parameter $\alpha(h)$ extracted from $M_{HC}(h)/H_{c2}$. (c) Empirical parameter $\beta(h)$ extracted in the same way as $\alpha(h)$ in panel (b). Both $\alpha(h)$ and $\beta(h)$ are essentially independent of κ for $\kappa > 50$.

should note that the parameter κ is the isotropic Ginzburg-Landau parameter $\kappa = \lambda/\xi$, where ξ is the coherence length, and λ is the magnetic penetration depth. However, for a layered superconductor, the Ginzburg-Landau parameter is anisotropic: κ has to be replaced by $\kappa(\theta) = \kappa_c/\epsilon(\theta)^2$, where $\kappa_c = \lambda_c/\xi_c = \gamma^2\lambda_{ab}/\xi_{ab} = \gamma^2\kappa_{ab}$. The functions $\alpha(h)$ and $\beta(h)$ then depend on the angle θ not only via $h(\theta)$, but also via $\kappa(\theta)$. For $YBa_2Cu_3O_7$ in a field of 1.4 T at $T = 80$ K, $h(\theta)$ varies approximately between 0.1 ($\theta = 0°$) and 0.01 ($\theta = 180°$) when the field is turned from the c-axis to the ab-plane. In this case, α and β strongly depend on $h(\theta)$ [see Figs. 1(b) and 1(c)], but for $\kappa(\theta) > 50$, they are independent of $\kappa(\theta)$. Using the values for $\lambda_{ab}(T = 0)$ and $\xi_{ab}(T = 0)$ for $YBa_2Cu_3O_7$ from Refs. 37 and 38, one gets $\kappa_{ab} \simeq 400$, which means that $\kappa(\theta) > 400$ for all θ. Thus, for $YBa_2Cu_3O_7$, the parameter $\kappa(\theta)$ has negligible influence on α and β. As a consequence, taking into account the anisotropy on the Ginzburg-Landau parameter κ in the HC model does not lead to a more reliable determination of α and β.

III. EXPERIMENTAL DETAILS

The sample studied is an overdoped detwinned single-crystal $YBa_2Cu_3O_7$ grown in $BaZrO_3$ crucibles, with dimensions $130 \times 160 \times 50$ μm^3 and $T_c \simeq 88$ K. Crystal growth in $BaZrO_3$ yields samples of highest purity.[39] To fully oxygenate the crystal, a high pressure in this way shows no anomalies, e.g., fishtail effect,[40] and has very low pinning.[41] A *Quantum Design* MPMS XL SQUID magnetometer was used to determine T_c (Fig. 2). The temperature dependence of the magnetic moment m was measured in a small field $\mu_0 H = 1$ mT parallel to the ab-plane in zero field cooled (ZFC) and field cooled (FC) mode. The small difference between $m(T)$ obtained in the two modes and the sharp transition observed indicate a good quality of the crystal.

The torque measurements were carried out using a home-made torque magnetometer.[6] The piezoresistive sensor used consists of a platform connected to piezoresistive legs which are bent when the sample mounted on the platform undergoes a torque. The resulting resistance change in the piezoresistors is detected by a Wheatstone bridge. The read-out voltage is proportional to the torque magnitude τ. The small dimensions needed for the sample allow the study of high-quality single crystals.

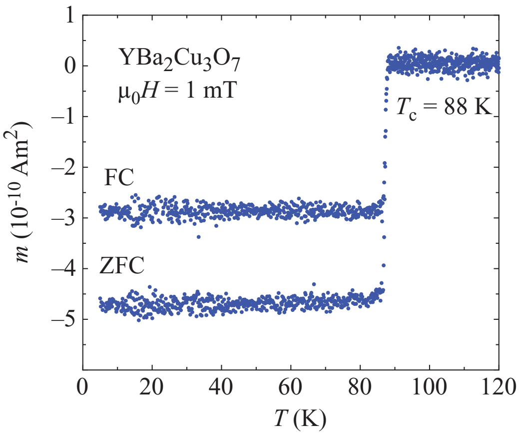

FIG. 2. (Color online) Magnetic moment $m(T)$ of the $YBa_2Cu_3O_7$ single crystal, measured in a magnetic field $\mu_0 H = 1$ mT parallel to the ab-plane. In the ZFC mode, the field is applied once the sample is cold, whereas in the FC mode, the sample is cooled while the field is applied. The ZFC and FC magnetization curves show a sharp transition with a transition temperature $T_c = 88$ K, indicating a high quality of the crystal.

IV. RESULTS AND DISCUSSION

The torque measurements were performed in an external field of 1.4 and 1 T in order to check for a possible field dependence of the anisotropy. Since the sample has diamagnetic and anisotropic properties, its magnetization $\vec{M}$ is not quite aligned with the field $\vec{H}$, which results in a torque $\vec{\tau} \propto \vec{M} \times \mu_0 \vec{H}$ according to Eq. (2).

In general, the torque signal is distorted by pinning effects: the vortex cores are pinned by defects in the sample, in which superconductivity is more easily suppressed. Consequently, the sample is not at thermodynamic equilibrium during the time span of one measurement. As a result, the torque signals are different for angular field measurements in opposite directions. In order to get reversible angular dependent torque data, a "vortex shaking" technique[4] was used. In this technique, a small ac field ($\simeq$200 Hz, 1 mT) is applied perpendicular to the main external field in order to shake the vortices out of their pinning sites (Fig. 3).

The temperature range of the angular measurements was 77–86 K. The lower temperature bound was chosen such as to avoid the lock-in effect (also known as intrinsic pinning),[42] which influences the torque in a way not accounted for in Eq. (9). When the external field direction becomes close to the ab-plane ($\theta = 90°$), the magnetization abruptly aligns with the ab-planes in order to minimize the magnetic energy in the superconducting state. However, it "jumps" back outside

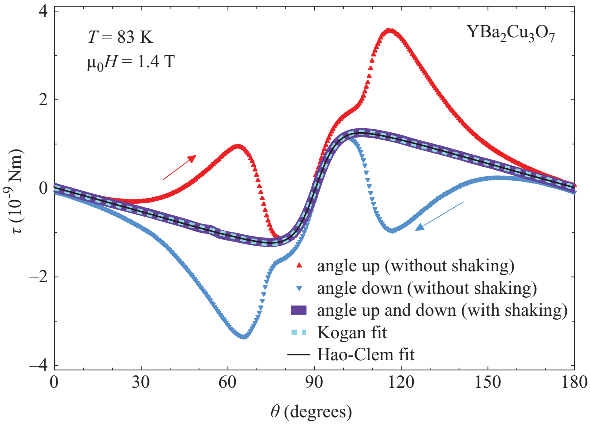

FIG. 3. (Color online) Magnetic torque τ as a function of θ for single-crystal $YBa_2Cu_3O_7$ with and without vortex shaking at 83 K and 1.4 T. The shaking removes the irreversibility between the increasing angle (up) and decreasing angle (down) measurements. The Kogan and the HC models both describe the data equally well.

the planes when the external field direction is sufficiently away from the ab-plane. The upper temperature bound was chosen such as to avoid fluctuation effects[5] close to T_c. Fluctuation effects are not taken into account in the mean-field approximation of the models considered here.

$YBa_2Cu_3O_7$ has an orthorhombic structure. Taking into account that, in this case, $\lambda_a \neq \lambda_b$, one has to replace γ by γ_{ca} or γ_{cb} in Eqs. (4), (5), (8), and (9), with the magnetic field direction in the ac- or bc-plane,[4,43] and $\lambda_{ab} = \sqrt{\lambda_a \lambda_b}$ is not equal to λ_a and λ_b as in the tetragonal case. In order to check the validity of this tetragonal approximation, measurements as a function of angle were performed in both the bc-plane and ac-plane (see Fig. 4). As expected, the data are similar for both orientations, thus allowing the analysis within a tetragonal model.

The torque data were analyzed with the HC and with the Kogan model. In order to reduce the number of free fit parameters, the upper critical field was fixed in the fitting procedure according to a Werthamer-Helfand-Hohenberg (WHH) temperature dependence[44] suitable for $YBa_2Cu_3O_7$:[38] $\mu_0 H_{c2}^{||c} \simeq -1.9$ T/K $\cdot (T - T_c)$. A paramagnetic, sinusoidal background signal present in the torque data was subtracted using the method described in Refs. 45 and 46. Figure 5 shows the temperature dependence of the anisotropy parameter γ_{cb} as determined from the torque data using the two models. As evident in Fig. 5(a), both models yield very similar values for γ_{cb} (within 2% accuracy). Moreover, the results depend only weakly on the value taken for $H_{c2}^{||c}$ [Fig. 5(b)] and on the external field [Figs. 5(c) and 5(d)]. The errors of the fit parameters γ_{ij} and λ_{ab} were estimated with a Monte-Carlo method: different fits were performed for randomly sampled points within the experimental error of the measured data points. The final values of the parameters γ and λ were taken as the average values obtained by this procedure, and their errors were defined as twice the standard deviation of these results. The estimated error bars are smaller than the size of the data points.

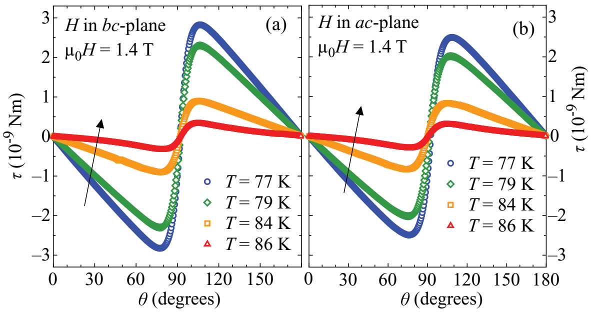

FIG. 4. (Color online) Angular-dependent torque measurements of a single-crystal $YBa_2Cu_3O_7$ taken in the temperature range between 77 K and T_c at 1.4 T. (For clarity not all temperatures are shown; the arrows indicate increasing temperature.) These raw data include a sinusoidal background. (a) Measurements with H in the bc-plane. (b) Measurements with H in the ac-plane.

Since the anisotropy parameter is only weakly field dependent [see Figs. 5(c) and 5(d)], we take as the final γ value the average for 1.4 and 1 T. The corresponding temperature dependences of γ_{ca} and γ_{cb} are shown in Fig. 6(a). The free fit parameters in Eqs. (5) and (9) are the anisotropy parameter γ_{ij} and the in-plane magnetic penetration depth λ_{ab}. Since the volume V of the sample is not known precisely, the here extracted value for λ_{ab} may deviate from the intrinsic value.

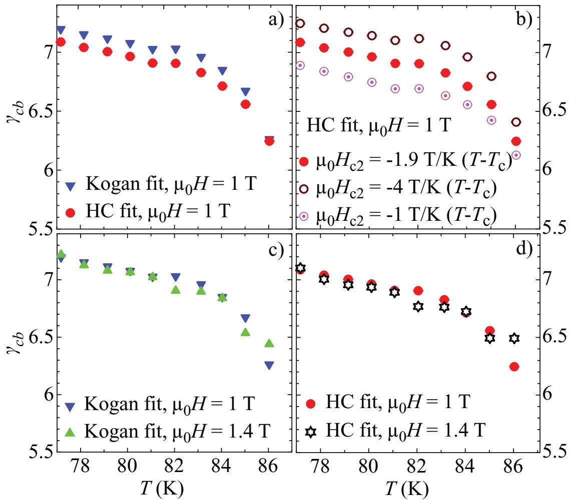

FIG. 5. (Color online) Overview of the results of the angular-dependent magnetic torque measurements of single-crystal $YBa_2Cu_3O_7$ for various temperatures and fields, using the models described in the text. (a) Comparison of γ_{cb} for the HC and Kogan model at fixed $\mu_0 H = 1$ T and fixed upper critical field ($\mu_0 dH_{c2}^{||c}/dT = -1.9$ T/K). The Kogan model yields a slightly larger anisotropy parameter than the HC model. (b) γ_{cb} for the HC model at $\mu_0 H = 1$ T and various upper critical fields, fixed in the fitting routine. The parameter $\mu_0 dH_{c2}^{||c}/dT$ does not change the shape of $\gamma(T)$. (c) γ_{cb} for the Kogan model at $\mu_0 H = 1$ and 1.4 T and fixed upper critical field ($\mu_0 dH_{c2}^{||c}/dT = -1.9$ T/K). (d) γ_{cb} for the HC model, same conditions as in panel (c). Panels (c) and (d) show that the field dependence of γ is only marginal.

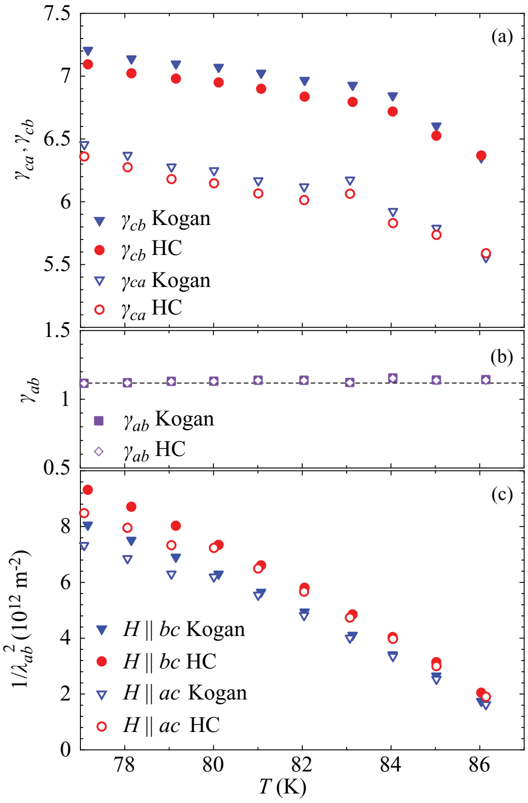

FIG. 6. (Color online) (a) Temperature dependence of the anisotropy parameters γ_{ca} and γ_{cb} for single-crystal $YBa_2Cu_3O_7$, obtained by averaging γ for both measured fields (1 and 1.4 T). (b) Temperature dependence of the in-plane anisotropy parameter γ_{ab}. The dotted line is the average $\gamma_{ab} = 1.12(5)$. (c) Temperature dependence of $1/\lambda_{ab}^2$ for measurements with H parallel to the ac- and bc-planes.

However, the shape of $\lambda_{ab}(T)$ reflects the true temperature dependence, because the superconducting volume V is only slightly temperature dependent. Figure 6(c) shows the temperature dependence of $1/\lambda_{ab}^2$ as estimated from the torque data using the Kogan and HC model. Over the temperature range studied, γ_{ca} as well as γ_{cb} slightly increases with decreasing temperature, whereas the in-plane anisotropy parameter γ_{ab} is temperature independent, in fair agreement with the previous μSR measurements of the magnetic penetration depth obtained for a similar sample.[18] However, since $\gamma_{ab} \simeq 1$, one should note that it is difficult to draw definite conclusions about its temperature dependence. The temperature dependence of the magnetic penetration depth from the previous μSR study[18] was measured along the three principal crystallographic axes and was interpreted in terms of a mixed order parameter of $s + d$ wave symmetry. The values of γ_{ca}, γ_{cb}, and γ_{ab} determined at $T \simeq 80$ K, together with the values obtained by various experimental techniques at different temperatures are summarized in Table I. The small differences in the values may be due to the different temperature ranges, the experimental techniques used, or slight differences in the doping of the samples. A determination of the anisotropy from the ratio of the penetration depths requires a careful evaluation of λ_c and λ_{ab}. Any misalignment of the sample with the applied magnetic field will result in an underestimation of λ_c and the deduced γ. In torque measurements, however, the anisotropy is extracted from a fit to the data, without orientation issues since the model describes the variation of torque in the full angular range. Therefore, the obtained values are much more reliable. The vortex shaking technique allows us to avoid an overestimation of the anisotropy due to pinning.[47] The parameters γ_{ca} and γ_{cb} are slightly different, because of the orthorhombicity of the crystal structure. The torque data were analyzed here under the assumption that the field and penetration depth anisotropy parameters are equal. It is possible to generalize this analysis to the multigap case, where these parameters are not equal.[22] However, such an analysis of the present torque data would not provide reliable results here due to the too large number of fit parameters.

Although no temperature dependence of the out-of-plane anisotropy parameter for Pr-doped $YBa_2Cu_3O_{7-\delta}$ was found,[8] it was noted that such a dependence cannot be ruled out due to the narrow temperature range studied (82–88 K). A temperature independent out-of-plane anisotropy parameter was also observed for $HgBa_2Ca_3Cu_4O_{10}$,[3] where the studied temperature range was very narrow as well. In contrast, a pronounced temperature dependence of the out-of-plane anisotropy parameter was seen in MgB_2,[7] which was consistently described in the framework of two-gap superconductivity. The temperature dependence of the out-of-plane anisotropy

TABLE I. Comparison of anisotropy parameters of $YBa_2Cu_3O_{7-\delta}$ obtained by various experimental techniques at different temperatures.

Technique	T (K)	γ_{ab}	γ_{cb}	γ_{ca}	Reference
Low-energy μSR	0	1.19(1)	. . .	. . .	37
SANS[a]	1.5	1.18(2)	. . .	. . .	48
μSR	10	1.15(2)	4.2(5)	3.6(4)	43
μSR	80	1.1(1)[b]	4.5(1)[b]	3.5(1)[b]	18
Specific heat	70–90[c]	. . .	5.3(5)	5.3(5)	49
Torque (shaken)	80	1.12(5)	7.00(5)	6.18(5)	This work
Torque	90	1.18(14)	8.95(76)	7.55(63)	50
Torque	93	1.1(2)	7.3(5)	6.6(5)	43

[a] Small angle neutron scattering.

[b] Estimated from Ref. 18.

[c] Temperature not specified; out-of-plane anisotropy parameter determined from H_{c2}.

parameter found later in iron-based superconductors was also attributed to multigap superconductivity.[13,46] This may suggest that the present results are a signature of two-gap superconductivity in $YBa_2Cu_3O_7$, as previously proposed in Ref. 18. However, we note that the temperature dependence of the out-of-plane anisotropy parameter observed for cuprates is extremely sensitive to the oxygen content. A well-pronounced temperature dependence of the anisotropy for strongly underdoped samples[9] becomes very weak for overdoped $YBa_2Cu_3O_7$. This may be related to the evolution of the pseudogap with doping in $YBa_2Cu_3O_{7-\delta}$. Moreover, it suggests that an additional energy scale to the superconducting energy gap in the system is necessary to get a temperature-dependent out-of-plane anisotropy parameter in layered superconductors. Such an energy scale may originate from the multigap nature of superconductivity in MgB_2 and in pnictides and from the appearance of the pseudogap in cuprates.

V. CONCLUSIONS

The magnetic torque of an overdoped $YBa_2Cu_3O_7$ single crystal was investigated at temperatures close to T_c in magnetic fields of 1 and 1.4 T. In the temperature range $0.87T_c < T < T_c$, the anisotropy parameters γ_{ca} and γ_{cb} were found to increase by more than 10% with decreasing temperature, but no field dependence was observed. In contrast, the in-plane anisotropy parameter γ_{ab} exhibits no temperature nor field dependence. The values of γ_{ca}, γ_{cb}, and γ_{ab} are in good agreement with those reported previously (see Table I). The analysis of the torque data with the Hao-Clem model yields, within 2%, the same results as the simpler Kogan model. The Hao-Clem model does not provide new information on the vortex state of $YBa_2Cu_3O_7$ in the present study.

The weak temperature dependence of the out-of-plane anisotropy parameter may indicate the presence of two energy scales in the superconducting behavior, related to multigap superconductivity or one-gap superconductivity with a pseudogap. To clarify this hypothesis, more experimental work is required.

ACKNOWLEDGMENTS

This work was supported in part by the Swiss National Science Foundation.

---

[*] sbosma@physik.uzh.ch

[1] J. G. Bednorz and K. A. Müller, Z. Phys. B **64**, 189 (1986).

[2] D. E. Farrell, C. M. Williams, S. A. Wolf, N. P. Bansal, and V. G. Kogan, Phys. Rev. Lett. **61**, 2805 (1988).

[3] D. Zech, J. Hofer, H. Keller, C. Rossel, P. Bauer, and J. Karpinski, Phys. Rev. B **53**, R6026 (1996).

[4] M. Willemin, C. Rossel, J. Hofer, H. Keller, and A. Revcolevschi, Phys. Rev. B **59**, R717 (1999).

[5] J. Hofer, T. Schneider, J. M. Singer, M. Willemin, H. Keller, T. Sasagawa, K. Kishio, K. Conder, and J. Karpinski, Phys. Rev. B **62**, 631 (2000).

[6] S. Kohout, T. Schneider, J. Roos, H. Keller, T. Sasagawa, and H. Takagi, Phys. Rev. B **76**, 064513 (2007).

[7] M. Angst, R. Puzniak, A. Wisniewski, J. Jun, S. M. Kazakov, J. Karpinski, J. Roos, and H. Keller, Phys. Rev. Lett. **88**, 167004 (2002).

[8] A. Kortyka, R. Puzniak, A. Wisniewski, M. Zehetmayer, H. W. Weber, Y. Q. Cai, and X. Yao, Supercond. Sci. Technol. **23**, 065001 (2010).

[9] A. Kortyka, R. Puzniak, A. Wisniewski, M. Zehetmayer, H. W. Weber, C. Y. Tang, X. Yao, and K. Conder, Phys. Rev. B **82**, 054510 (2010).

[10] J. C. Campuzano, G. Jennings, M. Faiz, L. Beaulaigue, B. W. Veal, J. Z. Liu, A. P. Paulikas, K. Vandervoort, H. Claus, R. S. List, A. J. Arko, and R. J. Bartlett, Phys. Rev. Lett. **64**, 2308 (1990).

[11] B. S. Chandrasekhar and D. Einzel, Ann. Phys. **505**, 535 (1993).

[12] J. Nagamatsu, N. Nakagawa, T. Muranaka, Y. Zenitani, and J. Akimitsu, Nature **410**, 63 (2001).

[13] S. Weyeneth, R. Puzniak, U. Mosele, N. D. Zhigadlo, S. Katrych, Z. Bukowski, J. Karpinski, S. Kohout, J. Roos, and H. Keller, J. Supercond. Nov. Magn. **22**, 325 (2009).

[14] L. Shan, Y. Wang, X. Zhu, G. Mu, L. Fang, C. Ren, and H.-H. Wen, Europhys. Lett. **83**, 57004 (2008).

[15] Y.-L. Wang, L. Shan, L. Fang, P. Cheng, C. Ren, and H.-H. Wen, Supercond. Sci. Technol. **22**, 015018 (2009).

[16] H. Ding, P. Richard, K. Nakayama, K. Sugawara, T. Arakane, Y. Sekiba, A. Takayama, S. Souma, T. Sato, T. Takahashi, Z. Wang, X. Dai, Z. Fang, G. F. Chen, J. L. Luo, and N. L. Wang, Europhys. Lett. **83**, 47001 (2008).

[17] L. Zhao, H.-Y. Liu, W.-T. Zhang, J.-Q. Meng, X.-W. Jia, G.-D. Liu, X.-L. Dong, G.-F. Chen, J.-L. Luo, N.-L. Wang, W. Lu, G.-L. Wang, Y. Zhou, Y. Zhu, X.-Y. Wang, Z.-Y. Xu, C.-T. Chen, and X.-J. Zhou, Chin. Phys. Lett. **25**, 4402 (2008).

[18] R. Khasanov, S. Strässle, D. Di Castro, T. Masui, S. Miyasaka, S. Tajima, A. Bussmann-Holder, and H. Keller, Phys. Rev. Lett. **99**, 237601 (2007).

[19] R. Khasanov, A. Shengelaya, A. Maisuradze, F. LaMattina, A. Bussmann-Holder, H. Keller, and K. A. Müller, Phys. Rev. Lett. **98**, 057007 (2007).

[20] R. Khasanov, A. Shengelaya, J. Karpinski, A. Bussmann-Holder, H. Keller, and K. A. Müller, J. Supercond. Nov. Magn. **21**, 81 (2008).

[21] T. Dahm and N. Schopohl, Phys. Rev. Lett. **91**, 017001 (2003).

[22] V. G. Kogan, Phys. Rev. Lett. **89**, 237005 (2002).

[23] W. H. Butler, Phys. Rev. Lett. **44**, 1516 (1980).

[24] N. R. Werthamer and W. L. McMillan, Phys. Rev. **158**, 415 (1967).

[25] T. Shibauchi, H. Kitano, K. Uchinokura, A. Maeda, T. Kimura, and K. Kishio, Phys. Rev. Lett. **72**, 2263 (1994).

[26] A. Hosseini, S. Kamal, D. A. Bonn, R. Liang, and W. N. Hardy, Phys. Rev. Lett. **81**, 1298 (1998).

[27] J. R. Kirtley, C. C. Tsuei, A. Ariando, C. J. M. Verwijs, S. Harkema, and H. Hilgenlamp, Nat. Phys. **2**, 190 (2006).

[28] H. J. H. Smilde, A. A. Golubov, Ariando, G. Rijnders, J. M. Dekkers, S. Harkema, D. H. A. Blank, H. Rogalla, and H. Hilgenkamp, Phys. Rev. Lett. **95**, 257001 (2005).

[29] Z. Hao and J. R. Clem, Phys. Rev. B **43**, 7622 (1991).

[30] V. L. Ginzburg and L. D. Landau, Zh. Eksp. Teor. Fiz. **20**, 1064 (1950).

[31] M. Tinkham, *Introduction to Superconductivity* (McGraw-Hill, New York, 1996).

[32] V. G. Kogan, Phys. Rev. B **38**, 7049 (1988).

[33] As indicated in Ref. 32, $YBa_2Cu_3O_7$ is the typical structure where this uniaxial approximation can be made.

[34] W. V. Pogosov, K. I. Kugel, A. L. Rakhmanov, and E. H. Brandt, Phys. Rev. B **64**, 064517 (2001).

[35] Z. Hao, J. R. Clem, M. W. McElfresh, L. Civale, A. P. Malozemoff, and F. Holtzberg, Phys. Rev. B **43**, 2844 (1991).

[36] Z. Hao and J. R. Clem, Phys. Rev. Lett. **67**, 2371 (1991).

[37] R. F. Kiefl, M. D. Hossain, B. M. Wojek, S. R. Dunsiger, G. D. Morris, T. Prokscha, Z. Salman, J. Baglo, D. A. Bonn, R. Liang, W. N. Hardy, A. Suter, and E. Morenzoni, Phys. Rev. B **81**, 180502(R) (2010).

[38] U. Welp, W. K. Kwok, G. W. Crabtree, K. G. Vandervoort, and J. Z. Liu, Phys. Rev. Lett. **62**, 1908 (1989).

[39] A. Erb, E. Walker, and R. Flükiger, Physica C **258**, 9 (1996).

[40] A. Erb, J.-Y. Genoud, F. Marti, M. Däumling, E. Walker, and R. Flükiger, J. Low Temp. Phys. **105**, 1023 (1996).

[41] A. Erb, A. A. Manuel, M. Dhalle, F. Marti, J.-Y. Genoud, B. Revaz, A. Junod, D. Vasumathi, S. Ishibashi, A. Shukla, E. Walker, Ø. Fischer, R. Flükiger, R. Pozzi, M. Mali, and D. Brinkmann, Solid State Commun. **112**, 245 (1999).

[42] D. Feinberg and A. M. Ettouhami, Int. J. Mod. Phys. B **7**, 2085 (1993).

[43] C. Ager, F. Y. Ogrin, S. L. Lee, C. M. Aegerter, S. Romer, H. Keller, I. M. Savić, S. H. Lloyd, S. J. Johnson, E. M. Forgan, T. Riseman, P. G. Kealey, S. Tajima, and A. Rykov, Phys. Rev. B **62**, 3528 (2000).

[44] N. R. Werthamer, E. Helfand, and P. C. Hohenberg, Phys. Rev. **147**, 295 (1966).

[45] L. Balicas, A. Gurevich, Y. J. Jo, J. Jaroszynski, D. C. Larbalestier, R. H. Liu, H. Chen, X. H. Chen, N. D. Zhigadlo, S. Katrych, Z. Bukowski, and J. Karpinski, e-print arXiv:0809.4223v2 (2008).

[46] S. Weyeneth, R. Puzniak, N. D. Zhigadlo, S. Katrych, Z. Bukowski, J. Karpinski, and H. Keller, J. Supercond. Nov. Magn. **22**, 347 (2009).

[47] M. Willemin, A. Schilling, H. Keller, C. Rossel, J. Hofer, U. Welp, W. K. Kwok, R. J. Olsson, and G. W. Crabtree, Phys. Rev. Lett. **81**, 4236 (1998).

[48] S. T. Johnson, E. M. Forgan, S. H. Lloyd, C. M. Aegerter, S. L. Lee, R. Cubitt, P. G. Kealey, C. Ager, S. Tajima, A. Rykov, and D. McK. Paul, Phys. Rev. Lett. **82**, 2792 (1999).

[49] M. Roulin, A. Junod, A. Erb, and E. Walker, Phys. Rev. Lett. **80**, 1722 (1998).

[50] T. Ishida, K. Inoue, K. Okuda, H. Asaoka, Y. Kazumata, K. Noda, and H. Takei, Physica C **263**, 260 (1996).

PHYSICAL REVIEW B **86**, 174502 (2012)

Vortex lock-in transition coinciding with the 3D to 2D crossover in $YBa_2Cu_3O_7$

S. Bosma,[1,*] S. Weyeneth,[1] R. Puzniak,[2] A. Erb,[3] and H. Keller[1]
[1]*Physik-Institut der Universität Zürich, Winterthurerstrasse 190, CH-8057 Zürich, Switzerland*
[2]*Institute of Physics, Polish Academy of Sciences, Aleja Lotników 32/46, PL-02-668 Warsaw, Poland*
[3]*Walther Meissner Institut, Bayerische Akademie der Wissenschaften, D-85748 Garching, Germany*
(Received 15 August 2012; revised manuscript received 1 October 2012; published 5 November 2012)

A vortex lock-in transition was directly detected by torque magnetometry in an overdoped $YBa_2Cu_3O_7$ single crystal of low anisotropy (≈ 7). The locked-in state was observed below the two- to three-dimensional crossover temperature $T_{cr} = 76$ K, independently of extrinsic pinning effects, thanks to a high-quality clean crystal and the use of a vortex shaking technique. The lock-in effect is enhanced by decreasing temperature and increasing magnetic field. The shape of the torque signal as a function of the angle between the applied magnetic field and the crystallographic *c* axis is in very good agreement with the model developed by Feinberg and Ettouhami [Int. J. Mod. Phys. B **7**, 2085 (1993)] for quasi-2D superconductors, despite the low anisotropy of the material.

DOI: 10.1103/PhysRevB.86.174502 PACS number(s): 74.20.De, 74.25.Ha, 74.72.−h

I. INTRODUCTION

Dimensionality is essential to understand the behavior of vortices in layered cuprate superconductors. A three-dimensional (3D) to two-dimensional (2D) crossover takes place when the superconducting coherence length along the *c* axis ξ_c becomes smaller than the distance s between the planes supporting superconductivity.[1] Since ξ_c decreases with decreasing temperature, it will in many cases become smaller than s below some temperature. The Lawrence-Donniach model should then be used to describe superconductivity.[2] The temperature T_{cr} at which this crossover happens is such that $\xi_c(T_{cr}) = \xi_{c,0}/\sqrt{1 - T_{cr}/T_c} = s$, where $\xi_{c,0} = \xi_c(T = 0\,\mathrm{K})$ and T_c is the superconductor critical temperature. For the studied $YBa_2Cu_3O_7$ crystal, taking $s \simeq 0.8$ nm,[3] $\xi_{c,0} \simeq 0.3$ nm,[4] and $T_c = 88$K,[5] one gets $T_{cr} \simeq 76$ K.

In the 2D regime, when the applied magnetic field direction is nearly parallel to the *ab* plane, a lock-in transition may take place.[6] In this case, the vortex cores are confined between the superconducting layers, even though the field is not aligned with these layers. This minimizes condensation energy at the cost of magnetic energy coming from the misalignment of vortices and fields, since the cores do not cross the layers anymore. This is also known as intrinsic pinning, since it locks the vortices independently of (extrinsic) impurities.

In high-anisotropy materials lock-in studies,[7–10] the 2D character is so strong that the lock-in is present almost up to T_c. However, the vicinity of the superconducting transition makes it difficult to observe the lock-in onset. Low-anisotropy cuprates like $YBa_2Cu_3O_7$ or $YBa_2Cu_4O_8$ are more suited for this purpose. The lock-in was observed in $YBa_2Cu_3O_7$ by torque magnetometry,[11,12] bulk resistivity measurements,[3,13] and ac transport in thin films.[14] The lock-in was also observed in various other layered superconductors.[15–21] It may be difficult to distinguish between pinning and lock-in effects (see, for example, Ref. 12). Besides, a large irreversibility due to extrinsic pinning effects may hide the appearance of the lock-in transition: in Ref. 22, the lock-in transition is identified much below the 3D to 2D crossover temperature T_{cr}. In this work, the appearance of the vortex lock-in is clearly observed by torque magnetometry at T_{cr} in a clean overdoped $YBa_2Cu_3O_7$ single crystal, and the lock-in torque profile is examined in various fields and temperatures.

A review of lock-in theoretical models is given in Ref. 1 (p. 1286). The most relevant models for this work are presented in Refs. 23 and 24. The lock-in angle corresponds to the angle between the applied magnetic field and the crystallographic *c* axis at which the lock-in appears. This angle is the crucial parameter turning the lock-in on and off. Previous experiments on various cuprate superconductors were in agreement with the theory whenever data accuracy made the comparison possible, but the data in the case of $YBa_2Cu_3O_7$ were rather sparse. In this work, we present a detailed study of the field and temperature dependence of the lock-in effect in a low-anisotropy cuprate superconductor. We note a very good qualitative agreement with the behavior described in Ref. 24, although the field dependence of the lock-in angle seems unconventional. The field H is chosen in the London domain $H_{c1} \ll H \ll H_{c2}$, where H_{c1} and H_{c2} are the lower and upper critical fields. This excludes the interference of other phenomena such as vortex lattice melting or glass behavior. The temperature range has a lower bound of 60 K, because irreversibility renders the data unreliable below this temperature; the torque ceases to conform to the model described in Ref. 24.

II. TORQUE MEASUREMENTS

The growth procedure, detwinning, and pinning suppression yielding the high-quality superconducting $YBa_2Cu_3O_7$ single crystal used in this experiment is described in Ref. 25. The dimensions of the platelet crystal are $130 \times 160 \times 50$ μm^3, and $T_c \simeq 88$ K. Magnetic torque investigations were carried out using a homemade magnetic torque sensor.[26] The sample is attached to a platform hanging on piezoresistive legs. When a magnetic field is applied on an anisotropic superconductor, the misalignment between field and diamagnetic moment results in a torque. This bends the legs, thus giving rise to a measurable electric signal proportional to the magnetic torque. For a uniaxial superconductor, the angular dependence of the magnetic torque $\vec{\tau} = \vec{m} \times \mu_0 \vec{H}$ (where $\vec{m}$ is the sample magnetic moment) in the London approximation

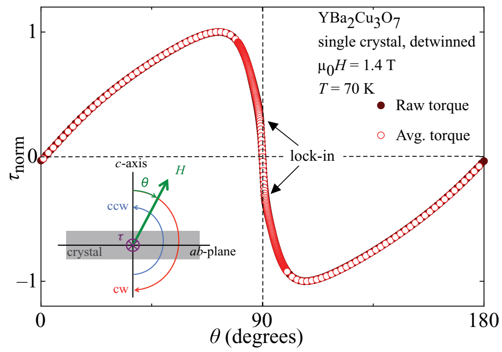

FIG. 1. (Color online) Normalized torque $\tau/\tau_{\max}$ of detwinned single-crystal $YBa_2Cu_3O_7$ in the full angular range at 70 K and 1.4 T. The irreversibility is very small; at this scale, the average of the clockwise (CW) and counterclockwise (CCW) branches of the torque (red open circles) overlaps the raw unaveraged signal (brown closed circles). Inset: Field orientation during CW and CCW measurements.

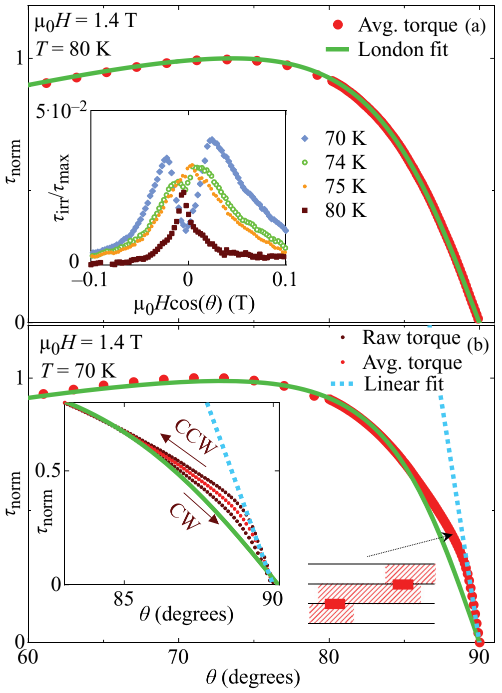

FIG. 2. (Color online) (a) Normalized torque of detwinned single-crystal $YBa_2Cu_3O_7$ as a function of angle at 80 K and 1.4 T. The torque follows the London dependence at all angles. The green line is a fit of Eq. (1) to the data. The light red points represent an average of the CW and CCW angle measurements. Inset: Irreversible component of the torque $\tau_{\rm irr} = (\tau_{\rm CW} - \tau_{\rm CCW})/2$ normalized to the maximum of the averaged torque at various temperatures at 1.4 T. (b) Normalized torque as a function of angle at 70 K and 1.4 T. The dotted blue line is a linear fit of the lock-in region. Inset: Close-up around the *ab* plane. The dark red dots represent the raw torque. The arrows indicate the field sweep direction for each branch. The schematic drawing (after Ref. 24) represents the staircase vortex configuration taking place between the linear region and the London region. Instead of a continuous normal state tube, the vortex consists of 2D cores (red rectangles) in the layers connected by Josephson cores between the layers (dashed red).

$(H_{c1} \ll H \ll H_{c2})$ can be written as[27]

$$\tau(\theta,H) = AH\frac{\sin(2\theta)}{\epsilon(\theta)}\ln\left(\frac{\eta H_{c2}^{||c}}{\epsilon(\theta)H}\right), \qquad (1)$$

where θ is the angle between the applied magnetic field H and the crystallographic c axis, $\epsilon(\theta) = \sqrt{\cos^2(\theta) + \sin^2(\theta)/\gamma_\lambda^2}$ is the angular scaling function, $H_{c2}^{||c}$ is the c axis upper critical field, and η is a dimensionless parameter of the order of unity. The anisotropy parameter $\gamma_\lambda = \lambda_c/\lambda_{ab}$ is the ratio of the out-of-plane and in-plane magnetic penetration depths; $A = -V\Phi_0(1 - 1/\gamma_\lambda^2)/(16\pi\lambda_{ab}^2)$ (V is the sample volume, Φ_0 is the flux quantum) is independent of angle. This model is three-dimensional.

A typical torque signal of $YBa_2Cu_3O_7$ measured in a magnetic field of 1.4 T at 70 K is shown in Fig. 1 as a normalized torque $\tau_{\rm norm} = \tau/\tau_{\max}$. During a torque measurement, the field direction is swept clockwise (CW) from the c axis (0°) through the *ab* plane (90°) and the opposite direction of the c axis (180°), then swept back counterclockwise (CCW), as shown in the inset of Fig. 1. The CW and CCW branches of the raw, unaveraged torque signal overlap when the torque is reversible. The torque signal is antisymmetric with regard to the *ab* plane, so the rest of the data are shown only in the angle range from 0° to 90° for clarity.

Figure 2 shows a torque measurement evidencing the lock-in effect; a deviation from Eq. (1) can be seen at low temperatures close to the *ab* plane for $\theta \simeq 85°$. This corresponds to a staircase configuration[24] of the vortices. The order parameter inside a vortex core is not suppressed between the layers, because the circulating currents are Josephson currents and not superconducting currents. The order parameter is only suppressed within the superconducting layers. The vortex consists of 2D cores in the layers, linked by Josephson cores between the layers. When the vortices are tilted enough that the Josephson coherence length is smaller than the distance between two consecutive vortex cores, the vortex line takes a staircase shape (see schematic drawing in Fig. 2). The physics stays 3D on large scales, but the free energy deviates from the 3D London model.[28] For $\theta \simeq 87°$ the lock-in starts: the torque becomes linear and changes slope. This shape of the averaged angular-dependent torque is identical to the prediction of the model presented in Ref. 24 for quasi-2D superconductors. This similarity is striking, as the anisotropy of our $YBa_2Cu_3O_7$ crystal is around 7 (these anisotropy measurements were performed on the same crystal [see Ref. 5]), which would not qualify as quasi-2D. The models presented in Ref. 24 relate to anisotropies around 50, as expected in $La_{2-x}Sr_xCuO_4$ for example.

The torque data exhibits an angular irreversibility between the CW and CCW branches. Such irreversible signals are usually due to vortex pinning. In this work, the so-called vortex-shaking technique[29] was applied to reduce irreversibility. This was done by applying a small ac field orthogonal to the main field H in order to enhance the vortex relaxation toward thermodynamic equilibrium. The irreversible part of the torque, $\tau_{\rm irr} = (\tau_{\rm CW} - \tau_{\rm CCW})/2$, normalized to the maximum

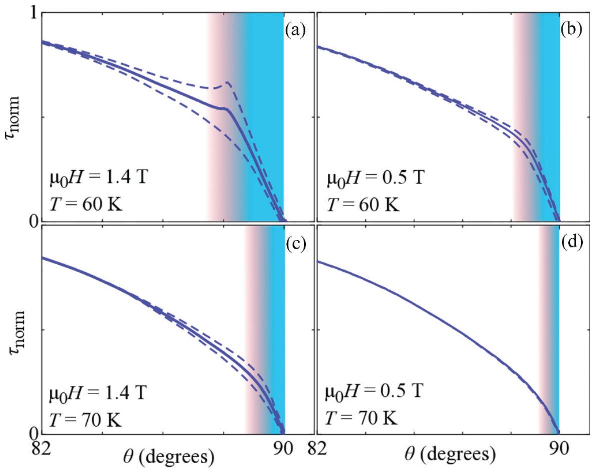

FIG. 3. (Color online) Normalized torque of detwinned single-crystal $YBa_2Cu_3O_7$ as a function of angle. The dashed line represents the raw irreversible data and the solid line the average between the CW and CCW measurements. The irreversibility is limited to the angle range where the torque does not follow the London model above 80°. The color gradients underline the lock-in region (blue) and the angular transition (red). The lock-in transition is not sharp at low fields and high temperatures. (a) 1.4 T and 60 K. At these low temperatures, the torque does not follow the shape described in Ref. 24. (b) 0.5 T and 60 K. This shape is predicted in Ref. 24. (c) 1.4 T and 70 K. (d) 0.5 T and 70 K. The shaking is optimal; the signal is fully reversible.

of the averaged torque, is shown in the inset of Fig. 2(a). The shape of τ_{irr} changes when the lock-in appears. Double peaks in τ_{irr} have been observed and linked to the lock-in state,[22] although they appeared out of the angular lock-in zone. This confirms the lock-in transition temperature around 75 K; the peak separation is just starting at 75 K, and is already well developed at 74 K. We thus estimate that the error on the lock-in starting temperature is less than 1 K. The small residual irreversibility as seen on the averaged torque could not be hiding a small higher temperature lock-in signal, because lock-in shows up as well in the shape of τ_{irr}. Besides, the difference between the London fit and the averaged torque is too large to be an artifact of irreversibility [Fig. 2(b) inset].

Figure 3 shows the angular torque at various temperatures and fields. A small residual irreversibility is visible close to the *ab* plane, at the same angles where the lock-in takes place. This irreversibility decreases with increasing temperature, as expected for vortex pinning. It also decreases with decreasing field, as observed in $YBa_2Cu_4O_8$,[22] but contrary to what was observed in $YBa_2Cu_3O_7$.[11] The variation of the pinning forces with field depends on the crystal quality and field range of the experiment, which may explain this different field behavior. In a clean crystal like the one used in this work, the only source of pinning is the layered structure; the appearance of irreversibility is thus a supplementary indication of the onset of lock-in.

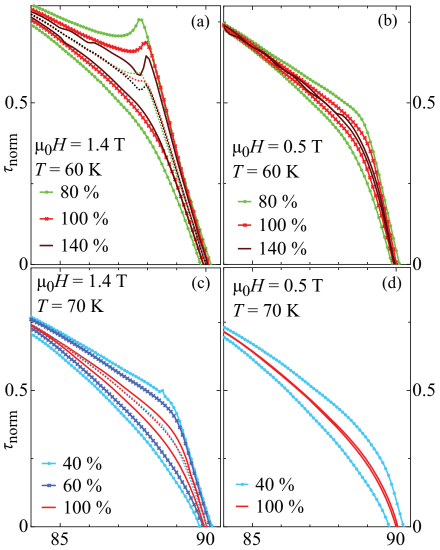

FIG. 4. (Color online) Effect of shaking power on the normalized angular torque of detwinned single-crystal $YBa_2Cu_3O_7$. 100% represents the maximal stable shaking field. Above this value, the shaking power is difficult to keep at a constant level for the whole duration of the measurement due to equipment limitations. (a) High field, low temperature: the averaged torque signal (dotted lines) depends on shaking power. (b) Low field, low temperature: the shaken torque can be made almost reversible, and the averaged torque (not shown for clarity) stays constant with shaking power. (c) High field, high temperature: the averaged torque signal (dotted lines) does not depend on shaking power. (d) Low field, high temperature: the shaking is optimally efficient in this field-temperature domain, i.e., the shaken torque can be made reversible.

In order to investigate the effect of vortex shaking on the lock-in phenomenon, we studied different shaking field amplitudes at various static fields and temperatures. At low temperature and high fields [Fig. 4(a)], the shaking is not sufficient to ensure reliable measurements, since the averaged data depend on the shaking power. The linear zone near the *ab* plane is reduced by increasing shaking power. The shaking efficiency limit is reached when a small peak appears at the limit of the lock-in domain. The peak feature in the CCW branch of the torque is characteristic of lock-in observed in conjunction with extrinsic pinning.[12] This usually masks the lock-in effect in lower quality crystals. In this work the peak appears only if the extrinsic pinning becomes too large to be suppressed at low temperatures. At low temperature and low field [Fig. 4(b)] and high temperature and high field [Fig. 4(c)], the shaking power is sufficient to get stable data. All the averaged torque signals for the various shaking powers are the same. At low fields and high temperatures [Fig. 4(d)], the shaking is even sufficient to get fully reversible data. We consider that the lock-in properties are reliably measured if increasing the shaking power does not change the shape of the averaged torque.

III. DISCUSSION

The analysis was done on the average of the CW and CCW data, since the deviation of the averaged data from the London model is larger than the irreversibility, as also reported in Ref. 11. The lock-in angle is often viewed as

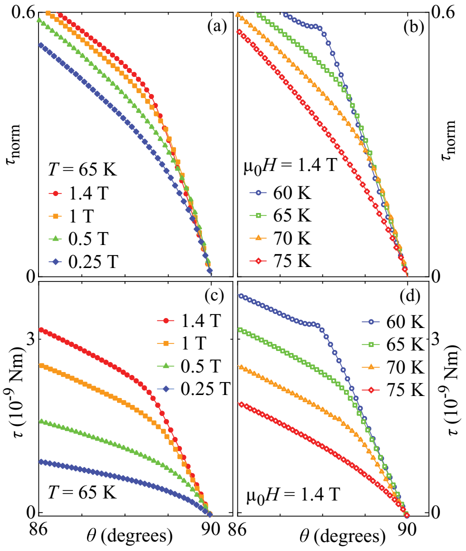

FIG. 5. (Color online) (a) Normalized torque of detwinned single-crystal $YBa_2Cu_3O_7$ as a function of angle at 65 K for various fields. The lock-in angular domain and the lock-in amplitude are smaller at low fields. (b) Normalized torque as a function of angle at 1.4 T for various temperatures. The lock-in angular domain and the lock-in amplitude are larger at high temperatures. (c) Torque as a function of angle at 65 K for various fields. (d) Torque as a function of angle at 1.4 T for various temperatures.

the angle at which the perpendicular component of the field goes below the lower critical field along the c axis. Field penetration across the layers is then impossible, effectively locking the vortices between the ab planes. In this model, the lock-in angle θ_{lock} should be such that the transverse lock-in field value $H^{||c}_{lock} = H\cos(\theta_{lock})$ matches $H^{||c}_{c1}$. Therefore, θ_{lock} should decrease with increasing field. This evolution was observed in high-anisotropy cuprates,[10] and a similar dependence was derived for $YBa_2Cu_3O_7$,[6,23] although not confirmed by experiments in this material. However, Ref. 30 reports in $La_{2-x}Sr_xCuO_4$ ($x = 0.075$) a $H^{||c}_{lock}$ value which is different from $H^{||c}_{c1}$. It is thus possible that this simple H_{c1} picture holds only for high-anisotropy compounds and that the lock-in angle is not necessarily inversely proportional to the field.

The vortices direction is along the magnetic induction $\vec{B}$; $\vec{B}$ is therefore aligned with the planes in the lock-in state (but $\vec{H}$ is not). Since $\vec{B} = \mu_0(\vec{H} + \vec{M})$ and M is small compared to H, B can be approximated as the parallel component of H: $B = \mu_0 H^{||ab} = \mu_0 H\cos(\theta)$. In that case, the torque $|\vec{\tau}| = |V\vec{M} \times \mu_0\vec{H}| = V\mu_0 HB\sin(\theta)$ becomes

$$\tau_{lock} = V\mu_0 H^2 \sin(\theta)\cos(\theta). \qquad (2)$$

Figure 5 shows the lock-in transition at various fields and temperatures. If we define the lock-in angle θ_{lock} as the angle where the torque slope changes (moves away from the linear region), θ_{lock} increases at low temperatures, but also at high fields. This is unconventional, because with higher fields one gets closer to the superconducting transition. In that case, the behavior should be increasingly 3D, which means the lock-in effect should weaken. However, θ_{lock} becomes more difficult to identify at higher temperatures and lower fields. It is possible that the observed unconventional increase of θ_{lock} at high fields is biased; since the transition is smoother at low fields, the field dependence of θ_{lock} might be drowned in the large transition. θ_{lock} can also be defined as the point at which the torque is no longer independent of temperature, and therefore not following Eq. (2). In that case, one may estimate the temperature dependence of θ_{lock} from measurements at constant field. Figures 5(c) and 5(d) show the non-normalized torque in the lock-in region; it appears that even though all curves merge around the ab plane, the torque slope depends slightly on temperature, contrary to the prediction of Eq. (2). At low temperatures, the transition sharpness increases and the slope depends more weakly on temperature. Since the lock-in transition is not sharp at higher temperatures, the curvature of the torque that accompanies this transition may skew the linear region and change the slope dependence given by Eq. (2).

IV. CONCLUSION

A lock-in transition was observed in a clean detwinned $YBa_2Cu_3O_7$ single crystal at the 2D to 3D crossover temperature. Although the angular torque signal matches theoretical shapes, it seems difficult to qualitatively confirm a simple model of the lock-in. The lock-in angle domain decreases with increasing temperature, as expected for vortex pinning. Surprisingly, this domain also seems to increase with field in the studied field range (0–1.4 T), although this dependence may be an artifact of a broad lock-in transition. This unconventional behavior might be related to the low anisotropy of the compound, which prevents it from having a strong 2D behavior, even at low temperatures.

ACKNOWLEDGMENTS

Helpful discussions with D. Feinberg and V. B. Geshkenbein are gratefully acknowledged. This work was supported by the Swiss National Science Foundation.

---

*sbosma@physik.uzh.ch

[1] G. Blatter, M. V. Feigel'man, V. B. Geshkenbein, A. I. Larkin, and V. M. Vinokur, Rev. Mod. Phys. **66**, 1125 (1994).
[2] W. E. Lawrence and S. Doniach, in *Proceedings of the Twelfth International Conference on Low Temperature Physics*, edited by E. Kanda (Academic Press, Kyoto, Japan, 1971), pp. 361–362.
[3] W. K. Kwok, U. Welp, V. M. Vinokur, S. Fleshler, J. Downey, and G. W. Crabtree, Phys. Rev. Lett. **67**, 390 (1991).
[4] U. Welp, W. K. Kwok, G. W. Crabtree, K. G. Vandervoort, and J. Z. Liu, Phys. Rev. Lett. **62**, 1908 (1989).
[5] S. Bosma, S. Weyeneth, R. Puzniak, A. Erb, A. Schilling, and H. Keller, Phys. Rev. B **84**, 024514 (2011).

[6] D. Feinberg and C. Villard, Phys. Rev. Lett. **65**, 919 (1990).

[7] F. Steinmeyer, R. Kleiner, P. Müller, H. Müller, and K. Winzer, Europhys. Lett. **25**, 459 (1994).

[8] B. Janossy, A. de Graaf, P. H. Kes, V. N. Kopylov, and T. G. Togonidze, Physica C **246**, 277 (1995).

[9] G. S. Okram, H. Aoki, M. Xu, and D. G. Hinks, Physica C **355**, 65 (2001).

[10] M. Zehetmayer, M. Eisterer, S. Sponar, H. Weber, A. Wisniewski, R. Puzniak, P. Panta, S. Kazakov, and J. Karpinski, Physica C **418**, 73 (2005).

[11] D. E. Farrell, J. P. Rice, D. M. Ginsberg, and J. Z. Liu, Phys. Rev. Lett. **64**, 1573 (1990).

[12] A. Kortyka, R. Puzniak, A. Wisniewski, M. Zehetmayer, H. W. Weber, Y. Q. Cai, and X. Yao, Supercond. Sci. Technol. **23**, 065001 (2010).

[13] S. N. Gordeev, A. A. Zhukov, P. A. J. de Groot, A. G. M. Jansen, R. Gagnon, and L. Taillefer, Phys. Rev. Lett. **85**, 4594 (2000).

[14] R. A. Doyle, A. M. Campbell, and R. E. Somekh, Phys. Rev. Lett. **71**, 4241 (1993).

[15] A. Vermeer, D. de Groot, N. Koeman, R. Griessen, and C. van Haesendonck, Physica C **185**, 2345 (1991).

[16] P. A. Mansky, P. M. Chaikin, and R. C. Haddon, Phys. Rev. Lett. **70**, 1323 (1993).

[17] S. Koleśnik, T. Skośkiewicz, J. Igalson, and Z. Tarnawski, Phys. Rev. B **54**, 13319 (1996).

[18] Y. V. Bugoslavsky, A. A. Zhukov, G. K. Perkins, A. D. Caplin, H. Kojima, and I. Tanaka, Phys. Rev. B **56**, 5610 (1997).

[19] M. A. Avila, L. Civale, A. V. Silhanek, R. A. Ribeiro, O. F. de Lima, and H. Lanza, Phys. Rev. B **64**, 144502 (2001).

[20] S. Khene, Physica B **349**, 227 (2004).

[21] S. Kohout, T. Schneider, J. Roos, H. Keller, T. Sasagawa, and H. Takagi, Phys. Rev. B **76**, 064513 (2007).

[22] D. Zech, C. Rossel, L. Lesne, H. Keller, S. L. Lee, and J. Karpinski, Phys. Rev. B **54**, 12535 (1996).

[23] L. N. Bulaevskii, Phys. Rev. B **44**, 910 (1991).

[24] D. Feinberg and A. M. Ettouhami, Int. J. Mod. Phys. B **7**, 2085 (1993).

[25] A. Erb, A. A. Manuel, M. Dhalle, F. Marti, J. Y. Genoud, B. Revaz, A. Junod, D. Vasumathi, S. Ishibashi, A. Shukla, E. Walker, Ø. Fischer, R. Flükiger, R. Pozzi, M. Mali, and D. Brinkmann, Solid State Commun. **112**, 245 (1999).

[26] S. Kohout, J. Roos, and H. Keller, Rev. Sci. Instrum. **78**, 013903 (2007).

[27] V. G. Kogan, Phys. Rev. B **38**, 7049 (1988).

[28] D. Feinberg, Physica C **194**, 126 (1992).

[29] M. Willemin, C. Rossel, J. Hofer, H. Keller, A. Erb, and E. Walker, Phys. Rev. B **58**, R5940 (1998).

[30] V. Vulcanescu, G. Collin, H. Kojima, I. Tanaka, and L. Fruchter, Phys. Rev. B **50**, 4139 (1994).

CHAPTER 4

Coexistence of magnetism and superconductivity in $\mathbf{Rb}_x\mathbf{Fe}_{2-y}\mathbf{Se}_2$

Among the recently discovered iron-based superconductors [85], the $A\mathrm{Fe}_2\mathrm{Se}_2$ family (A = K, Rb, Cs) [86, 87, 88] is especially intriguing due to the close coexistence of superconductivity and antiferromagnetism [89]. Such coexistence was also observed in cuprates by μSR [90]. The $A\mathrm{Fe}_2\mathrm{Se}_2$ compounds feature an ordering of the iron vacancies around 500 K, which in turn favors the formation of antiferromagnetically coupled blocks of iron moments at the slightly lower Néel temperature $T_\mathrm{N} \approx 500K$, which is much higher than the critical temperature $T_\mathrm{c} \approx 30$ K (Fig. 4.1 and [91]).

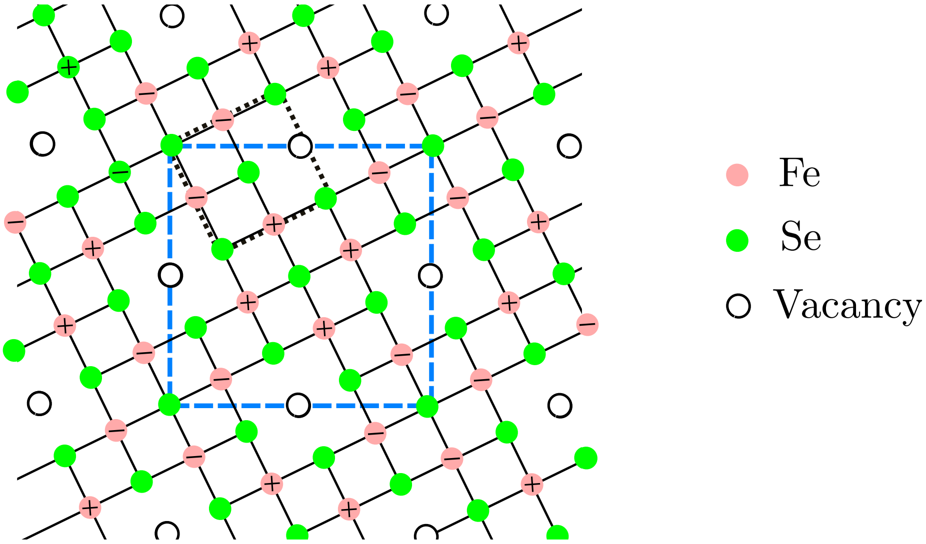

Figure 4.1: Top view of a FeSe layer at low temperatures in the iron vacancy ordered state. The empty dots are iron vacancies, the pink dots are iron atoms, and their spin direction is indicated by the + or - signs. The green dots are Se atoms. The dotted blue square underlines the unit cell in the vacancy disordered state, whereas the dotted black square shows the unit cell in the ordered state.

The intercalation of alkali ions A into the FeSe structure makes this system highly electron doped, without hole-like sheets at the Fermi surface [92]. The electron scattering between hole and electron-like bands, suggested to be crucial to superconductivity in iron-based superconductors [93, 94], is thus impossible [95]. Most experiments point towards a nanoscale phase separation between superconducting vacancy-disordered domains and antiferromagnetic vacancy-ordered ones [96, 97, 98, 99, 100]. So far no pure superconducting phase has been observed, but pure insulating phases were successfully grown [101]. The A atom site can sometimes be vacant, although these vacancies do not order in superconducting compounds. Additionally, it appears that annealing just below the phase separation onset temperature strongly improves the superconducting properties.

This Chapter first exposes anisotropy and penetration depth measurements of single crystal

$\mathrm{Rb}_x\mathrm{Fe}_{2-y}\mathrm{Se}_2$ by torque magnetometry. The effects of annealing at various temperatures relevant to the magnetic ordering is then described.

4.1 Superconductivity in phase-separated $\mathbf{Rb}_x\mathbf{Fe}_{2-y}\mathbf{Se}_2$ single crystals

The lower critical field of $\mathrm{K}_x\mathrm{Fe}_2\mathrm{Se}_2$ was found to be low and isotropic [102, 103], indicating that $\gamma_\lambda \approx 1$, where $\gamma_\lambda = \lambda_c/\lambda_{ab}$ is the penetration depth anisotropy. A low H_{c1} corresponds to a large magnetic penetration depth. Quantitatively, one gets from $\mu_0 H_{\mathrm{c1}} = \Phi_0(\ln\kappa + 0.5)/(4\pi\lambda_{\mathrm{eff}}^2)$, valid for an isotropic superconductor [104], that $\lambda_{\mathrm{eff}}(0) \simeq 1.6 - 1.8$ μm. This effective penetration depth is defined as $\lambda_{\mathrm{eff}} = (\lambda_{ab}^2\lambda_c)^{1/3}$. However, high field NMR experiments yield a much smaller in-plane magnetic penetration depth $\lambda_{ab}(0) \simeq 0.29$ μm [105]. The anisotropy of the upper critical field also seems to be larger at high fields [105, 106, 102, 107], corresponding to a larger $\gamma_H = H_{c2}/H_{c1}$.

In order to clarify the behavior of the anisotropy and the penetration depth, we performed SQUID and torque measurements on single crystal $\mathrm{Rb}_x\mathrm{Fe}_{2-y}\mathrm{Se}_2$. Similar measurements were performed on $\mathrm{Cs}_x\mathrm{Fe}_{2-y}\mathrm{Se}_2$, yielding similar results but noisier data due to a bad crystal quality. The magnetization as a function of temperature, measured by SQUID, shows that the superconducting transition at $T_{\mathrm{c}} \simeq 32$ K is sharp, and confirms the small anisotropy and small value of the lower critical field ($\mu_0 H_{\mathrm{c1}} \lesssim 0.3$ mT).

A typical torque measurement is shown in Fig. 4.2a. Instead of fitting the data with the usual Eq. (1.11), we used the following expression:

$$\tau(\theta) = -\frac{V\Phi_0 H \gamma_\lambda^{2/3}}{16\pi\lambda_{\mathrm{eff}}^2}\left(1 - \frac{1}{\gamma_\lambda^2}\right) \cdot \frac{\sin(2\theta)}{\epsilon(\theta)} \ln\left(\frac{\eta H_{\mathrm{c2}}^{||c}}{\epsilon(\theta) H}\right). \tag{4.1}$$

Rewriting Eq. (1.11) as Eq. (4.1) yields γ_λ and $\lambda_{\mathrm{eff}} = (\lambda_{ab}^2\lambda_c)^{1/3}$ as fit parameters instead of γ_λ and λ_{ab} (see Chap. 3 for details on the model). The studied crystal probably features phase separation between superconducting and non-superconducting regions, with a domain size smaller than the penetration depth [96]. Fitting torque data with the Kogan model yields a penetration depth which may be renormalized to a larger value than that which would be observed in a single phase superconductor, since the field penetrates more easily in this phase separated material. The details of the renormalization along the different crystallographic directions is not known, so it is more reliable to analyze the penetration depth averaged along all directions. We thus used the expression of the Kogan model where λ_{eff} appears instead of λ_{ab}, and expect to get larger penetration depths values than those measured by microscopic techniques. The good fitting of Eq. (4.1) to the data (Fig. 4.2b) confirms that this approach is well adapted to the material.

In the following we assume that $\eta = 1$ (see Chap. 3 and [67]). For the data analysis, the slope $dH_{\mathrm{c2}}^{||c}/dT$ at T_{c} is fixed to ~ -1 T/K, a value stemming from resistivity measurements [107]. The fit result does not depend heavily on the choice of H_{c2}(see Section 2.2).

The torque signal is the sum of a superconducting component described by Eq. (4.1) and a magnetic background component $\tau_{\mathrm{BG}} = -(\chi_{ab} - \chi_c)V\mu_0 H^2 \sin(2\theta)/2$ (derivation details in Appendix B). The variables χ_c and χ_{ab} denote the magnetic susceptibilities along the a-axis and c-axis, respectively. The background observed in this crystal shows that $\chi_{ab} > \chi_c$, in agreement with [105], and that τ_{BG} is large compared to the superconducting signal, consistent with a dominant bulk antiferromagnetic phase of magnetic moments aligned along the c-axis [89, 91].

Figure 4.3 summarizes the results of the torque measurements. Figure 4.3b shows $\gamma_\lambda(T)$ for various fields. It is almost temperature independent for $T_{\mathrm{c}}/2 < T < T_{\mathrm{c}}$ and $0.2\ \mathrm{T} < \mu_0 H < 1.4$ T. The small temperature dependencies near T_{c} and at low temperatures can be explained by

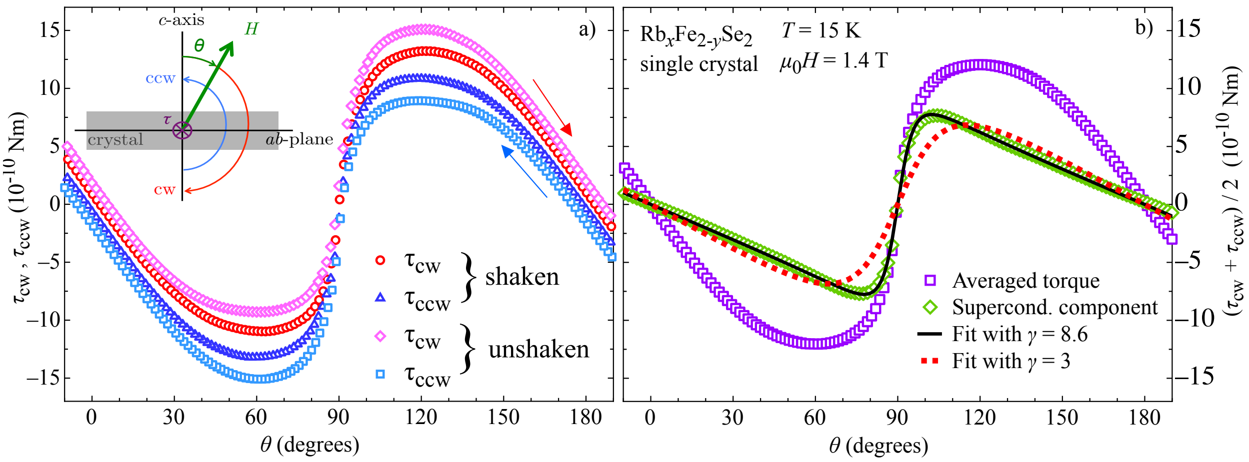

Figure 4.2: Angular dependent torque of single-crystal $Rb_xFe_{2-y}Se_2$ measured at 15 K and 1.4 T. (a) Comparison of unshaken and shaken magnetic torque data. The unshaken red data τ_{cw} (blue data τ_{ccw}) are gathered by turning H clockwise (counter-clockwise) around the sample. The inset explains schematically the field configuration during the experiment. The shaken data are obtained by applying a transverse AC field, yielding reduced irreversibility and enhanced data quality. (b) Angular dependence of the shaken magnetic torque averaged for both directions. The green curve is the superconducting component of the signal, obtained after subtracting the background as explained in the text. A fit by Eq. (4.1) yields $\gamma_\lambda(15\text{ K}, 1.4\text{ T}) \simeq 8.6$ (black line). For comparison, the red dotted line is calculated with a fixed $\gamma_\lambda = 3$.

the weakening of the superconducting signal and by pinning [108], respectively. Interestingly, the anisotropy is strongly field dependent, with an extrapolated value at zero field around 1. Figure 4.3c shows the field dependence of $\lambda_{\text{eff}}(H)$ for various temperatures. The effective penetration depth $\lambda_{\text{eff}}(H)$ tends to a constant value for $\mu_0 H \geq 1$ T for all studied temperatures. Figure 4.3d shows the field dependence of γ_λ.

The value of λ_{eff} at 0 K can be extrapolated using the power law $\lambda_{\text{eff}}^{-2}(T) = \lambda_{\text{eff}}^{-2}(0)[1-(T/T_c)^n]$ stemming from the two-fluid model (see Fig. 4.3a). This yields $\lambda_{\text{eff}}(0) \simeq 1.8$ μm, a value that is very large compared to microscopic results on the same crystal family ($\lambda_{ab} \approx 290$ nm [105], or 258 nm [109]), or compared to non-intercalated $FeSe_{0.5}Te_{0.5}$ ($\lambda_{ab} \approx 491$ nm [110]). This may be due to the easier penetration of the magnetic field in a material where the superconducting phase is in minority. Our bulk measurement technique averages the penetration depth on the whole volume of the sample, resulting in a higher effective penetration depth. However, since no pure phase AFe_2Se_2 superconductor has yet been synthesized, it is not clear if it is possible to define a superconducting penetration depth independently of coexisting non superconducting regions. Granular superconductor theories also invoke a renormalized penetration depth [111], although in those models the superconducting regions are the majority phase, separated by thin Josephson junctions. Since μSR experiments report approximately 10% of superconducting volume [109], a conventional granular model may not be adapted.

The large $\lambda_{\text{eff}}(0)$ is consistent with the very small $\mu_0 H_{c1} \lesssim 0.3$ mT observed by SQUID in this crystal and in [102]. The small $\gamma_\lambda(0\text{ T}) \sim 1-2$ at very low fields (Fig. 4.3d) is also in agreement with an isotropic H_{c1}. The increase of γ_λ with H and the field independent $\lambda_{\text{eff}} = (\lambda_{ab}^2\lambda_c)^{1/3}$ imply that $\lambda_{ab} = \lambda_{\text{eff}}\gamma_\lambda^{-1/3}$ decreases with increasing H. This is consistent with the high-field NMR result [105].

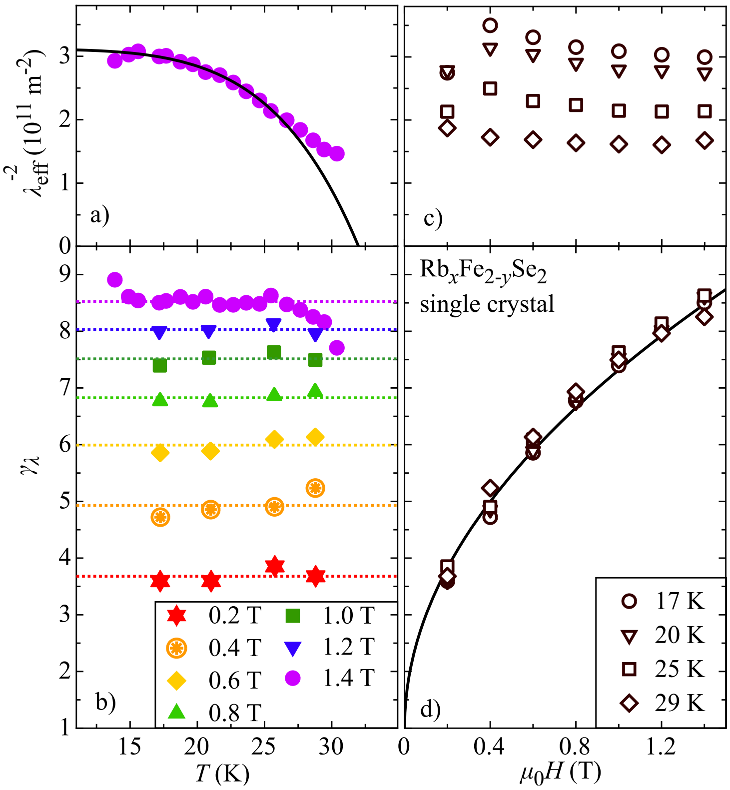

Figure 4.3: Summary of all the results obtained by analyzing the experimental torque signal of $Rb_xFe_{2-y}Se_2$ with Eq. (4.1). a) Temperature dependence of $\lambda_{\mathrm{eff}}^{-2}$. The line is a power law fit to the data at 1.4 T. b) Temperature dependence of γ_λ for various fields, showing that γ_λ is strongly increasing with H, but is almost independent of T. The dotted lines represent the average γ_λ for each field. c) Field dependence of $\lambda_{\mathrm{eff}}^{-2}$ for various temperatures. d) Field dependence of γ_λ for various T. The black line is a guide to the eye.

A field-dependent anisotropy has been linked to two-gap superconductivity in MgB_2 [36, 112], but in the two-gap scenario the field dependence should be accompanied by a temperature dependence [113]. In MgB_2, the superconductivity from the 3D π-band vanishes with increasing field, so the superconducting fluid density originates mainly from the 2D σ-band. The 2D character of the remaining band results in a larger anisotropy when closer to the superconducting transition. However, since the upper critical field anisotropy γ_H and the penetration depth anisotropy γ_λ have opposite variations, this band dimensionality argument can only apply to an anisotropy that increases with T or H, which is the case for γ_λ in MgB_2, but not in $Rb_xFe_{2-y}Se_2$. A temperature dependence of γ_λ and γ_H was also observed in FeSe based superconductors [114, 61, 39], in which multiband superconductivity is suggested from other experiments [115, 116]. The link between the temperature dependence of the anisotropy and multiband superconductivity is mostly derived from the different dimensionality of the bands. Anyway, it is not clear from band structure calculations nor ARPES measurements whether for our crystal a significant 3D band is to be expected [117, 118, 119, 120, 99], because the calculations and experiments are quite dependent on the exact chemical composition of the crystal.

The independence on temperature of γ_λ suggests that the origin of its field dependence is not related to the superconducting gap energy, which is strongly temperature dependent in the examined temperature range. However, the antiferromagnetic state's energy scale can be expected to be temperature independent in the superconducting temperature domain, because of the high

Néel temperature $T_N \approx 500$ K [121]. The superconducting temperature range is far too low to excite any change in such a strongly coupled antiferromagnet. Nevertheless, magnetic field modifications can lead to changes in the superconducting/antiferromagnetic domain structure, and change the coupling between superconducting areas. This could result in variations of the "averaged" effective anisotropy. The lattice parameters, in particular the pnictogen/selenide height in the iron-based superconductors, are directly related to superconductivity [122, 87]. It is also possible that magnetostrictive effects, which should increase with magnetic field, may influence the lattice parameters. This could result in changes of the system anisotropy.

4.2 Effect of annealing on $Rb_xFe_{2-y}Se_2$

Several studies report improved superconducting properties of $Rb_xFe_{2-y}Se_2$ post-annealed at 400°C [123, 124, 125]. Improved properties include higher critical current, higher upper critical field, and sharper superconducting transition.

Since this crystal family features several state transitions, it is interesting to investigate the effect of annealing near each of these transitions. Differential heat measurements show that $Rb_xFe_{2-y}Se_2$ (nominal composition $Rb_{0.85}Fe_{1.90}Se_2$) undergoes an iron vacancy ordering at T_s = 540 K, accompanied by a structural transition from $I4/mmm$ to $I4/m$. The Néel temperature, at which block antiferromagnetism appears, is $T_N = 517$ K. At $T_p = 489$ K, the vacancy ordered ($I4/m$) and disordered ($I4/mmm$) phases separate [126]. In order to study the effect of phase separation on the superconducting properties, three different annealing temperatures where chosen: well below, just before, and well above T_p, at respectively 413 K, 488 K, and 563 K (Fig. 4.4). The superconducting samples are conventionally named $A_T[t_{ann}]$, where t_{ann} is the duration of the annealing, and T is the annealing temperature. As-grown, shortly annealed, and lengthily annealed samples are compared.

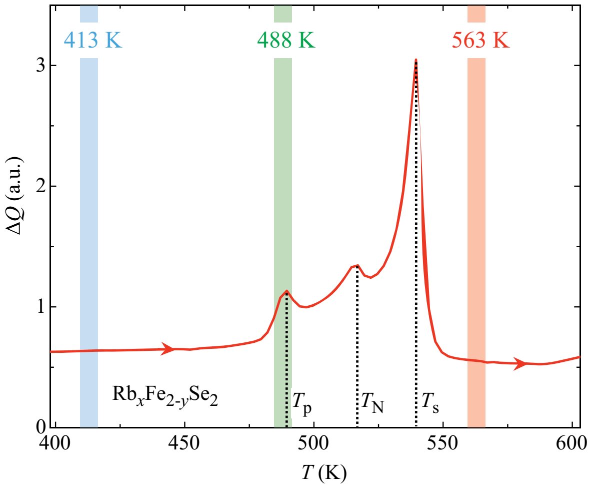

Figure 4.4: Differential heat ΔQ for a $Rb_xFe_{2-y}Se_2$ single crystal recorded between 400 and 600 K with a constant heating rate of 20 K/min. The three peaks are related to the three temperatures $T_p \approx 489$ K, $T_N \approx 517$ K, and $T_s \approx 540$ K. The temperatures 413 K, 488 K, and 563 K were chosen to anneal the $Rb_xFe_{2-y}Se_2$ crystals.

Figure 4.5 shows the zero field cooled magnetization of different samples. The * symbol denotes the best sample in terms of annealing induced changes. Annealing just at the phase separation onset temperature T_p clearly improves T_c (as also seen on resistivity measurements [126]) and the

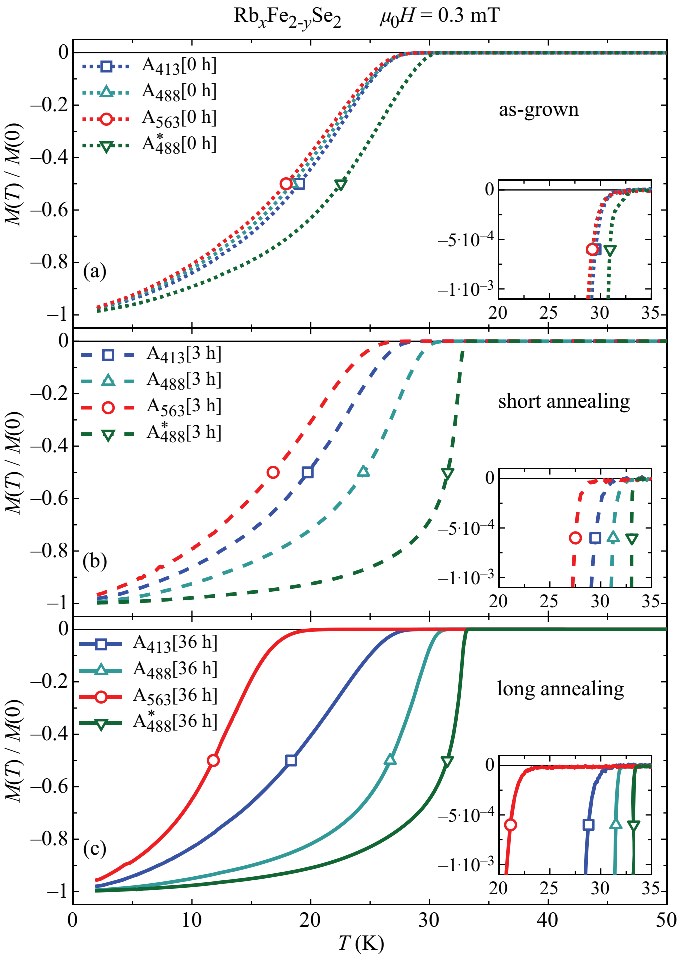

Figure 4.5: Normalized ZFC magnetization $M(T)/M(0)$ for the $Rb_xFe_{2-y}Se_2$ single crystals A_{413}, A_{488}, A_{563}, and A^*_{488} in a magnetic field $\mu_0H = 0.3$ mT applied along the c-axis. The panels present the data for the as-grown samples with $t_{ann} = 0$ h (a), annealed samples for $t_{ann} = 3$ h (b), and for $t_{ann} = 36$ h (c). The respective insets show close-ups of the onset of diamagnetism.

transition sharpness, whereas annealing well below or well after does not have a large effect, and may even be detrimental to superconductivity. The annealing time also plays a role; long annealings have stronger effects. Measurements of the magnetization as a function of the internal field show that H_{c1} increases with annealing just below T_p [126]. Resistivity measurements show that the upper critical field H_{c2} increases as well. The improvement of superconducting properties is visible from μSR data; the internal field distribution better matches the distribution of a regular vortex lattice after annealing just below T_p. Surprisingly, the volume fraction appears to be unchanged by annealing. In a 70 mT transverse field μSR experiment, the normal state relaxation rate increases with t_{ann}, which means that in the non AFM part of the sample, the field becomes more inhomogeneous. In a zero-field μSR experiment, no annealing effect was found, so the intrinsic fields stemming from the iron moments in the AFM phase do not change with annealing.

These results suggest that superconductivity in $Rb_xFe_{2-y}Se_2$ is boosted when there is more inhomogeneity, as was observed in FeSe-Te compounds [127]. Around 10% of the sample is superconducting (as seen by μSR [109, 126]), so boundaries between superconducting domains and AFM domains are expected to play an important role. In granular superconductors, the magnetic field penetration depth is renormalized as compared to the value in a pure superconductor. This is consistent with the fact that the penetration depth observed by macroscopic techniques (see Section 4.1) is larger than the one observed by local probes like μSR [109, 126]. However, granular theories were developed for majority superconducting grains separated by thin non-superconducting Josephson junctions, whereas with 10% superconducting volume, superconducting domains in $\mathrm{Rb}_x\mathrm{Fe}_{2-y}\mathrm{Se}_2$ would be of a more filamentary shape.

We can conclude from the present studies that the coexistence of magnetism and superconductivity in $\mathrm{Rb}_x\mathrm{Fe}_{2-y}\mathrm{Se}_2$ strongly affects the superconducting state. The anisotropy depends on the magnetic field and not on temperature, a quite unique feature in layered superconductors. Besides, annealing just at the phase separation of magnetic and non-magnetic domains seems to be related to modifications of the spatial distribution of those domains. Interestingly, these changes drastically improve the superconducting properties.

4.3 Publications related to Chapter 4

- *Magnetic-field tuned anisotropy in superconducting $Rb_xFe_{2-y}Se_2$*
  S. Bosma, R. Puzniak, A. Krzton-Maziopa, M. Bendele, E. Pomjakushina, K. Conder, H. Keller, and S. Weyeneth
  Physical Review B **85**, 064509 (2012)
  DOI: 10.1103/PhysRevB.85.064509

  e-prints:
  `http://arxiv.org/abs/1109.1430`
  `http://www.zora.uzh.ch/67291/`
  `http://prb.aps.org/abstract/PRB/v85/i6/e064509`

- *Superconductivity and magnetism in $Rb_xFe_{2-y}Se_2$: Impact of thermal treatment on mesoscopic phase separation*
  S. Weyeneth, M. Bendele, F. von Rohr, P. Dluzewski, R. Puzniak, A. Krzton-Maziopa, S. Bosma, Z. Guguchia, R. Khasanov, Z. Shermadini, A. Amato, E. Pomjakushina, K. Conder, A. Schilling, and H. Keller
  Physical Review B **86**, 134530 (2012)
  DOI: 10.1103/PhysRevB.86.134530

  e-prints:
  `http://arxiv.org/abs/1208.4760`
  `http://www.zora.uzh.ch/72338/`
  `http://prb.aps.org/pdf/PRB/v86/i13/e134530`

PHYSICAL REVIEW B **85**, 064509 (2012)

Magnetic-field tuned anisotropy in superconducting $Rb_xFe_{2-y}Se_2$

S. Bosma,[1,*] R. Puzniak,[2] A. Krzton-Maziopa,[3] M. Bendele,[1,4] E. Pomjakushina,[3] K. Conder,[3] H. Keller,[1] and S. Weyeneth[1,†]
[1]*Physik-Institut der Universität Zürich, Winterthurerstrasse 190, CH-8057 Zürich, Switzerland*
[2]*Institute of Physics, Polish Academy of Sciences, Aleja Lotników 32/46, PL-02-668 Warsaw, Poland*
[3]*Laboratory for Developments and Methods, Paul Scherrer Institute, CH-5232 Villigen PSI, Switzerland*
[4]*Laboratory for Muon Spin Spectroscopy, Paul Scherrer Institute, CH-5232 Villigen PSI, Switzerland*

(Received 6 September 2011; revised manuscript received 16 January 2012; published 9 February 2012)

The anisotropic superconducting properties of a $Rb_xFe_{2-y}Se_2$ single crystal with $T_c \simeq 32$ K were investigated by means of superconducting quantum interference device (SQUID) and torque magnetometry, probing the effective magnetic penetration depth $\lambda_{\rm eff}$ and the magnetic penetration depth anisotropy γ_λ. Interestingly, γ_λ is found to be temperature independent in the superconducting state but strongly field dependent: $\gamma_\lambda(0.2\ {\rm T}) < 4$ and $\gamma_\lambda(1.4\ {\rm T}) > 8$. This unusual anisotropic behavior, together with a large zero-temperature $\lambda_{\rm eff}(0) \simeq 1.8\ \mu$m, is possibly related to a superconducting state heavily biased by the coexisting antiferromagnetic phase.

DOI: 10.1103/PhysRevB.85.064509 PACS number(s): 74.70.Xa, 74.25.Bt, 74.25.Ha, 74.25.Op

I. INTRODUCTION

With the discovery of superconductivity in $LaFeAsO_{1-x}F_y$,[1] a new family of iron-based high-temperature superconductors was found. Its simplest member is $FeSe_{1-x}$, which consists of a stack of FeSe layers.[2] Its superconducting transition temperature $T_c \simeq 8$ K increases drastically with external pressure, reaching $T_c(8\ {\rm GPa}) \simeq 36$ K.[2,3] Interestingly, a similar high $T_c \simeq 30$ K is attained in the iron-selenide family $A_xFe_{2-y}Se_2$ by intercalating alkali atoms (A = K, Rb, Cs) between the FeSe layers.[4–6] However, T_c is found to decrease with pressure and is fully suppressed at 9 GPa for $K_xFe_{2-y}Se_2$ (Ref. 7) and at 8 GPa for $Cs_xFe_{2-y}Se_2$.[8] The critical temperature is almost insensitive to pressure below 1 GPa, suggesting that T_c is almost independent of small variations of the lattice constants. This provides an opportunity to study the temperature dependence of physical quantities without being affected by changes of the lattice constants due to thermal expansion. Early μSR experiments on $Cs_xFe_{2-y}Se_2$ indicate that superconductivity and antiferromagnetism coexist on microscopic length scales.[9] The Néel temperature $T_N \approx 500$ K (Ref. 10) of $K_{0.8}Fe_{2-y}Se_2$ is substantially higher than $T_c \simeq 30$ K. Several experiments point toward nanoscale phase separation between superconducting, vacancy-disordered domains and vacancy-ordered antiferromagnetic (AFM) domains.[11–14] In contrast to the slightly hole doped $FeSe_{1-x}$, the intercalation of alkali ions A into the FeSe structure introduces a large amount of electrons into the system.[15] Other experiments[16] suggested that this highly electron doped system contains no hole-like sheets at the Fermi surface, and thus electron scattering between hole and electron-like bands is impossible.[15] Moreover, Fe vacancies in the crystalline structure order at $\simeq 600$ K.[17] In $K_xFe_{2-y}Se_2$, the presence of vacancies appears to be detrimental to superconductivity.[18] This intriguing microscopic coexistence of vacancy ordering, antiferromagnetism, and superconductivity in $A_xFe_{2-y}Se_2$ points to an unconventional thermodynamic behavior of the superconducting state.

Recently, the lower critical field H_{c1} was investigated in tetragonal $K_xFe_{2-y}Se_2$ for magnetic fields H along different crystallographic directions, i.e., parallel to the ab plane and parallel to the c axis,[19,20] revealing a surprisingly low and isotropic $\mu_0 H_{c1} \simeq 0.3$ mT. Invoking the phenomenological relation between H_{c1} and the effective magnetic penetration depth $\lambda_{\rm eff}$ for an isotropic superconductor $\mu_0 H_{c1} = \Phi_0(\ln\kappa + 0.5)/(4\pi\lambda_{\rm eff}^2)$,[21] a value of $\lambda_{\rm eff}(0) \simeq 1.6$–$1.8\ \mu$m is obtained (assuming an approximate Ginzburg-Landau parameter $\kappa \sim 100$–200). This low field estimate of $\lambda_{\rm eff}$ deviates remarkably from the small in-plane magnetic penetration depth $\lambda_{ab}(0) \simeq 0.29\ \mu$m derived from NMR experiments at 8.3 T on a similar sample.[22] Moreover, the numerous observations of an anisotropic vortex lattice in high magnetic fields[19,22–24] contrast with the isotropic behavior of H_{c1} in low magnetic fields. In order to illuminate this intriguing field dependence of the superconducting properties, we performed a detailed magnetic study of $Rb_xFe_{2-y}Se_2$.

II. CRYSTAL GROWTH

A $Rb_xFe_{2-y}Se_2$ single crystal with composition $Rb_{0.77(2)}Fe_{1.61(3)}Se_2$ as refined by x-ray fluorescence was grown from a melt by the Bridgman method, using a presynthesized ceramic precursor of $FeSe_{0.98}$ and metallic rubidium. For the precursor synthesis high-purity (at least 99.99%; *Alfa Aesar*) powders of iron and selenium were mixed in the molar proportion 1 Fe : 0.98 Se and pressed into a rod. This nominal stoichiometry, chosen on the basis of our previous studies[25] of the Fe-Se chemical phase diagram, provides an iron selenide of pure tetragonal phase. The mixture was prereacted in a sealed silica ampoule at 700 °C for 15 h and then grounded in an inert atmosphere, pressed again into a rod, sealed in an evacuated double-wall quartz ampoule, and resintered at 700 °C. After 48 h the furnace was cooled down to 400 °C and kept at this temperature for 36 h more. For the single-crystal growth a piece of the Fe-Se rod was sealed in an evacuated silica Bridgman ampoule with an appropriate amount of pure alkali metal placed in an additional thin silica tube; 5% excess of Rb was added to compensate its loss during synthesis. The Bridgman ampoule was sealed in another protecting evacuated quartz tube. The ampoule was heated at 1030 °C for 2 h for homogenization, followed by cooling down the melt to 750 °C at a rate of 6 °C/h. Finally, the furnace was cooled down to room temperature at a rate of 200 °C/h. After synthesis the ampoules were transferred to a He glovebox and opened there to protect the crystal from oxidation in the air.

III. MAGNETIC MEASUREMENTS

The superconducting properties of the platelike crystal of dimensions $\sim 5 \times 1 \times 0.2$ mm^3 (thickness of 0.2 mm along the c axis) were characterized with a *Quantum Design* MPMS XL superconducting quantum interference device (SQUID) magnetometer. The temperature dependence of m/H, where m is the magnetic moment, is shown in Fig. 1 for various magnetic fields H applied after zero-field cooling. The onset transition temperature for this sample is estimated to be $T_c \simeq 32$ K. For both studied orientations [parallel to the c axis, shown in Fig. 1(a), and parallel to the ab plane, shown in Fig. 1(b)], the magnetic properties are very similar. For $\mu_0 H = 0.1$ mT a sharp diamagnetic transition is observed for both field orientations. In higher fields, the diamagnetism is rapidly suppressed, indicating that $\mu_0 H_{c1}$ for Rb$_x$Fe$_{2-y}$Se$_2$ is very low ($\mu_0 H_{c1} \lesssim 0.3$ mT, including demagnetizing field correction[26]).

A small piece of rectangular shape and approximate dimensions $150 \times 150 \times 90$ μm^3 was cleaved off the above Rb$_x$Fe$_{2-y}$Se$_2$ single crystal. Magnetic torque investigations were carried out using a homemade magnetic torque sensor.[27] For a uniaxial superconductor like tetragonal Rb$_x$Fe$_{2-y}$Se$_2$, the angular dependence of the magnetic torque $\vec{\tau} = \vec{m} \times \mu_0 \vec{H}$ in the London approximation ($H_{c1} < H < H_{c2}$) can be written as[28]

$$\tau(\theta) = -\frac{V\Phi_0 H \gamma_\lambda^{2/3}}{16\pi\lambda_{\text{eff}}^2}\left(1 - \frac{1}{\gamma_\lambda^2}\right)\frac{\sin(2\theta)}{\epsilon(\theta)} \ln\left(\frac{\eta H_{c2}^{||c}}{\epsilon(\theta) H}\right). \quad (1)$$

Here θ is the angle between H and the crystallographic c axis, $\epsilon(\theta) = [\cos^2(\theta) + \gamma_\lambda^{-2}\sin^2(\theta)]^{1/2}$ is the angular scaling function, $H_{c2}^{||c}$ is the c axis upper critical field, and η is a dimensionless parameter of the order of unity. Without loss of generality η is restricted to 1 within this work.[29] The anisotropy parameter $\gamma_\lambda = \lambda_c/\lambda_{ab}$ is the ratio of the out-of-plane and in-plane magnetic penetration depths, whereas $\lambda_{\text{eff}} = (\lambda_{ab}^2 \lambda_c)^{1/3}$ denotes the effective magnetic penetration depth. It is possible that our sample presents phase separation between superconducting nonmagnetic regions and antiferromagnetic, nonsuperconducting regions, with a domain size smaller than the penetration depth.[11] In that case, applying the Kogan model yields a λ_{eff} that may be renormalized to a larger value than the superconducting parameter $(\lambda_{ab}^2\lambda_c)^{1/3}$. The field penetrates more easily in this phase-separated material, and the Kogan model yields an "averaged" effective bulk penetration depth. The good agreement between Eq. (1) and the data [Fig. 2(b)] shows that the Kogan model is still useful, albeit with a broader interpretation of its parameters.

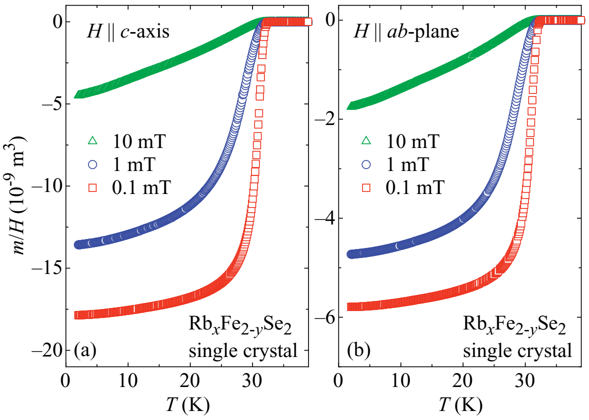

FIG. 1. (Color online) Zero-field-cooled measurements of m/H of single crystal Rb$_x$Fe$_{2-y}$Se$_2$ for (a) $H||c$ axis and (b) $H||ab$ plane. The change of vortex penetration with temperature is very similar for both directions, consistent with an isotropic $\mu_0 H_{c1} \lesssim 0.3$ mT. The sharp transition at $T_c \simeq 32$ K demonstrates the high quality of the crystal. Due to demagnetization the magnitude of m/H varies by a factor of $\sim$3 for both orientations. A rough estimation of the demagnetization factors from the sample dimensions yields $0.05 < N^{||ab} < 0.3$ and $N^{||c} \sim 0.65$.

The magnetic torque experiments at various T and H were performed by turning H around the sample in a plane containing the c axis [see inset in Fig. 2(a)] and measuring the resulting torque. As an example, Fig. 2(a) shows the angular dependence of the torque signal measured at 15 K in 1.4 T. Note that the torque signal is affected by an angular irreversibility between the clockwise (τ_{cw}) and counterclockwise (τ_{ccw}) branches. Such irreversible angular-dependent torque signals are usually observed in hard superconductors due to vortex pinning.[30,31] Due to the tetragonal structure of Rb$_x$Fe$_{2-y}$Se$_2$, twinning in the crystal manifests itself in the results only through pinning on the twin boundaries, and all in-plane parameters are not separated along the a and b axes in the analysis. In this work, the so-called vortex-shaking technique[32] was successfully applied to reduce irreversibility, allowing a more reliable determination of the superconducting parameters. This was done by applying a small ac field orthogonal to H in order to enhance the vortex relaxation toward thermodynamic equilibrium. As seen in Fig. 2(a), the vortex shaking clearly reduces the irreversible component, especially for H close to the ab plane. In Fig. 2(b) the average torque $\tau = (\tau_{\text{cw}} + \tau_{\text{ccw}})/2$ is presented. The torque signal consists of a superconducting component described by Eq. (1) and a magnetic background component $\tau_{\text{BG}} = -(\chi_{ab} - \chi_c)V\mu_0 H^2 \sin(2\theta)/2$. The variables χ_c and χ_{ab} denote the magnetic susceptibilities along the crystallographic axes. Here $\chi_{ab} > \chi_c$ (as also mentioned in Ref. 22) and τ_{BG} is large, consistent with a bulk antiferromagnetic phase having the magnetic moments aligned along the c axis.[9,17] The subtraction of this antiferromagnetic background can be performed either by adding a sinusoidal component in the fitting routine of Eq. (1) or by directly removing the symmetric sinusoidal component of the data, as discussed in Ref. 31. All results presented in this work are independent of the background treatment.

The parameters $H_{c2}^{||c}$, γ_λ, and λ_{eff} can be extracted simultaneously by analyzing the magnetic torque data with Eq. (1). However, in order to reduce the amount of free fit parameters, $H_{c2}^{||c}$ was fixed according to a Werthamer-Helfand-Hohenberg (WHH) temperature dependence.[33] The slope $dH_{c2}^{||c}/dT$ at T_c was fixed to ~ -1 T/K, in concordance with resistivity results of a similar sample.[24] Small variations in $dH_{c2}^{||c}/dT$ do not affect the results of the analysis since

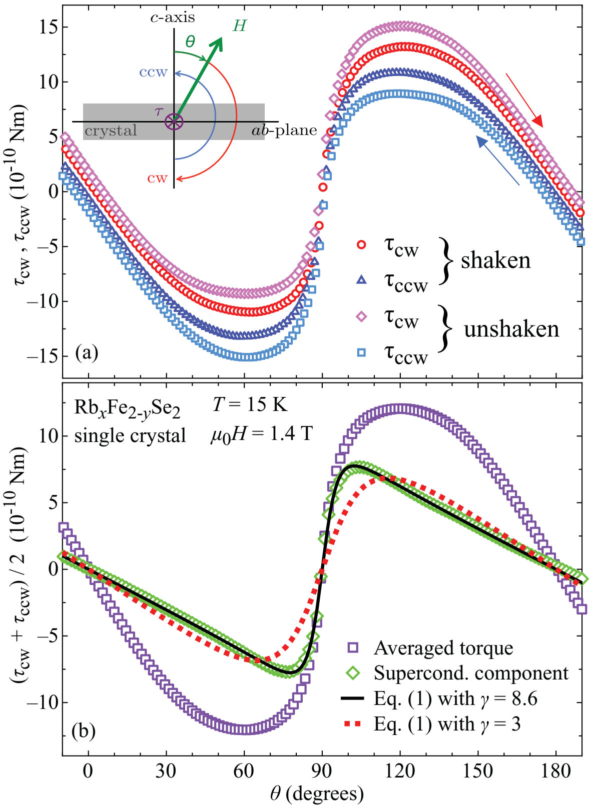

FIG. 2. (Color online) Angular-dependent torque of single-crystal $Rb_xFe_{2-y}Se_2$ measured at 15 K and 1.4 T. For clarity not all of the measured data are presented. (a) Comparison of magnetic torque data obtained without and with the shaking procedure as discussed in the text. The "unshaken" red data τ_{cw} (blue data τ_{ccw}) are gathered by turning H clockwise (counterclockwise) around the sample. The inset explains schematically the field configuration during the experiment. The "shaken" data are obtained by applying a transverse ac field, yielding reduced irreversibility and enhanced data quality. (b) Angular dependence of the "shaken" magnetic torque averaged for both directions. The green curve is the superconducting component of the signal, obtained after subtracting the background as explained in the text. A fit by Eq. (1) yields $\gamma_\lambda(15\text{ K}, 1.4\text{ T}) \simeq 8.6$ (black line). For comparison, the red dotted line is calculated with a fixed $\gamma_\lambda = 3$.

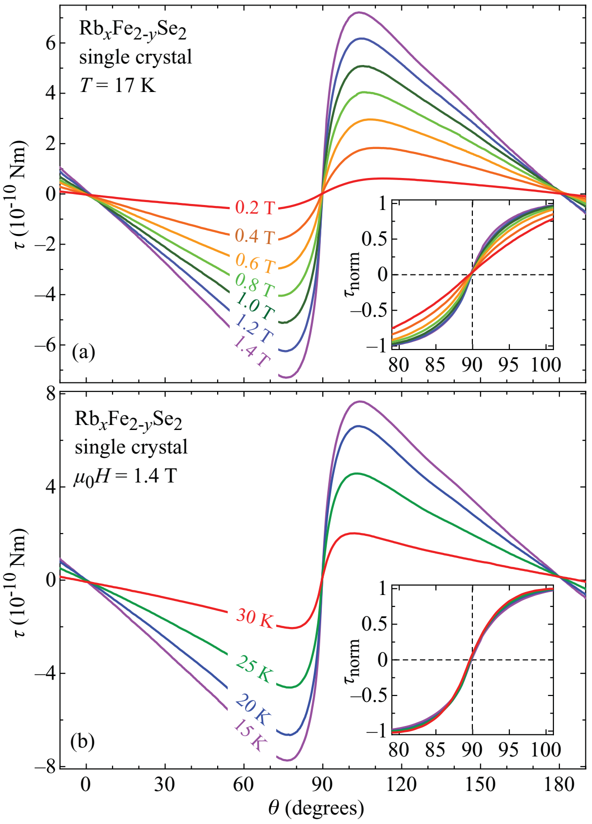

FIG. 3. (Color online) Angular dependence of the superconducting component of the magnetic torque of $Rb_xFe_{2-y}Se_2$. (a) Magnetic torque at 17 K for various magnetic fields. (b) Magnetic torque at 1.4 T for various temperatures. The insets in both panels show the evolution of τ_{norm} close to the *ab* plane.

H_{c2} contributes only logarithmically in Eq. (1) and has no weight in the determination of γ_λ and λ_{eff} in low magnetic fields.[31] Magnetic torque curves with the antiferromagnetic background subtracted are presented in Fig. 3 for various T [Fig. 3(a)] and H [Fig. 3(b)]. The insets show the normalized magnetic torque $\tau_{norm} = \tau(\theta)/\max[\tau(\theta)]$ close to the *ab* plane. A change of the shape of $\tau_{norm}(\theta)$ qualitatively reflects a change of γ_λ. Note that the slope of τ_{norm} vs θ changes strongly with H but not with T. This demonstrates that γ_λ is field dependent but not temperature dependent. As the field direction is approaching the *ab* plane, the screening currents start to flow not only in plane but also out of plane, which makes the torque depend strongly on λ_{ab} and λ_c in this angular region. The temperature and field effect on the anisotropy γ_λ are consequently already visible on the data taken around the *ab* plane, independently of the strict validity of Eq. (1) in a phase-separated material.

The temperature dependence of λ_{eff} presented in Fig. 4(a) can be fitted with the empirical power law $\lambda_{eff}^{-2}(T) = \lambda_{eff}^{-2}(0)[1 - (T/T_c)^n]$ with $T_c \simeq 32$ K, $n \simeq 5.2$, and $\lambda_{eff}(0) \simeq 1.8$ μm. This rather large value of the effective penetration depth may be due to phase separation, as mentioned above. The resulting value of n is substantially larger than the exponent 4 expected in a two-fluid model. This might be related to phase separation, as the links between superconducting domains could depend on temperature, changing the temperature dependence of the penetration depth. Figure 4(b) shows $\gamma_\lambda(T)$ for various H. It is almost temperature independent between T_c and $T_c/2$ for all fields studied. The slight drop observed at higher temperatures in 1.4 T may be due to the proximity of the transition, which reduces the superconducting signal. The increase of γ at 1.4 T at low temperatures is most likely due to pinning effects.[34] Most importantly, a remarkable monotonous field dependence of γ_λ is observed [Fig. 4(d)], with the strongest dependence in the lowest fields. In low fields, $\gamma_\lambda(0.2\text{ T}) \simeq 3.5$. An extrapolation of the measured values of

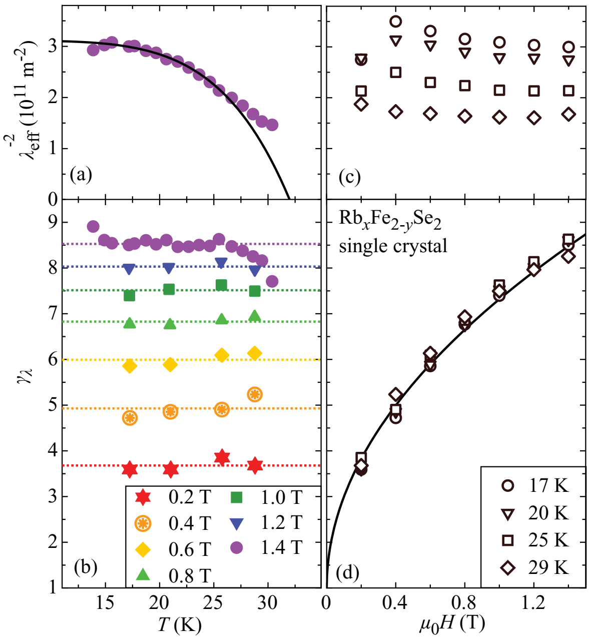

FIG. 4. (Color online) Summary of all the results obtained by analyzing the experimental torque signal of Rb$_x$Fe$_{2-y}$Se$_2$ with Eq. (1). (a) Temperature dependence of λ_{eff}^{-2}. The line is a power law fit to the data at 1.4 T. (b) Temperature dependence of γ_λ for various fields, showing that γ_λ is strongly increasing with H but is almost independent of T. The dotted lines represent the average γ_λ for each field. (c) Field dependence of λ_{eff}^{-2} for various temperatures. (d) Field dependence of γ_λ for various T. The black line is a guide to the eye.

γ_λ toward zero field yields $\gamma_\lambda(0\ \text{T}) \sim 1$–2. In Fig. 4(c) the field dependence of $\lambda_{eff}(H)$ is shown for various T. The effective penetration depth $\lambda_{eff}(H)$ tends to a constant value for $\mu_0 H \geqslant 1$ T for all studied T.

IV. DISCUSSION

The extrapolated $\lambda_{eff}(0) \simeq 1.8\ \mu$m is surprisingly large compared to that of other iron-based superconductors. In the related iron selenide FeSe$_{0.5}$Te$_{0.5}$ a much lower value of $\lambda_{eff}(0) \simeq 0.7\ \mu$m was reported.[35] However, for Rb$_x$Fe$_{2-y}$Se$_2$ such a large $\lambda_{eff}(0)$ is consistent with the very small $\mu_0 H_{c1} \lesssim 0.3$ mT observed in this work and in K$_x$Fe$_{2-y}$Se$_2$ by others.[19] The small $\gamma_\lambda(0\ \text{T}) \sim 1$–2 at very low fields is also in agreement with an isotropic H_{c1}. The increase of $\gamma_\lambda = \lambda_c/\lambda_{ab}$ with H and the field-independent $\lambda_{eff} = (\lambda_{ab}^2\lambda_c)^{1/3}$ imply that $\lambda_{ab} = \lambda_{eff}\gamma_\lambda^{-1/3}$ decreases with increasing H. This is consistent with the high-field NMR result.[22] The small high-field value of λ_{ab} reported in Ref. 22, in combination with the saturating $\lambda_{eff}(H)$ and the field dependence of $\gamma_\lambda(H)$ observed here, suggests that γ_λ continues to increase at higher fields. Note that the anisotropy of ~ 3 (Ref. 23) observed in very high fields by upper critical field measurements cannot be directly compared with the magnetic penetration-depth anisotropy γ_λ investigated here because, in general, $H_{c2}^{||ab}/H_{c2}^{||c} = \xi_{ab}/\xi_c = \gamma_\xi \neq \gamma_\lambda$.[31]

A field-dependent γ_λ might be associated with a complex band structure since in the case of multiple superconducting gaps originating from different bands the superconducting screening currents, related to λ_{ab} and λ_c, may give rise to an unusual behavior of γ_λ. A similar behavior was observed in MgB$_2$, where the two-gap excitation spectrum yields a strongly field-dependent anisotropy.[36,37] In MgB$_2$, as the field increases, the gap from the three-dimensional (3D) σ band is closed, so the main part of the superconducting fluid density comes from the two-dimensional (2D) π band. The 2D character of the remaining band implies a larger anisotropy.

Band structure calculations[38–40] in A_xFe$_{2-y}$Se$_2$ yield multiple bands, with four 2D sheets on the sides of the Brillouin zone and one cylindrical sheet at the center. Depending on doping, this cylinder can be split into two 3D cones in K$_{0.8}$Fe$_2$Se$_2$,[38] which are completely detached (3D) in the calculation of Ref. 39, although when the authors use experimental lattice parameters, these cones are replaced by a cylinder (2D). According to Ref. 40, the center band is a cylinder. In CsFe$_2$Se$_2$ and Cs$_{0.8}$Fe$_2$Se$_2$, this band consists of two almost detached cones.[38] In Tl$_{0.58}$Rb$_{0.42}$Fe$_{1.72}$Se$_2$,[41] two gaps of different amplitudes were observed on the side and center bands, but the candidate for a 3D inner band was too small for a gap to be observed. It is therefore not yet clear whether for Rb$_x$Fe$_{2-y}$Se$_2$ with the doping used in this work a 3D band is present. Clearly, more material-specific work is needed in order to clarify the interplay between multiband superconductivity and the anisotropy of Rb$_x$Fe$_{2-y}$Se$_2$. However, if a 2D-3D band scenario is the origin of the field dependence of the anisotropy of Rb$_x$Fe$_{2-y}$Se$_2$, it must be temperature dependent as well,[36] which is not the case according to Fig. 4(d).

The temperature-independent γ_λ suggests that the origin of its field dependence is not related to the superconducting gap energy, which is strongly temperature dependent in the examined temperature range. However, there is one energy scale that is almost temperature independent in the superconducting state: the Néel temperature $T_N \approx 500$ K.[10] A superconductor coexisting with an antiferromagnetic phase is expected to behave in a peculiar way, although the temperature range studied here is far too low to excite any change in this strongly coupled antiferromagnet. However, magnetic-field modifications can lead to changes in the domain structure and therefore changes of coupling between superconducting areas. This could result in variations of the "averaged" effective anisotropy. As was shown for various iron-based superconductors, the lattice parameters, in particular the pnictogen height in the iron-pnictides, are directly related to superconductivity.[42] Importantly, such scaling also works for the iron selenide layer.[5,42] It is also possible that magnetostrictive effects, which are expected to increase with magnetic field, may influence the lattice parameters and by that the anisotropy of the system. In such a case the strong curvature of $H_{c2}(T)$ in the vicinity of T_c often observed in pnictides and chalcogenides may be explained by the change of T_c with H caused by the change of pnictogen height.

V. SUMMARY

In summary, we present an investigation of the magnetic properties of Rb$_x$Fe$_{2-y}$Se$_2$, revealing a strong field dependence of γ_λ ranging from $\gamma_\lambda(0.2\ \text{T}) < 4$ to $\gamma_\lambda(1.4\ \text{T}) > 8$. This behavior stands out among other iron-based superconductors, consistent with the singular coexistence of magnetic ordering and superconductivity. In accordance with lower critical field measurements, our data suggest that in very low fields $\gamma_\lambda(0\,\text{T}) \sim 1$–2. At 1.4 T the effective magnetic penetration depth is $\lambda_{\text{eff}}(0) \simeq 1.8\ \mu$m. The vortex phase in $Rb_xFe_{2-y}Se_2$ is best described by an isotropic three-dimensional state in low fields that becomes strongly anisotropic with increasing field. In this respect the novel iron selenide $Rb_xFe_{2-y}Se_2$ could be a potential candidate for magnetic-field tuned applications of superconductivity.

ACKNOWLEDGMENTS

This work was supported by the Swiss National Science Foundation, in part by the NCCR program MaNEP and the Sciex-NMSch (project code 10.048), and by the National Science Centre (Poland) based on Decision No. DEC-2011/01/B/ST3/02374.

---

[*] sbosma@physik.uzh.ch
[†] wstephen@physik.uzh.ch

[1] Y. Kamihara, T. Watanabe, M. Hirano, and H. Hosono, J. Am. Chem. Soc. **130**, 3296 (2008).

[2] F.-C. Hsu, J.-Y. Luo, K.-W. Yeh, T.-K. Chen, T.-W. Huang, P. M. Wu, Y.-C. Lee, Y.-L. Huang, Y.-Y. Chu, D.-C. Yan, and M.-K. Wu, Proc. Natl. Acad. Sci. USA **105**, 14262 (2008).

[3] S. Margadonna, Y. Takabayashi, Y. Ohishi, Y. Mizuguchi, Y. Takano, T. Kagayama, T. Nakagawa, M. Takata, and K. Prassides, Phys. Rev. B **80**, 064506 (2009).

[4] J. Guo, S. Jin, G. Wang, S. Wang, K. Zhu, T. Zhou, M. He, and X. Chen, Phys. Rev. B **82**, 180520 (2010).

[5] A. Krzton-Maziopa, Z. Shermadini, E. Pomjakushina, V. Pomjakushin, M. Bendele, A. Amato, R. Khasanov, H. Luetkens, and K. Conder, J. Phys. Condens. Matter **23**, 052203 (2011).

[6] C.-H. Li, B. Shen, F. Han, X. Zhu, and H.-H. Wen, Phys. Rev. B **83**, 184521 (2011).

[7] J. Guo, X. Chen, C. Zhang, J. Guo, X. Chen, Q. Wu, D. Gu, P. Gao, X. Dai, L. Yang, H.-K. Mao, L. Sun, and Z. Zhao, e-print arXiv:1101.0092 [cond-mat.supr-con] (to be published).

[8] G. Seyfarth, D. Jaccard, P. Pedrazzini, A. Krzton-Maziopa, E. Pomjakushina, K. Conder, and Z. Shermadini, Solid State Commun. **151**, 747 (2011).

[9] Z. Shermadini, A. Krzton-Maziopa, M. Bendele, R. Khasanov, H. Luetkens, K. Conder, E. Pomjakushina, S. Weyeneth, V. Pomjakushin, O. Bossen, and A. Amato, Phys. Rev. Lett. **106**, 117602 (2011).

[10] R. H. Liu, X. G. Luo, M. Zhang, A. F. Wang, J. J. Ying, X. F. Wang, Y. J. Yan, Z. J. Xiang, P. Cheng, G. J. Ye, Z. Y. Li, and X. H. Chen, Europhys. Lett. **94**, 27008 (2011).

[11] A. Ricci, N. Poccia, G. Campi, B. Joseph, G. Arrighetti, L. Barba, M. Reynolds, M. Burghammer, H. Takeya, Y. Mizuguchi, Y. Takano, M. Colapietro, N. L. Saini, and A. Bianconi, Phys. Rev. B **84**, 060511 (2011).

[12] B. Shen, B. Zeng, G. F. Chen, J. B. He, D. M. Wang, H. Yang, and H. H. Wen, Europhys. Lett. **96**, 37010 (2011).

[13] V. Ksenofontov, G. Wortmann, S. A. Medvedev, V. Tsurkan, J. Deisenhofer, A. Loidl, and C. Felser, Phys. Rev. B **84**, 180508(R) (2011).

[14] Z. Wang, Y. J. Song, H. L. Shi, Z. W. Wang, Z. Chen, H. F. Tian, G. F. Chen, J. G. Guo, H. X. Yang, and J. Q. Li, Phys. Rev. B **83**, 140505 (2011).

[15] A. L. Ivanovskii, Phys. C **471**, 409 (2011).

[16] Y. Zhang, L. X. Yang, M. Xu, Z. R. Ye, F. Chen, C. He, H. C. Xu, J. Jiang, B. P. Xie, J. J. Ying, X. F. Wang, X. H. Chen, J. P. Hu, M. Matsunami, S. Kimura, and D. L. Feng, Nat. Mater. **10**, 273 (2011).

[17] W. Bao, Q. Huang, G. F. Chen, M. A. Green, D. M. Wang, J. B. He, X. Q. Wang, and Y. Qiu, Chin. Phys. Lett. **28**, 086104 (2011).

[18] W. Li, H. Ding, P. Deng, K. Chang, C. Song, K. He, L. Wang, X. Ma, J.-P. Hu, X. Chen, and Q.-K. Xue, Nat. Phys. **8**, 126 (2012).

[19] H. Lei and C. Petrovic, Phys. Rev. B **83**, 184504 (2011).

[20] M. I. Tsindlekht, I. Felner, M. Zhang, A. F. Wang, and X. H. Chen, Phys. Rev. B **84**, 052503 (2011).

[21] R. A. Klemm and J. R. Clem, Phys. Rev. B **21**, 1868 (1980).

[22] D. A. Torchetti, M. Fu, D. C. Christensen, K. J. Nelson, T. Imai, H. C. Lei, and C. Petrovic, Phys. Rev. B **83**, 104508 (2011).

[23] E. D. Mun, M. M. Altarawneh, C. H. Mielke, V. S. Zapf, R. Hu, S. L. Bud'ko, and P. C. Canfield, Phys. Rev. B **83**, 100514(R) (2011).

[24] V. Tsurkan, J. Deisenhofer, A. Günther, H.-A. Krug von Nidda, S. Widmann, and A. Loidl, Phys. Rev. B **84**, 144520 (2011).

[25] E. Pomjakushina, K. Conder, V. Pomjakushin, M. Bendele, and R. Khasanov, Phys. Rev. B **80**, 024517 (2009).

[26] J. A. Osborn, Phys. Rev. **67**, 351 (1945).

[27] S. Kohout, J. Roos, and H. Keller, Rev. Sci. Instrum. **78**, 013903 (2007).

[28] V. G. Kogan, Phys. Rev. B **38**, 7049 (1988).

[29] S. Bosma, S. Weyeneth, R. Puzniak, A. Erb, A. Schilling, and H. Keller, Phys. Rev. B **84**, 024514 (2011).

[30] S. Weyeneth, R. Puzniak, U. Mosele, N. D. Zhigadlo, S. Katrych, Z. Bukowski, J. Karpinski, S. Kohout, J. Roos, and H. Keller, J. Supercond. Novel Magn. **22**, 325 (2009).

[31] S. Weyeneth, R. Puzniak, N. D. Zhigadlo, S. Katrych, Z. Bukowski, J. Karpinski, and H. Keller, J. Supercond. Novel Magn. **22**, 347 (2009).

[32] M. Willemin, C. Rossel, J. Hofer, H. Keller, A. Erb, and E. Walker, Phys. Rev. B **58**, R5940 (1998).

[33] N. R. Werthamer, E. Helfand, and P. C. Hohenberg, Phys. Rev. **147**, 295 (1966).

[34] M. Willemin, A. Schilling, H. Keller, C. Rossel, J. Hofer, U. Welp, W. K. Kwok, R. J. Olsson, and G. W. Crabtree, Phys. Rev. Lett. **81**, 4236 (1998).

[35] M. Bendele, S. Weyeneth, R. Puzniak, A. Maisuradze, E. Pomjakushina, K. Conder, V. Pomjakushin, H. Luetkens, S. Katrych, A. Wisniewski, R. Khasanov, and H. Keller, Phys. Rev. B **81**, 224520 (2010).

[36] M. Angst, R. Puzniak, A. Wisniewski, J. Jun, S. M. Kazakov, J. Karpinski, J. Roos, and H. Keller, Phys. Rev. Lett. **88**, 167004 (2002).

[37] M. Angst and R. Puzniak, in *Focus on Superconductivity* (Nova Science, New York, 2004), Chap. 1, pp. 1–49, e-print arXiv:cond-mat/0305048.

[38] I. A. Nekrasov and M. V. Sadovskii, JETP Lett. **93**, 166 (2011).
[39] I. R. Shein and A. L. Ivanovskii, Phys. Lett. A **375**, 1028 (2011).
[40] C. Cao and J. Dai, Chin. Phys. Lett. **28**, 057402 (2011).
[41] D. Mou, S. Liu, X. Jia, J. He, Y. Peng, L. Zhao, L. Yu, G. Liu, S. He, X. Dong, J. Zhang, H. Wang, C. Dong, M. Fang, X. Wang, Q. Peng, Z. Wang, S. Zhang, F. Yang, Z. Xu, C. Chen, and X. J. Zhou, Phys. Rev. Lett. **106**, 107001 (2011).
[42] Y. Mizuguchi, Y. Hara, K. Deguchi, S. Tsuda, T. Yamaguchi, K. Takeda, H. Kotegawa, H. Tou, and Y. Takano, Supercond. Sci. Technol. **23**, 054013 (2010).

PHYSICAL REVIEW B **86**, 134530 (2012)

Superconductivity and magnetism in $\mathrm{Rb}_x\mathrm{Fe}_{2-y}\mathrm{Se}_2$: Impact of thermal treatment on mesoscopic phase separation

S. Weyeneth,[1,*] M. Bendele,[1,2,†] F. von Rohr,[1] P. Dluzewski,[3] R. Puzniak,[3] A. Krzton-Maziopa,[4,‡] S. Bosma,[1] Z. Guguchia,[1]
R. Khasanov,[2] Z. Shermadini,[2] A. Amato,[2] E. Pomjakushina,[4] K. Conder,[4] A. Schilling,[1] and H. Keller[1]
[1]*Physik-Institut der Universität Zürich, Winterthurerstrasse 190, CH-8057 Zürich, Switzerland*
[2]*Laboratory for Muon Spin Spectroscopy, Paul Scherrer Institute, CH-5232 Villigen PSI, Switzerland*
[3]*Institute of Physics, Polish Academy of Sciences, Aleja Lotników 32/46, PL-02-668 Warsaw, Poland*
[4]*Laboratory for Developments and Methods, Paul Scherrer Institute, CH-5232 Villigen PSI, Switzerland*
(Received 23 August 2012; revised manuscript received 9 October 2012; published 25 October 2012)

An extended study of the superconducting and normal-state properties of various as-grown and post-annealed $\mathrm{Rb}_x\mathrm{Fe}_{2-y}\mathrm{Se}_2$ single crystals is presented. Magnetization experiments evidence that annealing of $\mathrm{Rb}_x\mathrm{Fe}_{2-y}\mathrm{Se}_2$ at 413 K, well below the onset of phase separation $T_\mathrm{p} \simeq 489$ K, neither changes the magnetic nor the superconducting properties of the crystals. In addition, annealing at 563 K, well above T_p, suppresses the superconducting transition temperature T_c and leads to an increase of the antiferromagnetic susceptibility accompanied by the creation of ferromagnetic impurity phases, which are developing with annealing time. However, annealing at $T = 488\ \mathrm{K} \simeq T_\mathrm{p}$ increases T_c up to 33.3 K, sharpens the superconducting transition, increases the lower critical field, and strengthens the screening efficiency of the applied magnetic field. Resistivity measurements of the as-grown and optimally annealed samples reveal an increase of the upper critical field along both crystallographic directions as well as its anisotropy. Muon spin rotation and scanning transmission electron microscopy experiments suggest the coexistence of two phases below T_p: a magnetic majority phase of $\mathrm{Rb}_2\mathrm{Fe}_4\mathrm{Se}_5$ and a nonmagnetic minority phase of $\mathrm{Rb}_{0.5}\mathrm{Fe}_2\mathrm{Se}_2$. Both microscopic techniques indicate that annealing the specimens just at T_p does not affect the volume fraction of the two phases, although the magnetic field distribution in the samples changes substantially. This suggests that the microstructure of the sample, caused by mesoscopic phase separation, is modified by annealing just at T_p, leading to an improvement of the superconducting properties of $\mathrm{Rb}_x\mathrm{Fe}_{2-y}\mathrm{Se}_2$ and an enhancement of T_c.

DOI: 10.1103/PhysRevB.86.134530 PACS number(s): 74.25.−q, 74.62.Bf, 74.70.Xa, 75.30.Kz

I. INTRODUCTION

Iron-chalcogenide superconductors are usually related to the selenium-deficient compound FeSe_{1-x}, having a transition temperature $T_\mathrm{c} \simeq 8$ K.[1,2] Higher T_c's can be accessed by applying hydrostatic pressure p,[3] by inducing chemical pressure,[4,5] or by intercalating alkali atoms between the $\mathrm{Fe}_2\mathrm{Se}_2$ layers, yielding $A_x\mathrm{Fe}_{2-y}\mathrm{Se}_2$ (A = K, Rb, Cs).[6–8] Aside from superconductivity, many iron chalcogenides feature coexisting magnetic order, where subtle modifications of the crystal structure lead to drastic changes in superconducting and magnetic properties. This is the case for the compound $\mathrm{Rb}_x\mathrm{Fe}_{2-y}\mathrm{Se}_2$, which is superconducting below $T_\mathrm{c} \simeq 33$ K and antiferromagnetic below the Néel temperature T_N as high as 500 to 540 K.[9,10] In addition to these superconducting and magnetic orders, iron-vacancy ordering accompanied by a structural distortion at the temperature T_s as well as phase separation in magnetic and nonmagnetic domains at the temperature T_p are observed.[11]

Although it was shown by various groups that $A_x\mathrm{Fe}_{2-y}\mathrm{Se}_2$ exhibits bulk superconductivity,[12–14] muon spin rotation (μSR) experiments reported that only a minor volume fraction of ~10% of the sample is superconducting, whereas ~90% of the volume is antiferromagnetic.[15] From neutron experiments, the minority phase was identified to have the $I4/mmm$ space group with a small in-plane lattice constant a and a large out-of-plane lattice constant c.[16] It was discussed whether $A_x\mathrm{Fe}_{2-y}\mathrm{Se}_2$ should be treated as a filamentary or granular superconductor.[17] Besides, mesoscopic phase separation in $\mathrm{Rb}_x\mathrm{Fe}_{2-y}\mathrm{Se}_2$ was reported to prevail down to the nanoscale.[18–23] Microscopic techniques probing the stoichiometry of these distinct phases yield in average the composition $\mathrm{Rb}_2\mathrm{Fe}_4\mathrm{Se}_5$ for the antiferromagnetic vacancy-ordered majority phase (245-phase) and the composition $\mathrm{Rb}_{1-x}\mathrm{Fe}_2\mathrm{Se}_2$ for the superconducting Rb-deficient minority phase (122-phase).[24,25] Thus, the studied material may be treated as follows: the minority 122-phase is superconducting and is embedded in an antiferromagnetic matrix of the vacancy-ordered 245-phase.

Interestingly, it was observed that some post-annealed iron-chalcogenide samples may become superconducting despite their insulating as-grown behavior.[26–29] It was discussed that a possible change in the vacancy ordering and the related phase separation might be related to the observed changes in the electronic properties.[28] Obviously, by carefully tuning the conditions of annealing, one may gain direct control of the phase separation in $A_x\mathrm{Fe}_{2-y}\mathrm{Se}_2$ and by that of the superconducting and magnetic properties. In order to examine this scenario and to investigate the influence of vacancy ordering and phase separation on superconductivity and magnetism, we performed an extended study of thermally treated $\mathrm{Rb}_x\mathrm{Fe}_{2-y}\mathrm{Se}_2$ single crystals.

II. EXPERIMENTAL DETAILS

A set of $\mathrm{Rb}_x\mathrm{Fe}_{2-y}\mathrm{Se}_2$ single crystals with nominal composition $\mathrm{Rb}_{0.85}\mathrm{Fe}_{1.90}\mathrm{Se}_2$ was grown by the Bridgman method, similarly as described in Refs. 7 and 30. Here, a mixture of high-purity Fe, Se, and Rb (at least 99.99%; Alfa Aesar)

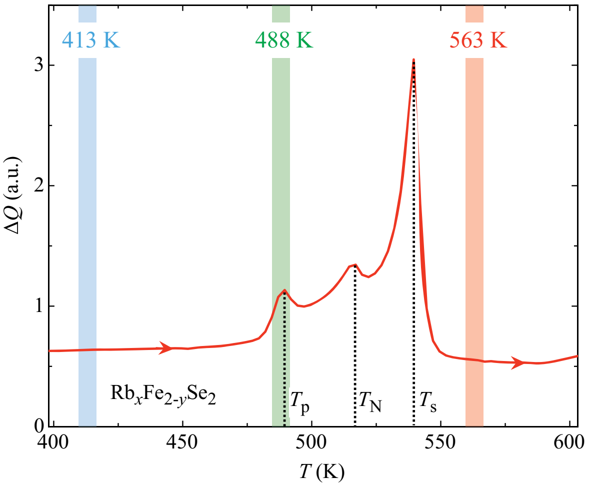

FIG. 1. (Color online) Differential heat ΔQ for a $Rb_xFe_{2-y}Se_2$ single crystal recorded between 400 and 600 K with a constant heating rate of 20 K/min. Three distinct peaks are observed, related to the three onset temperatures $T_p \simeq 489$ K, $T_N \simeq 517$ K, and $T_s \simeq 540$ K (see text). The three annealing temperatures 413, 488, and 563 K were chosen to post anneal the as-grown $Rb_xFe_{2-y}Se_2$ crystals for the subsequent experiments.

was sealed in an evacuated quartz ampoule. This ampoule, protected by a surrounding evacuated quartz tube, was heated to 1030 °C for 2 h. The melt was cooled first with −6 °C/h to 750 °C and finally to room temperature at a fast rate of −200 °C/h. After synthesis, the ampoule was transferred to a glove box and opened there to protect the crystals from degradation in air.

In order to study the thermal evolution of the mesoscopic phase separation, an as-grown $Rb_xFe_{2-y}Se_2$ single crystal was initially characterized by differential scanning calorimetry (DSC). With DSC, the differential amount of heat ΔQ required to increase the sample temperature T by ΔT with respect to a reference is recorded.[31] Measurements were performed with a *Netzsch* DSC 204F1 system, by heating up from 290 to 670 K with a constant heating rate of 20 K/min. Both sample and reference were always maintained at the same temperature throughout the experiment. In Fig. 1, the measured ΔQ in the temperature range between 400 and 600 K for the as-grown single crystal is presented. The three peaks at the temperatures T_s, T_N, and T_p are related to three distinct onset temperatures of this system: (i) $T_s \simeq 540$ K corresponds to the onset temperature of iron-vacancy ordering, at which the unit cell transforms from the high-temperature $I4/mmm$ structure into a low-temperature superstructure $I4/m$, (ii) $T_N \simeq 517$ K is the Néel temperature, and (iii) $T_p \simeq 489$ K corresponds to the onset temperature of phase separation between coexisting $I4/mmm$ and $I4/m$ phases.[16]

The mesoscopic phase separation of as-grown $Rb_xFe_{2-y}Se_2$ is visualized with scanning transmission electron microscopy (STEM) at room temperature using a Titan 80-300 Cubed instrument operating at 300 keV. The specimens for STEM investigations were carefully prepared by a focused ion beam (FIB) to avoid degradation on air exposition. The STEM images taken with the electron beam perpendicular to the tetragonal c axis are shown in Fig. 2. The brightness of the STEM images allows us to distinguish the actual composition of the sample. According to the results of energy dispersive x-ray spectroscopy (EDXS), the composition of the darker and brighter regions is $Rb_{0.5}Fe_2Se_2$ and $Rb_{0.4}Fe_{1.6}Se_2$, respectively.

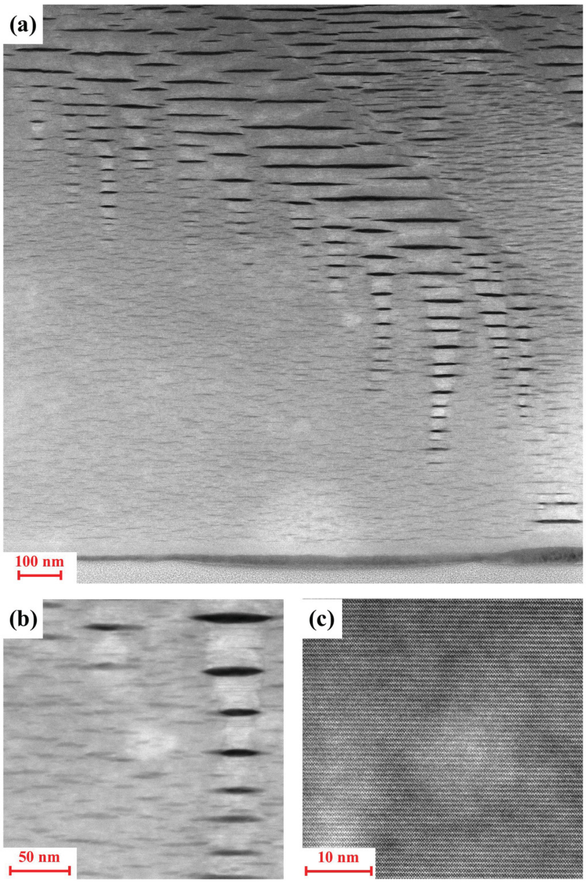

FIG. 2. (Color online) STEM images of as-grown $Rb_xFe_{2-y}Se_2$ single crystal taken with the direction of the electron beam perpendicular to the tetragonal c axis. Picture (a) was taken on a square of ∼1.5 × 1.5 μm^2, (b) on a square of ∼250 × 250 nm^2, (c) on a square of ∼50 × 50 nm^2. The atomic composition of the darker regions was found to correspond to $Rb_{0.5}Fe_2Se_2$, whereas in the brighter regions, the composition is Fe- and Rb-deficient $Rb_{0.4}Fe_{1.6}Se_2$.

Although the transition temperatures T_N and T_s both correspond to thermodynamic ordering phenomena in this system, the onset of phase separation T_p is of different origin. It can be presumed that thermal history of this material crucially influences the phase separation in the sample. This rises the question as to whether it might be possible to tune the phase separation in $Rb_xFe_{2-y}Se_2$ by proper thermal treatment, and by that to control the superconducting and magnetic properties. In order to study the influence of post annealing on the properties of $Rb_xFe_{2-y}Se_2$ single crystals, a set of samples was annealed with an Elite Thermal Systems Ltd. single-zone high-temperature furnace at three annealing temperatures characteristic for the studied samples (see Fig. 1): (i) $T \simeq 413$ K (well below T_p), (ii) $T \simeq 488$ K (just at T_p), and (iii) $T \simeq 563$ K (well above T_p). For this purpose, the samples were loaded in a furnace, which was heated from room temperature with a fast rate of ~10 K/min. Having reached the desired annealing temperature T_{ann}, the temperature was kept constant for a time t_{ann}, after which the samples were removed from the hot furnace and were rapidly cooled back to room temperature. As-grown and annealed samples were systematically studied by various experimental methods. The superconducting and normal-state magnetization was studied with a Quantum Design Magnetic Property Measurement System (MPMS) XL with a differential superconducting quantum interference device (SQUID) equipped with a reciprocating sample option (RSO). In order to prevent these samples from degradation in air, all investigated crystals were vacuum sealed in quartz ampoules of 5 mm diameter and approximately 10 cm length. The platelike crystals were oriented with their crystallographic c axis along the ampoule axis and were fixed between two quartz cylinders of approximately 5 cm length. The diameter of the crystals was adapted to the inner diameter of the quartz tube. Such sample mounting provides a homogeneous surrounding of the examined crystal and produces only a minor background signal during the measurements. Resistivity measurements with electrical current flowing in the ab plane were performed with a Quantum Design Physical Property Measurement System (PPMS). The $Rb_xFe_{2-y}Se_2$ single crystal was cleaved along the ab plane in argon atmosphere inside a glove box and contacted on the cleaved surface by the four-probe technique with gold wires (50 μm diameter) and silver epoxy. The as-grown sample was sealed directly after the initial measurements inside a quartz ampoule and was subsequently annealed and remeasured. By this procedure we ensured the measurement geometry to stay exactly the same for all the measurements. The μSR investigations with magnetic fields applied along the c axis were performed with the General Purpose Surface (GPS) μSR Instrument located at the πM3 beam line at the Swiss Muon Source (SμS) at the Paul Scherrer Institute. The μSR time spectra have been analyzed using the free software package MUSRFIT.[32] STEM measurements were done as described above. A list of the various as-grown and annealed samples studied in this work is presented in Table I.

TABLE I. List of all as-grown and annealed $Rb_xFe_{2-y}Se_2$ single-crystal samples investigated by various experimental techniques in this work. The samples with almost identical T_c were annealed at a certain temperature T_{ann} during a certain time t_{ann}. The as-grown samples are those with $t_{ann} = 0$ h. The sample exhibiting the highest T_c among the as-grown crystals was annealed at 488 K and is named as $A^*_{488}[t_{ann}]$.

Sample	T_{ann}	t_{ann}	Experiment
A_{413}[0 h]	413 K	0 h	Magnetometry
A_{413}[3 h]	413 K	3 h	Magnetometry
A_{413}[36 h]	413 K	36 h	Magnetometry
A_{488}[0 h]	488 K	0 h	Magnetometry
A_{488}[3 h]	488 K	3 h	Magnetometry
A_{488}[36 h]	488 K	36 h	Magnetometry
A_{563}[0 h]	563 K	0 h	Magnetometry
A_{563}[3 h]	563 K	3 h	Magnetometry
A_{563}[36 h]	563 K	36 h	Magnetometry
A^*_{488}[0 h]	488 K	0 h	Magnetometry
A^*_{488}[3 h]	488 K	3 h	Magnetometry
A^*_{488}[36 h]	488 K	36 h	Magnetometry
B_{488}[0 h]	488 K	0 h	Transport
B_{488}[3 h]	488 K	3 h	Transport
C_{488}[0 h]	488 K	0 h	μSR
C_{488}[60 h]	488 K	60 h	μSR
D_{488}[0 h]	488 K	0 h	STEM
D_{488}[3 h]	488 K	3 h	STEM

III. RESULTS

In Fig. 3, the zero-field-cooled (ZFC) magnetization, measured in a magnetic field $\mu_0 H = 0.3$ mT applied along the c axis for the samples $A_{413}[t_{ann}]$, $A_{488}[t_{ann}]$, $A_{563}[t_{ann}]$, and $A^*_{488}[t_{ann}]$ (see Table I) with $t_{ann} = 0$, 3, and 36 h are shown. The magnetization M was normalized to the individual linearly extrapolated value of $M(0)$. This allows us to directly compare the curves of the various crystals to each other despite their different masses and shapes. In a first step, the properties of the pristine as-grown samples (i.e., for $t_{ann} = 0$ h) were investigated [see Fig. 3(a)]. After these measurements, the samples were annealed at T_{ann} for 3 h and were remeasured afterwards [see Fig. 3(b)], then again annealed at T_{ann} for another 33 h (leading to a total annealing time of $t_{ann} =$ 36 h), and finally remeasured [see Fig. 3(c)]. During all the measurements and annealings, the samples were kept inside the sealed ampoules. The as-grown samples A_{413}[0 h], A_{488}[0 h], and A_{563}[0 h] show very similar behavior, exhibiting superconducting diamagnetism with a rather broad transition width. Only the sample A^*_{488}[0 h] exhibits a slightly higher T_c and a narrower transition width. The insets to Fig. 3 present a closeup of the onset of diamagnetism. Importantly, the transition temperature T_c clearly changes for most of the samples after annealing for $t_{ann} = 3$ h and for $t_{ann} = 36$ h. Only T_c for the sample $A_{413}[t_{ann}]$ is essentially independent of t_{ann}. Note that both samples A_{488}[36 h] and A^*_{488}[36 h] exhibit a clearly narrower transition to the superconducting state with a higher T_c. In contrast, sample A_{563}[36 h] behaves in the opposite way, showing a drastically lower T_c. The transition width ΔT_c was defined as the inverse of the maximal slope of the normalized magnetization $M/M(0)$ as a function of T:

$$\Delta T_c = \left(\frac{1}{M(0)} \max \left[\frac{dM}{dT} \right] \right)^{-1}. \tag{1}$$

The estimated values for T_c and ΔT_c for all the samples studied are listed in Table II. In order to better specify the change for a measured property P with annealing time t_{ann}, we introduce the following quantity:

$$\delta_{t_{ann}}(P) = \frac{P(t_{ann}) - P(0\text{ h})}{P(0\text{ h})}. \tag{2}$$

With this formula, a clear increase of T_c by ~5%–6% is found for the samples A_{488}[36 h] and A^*_{488}[36 h] in comparison to the as-grown specimens (see Table II), whereas T_c decreases for sample A_{563}[36 h] by $\simeq$27.3% and remains almost constant for sample A_{413}[36 h]. The relative transition width $\Delta T_c/T_c$ of the samples $A_{413}[t_{ann}]$ and $A_{563}[t_{ann}]$ changes only slightly with annealing, whereas for the samples $A_{488}[t_{ann}]$ and $A^*_{488}[t_{ann}]$,

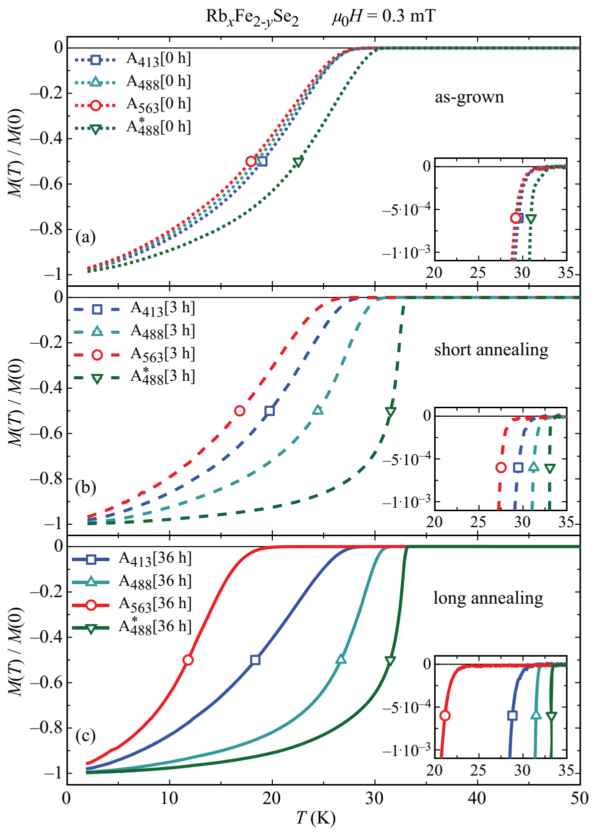

FIG. 3. (Color online) Normalized ZFC magnetization $M(T)/M(0)$ for the $Rb_xFe_{2-y}Se_2$ single crystals $A_{413}[t_{ann}]$, $A_{488}[t_{ann}]$, $A_{563}[t_{ann}]$, and $A^*_{488}[t_{ann}]$ in a magnetic field $\mu_0 H = 0.3$ mT applied along the c axis. The panels present the data for the as-grown samples with $t_{ann} = 0$ h (a), annealed samples for $t_{ann} = 3$ h (b), and for $t_{ann} = 36$ h (c). The respective insets show closeups of the onset of diamagnetism.

TABLE II. Evolution of the transition temperature T_c and transition width ΔT_c [see Eq. (1)] of the samples $A_{413}[t_{ann}]$, $A_{488}[t_{ann}]$, $A_{563}[t_{ann}]$, and $A^*_{488}[t_{ann}]$ with annealing time t_{ann}. The changes with annealing $\delta_{t_{ann}}(T_c)$ and $\delta_{t_{ann}}(\Delta T_c)$ were calculated applying Eq. (2).

Sample	T_c (K)	$\delta_{t_{ann}}(T_c)$	ΔT_c (K)	$\delta_{t_{ann}}(\Delta T_c)$	$\Delta T_c/T_c$
A_{413}[0 h]	30.1(1)		14(1)		47(2)%
A_{413}[3 h]	30.1(1)	±0.0%	14(1)	±0%	47(2)%
A_{413}[36 h]	29.5(1)	−2.0%	16(1)	+14%	54(2)%
A_{488}[0 h]	30.0(1)		16(1)		53(3)%
A_{488}[3 h]	31.7(1)	+5.7%	9.5(5)	−41%	30(1)%
A_{488}[36 h]	31.8(1)	+6.0%	7.0(4)	−56%	22(1)%
A_{563}[0 h]	30.0(1)		17(1)		57(3)%
A_{563}[3 h]	28.0(1)	−6.7%	15(1)	−12%	54(3)%
A_{563}[36 h]	21.8(1)	−27.3%	10(1)	−41%	46(4)%
A^*_{488}[0 h]	31.6(1)		13(1)		41(2)%
A^*_{488}[3 h]	33.1(1)	+4.7%	2.2(2)	−83%	6.6(3)%
A^*_{488}[36 h]	33.3(1)	+5.4%	2.1(2)	−84%	6.3(3)%

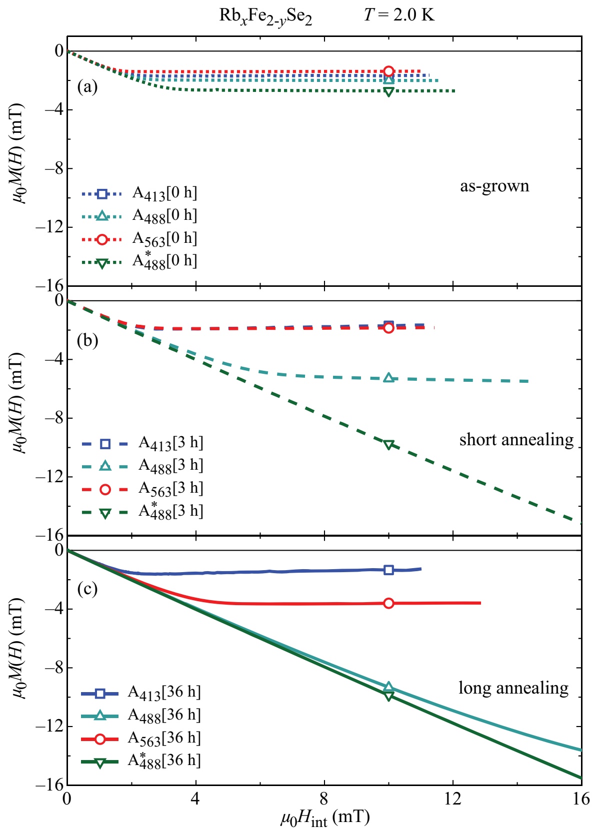

FIG. 4. (Color online) Zero-field-cooled (ZFC) magnetization curves for the $Rb_xFe_{2-y}Se_2$ single crystals $A_{413}[t_{ann}]$, $A_{488}[t_{ann}]$, $A_{563}[t_{ann}]$, and $A^*_{488}[t_{ann}]$ measured at 2.0 K as a function of H_{int} along the c axis. The corresponding t_{ann} of the different panels are $t_{ann} = 0$ h (a), $t_{ann} = 3$ h (b), and $t_{ann} = 36$ h (c).

a clear improvement is seen. Note that the transition for $A^*_{488}[t_{ann}]$ becomes almost ideally sharp with long annealing.

Field-dependent magnetization measurements were performed to further investigate the superconducting properties of the samples $A_{413}[t_{ann}]$, $A_{488}[t_{ann}]$, $A_{563}[t_{ann}]$, and $A^*_{488}[t_{ann}]$. In Fig. 4, the corresponding ZFC magnetization curves measured at $T = 2.0$ K with variable t_{ann} are presented. The internal magnetic field H_{int} was calculated by correcting the applied magnetic field H for the demagnetization of the samples

$$H_{int} = H - DM, \tag{3}$$

where D is the demagnetization factor. The dimensions of the crystals used in this experiment were $\sim 2 \times 2 \times 0.5$ mm^3, yielding $D \simeq 0.8$ for the measurements with H applied along the c axis being the shortest dimension.[33] Hence, it was possible to determine the magnetization M as a function of H_{int}. In Fig. 4(a), the $M(H_{int})$ data for $t_{ann} = 0$ h are presented. All samples show rather poor superconducting properties. Although $M(H_{int}) \simeq -H_{int}$ for low magnetic fields (almost ideal diamagnetism), the $M(H_{int})$ curves strongly deviate from this linear behavior for fields exceeding 1–2 mT, indicating a rather small out-of-plane lower critical field $H_{c1}^{\parallel c}$. By means of

TABLE III. Evolution of the superconducting susceptibility $\chi_{\mathrm{sc}}(\mu_0 H_{\mathrm{int}})$ [see Eq. (5)] of the samples $\mathrm{A}_{413}[t_{\mathrm{ann}}]$, $\mathrm{A}_{488}[t_{\mathrm{ann}}]$, $\mathrm{A}_{563}[t_{\mathrm{ann}}]$, and $\mathrm{A}^{*}_{488}[t_{\mathrm{ann}}]$ with annealing time t_{ann}.

Sample	χ_{sc} (1 mT)	χ_{sc} (10 mT)
A_{413}[0 h]	−0.954(6)	−0.172(8)
A_{413}[3 h]	−0.962(5)	−0.174(9)
A_{413}[36 h]	−0.920(7)	−0.134(5)
A_{488}[0 h]	−0.915(7)	−0.175(9)
A_{488}[3 h]	−0.955(9)	−0.453(9)
A_{488}[36 h]	−0.984(3)	−0.881(4)
A_{563}[0 h]	−0.906(3)	−0.124(6)
A_{563}[3 h]	−0.908(6)	−0.162(8)
A_{563}[36 h]	−0.977(4)	−0.322(9)
A^{*}_{488}[0 h]	−0.976(3)	−0.240(9)
A^{*}_{488}[3 h]	−0.989(2)	−0.940(2)
A^{*}_{488}[36 h]	−0.990(2)	−0.954(2)

the relation between $H_{\mathrm{c1}}^{\parallel c}$ and the in-plane magnetic penetration depth λ_{ab},

$$\mu_0 H_{\mathrm{c1}}^{\parallel c} = \frac{\Phi_0}{4\pi\lambda_{ab}^2}\left(\ln\kappa_{ab} + \frac{1}{2}\right), \tag{4}$$

it was argued that a very small $\mu_0 H_{\mathrm{c1}} \simeq 0.3$ mT is consistent with a large $\lambda \simeq 1$–2 μm.[12] However, this behavior is drastically changed with annealing as seen in Figs. 4(b) and 4(c). Although the measurements for sample $\mathrm{A}_{413}[t_{\mathrm{ann}}]$ reveal no obvious change with increasing t_{ann}, the samples $\mathrm{A}_{488}[t_{\mathrm{ann}}]$ and $\mathrm{A}^{*}_{488}[t_{\mathrm{ann}}]$ show both a considerably higher diamagnetic response at higher H_{int}, indicating an improved screening of the applied magnetic field. By defining H_{c1} as the magnetic field where the curves deviate from ideal diamagnetism, the best sample $\mathrm{A}^{*}_{488}[t_{\mathrm{ann}}]$ yields a considerably larger $\mu_0 H_{\mathrm{c1}} \simeq 10$ mT compared to the estimate $\lesssim 1$ mT for the as-grown samples. Such a large value of 10 mT is consistent with $\lambda \simeq 270$ nm, assuming a realistic Ginzburg-Landau parameter $\kappa_{ab} \simeq 100$ in Eq. (4). For a quantitative comparison of the superconducting properties of the different samples, the superconducting susceptibility $\chi_{\mathrm{sc}}(\mu_0 H_{\mathrm{int}})$ was estimated using the relation

$$\chi_{\mathrm{sc}}(\mu_0 H_{\mathrm{int}}) = \frac{M(\mu_0 H_{\mathrm{int}})}{H_{\mathrm{int}}}. \tag{5}$$

In Table III, $\chi_{\mathrm{sc}}(1\ \mathrm{mT})$ and $\chi_{\mathrm{sc}}(10\ \mathrm{mT})$ are listed. Comparing $\chi_{\mathrm{sc}}(\mu_0 H_{\mathrm{int}})$ for the sample $\mathrm{A}_{413}[t_{\mathrm{ann}}]$ with increasing t_{ann}, no improvement of the diamagnetic response was found with annealing. However, for all other samples $\mathrm{A}_{488}[t_{\mathrm{ann}}]$, $\mathrm{A}_{563}[t_{\mathrm{ann}}]$, and $\mathrm{A}^{*}_{488}[t_{\mathrm{ann}}]$, both $\chi_{\mathrm{sc}}(1\ \mathrm{mT})$ and $\chi_{\mathrm{sc}}(10\ \mathrm{mT})$ increase substantially with increasing t_{ann}. Whereas the improvement of screening in 10 mT indicates an increase of critical current density, the changes observed in very low magnetic fields are rather related to an increase of H_{c1} connected with a decrease of λ. This suggests that the changes induced by annealing directly influence the density and the mobility of the charge carriers in the superconducting phase.

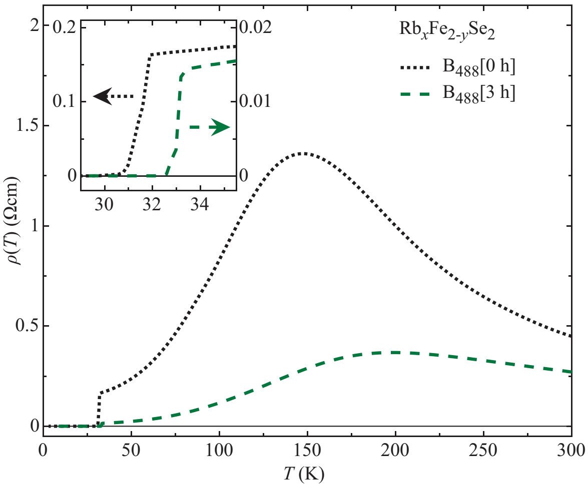

FIG. 5. (Color online) In-plane resistivity ρ of the $\mathrm{Rb}_x\mathrm{Fe}_{2-y}\mathrm{Se}_2$ samples B_{488}[0 h] and B_{488}[3 h]. The pronounced hump in the normal-state resistivity of the as-grown sample B_{488}[0 h] decreases dramatically after annealing and the superconducting T_{c} increases from 31.5 to 33.1 K.

Aside from magnetization, also resistivity experiments are expected to exhibit pronounced changes with annealing. Resistivity studies may provide independent and complementary information to the magnetization experiments. Whereas magnetization measurements probe the global macroscopic properties of a sample, its resistivity is sensitive to microscopic currents flowing through this mesoscopic phase-separated material. Figure 5 shows the in-plane resistivity ρ for the $\mathrm{Rb}_x\mathrm{Fe}_{2-y}\mathrm{Se}_2$ single crystal, measured in zero magnetic field by cooling from 300 to 5 K. The measurements were performed on the as-grown sample (B_{488}[0 h]) and were repeated after annealing in 488 K for 3 h (B_{488}[3 h]) using the same contacts. A clear reduction of ρ in the normal state was found together with an increase of T_{c} from 31.5 K in the pristine sample to 33.1 K for the annealed sample (see Table IV), in very good agreement with the increase observed by magnetization (see Table II). The hump in $\rho(T)$ between 100 and 150 K for the as-grown sample B_{488}[0 h] seen in Fig. 5 was earlier interpreted as a possible metal-insulator transition.[28] Such a transition would be likely related to the mesoscopic phase separation present in $\mathrm{Rb}_x\mathrm{Fe}_{2-y}\mathrm{Se}_2$. In this picture, the minority phase is connected with percolative paths along which electrical current may flow.[17] Interestingly, this hump is strongly decreased with annealing at 488 K for 3 h, indicating that normal-state electric conductivity is enhanced in the annealed sample.

In Figs. 6(a)–6(d), the resistivity measurements at low temperatures performed on the pristine and annealed $\mathrm{Rb}_x\mathrm{Fe}_{2-y}\mathrm{Se}_2$ single crystal $\mathrm{B}_{488}[t_{\mathrm{ann}}]$ for various magnetic fields applied along the c axis and in the ab plane are presented. The transition temperature T_{c} is reduced with increasing H for all configurations. In order to quantify this phase transition, the upper critical field H_{c2} is determined by following field and temperature at which 50% of the normal-state resistivity is suppressed [dashed lines in Figs. 6(a)–6(d)]. Figure 6(e) shows the estimated upper critical field along the c axis $[H_{\mathrm{c2}}^{\parallel c}(T)]$ and in the ab plane $[H_{\mathrm{c2}}^{\parallel ab}(T)]$ for the as-grown and annealed samples. An increase of $T_{\mathrm{c}}(H)$ with annealing is observed in the whole temperature-field phase diagram. The slopes $-\mu_0 dH_{\mathrm{c2}}^{\parallel\alpha}/dT$ ($\alpha = c,ab$) of the phase

TABLE IV. Evolution of T_c, $-dH_{c2}^{\|c}/dT$, and $-dH_{c2}^{\|ab}/dT$ with annealing time t_{ann} for fields applied parallel to the c axis and to the ab plane for samples B_{488}[0 h] and B_{488}[3 h]. The changes with annealing $\delta_{t_{ann}}(T_c)$, $\delta_{t_{ann}}(dH_{c2}^{\|c}/dT)$, and $\delta_{t_{ann}}(dH_{c2}^{\|ab}/dT)$ were calculated applying Eq. (2).

Sample	T_c (K)	$\delta_{t_{ann}}(T_c)$	$-\mu_0 dH_{c2}^{\|c}/dT$ (T/K)	$\delta_{t_{ann}}(dH_{c2}^{\|c}/dT)$	$-\mu_0 dH_{c2}^{\|ab}/dT$ (T/K)	$\delta_{t_{ann}}(dH_{c2}^{\|ab}/dT)$
B_{488}[0 h]	31.54(5)		1.58(3)		4.6(1)	
B_{488}[3 h]	33.07(5)	+4.9%	1.59(2)	+0.6%	5.8(1)	+26.1%

boundaries for sufficiently high H are summarized in Table IV. From these, the upper critical fields at zero temperature were estimated applying the Werthamer-Helfand-Hohenberg (WHH) approximation[34]

$$H_{c2}(0) = -0.69 T_c \frac{dH_{c2}}{dT}, \tag{6}$$

where $-dH_{c2}/dT$ is defined as the maximal slope of the $H_{c2}(T)$ curve in the vicinity of T_c. Here, we considered the linear part of the curve well below but not too far from T_c, emphasized in Fig. 6(e), which yields a more reliable estimate for the upper critical field of superconductors with an upturn curvature close to T_c.[35] Interestingly, the upper critical field anisotropy

$$\gamma_H = H_{c2}^{\|ab} / H_{c2}^{\|c} \tag{7}$$

increases with annealing by 24.1% (see Table V). This suggests that thermally treated iron-chalcogenide superconductors with improved macroscopic physical properties are more anisotropic.

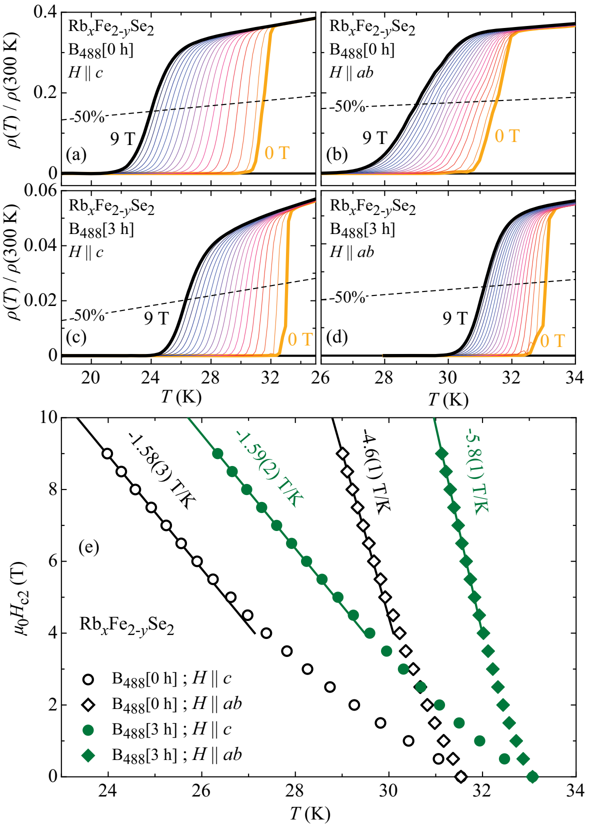

FIG. 6. (Color online) Resistivity of the samples $B_{488}[t_{ann}]$ for magnetic fields between 0 and 9 T, varied by 0.5-T steps, for fields in the ab plane and along the c axis. The measurements were performed for the as-grown sample B_{488}[0 h] [panels (a) and (b)] and for the annealed sample B_{488}[3 h] [panels (c) and (d)], with H applied along the c axis and in the ab plane. The dashed lines denotes 50% of the extrapolated normal-state resistivity, which was used as a criterion to determine $H_{c2}(T)$, shown in panel (e). The transition temperature T_c increases by 1.6 K as a result of annealing. The solid lines are guides to the linear part of the $H_{c2}(T)$ curves, used in the WHH approximation [Eq. (6)].

Aside from investigating the properties in the superconducting state, it is also important to monitor the changes in normal-state properties of the $Rb_xFe_{2-y}Se_2$ single crystals as a result of post annealing. In Fig. 7, we present the magnetic moment m measured in 1 T and in 3 T for $A_{413}[t_{ann}]$, $A_{488}[t_{ann}]$, $A_{563}[t_{ann}]$, and $A^*_{488}[t_{ann}]$ with $t_{ann} = 0$, 3, and

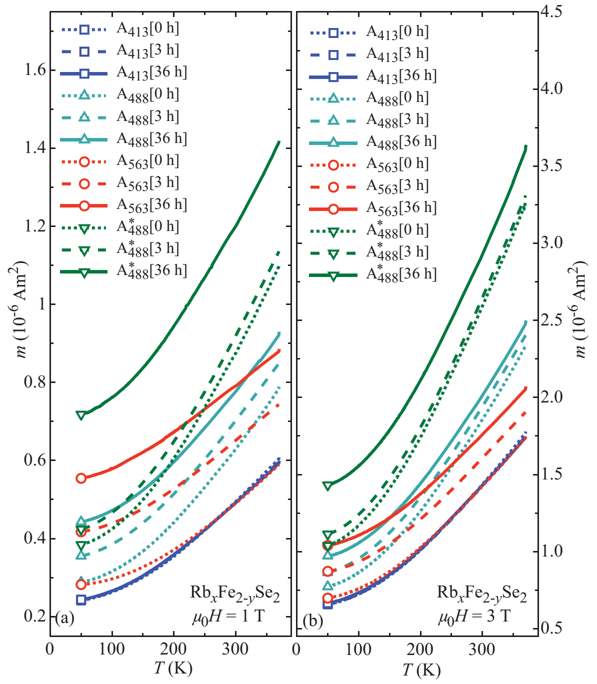

FIG. 7. (Color online) Measured magnetic moment $m(T)$ of pristine and annealed $Rb_xFe_{2-y}Se_2$ single crystals in the temperature range between 50 and 370 K for magnetic fields of 1 T (a) and 3 T (b), applied along the c axis.

TABLE V. Evolution of $H_{c2}^{\|c}(0)$, $H_{c2}^{\|ab}(0)$, and γ_H with annealing time t_{ann} for samples B_{488}[0 h] and B_{488}[3 h]. The changes with annealing $\delta_{t_{\mathrm{ann}}}[H_{c2}^{\|c}(0)]$, $\delta_{t_{\mathrm{ann}}}[H_{c2}^{\|ab}(0)]$, and $\delta_{t_{\mathrm{ann}}}(\gamma_H)$ were calculated applying Eq. (2).

Sample	$\mu_0 H_{c2}^{\|c}(0)$ (T)	$\delta_{t_{\mathrm{ann}}}[H_{c2}^{\|c}(0)]$	$\mu_0 H_{c2}^{\|ab}(0)$ (T)	$\delta_{t_{\mathrm{ann}}}[H_{c2}^{\|ab}(0)]$	γ_H	$\delta_{t_{\mathrm{ann}}}(\gamma_H)$
B_{488}[0 h]	34.6(7)		101(3)		2.9(2)	
B_{488}[3 h]	36.5(5)	+5.5%	133(3)	+31.7%	3.6(2)	+24.1%

36 h. The magnetic moment in the normal state, recorded between 50 and 370 K, systematically increases with t_{ann} for *all* investigated samples. In the normal state, the major component of the magnetic moment is stemming from the antiferromagnetic phase. However, some small ferromagnetic contribution is present in all $\mathrm{Rb}_x\mathrm{Fe}_{2-y}\mathrm{Se}_2$ crystals, most likely due to a ferromagnetic impurity phase. From the measurements presented in Fig. 7 we determined the antiferromagnetic susceptibility $\chi_{\mathrm{AFM}}(T)$ according to

$$\chi_{\mathrm{AFM}}(T) = \frac{1}{\mathcal{M}} \frac{m(\mu_0 H) - m(\mu_0 H')}{H - H'}, \qquad (8)$$

where $\mathcal{M}$ denotes the sample mass. Here, $\mu_0 H$ and $\mu_0 H'$ are 1 and 3 T, respectively. The ferromagnetic contribution to the magnetization is assumed to be constant in field and is derived accordingly:

$$M_{\mathrm{FM}}(T) = \frac{m(\mu_0 H)}{\mathcal{M}} - \chi_{\mathrm{AFM}}(T) H. \qquad (9)$$

The antiferromagnetic susceptibility for all the as-grown samples and those annealed for 3 h and for 36 h are shown in Fig. 8(a). The ferromagnetic component of the magnetization $M_{\mathrm{FM}}(T)$ is shown in Fig. 8(b). Sample $\mathrm{A}_{413}[t_{\mathrm{ann}}]$ remains unaffected by annealing, as already observed in the ZFC magnetization experiments performed in the superconducting state as discussed above. However, for the samples $\mathrm{A}_{488}[t_{\mathrm{ann}}]$, $\mathrm{A}_{563}[t_{\mathrm{ann}}]$, and $\mathrm{A}^*_{488}[t_{\mathrm{ann}}]$, the high-field susceptibility $\chi_{\mathrm{AFM}}(T)$ increases substantially with increasing t_{ann}. In Table VI, we list the observed values for $\chi_{\mathrm{AFM}}(50\text{ K})$ for all samples and t_{ann}. Obviously, the change in $\chi_{\mathrm{AFM}}(50\text{ K})$ is most pronounced for the sample $\mathrm{A}_{563}[t_{\mathrm{ann}}]$, annealed at 563 K. In addition, the ferromagnetic component $M_{\mathrm{FM}}(T)$ is almost unchanged for sample $\mathrm{A}_{413}[t_{\mathrm{ann}}]$, but increases for the samples $\mathrm{A}_{488}[t_{\mathrm{ann}}]$, $\mathrm{A}_{563}[t_{\mathrm{ann}}]$, and $\mathrm{A}^*_{488}[t_{\mathrm{ann}}]$ with increasing t_{ann}. Again, the change in $M_{\mathrm{FM}}(50\text{ K})$ is maximal for sample $\mathrm{A}_{563}[t_{\mathrm{ann}}]$.

The effect of annealing on the magnetic and superconducting properties of $\mathrm{Rb}_x\mathrm{Fe}_{2-y}\mathrm{Se}_2$ single crystals was further investigated by means of transverse-field (TF) and zero-field (ZF) μSR experiments. The μSR measurements are based on the observation of the time evolution of the muon spin polarization. (For a detailed description of the μSR technique, see e.g. Ref. 36.) For these experiments, two mosaics of samples were prepared: (i) C_{488}[0 h], consisting of three as-grown $\mathrm{Rb}_x\mathrm{Fe}_{2-y}\mathrm{Se}_2$ single crystals, and (ii) C_{488}[60 h], consisting of three $\mathrm{Rb}_x\mathrm{Fe}_{2-y}\mathrm{Se}_2$ single crystals simultaneously annealed in 488 K for 60 h. Previous μSR experiments revealed that $\mathrm{Rb}_x\mathrm{Fe}_{2-y}\mathrm{Se}_2$ consists of a magnetic (~90%) and a nonmagnetic superconducting (~10%) phase.[15] In order to investigate the superconducting properties, a field of 70 mT was applied transverse to the initial muon spin polarization and parallel to the crystallographic c axis. In this TF configuration, the muons probe the local magnetic field distribution $P(B)$ of the vortex lattice formed in the superconducting areas. Simultaneously, the signal stemming from the magnetic regions of the sample is suppressed since the

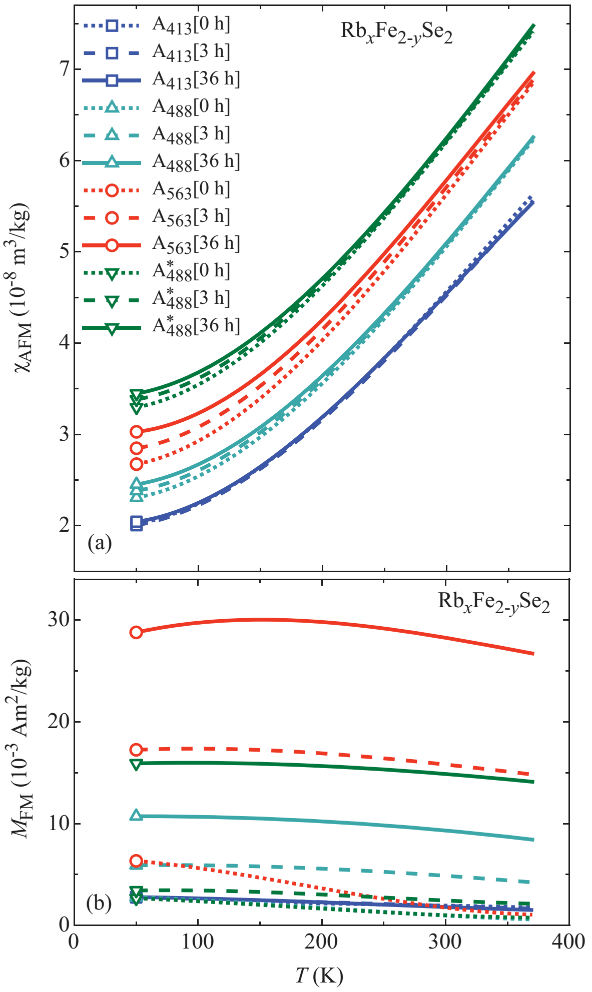

FIG. 8. (Color online) (a) Antiferromagnetic susceptibility $\chi_{\mathrm{AFM}}(T)$ in the normal state of pristine and annealed $\mathrm{Rb}_x\mathrm{Fe}_{2-y}\mathrm{Se}_2$ single crystals determined from the data shown in Fig. 7 using Eq. (8). For clarity, the curves representing the four different annealing sets are vertically shifted to each other. Whereas no change of $\chi_{\mathrm{AFM}}(T)$ is found by annealing for sample $\mathrm{A}_{413}[t_{\mathrm{ann}}]$, for all other samples, $\chi_{\mathrm{AFM}}(T)$ increases with increasing t_{ann}. (b) Ferromagnetic component $M_{\mathrm{FM}}(T)$, being constant for sample $\mathrm{A}_{413}[t_{\mathrm{ann}}]$ as a function of t_{ann}. For all other samples, $M_{\mathrm{FM}}(50\text{ K})$ increases substantially with increasing t_{ann}.

TABLE VI. Evolution of $\chi_{\mathrm{AFM}}(50\ \mathrm{K})$ [see Eq. (8)] and $M_{\mathrm{FM}}(50\ \mathrm{K})$ [see Eq. (9)] with annealing time t_{ann} for the samples $\mathrm{A}_{413}[t_{\mathrm{ann}}]$, $\mathrm{A}_{488}[t_{\mathrm{ann}}]$, $\mathrm{A}_{563}[t_{\mathrm{ann}}]$, and $\mathrm{A}^{*}_{488}[t_{\mathrm{ann}}]$. The changes with annealing $\delta_{t_{\mathrm{ann}}}[\chi_{\mathrm{AFM}}(50\ \mathrm{K})]$ and $\delta_{t_{\mathrm{ann}}}[M_{\mathrm{FM}}(50\ \mathrm{K})]$ were calculated applying Eq. (2).

Sample	$\chi_{\mathrm{AFM}}(50\ \mathrm{K})$ (10^{-8} m^3/kg)	$\delta_{t_{\mathrm{ann}}}[\chi_{\mathrm{AFM}}(50\ \mathrm{K})]$	$M_{\mathrm{FM}}(50\ \mathrm{K})$ (10^{-3} Am^2/kg)	$\delta_{t_{\mathrm{ann}}}[M_{\mathrm{FM}}(50\ \mathrm{K})]$
A_{413}[0 h]	2.020(1)		2.79(1)	
A_{413}[3 h]	2.006(1)	−0.7%	2.75(1)	−1.4%
A_{413}[36 h]	2.044(1)	+1.2%	2.79(1)	±0.0%
A_{488}[0 h]	1.808(1)		2.77(1)	
A_{488}[3 h]	1.883(1)	+4.1%	5.91(1)	+113%
A_{488}[36 h]	1.953(1)	+8.0%	10.73(1)	+287%
A_{563}[0 h]	2.400(1)		6.91(1)	
A_{563}[3 h]	2.598(1)	+8.3%	17.25(1)	+150%
A_{563}[36 h]	2.778(1)	+15.8%	28.78(1)	+317%
A^{*}_{488}[0 h]	1.796(1)		2.67(1)	
A^{*}_{488}[3 h]	1.883(1)	+4.8%	3.43(1)	+28.5%
A^{*}_{488}[36 h]	1.947(1)	+8.4%	15.92(1)	+496%

superposition of the strong internal field and the weak external field leads to a fast depolarization and to a loss of asymmetry.

Consistent with the above presented macroscopic magnetization and resistivity results, also the intrinsic superconducting properties are significantly improved after annealing. The line shape of the local magnetic field distribution $P(B)$ of C_{488}[60 h] shown in Fig. 9(a) is more asymmetric as compared to that of C_{488}[0 h], indicating the presence of a more homogeneous and more regular vortex lattice in the superconducting regions. Note that the sharp peak of $P(B)$ at 70 mT is stemming from the signal of background muons, the spins of which rotate simply in the applied magnetic field. A more detailed analysis of the as obtained $P(B)$ yields that the shielding of the magnetic field for C_{488}[60 h] is substantially larger due to a reduction of the first moment $\langle B\rangle$ of $P(B)$ by ∼5%. This is surprising since the microscopic in-plane magnetic penetration depth $\lambda_{ab}(0) \simeq 258(2)$ nm,[15] as well as the total asymmetry of the superconducting part, remain essentially unchanged after 60 h annealing [see Fig. 9(b)]. These results imply that the volume fraction of the magnetic and the nonmagnetic phases is unaffected by annealing, in contradiction to the conclusions of a neutron diffraction study, reporting a reduction of the minority phase after annealing of $\mathrm{Rb}_x\mathrm{Fe}_{2-y}\mathrm{Se}_2$ single crystals for 100 h at 488 K.[16] This discrepancy might arise from the difference in T_{p} of the samples studied here (489 K) and in Ref. 16 (475 K).

Importantly, the normal-state relaxation rate σ of the μSR time spectra derived from the data at 40 K (well above T_{c}) increases drastically with t_{ann} [see Figs. 9(b) and 9(c)]. Whereas for the as-grown sample C_{488}[0 h] $\sigma = 0.141(33)\ \mu\mathrm{s}^{-1}$, the relaxation rate of the 60-h annealed sample C_{488}[60 h] is considerably larger [$\sigma = 0.303(43)\ \mu\mathrm{s}^{-1}$]. This indicates a substantially increased field inhomogeneity in the nonmagnetic part of the sample. Since the volume fraction is unchanged during annealing, this suggests that the microstructure of the sample caused by mesoscopic phase separation is modified by annealing at 488 K, in such a way that the individual size of the nonmagnetic regions is reduced and their number is increased, *but their total volume remains unaffected.*

In order to examine our samples for the internal magnetic field distribution when no magnetic field is applied, low-temperature ZF μSR experiments were performed on the same $\mathrm{Rb}_x\mathrm{Fe}_{2-y}\mathrm{Se}_2$ single crystals. Consistent with the results of the TF experiments, the total volume of the nonmagnetic regions was found to be ∼10% of the total sample volume only. In the ZF data, a clear oscillating signal may be found in all samples for very short time scales as shown in Fig. 10. An analysis of the time evolution of this signal revealed that two internal magnetic fields $B_{\mathrm{int},1} \approx 1$ T and $B_{\mathrm{int},2} \approx 3$ T are present in the samples. In analogy to the evolution of the magnetic volume fraction, $B_{\mathrm{int},1}$ and $B_{\mathrm{int},2}$ are not affected by annealing at 488 K. They are directly proportional to the iron moment in the antiferromagnetic phase. Moreover, annealing again does not affect the ratio $B_{\mathrm{int},1}/B_{\mathrm{int},2}$. Hence, no changes in the internal magnetic fields were observed by μSR after annealing the as-grown $\mathrm{Rb}_x\mathrm{Fe}_{2-y}\mathrm{Se}_2$ single crystals, even though the macroscopic superconducting properties were substantially improved (see Figs. 3 and 4).

In order to visualize microscopic changes in the phase separation of our $\mathrm{Rb}_x\mathrm{Fe}_{2-y}\mathrm{Se}_2$ single crystals with annealing, additional STEM images were taken on as-grown and annealed samples D_{488}[0 h] and D_{488}[3 h] (see Fig. 11). The microstructure caused by mesoscopic phase separation in the annealed sample D_{488}[3 h], shown in Fig. 11(b), is modified compared to the one of the as-grown sample D_{488}[0 h], shown in Fig. 11(a). Whereas a few inclusions of the minority phases only are observed at the surface of D_{488}[0 h], sample D_{488}[3 h] reveals plenty of such inclusions in the same area. However, the inclusions of the minority phase of sample D_{488}[3 h] are in general smaller in size than the ones of the as-grown sample D_{488}[0 h], in agreement with the results of the above μSR experiments.

IV. DISCUSSION

The superconducting and normal-state properties of mesoscopically phase-separated $\mathrm{Rb}_x\mathrm{Fe}_{2-y}\mathrm{Se}_2$, where nonmagnetic regions exist in a magnetic surrounding, are strikingly similar to those expected for granular superconductors. From early work on granular superconductors it is known that

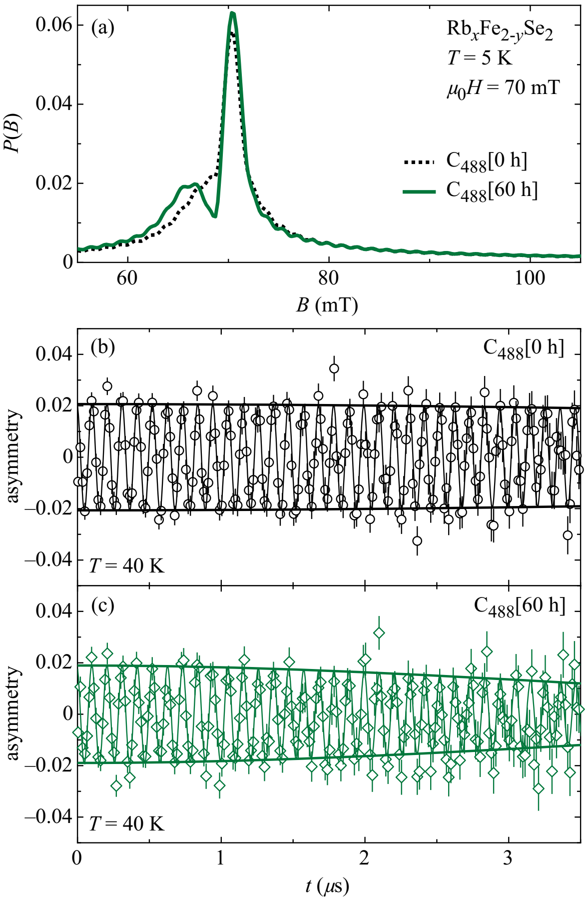

FIG. 9. (Color online) Results of the TF μSR investigation of as-grown and 60-h annealed $\mathrm{Rb}_x\mathrm{Fe}_{2-y}\mathrm{Se}_2$ single crystals, C_{488}[0 h] and C_{488}[60 h], in a magnetic field of 70 mT applied along the c axis. (a) $P(B)$ for both samples at 5 K. The line shape for C_{488}[60 h] is more asymmetric compared to that for the as-grown sample C_{488}[0 h]. (b) and (c) μSR time spectra at 40 K for sample C_{488}[0 h] and C_{488}[60 h]. The thin solid line is a fit to the data assuming a single relaxation rate σ. The thick solid line is the envelope of the oscillating function. The data for the annealed sample C_{488}[60 h] exhibit a significantly faster damping.

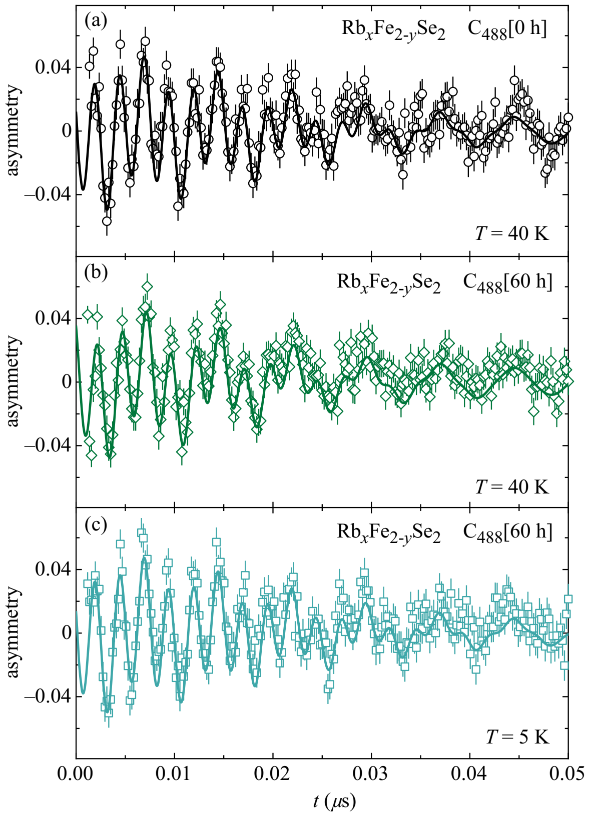

FIG. 10. (Color online) Results of the ZF μSR investigation of as-grown and 60-h annealed $\mathrm{Rb}_x\mathrm{Fe}_{2-y}\mathrm{Se}_2$ single crystals, C_{488}[0 h] and C_{488}[60 h]. All data were modeled assuming two internal magnetic fields $B_{\mathrm{int},1} \approx 1$ T and $B_{\mathrm{int},2} \approx 3$ T.

the macroscopic properties of such materials studied by various techniques may vary substantially, depending on the particular grain-size distribution and their coupling by Josephson links.[37–39] Importantly, granular superconductors may easily appear as bulk superconducting, however, their superconducting-state parameters, such as the magnetic penetration depth λ, the coherence length ξ, and the lower and upper critical fields (H_{c1} and H_{c2}) differ substantially from those of related nongranular superconductors. Such a scenario may also hold for mesoscopically phase-separated $\mathrm{Rb}_x\mathrm{Fe}_{2-y}\mathrm{Se}_2$ since various experimental techniques provide quite different values for λ. For $\mathrm{Rb}_x\mathrm{Fe}_{2-y}\mathrm{Se}_2$, recent μSR studies yielded $\lambda_{ab}(0) \simeq$ 250–260 nm,[15,40] in agreement with $\lambda_{ab}(0) \simeq 290$ nm obtained for $\mathrm{K}_x\mathrm{Fe}_{2-y}\mathrm{Se}_2$ by means of high-field nuclear magnetic resonance (NMR) experiments.[41] These values are considerably smaller than those usually obtained by macroscopic techniques [$\lambda_{ab}(0) \simeq 1.6–2.2\ \mu$m].[12,42,43] In a mesoscopically phase-separated superconductor, macroscopic experiments yield an effective magnetic penetration depth, which is a measure of the length scale over which the magnetic field penetrates the sample. On the other hand, μSR is a microscopic probe of the vortex state and is only sensitive to the superconducting fraction of the sample. Therefore, μSR measures a value of the magnetic penetration depth which is closer to the intrinsic value than the values usually obtained by macroscopic techniques. Since so far no single-phase superconducting $A_x\mathrm{Fe}_{2-y}\mathrm{Se}_2$ sample could be synthesized, it should not be excluded that granularity might be an important ingredient for the appearance of superconductivity in this system.

As strongly suggested by the presented magnetization and resistivity data, pronounced changes of the physical properties of $\mathrm{Rb}_x\mathrm{Fe}_{2-y}\mathrm{Se}_2$ are caused by tuning the annealing conditions. Whereas annealing at 413 K, well below T_{p}, does not lead to any significant change in magnetic and transport properties, annealing just at T_{p}, the onset of phase separation, favors the enhancement of superconductivity. Accordingly, T_{c} increases, the transition sharpens, the normal-state resistivity decreases, and H_{c2} increases. However, after annealing at 563 K, well above T_{p}, all superconducting properties get drastically sup-

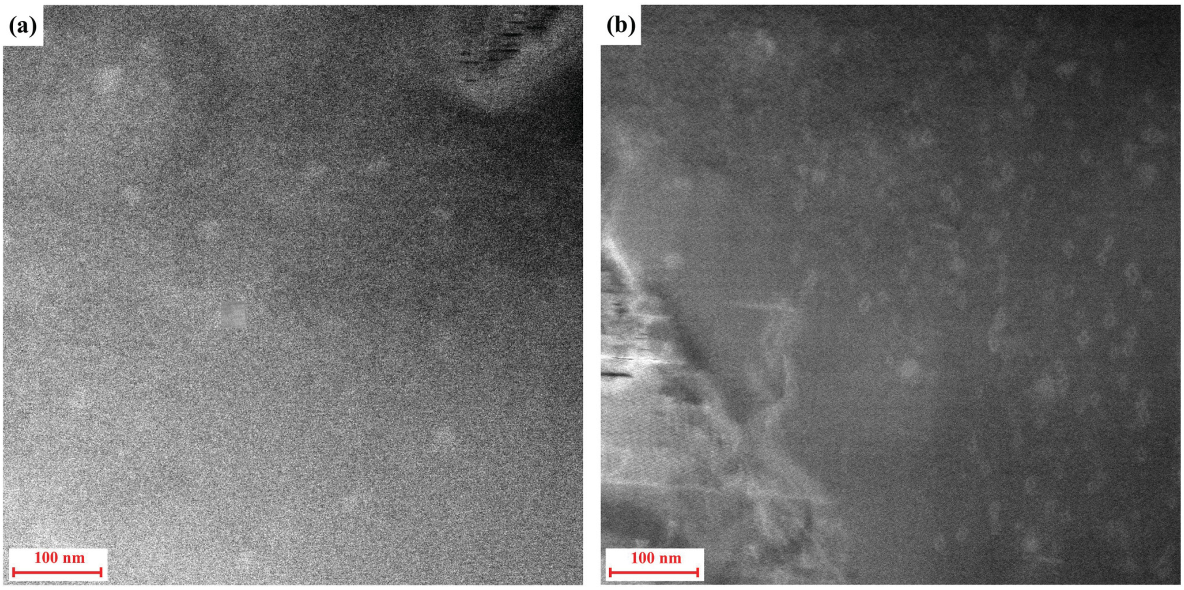

FIG. 11. (Color online) STEM images of as-grown and annealed $\mathrm{Rb}_x\mathrm{Fe}_{2-y}\mathrm{Se}_2$ single crystals D_{488}[0 h] and D_{488}[3 h]. The microstructure caused by mesoscopic phase separation in the annealed sample D_{488}[3 h], shown in panel (b), is modified compared to the one of the as-grown sample D_{488}[0 h], shown in panel (a).

pressed. In addition, the antiferromagnetic susceptibility and the ferromagnetic saturation magnetization of the investigated samples systematically increase. This may be related to the change in iron valency as observed in annealed $\mathrm{K}_{0.8}\mathrm{Fe}_{1.6}\mathrm{Se}_2$,[44] or with an increase of Fe-based impurity phases.

A recent neutron diffraction study of the $\mathrm{Rb}_x\mathrm{Fe}_{2-y}\mathrm{Se}_2$ system reports a pronounced reduction of the minority 122-phase when the samples were annealed at 488 K for 100 h.[16] However, the present μSR experiments yield clear evidence that the volume fraction of the two phases remains unchanged by annealing, while the field inhomogeneity in the nonmagnetic parts of the sample increases substantially. This implies that the microstructure caused by mesoscopic phase separation in the sample is modified by annealing just at T_p in such a way that the size of nonmagnetic regions is reduced, and the number of regions is increased, but their total volume remains unaffected. Since the μSR results clearly demonstrate that the total volume of the minority phase is constant, even after 60 h of annealing, this rearrangement of the coexisting phases leads to the conclusion that changes of the coupling between these regions must be related to the improvement of superconductive properties. Whereas 488 K was chosen to match the onset of phase separation $T_\mathrm{p} \simeq 489$ K in the single crystals studied here, the samples used in the neutron diffraction study had a significantly lower $T_\mathrm{p} \simeq 475$ K.[16] Therefore, the observed reduction of the minority phase found by the neutron study might be due to a partial degradation of the minority phase as a result of 100-h annealing at temperatures exceeding T_p. That this scenario appears to be reasonable is further supported by the data presented in Fig. 12, where a series of magnetization measurements are shown for a $\mathrm{Rb}_x\mathrm{Fe}_{2-y}\mathrm{Se}_2$ single crystal of a similar batch as the one used above. Here, always the same temperature dependence of the ZFC magnetization measurement in a magnetic field of $\mu_0 H = 0.3$ mT along the c axis was performed after each subsequent annealing of the sealed single crystal in a quartz ampoule. Note that T_c of the as-grown sample is easily shifted to higher values by an annealing at 488 K for some hours. However, after the subsequent annealings during which the temperature was modestly increased up to 563 K, superconductivity is strongly suppressed, as seen by the decrease of T_c and the broadening of the transition. During the final annealing, again the optimal annealing temperature of 488 K was chosen, this

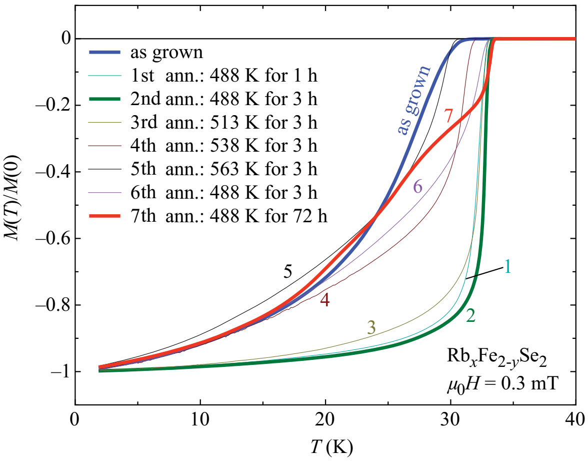

FIG. 12. (Color online) Series of temperature-dependent ZFC magnetization measurements on a $\mathrm{Rb}_x\mathrm{Fe}_{2-y}\mathrm{Se}_2$ single crystal in 0.3 mT. The curves obtained after the various post annealings of the sample are labeled by the respective number.

time for a very long annealing time up to 72 h. However, superconductivity did not fully recover. Obviously, the short annealings at temperatures exceeding T_p formed additional magnetic phases, which can not be reversed anymore, even by choosing a very long annealing time.

All changes of superconducting and magnetic properties caused by annealing are evidently related to changes in the microstructure of the sample caused by mesoscopic phase separation in $Rb_xFe_{2-y}Se_2$. The difference of the superconducting properties between the as-grown and annealed single crystals is likely explained by assuming that inhomogeneities (in particular, phase boundaries and/or stripes) are necessary to enhance superconductivity.[45–49] In the present case, the existing boundaries between the magnetic majority regions and nonmagnetic minority regions may play the role of such inhomogeneities. In the current case, reviewing the changes observed of the superconducting and normal-state properties with annealing, it is likely that the intergrain coupling between magnetic and nonmagnetic domains is crucial. Annealing of $Rb_xFe_{2-y}Se_2$ single crystals just at T_p favors the mesoscopic phase separation in such a way that domain boundaries are further developed, improving all superconducting properties. However, if the samples are annealed at higher temperature, the superconducting phase degrades and by that it is more difficult to build up a percolative network favorable for superconductivity. In total, $\sim 10\%$ of the sample remains superconducting in a magnetic field of 70 mT, whereas its macroscopic properties strongly depend on the optimal coupling between the superconducting regions, being strongly field and temperature dependent. This scenario appears similar to that of a granular superconductor in which the macroscopic physics is directly connected to the microscopic Josephson coupling between the individual grains. In addition, all changes in the phase separation may be related to changes in crystal structure and lattice parameters.[16] Thus, internal pressure on the superconducting and nonsuperconducting domains may be likely involved in the appearance of superconductivity. Besides, also metallic nanoclusters were reported to show enhanced superconducting properties.[50]

V. CONCLUSIONS

Extended magnetization and resistivity measurements of $Rb_xFe_{2-y}Se_2$ single crystals revealed that post annealing at a temperature well below the onset temperature of phase separation T_p neither changes the magnetic nor the superconducting properties of the crystals. Annealing at a temperature above T_p reduces the value of T_c drastically and suppresses antiferromagnetic order. However, annealing at 488 K just at T_p leads to a substantial increase of T_c and sharpens the transition to the superconducting state. These results suggest that the superconducting properties of mesoscopically phase-separated $Rb_xFe_{2-y}Se_2$ can be tuned by the annealing temperature. In addition, μSR and STEM investigations indicate that nonmagnetic regions of the sample rearrange with annealing at 488 K in such a way that their individual size is reduced and the number of regions is increased, but their total volume remains unaffected. At temperatures exceeding T_p, where the majority $I4/m$ phase prevails, ferromagnetism is enhanced with annealing time, but is presumably detrimental to the formation of the superconducting phase. In conclusion, by annealing single crystals of $Rb_xFe_{2-y}Se_2$, the microstructure of the crystals arising from mesoscopic phase separation is changed, leading to an improvement of the superconducting properties and an enhancement of T_c.

ACKNOWLEDGMENTS

Helpful discussions with K. A. Müller, V. Yu. Pomjakushin, and B. M. Wojek are gratefully acknowledged. S.W. thanks A. Feierls and S. Rösch for their help during part of the experiments. The μSR measurements were performed at the Swiss Muon Source, Paul Scherrer Institute, Villigen, Switzerland. This work was supported by the Swiss National Science Foundation, the NCCR program MaNEP, the National Science Centre of Poland based on Decision No. DEC-2011/01/B/ST3/02374, and the European Regional Development Fund within the Innovative Economy Operational Programme 2007-2013 No. POIG.02.01-00-14-032/08.

---

[*] wstephen@physik.uzh.ch

[†] Current address: Dipartimento di Fisica, Universitá di Roma "La Sapienza"-P. le Aldo Moro 2, I-00185 Roma, Italy.

[‡] On leave from Faculty of Chemistry, Warsaw University of Technology, PL-00-664 Warsaw, Poland.

[1] F. C. Hsu, J. Y. Luo, K.-W. Yeh, T.-K. Chen, T.-W. Huang, P.-M. Wu, Y.-C. Lee, Y.-L. Huang, Y.-Y. Chu, D.-C. Yan, and M.-K. Wu, Proc. Natl. Acad. Sci. USA **105**, 14262 (2008).

[2] E. Pomjakushina, K. Conder, V. Pomjakushin, M. Bendele, and R. Khasanov, Phys. Rev. B **80**, 024517 (2009).

[3] S. Medvedev, T. M. McQueen, I. A. Troyan, T. Palasyuk, M. I. Eremets, R. J. Cava, S. Naghavi, F. Casper, V. Ksenofontov, G. Wortmann, and C. Felser, Nat. Mater. **8**, 630 (2009).

[4] Y. Mizuguchi, F. Tomioka, S. Tsuda, T. Yamaguchi, and Y. Takano, J. Phys. Soc. Jpn. **78**, 074712 (2009).

[5] B. C. Sales, A. S. Sefat, M. A. McGuire, R. Y. Jin, D. Mandrus, and Y. Mozharivskyj, Phys. Rev. B **79**, 094521 (2009).

[6] J. Guo, S. Jin, G. Wang, S. Wang, K. Zhu, T. Zhou, M. He, and X. Chen, Phys. Rev. B **82**, 180520(R) (2010).

[7] A. Krzton-Maziopa, Z. Shermadini, E. Pomjakushina, V. Pomjakushin, M. Bendele, A. Amato, R. Khasanov, H. Luetkens, and K. Conder, J. Phys.: Condens. Matter **23**, 052203 (2011).

[8] C.-H. Li, B. Shen, F. Han, X. Zhu, and H.-H. Wen, Phys. Rev. B **83**, 184521 (2011).

[9] R. H. Liu, X. G. Luo, M. Zhang, A. F. Wang, J. J. Ying, X. F. Wang, Y. J. Yan, Z. J. Xiang, P. Cheng, G. J. Ye, Z. Y. Li, and X. H. Chen, Europhys. Lett. **94**, 27008 (2011).

[10] Z. Shermadini, A. Krzton-Maziopa, M. Bendele, R. Khasanov, H. Luetkens, K. Conder, E. Pomjakushina, S. Weyeneth, V. Pomjakushin, O. Bossen, and A. Amato, Phys. Rev. Lett. **106**, 117602 (2011).

[11] V. Yu. Pomjakushin, E. V. Pomjakushina, A. Krzton-Maziopa, K. Conder, and Z. Shermadini, J. Phys.: Condens. Matter **23**, 156003 (2011).

[12]S. Bosma, R. Puzniak, A. Krzton-Maziopa, M. Bendele, E. Pomjakushina, K. Conder, H. Keller, and S. Weyeneth, Phys. Rev. B **85**, 064509 (2012).

[13]V. Tsurkan, J. Deisenhofer, A. Günther, H.-A. Krug von Nidda, S. Widmann, and A. Loidl, Phys. Rev. B **84**, 144520 (2011).

[14]J. J. Ying, X. F. Wang, X. G. Luo, A. F. Wang, M. Zhang, Y. J. Yan, Z. J. Xiang, R. H. Liu, P. Cheng, G. J. Ye, and X. H. Chen, Phys. Rev. B **83**, 212502 (2011).

[15]Z. Shermadini, H. Luetkens, R. Khasanov, A. Krzton-Maziopa, K. Conder, E. Pomjakushina, H.-H. Klauss, and A. Amato, Phys. Rev. B **85**, 100501(R) (2012).

[16]V. Yu. Pomjakushin, E. V. Pomjakushina, A. Krzton-Maziopa, K. Conder, D. Chernyshov, V. Svitlyk, and A. Bosak, J. Phys.: Condens. Matter **24**, 435701 (2012).

[17]B. Shen, B. Zeng, G. F. Chen, J. B. He, D. M. Wang, H. Yang, and H. H. Wen, Europhys. Lett. **96**, 37010 (2011).

[18]A. Ricci, N. Poccia, G. Campi, B. Joseph, G. Arrighetti, L. Barba, M. Reynolds, M. Burghammer, H. Takeya, Y. Mizuguchi, Y. Takano, M. Colapietro, N. L. Saini, and A. Bianconi, Phys. Rev. B **84**, 060511(R) (2011).

[19]A. Ricci, N. Poccia, B. Joseph, G. Arrighetti, L. Barba, J. Plaisier, G. Campi, Y. Mizuguchi, H. Takeya, Y. Takano, N. L. Saini, and A. Bianconi, Supercond. Sci. Technol. **24**, 082002 (2011).

[20]H. Lei and C. Petrovic, Phys. Rev. B **83**, 184504 (2011).

[21]Y. J. Yan, M. Zhang, A. F. Wang, J. J. Ying, Z. Y. Li, W. Qin, X. G. Luo, J. Q. Li, J. Hu, and X. H. Chen, Sci. Rep. **2**, 212 (2012).

[22]C. N. Wang, P. Marsik, R. Schuster, A. Dubroka, M. Rössle, C. Niedermayer, G. D. Varma, A. F. Wang, X. H. Chen, T. Wolf, and C. Bernhard, Phys. Rev. B **85**, 214503 (2012).

[23]A. Bosak, V. Svitlyk, A. Krzton-Maziopa, E. Pomjakushina, K. Conder, V. Pomjakushin, A. Popov, D. de Sanctis, D. Chernyshov, arXiv:1112.2569.

[24]Y. Texier, J. Deisenhofer, V. Tsurkan, A. Loidl, D. S. Inosov, G. Friemel, and J. Bobroff, Phys. Rev. Lett. **108**, 237002 (2012).

[25]S. C. Speller, T. B. Britton, G. M. Hughes, A. Krzton-Maziopa, E. Pomjakushina, K. Conder, A. T. Boothroyd, and C. R. M. Grovenor, Supercond. Sci. Technol. **25**, 084023 (2012).

[26]H. Ryu, H. Lei, A. I. Frenkel, and C. Petrovic, Phys. Rev. B **85**, 224515 (2012).

[27]T. Ozaki, H. Takeya, H. Okazaki, K. Deguchi, S. Demura, Y. Kawasaki, H. Hara, T. Watanabe, T. Yamaguchi, and Y. Takano, Europhys. Lett. **98**, 27002 (2012).

[28]F. Han, H. Yang, B. Shen, Z.-Y. Wang, C.-H. Li, and H.-H. Wen, Philos. Mag. **92**, 2553 (2012).

[29]H. Lei and C. Petrovic, Phys. Rev. B **84**, 212502 (2011).

[30]A. Krzton-Maziopa, E. Pomjakushina, and K. Conder, J. Cryst. Growth, doi: 10.1016/j.jcrysgro.2012.01.016 (to be published).

[31]B. Wunderlich, *Thermal Analysis* (Academic, New York, 1990), pp. 137-140.

[32]A. Suter and B. M. Wojek, Phys. Procedia **30**, 69 (2012).

[33]J. A. Osborn, Phys. Rev. **67**, 351 (1945).

[34]N. R. Werthamer, E. Helfand, and P. C. Hohenberg, Phys. Rev. **147**, 295 (1966).

[35]Z. Bukowski, S. Weyeneth, R. Puzniak, P. Moll, S. Katrych, N. D. Zhigadlo, J. Karpinski, H. Keller, and B. Batlogg, Phys. Rev. B **79**, 104521 (2009).

[36]A. Amato, Rev. Mod. Phys. **69**, 1119 (1997).

[37]V. Ambegaokar and A. Baratoff, Phys. Rev. Lett. **10**, 486 (1963).

[38]C. Ebner and D. Stroud, Phys. Rev. B **31**, 165 (1985).

[39]J. R. Clem, Phys. C (Amsterdam) **153–155**, 50 (1988).

[40]A. Charnukha, A. Cvitkovic, T. Prokscha, D. Pröpper, N. Ocelic, A. Suter, Z. Salman, E. Morenzoni, J. Deisenhofer, V. Tsurkan, A. Loidl, B. Keimer, and A. V. Boris, Phys. Rev. Lett. **109**, 017003 (2012).

[41]D. A. Torchetti, M. Fu, D. C. Christensen, K. J. Nelson, T. Imai, H. C. Lei, and C. Petrovic, Phys. Rev. B **83**, 104508 (2011).

[42]A. Charnukha, J. Deisenhofer, D. Pröpper, M. Schmidt, Z. Wang, Y. Goncharov, A. N. Yaresko, V. Tsurkan, B. Keimer, A. Loidl, and A. V. Boris, Phys. Rev. B **85**, 100504(R) (2012).

[43]C. C. Homes, Z. J. Xu, J. S. Wen, and G. D. Gu arXiv:1208.2240.

[44]L. Simonelli, N. L. Saini, M. M. Sala, Y. Mizuguchi, Y. Takano, H. Takeya, T. Mizokawa, and G. Monaco, Phys. Rev. B **85**, 224510 (2012).

[45]A. Bianconi, N. L. Saini, T. Rossetti, A. Lanzara, A. Perali, M. Missori, H. Oyanagi, H. Yamaguchi, Y. Nishihara, and D. H. Ha, Phys. Rev. B **54**, 12018 (1996).

[46]C. Y. Moon and H. J. Choi, Phys. Rev. Lett. **104**, 057003 (2010).

[47]T. Das and A. V. Balatsky, Phys. Rev. B **84**, 014521 (2011).

[48]O. K. Andersen and L. Boeri, Ann. Phys. (NY) **523**, 8 (2011).

[49]A. Wittlin, P. Aleshkevych, H. Przybylinska, D. J. Gawryluk, P. Dluzewski, M. Berkowski, R. Puzniak, M. U. Gutowska, and A. Wisniewski, Supercond. Sci. Technol. **25**, 065019 (2012).

[50]V. Kresin, J. Supercond. Nov. Magn. **25**, 711 (2012).

Chapter 5

Magnetic ordering and superconductivity in $EuFe_{2-x}Co_xAs_2$

$EuFe_2As_2$ is a particularly interesting member of the AFe_2As_2 superconductor family (A being a lanthanide atom), since the Eu atoms have a huge magnetic moment due to their $4f$ electron shell. Undoped $EuFe_2As_2$ orders antiferromagnetically at $T_{\mathrm{AFM}} = 19$ K [128] with an A-type structure [129]: the Eu^{2+} spins align ferromagnetically within the planes, and these planes are coupled antiferromagnetically to their neighbors (Fig. 5.1). The Fe moments form a spin density wave state. Re-entrant superconductivity can be achieved by Co doping on the Fe site. Full superconductivity (*i.e.* zero resistance) can only be reached by suppressing the magnetic moments with high pressures [130]. NMR results [131] indicate a strong interplay of superconductivity (in the FeAs planes) with the magnetic moments (on the Eu atoms). Studying the magnetization of $EuFe_{2-x}Co_xAs_2$ as a function of Co doping x (here $x = 0$ and 0.2) therefore helps to understand the interplay between magnetism and superconductivity.

In this Chapter, different magnetic configurations and transitions in $EuFe_2As_2$ and $EuFe_{2-x}Co_x$-As_2 ($x = 0.2$) are studied by angular torque measurements. The torque results are found to be consistent with SQUID magnetometry data. They confirm the presence of an antiferromagnetic order of the Eu moments at low temperature and low fields, which disappears with Co doping.

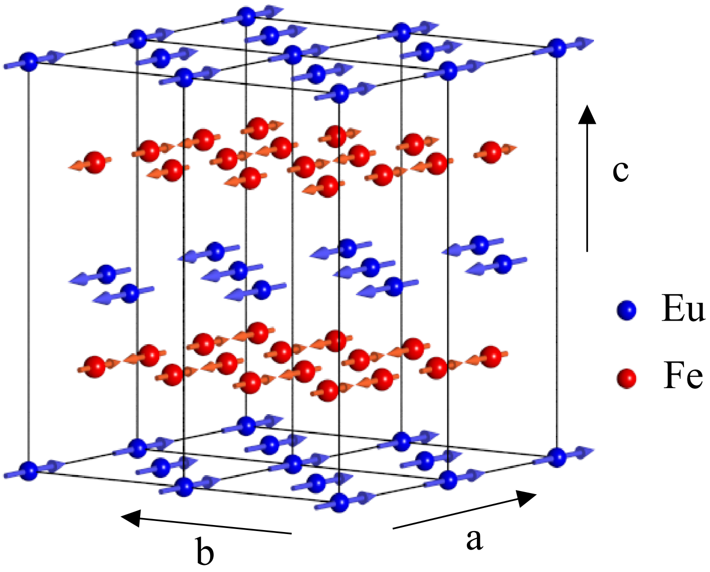

Figure 5.1: Schematic illustration of the zero-field, low temperature magnetic structure of $EuFe_2As_2$. For clarity, the arsenic atoms are not shown, and the iron atoms are represented as a uniform layer (see also Fig. 5.2). The Eu moments order ferromagnetically in the ab-plane and align antiferromagnetically along the c-axis. The Fe moments form a spin density wave state.

5.1 Observation of magnetic orders

SQUID measurements [132] on $EuFe_2As_2$ show that a canted antiferromagnetic (C-AFM) state exists at low temperatures and intermediate fields, when the field is high enough to move the magnetic moments out of their low field antiferromagnetic (AFM) orientation, but not high enough to get a complete ferromagnetic (FM) alignment. A C-AFM phase was observed by SQUID experiments in doped $EuFe_{2-x}Co_xAs_2$ as well, and the AFM phase has even completely disappeared. The full phase diagram extracted from SQUID measurements is presented in Fig. 5.4. Cobalt doping, which can induce superconductivity, obviously has an effect on the magnetic structure, since the AFM order at low fields disappears with doping. Figure 5.2 shows a schematic representation of the Eu moments in the AFM and C-AFM configuration.

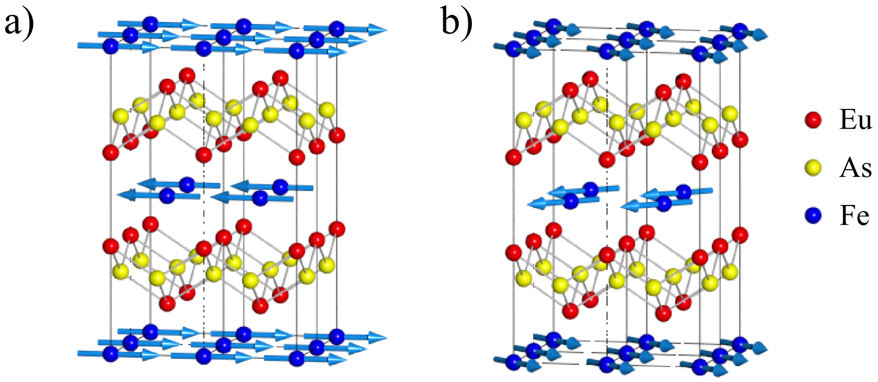

Figure 5.2: Magnetic order in $EuFe_2As_2$. a) AFM configuration of the Eu moments. b) At high fields, the Eu moments are canted within the *ab*-plane. The canting angle shown here is arbitrary.

In a ferromagnetic material, the magnetization M can be expressed as $M = \chi H$, where χ is the susceptibility matrix and H is the applied field. The torque can be calculated using Eq. (2.1), by projecting the magnetic moment along the susceptibility matrix eigenvectors. For a uniaxial material one obtains (see Appendix B):

$$\tau(\theta) = V\frac{\chi_c - \chi_{ab}}{2}\mu_0 H^2 \sin(2\theta), \tag{5.1}$$

with θ the angle between H and the crystallographic c-axis, V the volume of the sample, and χ_{ab} and χ_c the magnetic susceptibilities for $H||ab$ and $H||c$, respectively. The sign of the torque depends on the orientation of M with regards to H, which changes the projected moment sign. The in-plane anisotropy of $EuFe_2As_2$ is small enough to allow a uniaxial approximation [133].

An angular dependence of τ following Eq. (5.1) is observed in $EuFe_2As_2$ at low temperature and low field (Fig. 5.3a and b). Upon increasing the field, the sinusoidal AFM signal is abruptly replaced by another sinusoidal signal of opposite sign at a field corresponding to the departure from AFM behavior observed by SQUID experiments. The sign change is also consistent with the susceptibilities measured by SQUID: χ_{ab} - χ_c changes sign around the same field, thus changing the torque sign. At higher temperatures, the behavior is paramagnetic: the small AFM signal is not present anymore, and the sinusoidal torque amplitude increases quadratically in field, then saturates (Fig. 5.3c and d). This is also consistent with SQUID measurements. The global temperature and field dependence of the torque signal scaled by field is presented as a color map in Fig. 5.5. The color value corresponds to the torque amplitude (individually normalized in each graph).

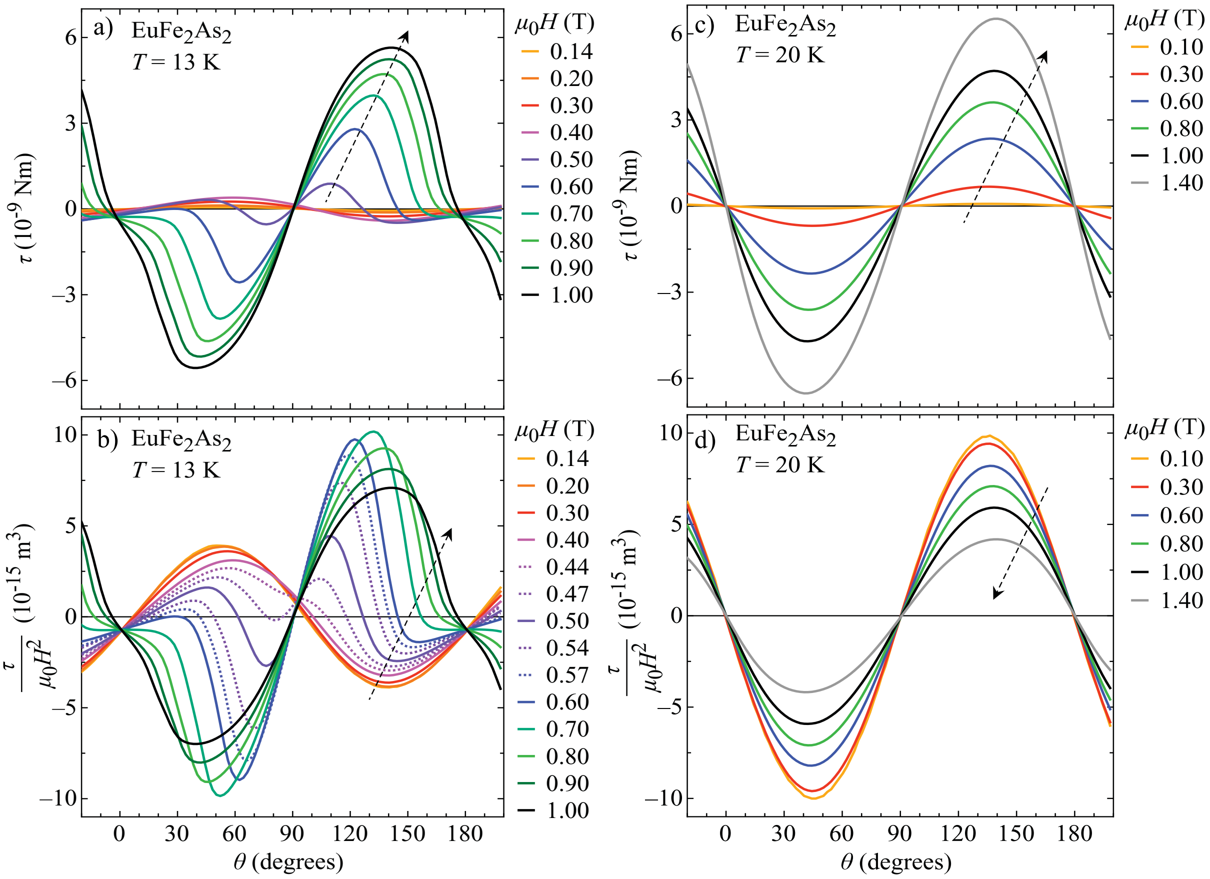

Figure 5.3: a) Angular dependence of the magnetic torque τ of single-crystal EuFe$_2$As$_2$ at 13 K in various magnetic fields. For clarity, not all measured data are shown. b) Angular dependence of $\tau/(\mu_0H^2)$. This quantity scales as the magnetic susceptibility. c) Angular dependence of τ in single-crystal EuFe$_2$As$_2$ in various magnetic fields at 20 K. d) Angular dependence of $\tau/(\mu_0H^2)$ in single-crystal EuFe$_2$As$_2$ in various magnetic fields at 20 K. The dashed arrows denote the direction of increasing magnetic field.

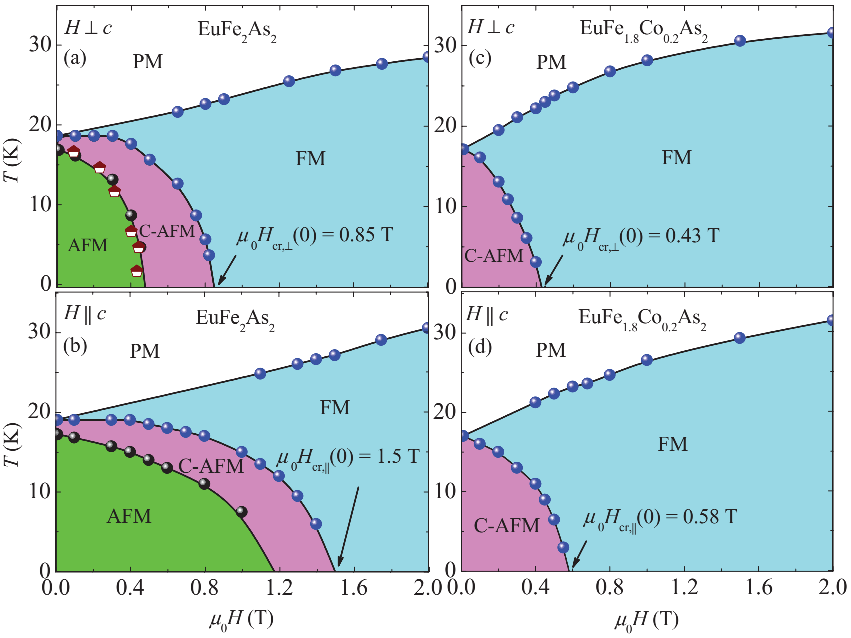

Figure 5.4: Magnetic phase diagrams of single-crystal EuFe$_2$As$_2$ [(a) and (b)] and single-crystal EuFe$_{2-x}$Co$_x$As$_2$ [(c)and (d)] for $H \parallel ab$ and for $H \parallel c$. The various phases in the phase diagrams are denoted as follows: paramagnetic (PM), antiferromagnetic (AFM), canted antiferromagnetic (C-AFM), and ferromagnetic (FM). The filled and open symbols are from susceptibility and field-dependent magnetization measurements, respectively. The solid lines are guides to the eyes.

5.2 Canting transition

In order to cant the magnetic moments of a planar antiferromagnet, the in-plane component H_{ab} of the magnetic field H must overcome the in-plane magnetization $\mathcal{M}_{ab}$ of an antiferromagnetic sublattice. $\mathcal{M}_{ab}$ is not to be confused with M_{ab}, the average magnetization of the whole Eu lattice, which is 0 in the AFM state. Assuming that $H_{ab} \propto \mathcal{M}_{ab}$ at the transition, we get above the transition:

$$H_{ab} \geq A\mathcal{M}_{ab} = A\sqrt{\mathcal{M}^2 - \mathcal{M}_c^2}, \tag{5.2}$$

where A is an unknown proportionality constant and $\mathcal{M}$ is the saturation magnetization of an AFM sublattice. The following calculation allows us to estimate the angular shape of the total field H_{cant} needed to cant the Eu^{2+} moments. Taking into account that

$$H_{ab} = H \sin\theta \tag{5.3}$$

$$\mathcal{M}_c = \frac{1}{2}\chi_c H \cos\theta \tag{5.4}$$

where χ_c is the susceptibility of the total Eu^{2+} magnetic lattice (the susceptibility of the sublattice is assumed to be $\chi_c/2$), we obtain for the canting boundary condition:

$$H_{\text{cant}}^2 \sin^2(\theta) = A^2(\mathcal{M}^2 - \frac{1}{4}\chi_c^2 H_{\text{cant}} \cos^2\theta) \tag{5.5}$$

$$H_{\text{cant}} = \frac{A\mathcal{M}}{\sqrt{\sin^2(\theta) + \frac{1}{4}A^2\chi_c^2\cos^2(\theta)}} \tag{5.6}$$

This profile of the transition between the AFM and C-AFM phases in the (H, θ) space is shown in Fig. 5.5a as a dashed line. It is in good qualitative agreement with experimental torque data. The torque sign change is not observed in $\mathrm{EuFe}_{2-x}\mathrm{Co}_x\mathrm{As}_2$ [Fig 5.5d, e, f], consistent with SQUID measurements which find no crossing in the field dependencies of the in-plane and out-of-plane susceptibilities [132]. Therefore, the AFM phase is not present in $\mathrm{EuFe}_{2-x}\mathrm{Co}_x\mathrm{As}_2$.

To conclude, torque measurements did confirm the SQUID phase diagram; Co doping on the Fe site has an effect on the ordering of the Eu moments, showing a link between the superconducting plane and the magnetic layer.

5.3 Publication related to Chapter 5

- *Anisotropic magnetic order of the Eu sublattice in single crystals of $EuFe_{2-x}Co_xAs_2$ ($x = 0, 0.2$) studied by means of magnetization and magnetic torque*
  Z. Guguchia, S. Bosma, S. Weyeneth, A. Shengelaya, R. Puzniak, Z. Bukowski, J. Karpinski, and H. Keller
  Physical Review B **84**, 144506 (2011)
  DOI: 10.1103/PhysRevB.84.144506

  e-prints:
  `http://arxiv.org/abs/1107.2103`
  `http://www.zora.uzh.ch/50935/`
  `http://prb.aps.org/abstract/PRB/v84/i14/e144506`

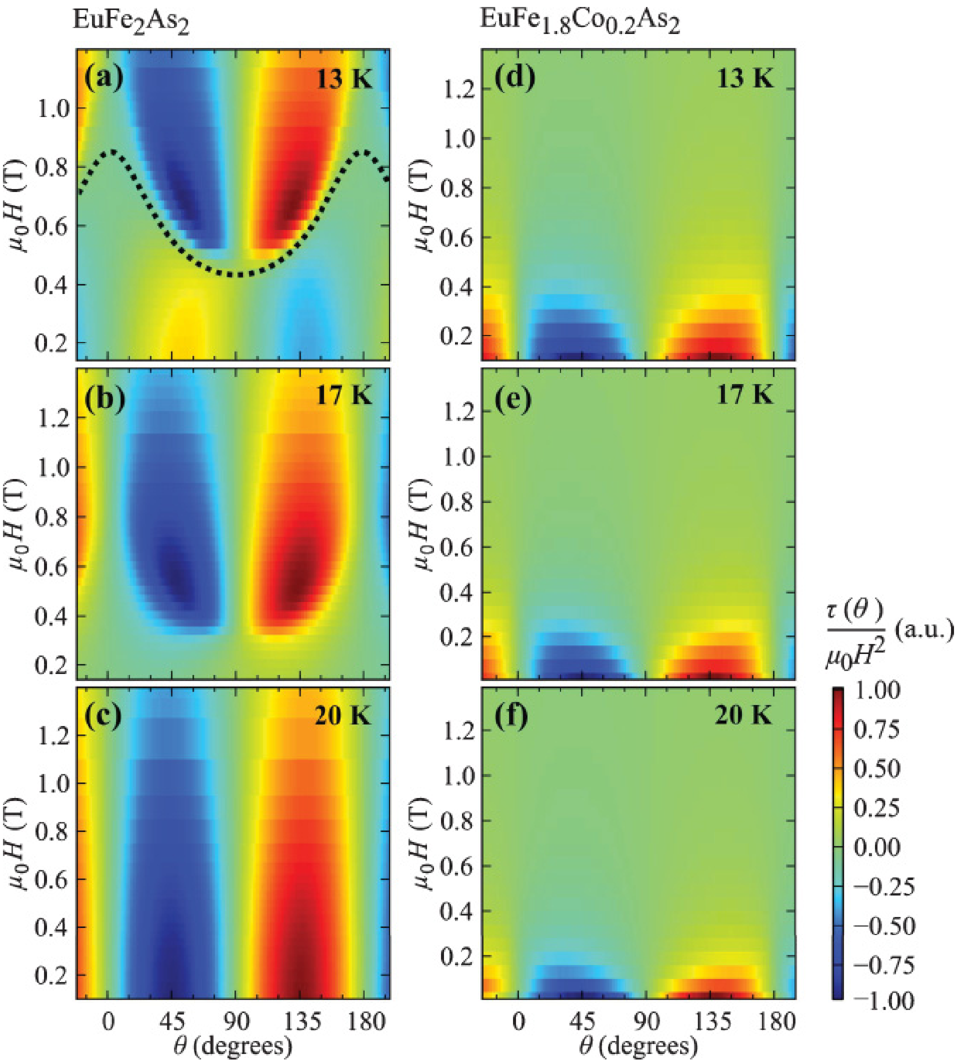

Figure 5.5: Color map of $\tau/\mu_0 H^2$ in arbitrary units (a.u.) for EuFe$_2$As$_2$ and EuFe$_{2-x}$Co$_x$As$_2$ as a function of angle θ and field H for T = 13, 17, and 20 K. The dotted line in a) is calculated according to Eq. (5.6). Panels a), (b), and (c) are the data for EuFe$_2$As$_2$ at 13, 17, and 20 K, respectively, whereas d), e), and f) are the data for EuFe$_{2-x}$Co$_x$As$_2$ at 13, 17, and 20 K, respectively.

PHYSICAL REVIEW B **84**, 144506 (2011)

Anisotropic magnetic order of the Eu sublattice in single crystals of $EuFe_{2-x}Co_xAs_2$ ($x = 0,0.2$) studied by means of magnetization and magnetic torque

Z. Guguchia,[*] S. Bosma, and S. Weyeneth
Physik-Institut der Universität Zürich, Winterthurerstrasse 190, CH-8057 Zürich, Switzerland

A. Shengelaya
Department of Physics, Tbilisi State University, Chavchavadze 3, GE-0128 Tbilisi, Georgia

R. Puzniak
Institute of Physics, Polish Academy of Sciences, Aleja Lotników 32/46, PL-02-668 Warsaw, Poland

Z. Bukowski[†] and J. Karpinski
Laboratory for Solid State Physics, ETH Zürich, CH-8093 Zürich, Switzerland

H. Keller
Physik-Institut der Universität Zürich, Winterthurerstrasse 190, CH-8057 Zürich, Switzerland

(Received 11 July 2011; published 4 October 2011)

We present a combination of magnetization and magnetic torque experiments to investigate the magnetic orders in undoped $EuFe_2As_2$ and Co-doped $EuFe_{1.8}Co_{0.2}As_2$ single crystals. Although at low temperatures typical results for an antiferromagnetic (AFM) state in $EuFe_2As_2$ were found, our data strongly indicate the occurrence of a canted antiferromagnetic (C-AFM) order of the Eu^{2+} moments between 17 and 19 K, observed even in the lowest studied magnetic fields. However, unlike in the parent compound, no low-field and low-temperature AFM state of the Eu^{2+} moments was observed in the doped $EuFe_{1.8}Co_{0.2}As_2$. Only a C-AFM phase is present at low fields and low temperatures, with a reduced magnetic anisotropy as compared to the undoped system. We discuss for both $EuFe_2As_2$ and $EuFe_{1.8}Co_{0.2}As_2$ the experimentally deduced magnetic phase diagrams of the magnetic ordering of the Eu^{2+} sublattice with respect to the temperature, the applied magnetic field, and its orientation to the crystallographic axes. It is likely that the magnetic coupling of the Eu and the Fe sublattice is strongly dependent on Co doping, having detrimental influence on the magnetic phase diagrams as determined in this work. Their impact on the occurrence of superconductivity with higher Co doping is discussed.

DOI: 10.1103/PhysRevB.84.144506 PACS number(s): 74.70.Xa, 75.30.Gw, 75.30.Kz, 75.50.Ee

I. INTRODUCTION

The discovery of superconductivity in the iron-based pnictides[1] provided a new class of compounds to the high-temperature-superconductor (HTS) family. Three main groups of these iron-based superconductors are intensively studied: the RFeAsO compounds with R = La-Gd (1111),[1,2] the ternary arsenides AFe_2As_2 with A = Ba, Sr, Ca, Eu (122),[3] and the binary chalcogenides such as $FeSe_{1-x}$ (11).[4] Similar to the cuprate HTS's, the undoped iron pnictides are not superconducting (SC) at ambient pressure and undergo a spin-density wave (SDW) transition at high temperatures.[5] The SC state in iron-based compounds can be achieved either under pressure (chemical and hydrostatic)[6–15] or by appropriate charge-carrier doping of the parent compounds,[16–18] both accompanied by a suppression of the SDW state.

Here, we focus on $EuFe_2As_2$, which is a particularly interesting member of the ternary system AFe_2As_2, since the A site is occupied by a rare-earth Eu^{2+} S-state (orbital moment $L = 0$) ion with a $4f^7$ electronic configuration. Eu^{2+} has a total electron spin $S = 7/2$, corresponding to a theoretical effective magnetic moment of 7.94 μ_B. It is the only known member of the 122 family containing $4f$ electrons. In addition to the SDW ordering of the Fe moments at $T_{SDW} \simeq 190$ K, an antiferromagnetic (AFM) order of the Eu^{2+} spins at $T_{AFM} \simeq 19$ K was reported by Mössbauer and susceptibility measurements.[19–21] Recently, neutron diffraction measurements were performed on $EuFe_2As_2$ and the magnetic structure illustrated in Fig. 1 was established.[5] This material exhibits an A-type AFM order of the Eu^{2+} moments, e.g., the Eu^{2+} spins align ferromagnetically in the planes, while the planes are coupled antiferromagnetically.[5,22] It was demonstrated that, by applying a high enough magnetic field, the Eu^{2+} moments can be realigned ferromagnetically in both the parent compound $EuFe_2As_2$ (Refs. 21 and 23) as well as in the Co-doped system $EuFe_{2-x}Co_xAs_2$ ($x = 0.22$).[24] In addition, neutron diffraction measurements[23] suggested a canted AFM (C-AFM) structure of the Eu^{2+} moments in $EuFe_2As_2$ at intermediate magnetic fields.

Co-substitution induces superconductivity in $EuFe_{2-x}Co_xAs_2$ with a reentrant behavior of resistivity due to the AFM ordering of the Eu^{2+} spins.[25] Reentrant superconducting behavior was also observed in resistivity experiments on $EuFe_2As_2$ under an applied pressure up to 2.5 GPa.[14,15] However, only above 2.8 GPa, where a valence change of the Eu ions from a divalent magnetic state ($4f^7$, $J = 7/2$) to a trivalent nonmagnetic state ($4f^6$, $J = 0$) was suggested to occur,[7] a sharp transition to a zero-resistivity state was observed.[14] Bulk superconductivity was also achieved in $EuFe_2As_{2-x}P_x$,[7,26] where isovalent P substitution of the As site induces chemical pressure in $EuFe_2As_2$. No

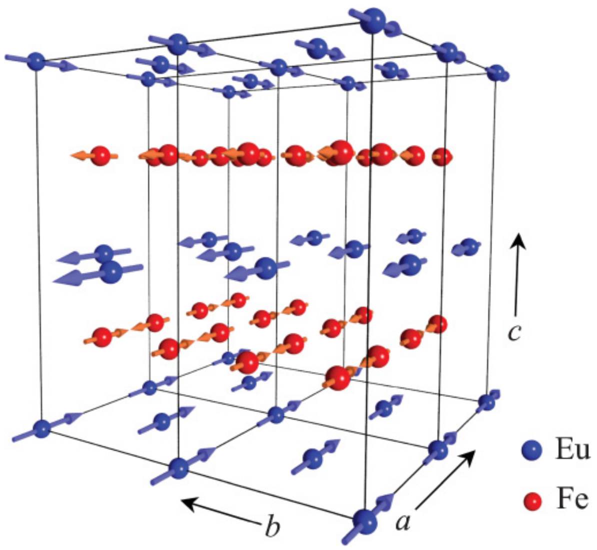

FIG. 1. (Color online) Schematic illustration of the magnetic structure of $EuFe_2As_2$. The Fe moments (red) form a SDW state, whereas the Eu moments (blue) order ferromagnetically in the *ab* plane and align antiferromagnetically along the *c* axis.

superconductivity was detected in $EuFe_{2-x}Ni_xAs_2$,[27] while superconductivity with a maximum $T_c \simeq 20$ K was reported for $BaFe_{2-x}Ni_xAs_2$.[28] It was suggested in various reports[21,27,29,30] that there is a strong coupling between the localized Eu^{2+} spins and the conduction electrons of the Fe_2As_2 layers. Recently, the hyperfine coupling constant A_{Eu} between the ^{75}As nuclei and the Eu $4f$ states in $EuFe_{1.9}Co_{0.1}As_2$ was quantitatively determined from ^{75}As nuclear magnetic resonance (NMR) to be $A_{Eu} = -1.9 \times 10^7$ A/mμ_B.[31] This large value of A_{Eu} indicates a strong coupling between the Eu^{2+} localized moments and the charge carriers in the Fe_2As_2 layers, and points to a strong correlation between the ordering of the localized magnetic moments and superconductivity in $EuFe_{2-x}Co_xAs_2$.

It is well established that the SDW state of the Fe moments is suppressed as a result of Co doping. However, at present, there is no clear picture as to how the ordering of the Eu spins develops with increasing Co concentration. Generally, it was assumed that, in the 122 systems, the direction of the sublattice magnetization of the Eu^{2+} magnetic moments is strongly affected by the magnetic behavior of the Fe atoms.[5,32–36] Thus, it is important to compare the magnetic properties of the Eu sublattice in $EuFe_{2-x}Co_xAs_2$ without and with Co doping in order to study the correlation between ordering of Eu^{2+} moments and the magnetism of the Fe sublattice. This, in turn, is crucial to understand the interplay between magnetism of localized moments and superconductivity in $EuFe_{2-x}Co_xAs_2$.

In this paper, we present magnetic susceptibility, magnetization, and magnetic torque experiments performed on single crystals of $EuFe_{2-x}Co_xAs_2$ ($x = 0$, 0.2). The goal of this study is to investigate the macroscopic magnetic properties of the Eu sublattice. Magnetic susceptibility and magnetization investigations provide information on the magnetic structure of a single-crystal sample in magnetic fields applied along the principal axes. In addition, the evolution of the magnetic structure as a function of the tilting angle of the magnetic field and the crystallographic axis can be studied by magnetic torque. This paper is organized as follows: Experimental details are described in Sec. II. The results of the magnetic susceptibility, the magnetization, and the magnetic torque measurements are presented and discussed in Sec. III. In Sec. IV, the magnetic phase diagrams of the Eu^{2+} sublattice ordering with respect to magnetic field and temperature in single crystals of $EuFe_{2-x}Co_xAs_2$ ($x = 0$, 0.2) are discussed. The conclusions follow in Sec. V.

II. EXPERIMENTAL DETAILS

Single crystals of $EuFe_{2-x}Co_xAs_2$ ($x = 0$, 0.2) were grown out of Sn flux.[31] The magnetization measurements of the $EuFe_{2-x}Co_xAs_2$ ($x = 0$, 0.2) samples were performed with a commercial SQUID magnetometer (*Quantum Design* MPMS-XL) with the magnetic field H applied parallel ($H \parallel c$) or perpendicular ($H \perp c$) to the crystallographic c axis. The magnetic torque measurements were carried out using a homemade torque sensor.[37] The sample is mounted on a platform hanging on piezoresistive legs. A magnetic field $\vec{H}$ applied to the sample having magnetic moment $\vec{m}$ results in a mechanical torque $\vec{\tau} = \mu_0 \vec{m} \times \vec{H}$. This torque bends the legs, and thus creates a measurable electric signal proportional to the torque amplitude. The temperature is controlled by an *Oxford* flow cryostat, and the magnetic field is provided by a rotatable resistive *Bruker* magnet with a maximum magnetic field of 1.4 T.

III. RESULTS

A. Magnetization measurements

1. Temperature dependence

The temperature dependence of the magnetic susceptibility $\chi = M/H$ (here M is the magnetization determined as magnetic moment per mol) for the crystal of $EuFe_2As_2$ in a field of $\mu_0 H = 0.01$ T for $H \perp c$ and for $H \parallel c$ is shown in Fig. 2(a). In agreement with previous reports,[20,21] the magnetic susceptibility for $H \perp c$ ($\chi_\perp$) and for $H \parallel c$ ($\chi_\parallel$), determined in the temperature range from 30 to 190 K (i.e., far above $T_{AFM} \simeq 19$ K of the Eu moments up to $T_{SDW} \simeq 190$ K of the Fe moments) is well described by the Curie-Weiss law

$$\chi(T) = \frac{C}{T - \theta_{CW}}. \tag{1}$$

Here, C denotes the Curie constant and θ_{CW} the Curie-Weiss temperature. Analyzing the data in Fig. 2(a) with Eq. (1) yields $C = 1853(15) \times 10^{-7}$ m^3 K/mol, $\theta_{CW} = 19.74(8)$ K for $H \parallel c$ and $C = 2127(23) \times 10^{-7}$ m^3 K/mol, $\theta_{CW} = 20.69(4)$ K for $H \perp c$. The calculated effective magnetic moment is $\mu_{eff} \simeq 7.6\,\mu_B$ for $H \parallel c$ and $\mu_{eff} \simeq 8.3\,\mu_B$ for $H \perp c$. These estimates of μ_{eff} are close to the theoretical value of the magnetic moment of a free Eu^{2+} ion ($\mu_{Eu^{2+}} = 7.94\,\mu_B$). The positive value of θ_{CW} for both $H \parallel c$ and $H \perp c$ is consistent with previous magnetization measurements,[20,21] indicating that the direct interaction between the Eu^{2+} moments is ferromagnetic (FM). This is in agreement with the magnetic structure of $EuFe_2As_2$ suggested by zero-field neutron diffraction measurements,[5]

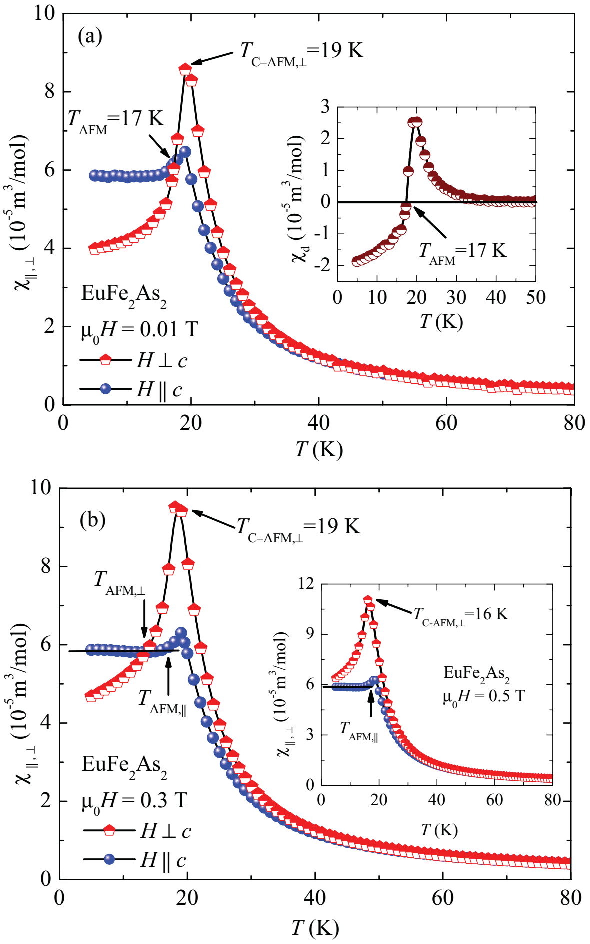

FIG. 2. (Color online) Temperature dependence of the magnetic susceptibility measured at fixed magnetic fields applied perpendicular ($H \perp c$) and parallel ($H \parallel c$) to the crystallographic c axis of single-crystal EuFe$_2$As$_2$: (a) $\mu_0 H = 0.01$ T; (b) $\mu_0 H = 0.3$ T and $\mu_0 H = 0.5$ T (inset). The inset of panel (a) illustrates the temperature dependence of the difference between both susceptibilities ($\chi_{\text{d}} = \chi_\perp - \chi_\parallel$). The arrows mark the AFM and C-AFM ordering temperatures of the Eu^{2+} moments, and $T_{\text{AFM},\perp}$ and $T_{\text{AFM},\parallel}$ refer to the AFM ordering temperatures for $H \perp c$ and $H \parallel c$, respectively. The canted-AFM ordering temperature for $H \perp c$ is denoted by $T_{\text{C-AFM},\perp}$.

revealing that the intralayer arrangement of the Eu^{2+} spins is FM. The sharp increase of χ with decreasing temperature below 30 K also indicates a FM coupling between the Eu^{2+} moments. The Eu moments align with respect to the Fe moments along the a axis[5] as illustrated in Fig. 1.

With decreasing temperature from 19 to 17 K, the susceptibility $\chi_\perp$ of single-crystal EuFe$_2$As$_2$ decreases rapidly, and below 17 K, the decrease of $\chi_\perp$ is less pronounced. On the other hand, $\chi_\parallel$ decreases with decreasing temperature from 19 to 17 K and remains constant below 17 K. Moreover, the values of $\chi_\perp$ and $\chi_\parallel$ at 19 K are substantially different ($\chi_\perp/\chi_\parallel \simeq 1.33$), already in a rather low magnetic field $\mu_0 H = 0.01$ T [see Fig. 2(a)]. Note that within the classical picture of an ideal antiferromagnet, the magnetic susceptibility χ in a magnetic field perpendicular to the easy axis is constant, and χ in a field parallel to the easy plane decreases linearly with decreasing temperature. In addition, for an antiferromagnet, the values of χ at the antiferromagnetic (AFM) transition temperature are the same for both $H \perp c$ and $H \parallel c$.[22] The inset of Fig. 2(a) illustrates the temperature dependence of the difference between both susceptibilities $\chi_{\text{d}} = \chi_\perp - \chi_\parallel$. Note that, below 19 K, the quantity χ_{d} decreases with decreasing temperature and reaches zero at around 17 K. This behavior of $\chi_{\text{d}}(T)$ can be explained by invoking a transition from the high-temperature paramagnetic state to a FM state or to a C-AFM state at about 19 K. The transition from a FM or a C-AFM to an AFM state of the Eu^{2+} spins occurs only below 17 K. The pronounced increase of $\chi_\parallel$ above 17 K indicates the appearance of a magnetic moment along the c axis. Since $\chi_\parallel$ is smaller than $\chi_\perp$ in the FM/C-AFM state, it is suggested that the ab plane is the easy plane of this ordered state. In Fig. 2(b), the temperature dependences of $\chi_\perp$ and $\chi_\parallel$ of single-crystal EuFe$_2$As$_2$ in a magnetic field of 0.3 and 0.5 T (inset) are shown. Obviously, the AFM transition temperatures for $H \perp c$ (crossing point of $\chi_\perp$ and $\chi_\parallel$) and for $H \parallel c$ (temperature at which $\chi_\parallel$ starts to increase) are shifted to lower temperature with higher magnetic field [see Fig. 2(a) for comparison]. However, at $\mu_0 H = 0.5$ T, the curves $\chi_\perp$ and $\chi_\parallel$ do not cross in the investigated temperature range, indicating that the AFM state of the Eu^{2+} ions is suppressed in EuFe$_2$As$_2$ in magnetic fields $H \perp c$ exceeding $\mu_0 H \simeq 0.5$ T. For $H \parallel c$, the suppression of the AFM state occurs in fields higher than $\mu_0 H \simeq 1.2$ T since, above this field, the susceptibility for $H \parallel c$ is temperature dependent even at temperature as low as 2 K [see Fig. 3(b)]. Importantly, the magnetic field at which the magnetic moments of the Eu sublattice saturate (i.e., the field at which the FM state is reached) is much higher than the field of suppression of the AFM state. This implies that a FM state appears in a magnetic field higher than the field of suppression of antiferromagnetism and that those two transitions are distinguishable. The peak in the magnetic susceptibility at about 19 K in low fields (see Fig. 2) can be associated with the transition from a PM to a C-AFM state. This peak is shifted to lower temperatures with applied magnetic field above $\mu_0 H \simeq 0.3$ T for $H \perp c$ and above $\mu_0 H \simeq 0.5$ T for $H \parallel c$ [see Figs. 2(b) and 3(b)]. Finally, we may conclude that a field-induced magnetic phase transition from an AFM via a C-AFM configuration to a FM state takes place below 17 K. Such a transition is visible even at the lowest temperature of 2 K reached in our experiment.

The magnetization $M(T)$ in the FM state in the vicinity of the Curie temperature T_{C} can be described by the power law

$$M(T) = M_0 \left(1 - \frac{T}{T_{\text{C}}}\right)^{\tilde{\beta}}. \qquad (2)$$

Here, $\tilde{\beta}$ and M_0 are empirical constants. Analyzing the data at 1.5 T with Eq. (2) yields $T_{\text{C}} = 27.2(1)$ K and $\tilde{\beta} = 0.39(1)$ for both directions of the magnetic field [solid lines in the insets of Figs. 3(a) and 3(b)]. It was found that T_{C} increases gradually with increasing applied magnetic field for $H \perp c$ and $H \parallel c$. By extrapolating $T_{\text{C}}(H)$ to low fields, the zero-field value of

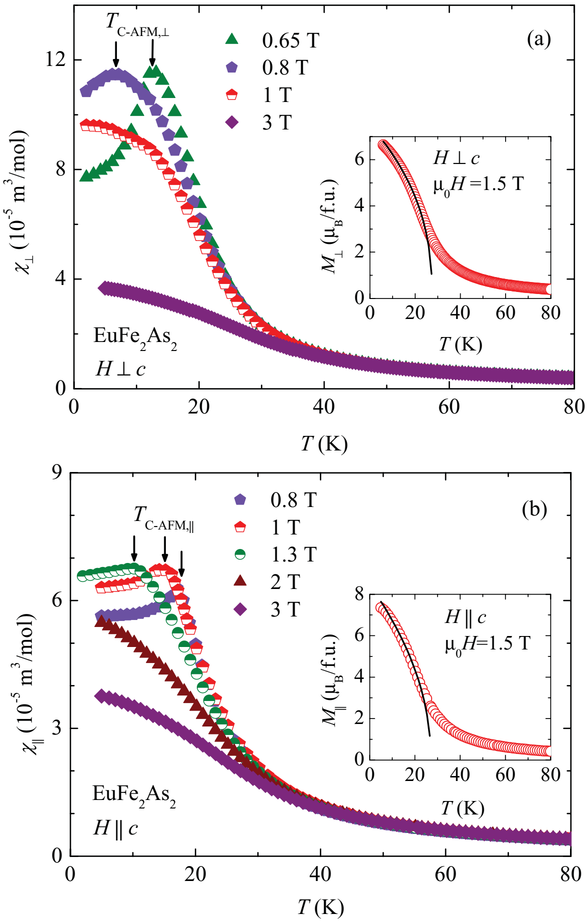

FIG. 3. (Color online) Temperature dependence of the magnetic susceptibility measured at fixed magnetic fields of single-crystal $EuFe_2As_2$ for $H \perp c$ (a) and $H \parallel c$ (b). The arrows mark the canted antiferromagnetic ordering temperature $T_{\text{C-AFM}}$ of the Eu^{2+} moments in low fields. $T_{\text{C-AFM},\perp}$ and $T_{\text{C-AFM},\parallel}$ refer to the C-AFM ordering temperatures for $H \perp c$ and $H \parallel c$, respectively. The insets illustrate the determination of T_C using the power law given in Eq. (2).

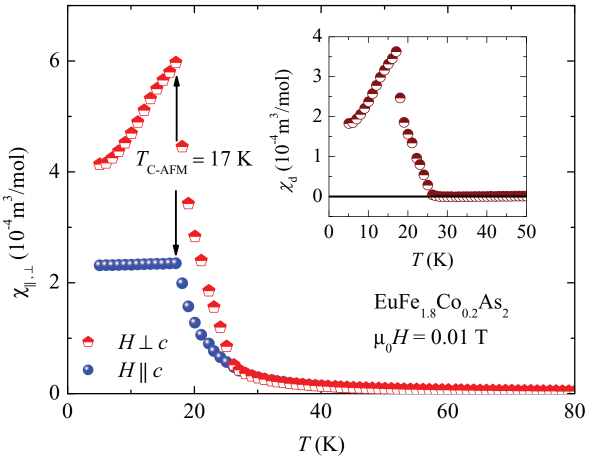

FIG. 4. (Color online) Temperature dependence of the magnetic susceptibility measured in a field of $\mu_0 H = 0.01$ T of single-crystal $EuFe_{1.8}Co_{0.2}As_2$ for $H \perp c$ and $H \parallel c$. The arrows mark the canted antiferromagnetic ordering temperature $T_{\text{C-AFM}} \simeq 17$ K of the Eu^{2+} moments. In the inset, the difference between the susceptibilities for the two different field configurations ($\chi_d = \chi_\perp - \chi_\parallel$) is plotted as a function of temperature.

T_C was found to be $\simeq$19 K. The present values of $T_C(H)$ are in agreement with those reported by Xiao *et al.*[23]

The temperature dependence of the magnetic susceptibility for the Co-doped crystal of $EuFe_{1.8}Co_{0.2}As_2$ in an applied field of $\mu_0 H = 0.01$ T for $H \perp c$ and $H \parallel c$ is presented in Fig. 4. In the inset, the temperature dependence of the difference between the susceptibilities for two field configurations $\chi_d = \chi_\perp - \chi_\parallel$ is shown. Analyzing the susceptibility data above 30 K with Eq. (1) yields $C = 2108(32)\times10^{-7}$ m^3 K/mol, $\theta_{\text{CW}} = 21.86(6)$ K for $H \perp c$ and $C = 1915(34)\times10^{-7}$ m^3 K/mol, $\theta_{\text{CW}} = 20.67(7)$ K for $H \parallel c$. Again, θ_{CW} turns out to be positive. Like in the parent compound, a sharp increase of χ below 30 K is observed, which is attributed to the in-plane FM coupling between the Eu^{2+} moments. Below 17 K, the susceptibility $\chi_\perp$ starts to decrease with decreasing temperature, indicating the onset of an AFM transition of the Eu^{2+} spins. On the other hand, $\chi_\parallel$ remains almost constant below 17 K. This suggests that the Eu^{2+} moments align along the *ab* plane, similar to undoped $EuFe_2As_2$. However, for $EuFe_2As_2$, the AFM ordering temperature of the Eu^{2+} spins is about 2 K higher. Below 17 K, $\chi_\perp$ is significantly larger than $\chi_\parallel$, even in magnetic fields as low as $\mu_0 H = 0.01$ T (see Fig. 4). Thus, no crossing between $\chi_\perp$ and $\chi_\parallel$ is observed (inset of Fig. 4), in contrast to the parent compound $EuFe_2As_2$ (see Fig. 2). Furthermore, $\chi_\perp$ is temperature dependent even at the lowest applied magnetic field. This is inconsistent with an AFM state with an easy *c* axis. Hence, we suggest that, for all temperatures below 17 K, the ground state of the coupled Eu^{2+} spins in $EuFe_{1.8}Co_{0.2}As_2$ is a C-AFM state with a FM component in the *ab* plane. This implies that the magnetic configuration of the Eu moments is strongly influenced by the magnetization of the Fe sublattice. This is consistent with previous NMR studies, revealing a strong coupling between the Eu and $Fe_{2-x}Co_xAs_2$ layers.[31]

The temperature dependences of $\chi_\perp$ and $\chi_\parallel$ at different magnetic fields of single-crystal $EuFe_{1.8}Co_{0.2}As_2$ are shown in Fig. 5. Zero-field cooling (ZFC) and field cooling (FC) susceptibilities $\chi_\perp(T)$ measured in an applied field of $\mu_0 H = 0.001$ T are shown in the inset of Fig. 5(a). Below 17 K, the ZFC and FC curves deviate from each other, indicating the presence of a C-AFM state of the Eu^{2+} moments. The data reveal a decrease of the C-AFM ordering temperature $T_{\text{C-AFM}}$ with increasing magnetic field for both field orientations, similar as for the parent compound $EuFe_2As_2$. However, the values for $T_{\text{C-AFM}}$ for $EuFe_{1.8}Co_{0.2}As_2$ are substantially smaller than those for $EuFe_2As_2$.

2. *Field dependence*

The susceptibility investigations of the preceding section clearly demonstrate that the system $EuFe_{2-x}Co_xAs_2$

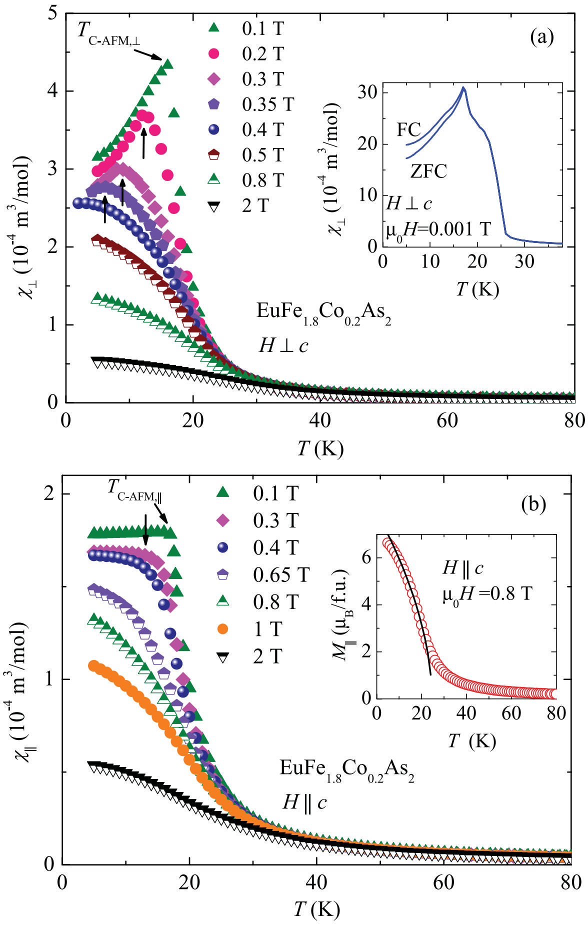

FIG. 5. (Color online) Temperature dependence of the ZFC magnetic susceptibility measured at various fixed magnetic fields of single-crystal $\mathrm{EuFe_{1.8}Co_{0.2}As_2}$ for $H \perp c$ (a) and $H \parallel c$ (b). The arrows mark the canted antiferromagnetic ordering temperature $T_{\text{C-AFM}}$ of the $\mathrm{Eu^{2+}}$ moments in low magnetic fields. $T_{\text{C-AFM},\perp}$ and $T_{\text{C-AFM},\parallel}$ refer to the C-AFM ordering temperatures for $H \perp c$ and $H \parallel c$, respectively. In the inset of (a), $\chi_\perp(T)$ for FC and ZFC in an applied field of $\mu_0 H = 0.001$ T is plotted. The inset of (b) shows the approximation of $M_\parallel(T)$ in $\mu_0 H = 0.8$ T by the power law (solid curve) given in Eq. (2).

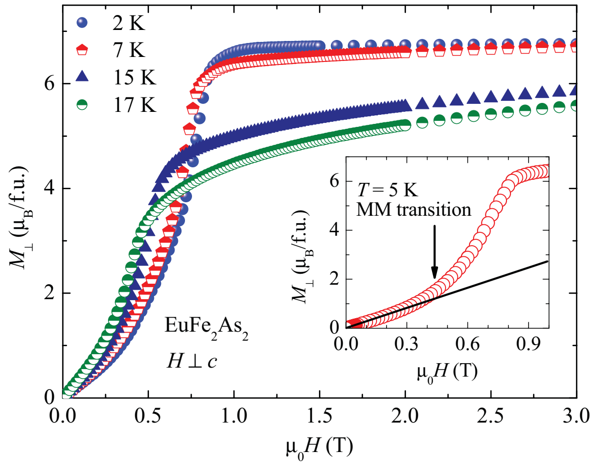

FIG. 6. (Color online) Field dependence of the magnetization at various temperatures of single-crystal $\mathrm{EuFe_2As_2}$ for $H \perp c$. The inset shows the low-field $M_\perp$ data at 5 K, illustrating the metamagnetic (MM) transition marked by the arrow.

($x = 0$, 0.2) shows a rich variety of magnetic phases. In order to explore in detail the various magnetic field-induced phases, magnetization experiments were also performed as a function of the applied magnetic field at different temperatures.

The field dependence of the magnetization of single-crystal $\mathrm{EuFe_2As_2}$ at different temperatures for $H \perp c$ is shown in Fig. 6. In the inset, the low-field magnetization $M_\perp$ at 5 K is shown. $M_\perp$ increases almost linearly with increasing magnetic field H up to $\mu_0 H \simeq 0.45$ T, where a sudden increase of $M_\perp$ appears. Then, $M_\perp$ further increases with increasing H, and finally saturates for $\mu_0 H \geqslant 0.8$ T. The value of the saturation magnetization corresponds to an effective magnetic moment of 6.8 μ_B/f.u., which is close to $g\mu_B S = 7\ \mu_B$/f.u. expected for $\mathrm{Eu^{2+}}$ moments. This result suggests that there is a metamagnetic[38,39] (MM) transition at $\mu_0 H_{\text{MM}} \simeq 0.45$ T at 5 K in $\mathrm{EuFe_2As_2}$, consistent with previous observations.[20,21] Such a metamagnetic transition is characteristic for A-type antiferromagnetism in layered systems as, e.g., $\mathrm{Na_{0.85}CoO_2}$ (Ref. 38) and $\mathrm{La_{2-x}Sr_{1+x}Mn_2O_7}$.[40] Figure 6 shows that the MM transition shifts toward lower fields with increasing temperature. The values of the magnetic field at which the MM transition occurs is in agreement with the results obtained from the susceptibility for the AFM to C-AFM transition. Thus, we propose that the MM transition corresponds to the onset of a spin-flop transition[22] from an AFM to a C-AFM state in $\mathrm{EuFe_2As_2}$. However, no MM transition for $H \perp c$ is detected in $\mathrm{EuFe_{1.8}Co_{0.2}As_2}$ [Fig. 7(a)]. Both $M_\perp$ and $M_\parallel$ first increase almost linearly with increasing H and then saturate at higher fields (Fig. 7). The absence of a MM transition in $\mathrm{EuFe_{1.8}Co_{0.2}As_2}$ is consistent with the susceptibility measurements presented above, suggesting that the $\mathrm{Eu^{2+}}$ moments exhibit a C-AFM ground state even at very low H. This conclusion is also supported by magnetic hysteresis measurements at 5 K performed in magnetic fields up to 0.5 T. As demonstrated in the inset of Fig. 7(a), the field dependence of $M_\perp$ at 5 K shows a well-developed hysteresis for $\mathrm{EuFe_{1.8}Co_{0.2}As_2}$, in contrast to the parent compound $\mathrm{EuFe_2As_2}$ where no hysteresis is observed.

Obviously, the presented susceptibility and magnetization measurements reveal a complex and rather sophisticated interplay of magnetic phases in the $\mathrm{EuFe_{2-x}Co_xAs_2}$ system. Additional information on the complex magnetic phases in $\mathrm{EuFe_{2-x}Co_xAs_2}$ is obtained from angular-dependent magnetic torque studies presented in the next section.

B. Magnetic torque

In low magnetic fields, the $\mathrm{Eu^{2+}}$ magnetic moments prefer to order antiferromagnetically in $\mathrm{EuFe_2As_2}$. High magnetic fields reorient the magnetic moments, leading to various

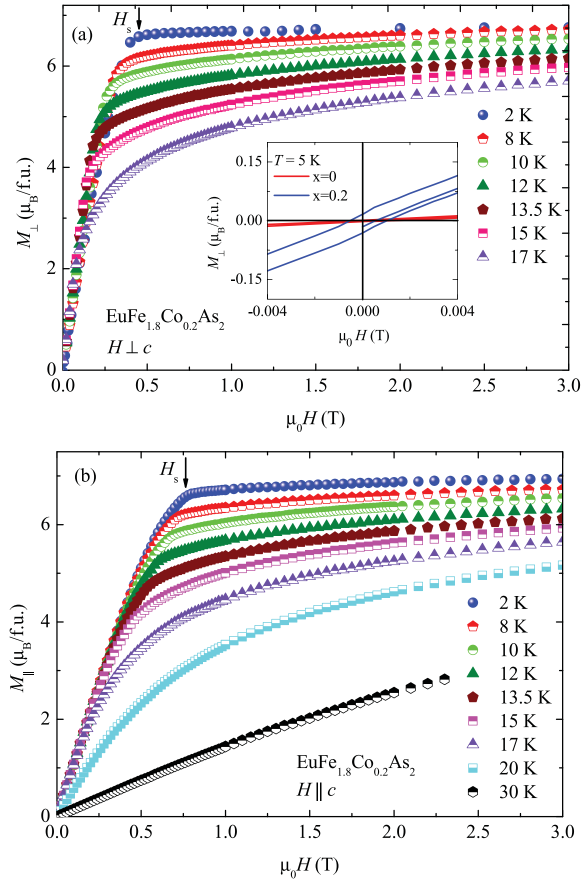

FIG. 7. (Color online) Field dependence of the magnetization at low temperatures of single-crystal $EuFe_{1.8}Co_{0.2}As_2$ for $H \perp c$ (a) and $H \parallel c$ (b). The saturation field H_s at 2 K is marked by arrows. The inset of (a) shows the field dependence of $M_\perp$ for $EuFe_2As_2$ and $EuFe_{1.8}Co_{0.2}As_2$ at 5 K.

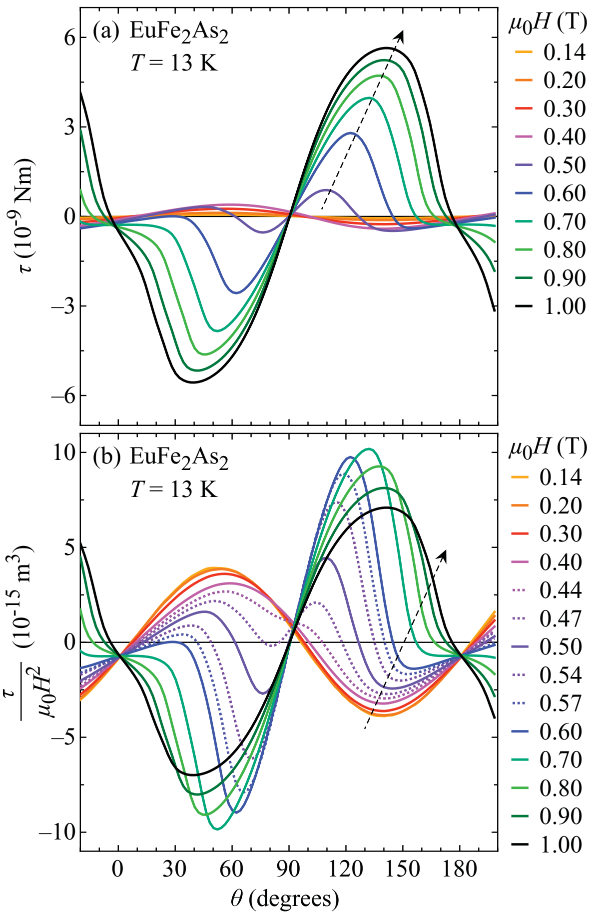

FIG. 8. (Color online) (a) Angular-dependent magnetic torque τ of single-crystal $EuFe_2As_2$ at 13 K in various magnetic fields. For clarity, not all measured data are shown. (b) Angular dependence of the quantity $\tau/(\mu_0H^2)$. The dashed arrows denote the direction of increasing magnetic field.

magnetic field-induced phases. Magnetic torque allows us to investigate multiple aspects of magnetic order as a function of the magnetic field with respect to the principal axes. Whereas magnetization provides direct information on the magnetic moment oriented along the field, magnetic torque directly probes the anisotropy of the susceptibility in magnetic systems.

The angular dependence of the magnetic torque τ of single-crystal $EuFe_2As_2$ measured at 13 K in various magnetic fields is presented in Fig. 8(a). In Fig. 8(b), the same data are plotted in terms of $\tau/(\mu_0H^2)$. The torque data below 0.3 T are of sinusoidal shape, following the simple angular dependence for a uniaxial antiferromagnet[41]:

$$\tau(\theta) = -V\frac{(\chi_\perp - \chi_\parallel)}{2}\mu_0H^2\sin(2\theta). \qquad (3)$$

Here, θ denotes the angle between the field H and the crystallographic c axis, V is the volume of the sample, and $\chi_\perp$ and $\chi_\parallel$ are the magnetic susceptibilities for $H \perp c$ and for $H \parallel c$, respectively. Above 0.3 T, the shape of the torque signal changes drastically (see Fig. 8). For $\theta \simeq 90^\circ$(H almost parallel to the ab plane), an additional torque signal appears, with an opposite sign relative to the AFM torque. Upon increasing the magnetic field, this additional signal rises steeply and leads to a sign change of the torque signal for all angles θ. A similar behavior was observed in $RbVBr_3$ (Ref. 42) and was interpreted as the appearance of a weak field-induced magnetic moment. This additional contribution to the torque signal observed here is substantially larger than the AFM torque signal. This is consistent with the magnetization data (see Sec. III A), from which the presence of a C-AFM phase was concluded above 0.3 T at 13 K. The sign change of the torque signal is in agreement with the sign change of the quantity $\chi_d = \chi_\perp - \chi_\parallel$, which was interpreted as a signature of a transition to a C-AFM state of the Eu^{2+} magnetic moments. It was shown previously[29] that $EuFe_2As_2$ exhibits a weak in-plane anisotropy. Since the in-plane anisotropy is much weaker than the out-of-plane anisotropy, this system can be treated approximately

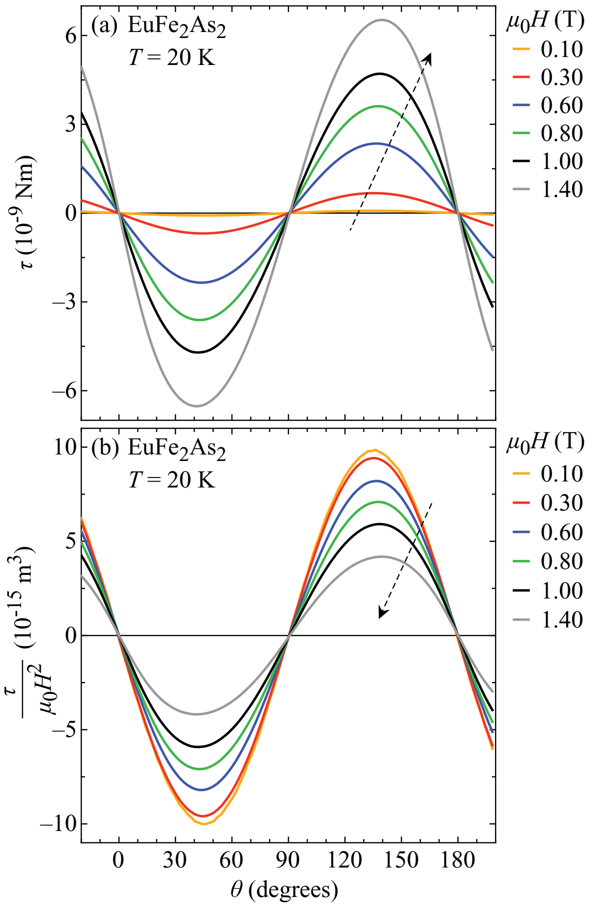

FIG. 9. (Color online) Magnetic torque τ (a) and the quantity $\tau/(\mu_0 H^2)$ (b) as a function of the angle θ of single-crystal EuFe$_2$As$_2$ in various magnetic fields at 20 K. The dashed arrows denote the direction of increasing magnetic field.

as a uniaxial anisotropic antiferromagnet. However, even a small in-plane anisotropy may lead to discrepancies between experimental results and theoretical predictions for a uniaxial anisotropic ferromagnet. Particularly, the torque signal of the AFM state shown in Fig. 8(a) is shifted by $\Delta\theta \sim 10^\circ$ with respect to one of the C-AFM state [see Fig. 8(b)]. A similar phase shift $\Delta\theta$ was observed in λ-(BETS)$_2$FeCl$_4$ (Ref. 43) and interpreted as a change of the easy axis. However, here the phase shift appears to indicate a crystallographic multidomain state due to a twinning of the crystal in the AFM state.

Figure 9(a) shows the measured magnetic torque for the same EuFe$_2$As$_2$ single crystal at 20 K, where, according to the magnetization results, the AFM regime has disappeared. Consistently, no AFM torque signal is observed. Instead, the magnetic torque amplitude increases like H^2 and saturates at higher H. Such a behavior is characteristic for a paramagnet. Consistently, the quantity $\tau/(\mu_0 H^2)$ plotted in in Fig. 9(b) decreases with increasing field.

In Fig. 10, the scaled magnetic torque $\tau/(\mu_0 H^2)$ for EuFe$_2$As$_2$ and EuFe$_{1.8}$Co$_{0.2}$As$_2$ is shown in a color map for the representative temperatures of 13, 17, and 20 K as a function of angle θ and field H. Note that $\tau/(\mu_0 H^2)$ is scaling according to the magnetic susceptibility. As seen in Fig. 10(a), the low-field regime of undoped EuFe$_2$As$_2$ at 13 K is dominated by the AFM state, whereas for higher fields, the C-AFM state appears abruptly along a clearly angular-dependent boundary line (dotted line), demonstrating the anisotropy of this magnetically ordered system. At 17 K [Fig. 10(b)], the AFM phase is not present, consistent with the conclusions from the above susceptibility measurements. At 20 K [Fig. 10(c)], the signal is clearly sinusoidal, consistent with FM behavior. In order to induce a canting of a planar antiferromagnetically ordered subsystem, the in-plane component of the magnetic field $H_\perp$ must overcome the in-plane magnetization $\mathcal{M}_\perp$ in one of the two magnetic sublattices

$$H_\perp \geqslant A \cdot \mathcal{M}_\perp = A \cdot \sqrt{\mathcal{M}^2 - \mathcal{M}_\parallel^2}. \tag{4}$$

Here, $\mathcal{M}$ is the saturation magnetization of the magnetic sublattice, $\mathcal{M}_\parallel$ its out-of-plane component, and A is a constant. Taking into account

$$\begin{aligned} H_\perp &= H \sin(\theta), \\ \mathcal{M}_\parallel &= \tfrac{1}{2}\chi_\parallel H \cos(\theta), \end{aligned} \tag{5}$$

where $\chi_\parallel$ is the susceptibility of the total Eu^{2+} magnetic sublattice, we obtain for the boundary condition

$$H^2 \sin^2(\theta) = A^2\left(\mathcal{M}^2 - \tfrac{1}{4}\chi_\parallel^2 H^2 \cos^2(\theta)\right). \tag{6}$$

Solving this equality for H yields the angle-dependent canting field

$$H_{\mathrm{cant}}(\theta) = \frac{A \cdot \mathcal{M}}{\sqrt{\sin^2(\theta) + \frac{1}{4}\chi_\parallel^2 A^2 \cos^2(\theta)}}. \tag{7}$$

Interestingly, the resulting $H_{\mathrm{cant}}(\theta)$ is analog to the expression for the angular dependence of the upper critical field $H_{c2}(\theta)$ in a type-II superconductor.[44] Hence, Eq. (7) can be simplified according to

$$H_{\mathrm{cant}}(\theta) = \frac{H_{\mathrm{cant},\perp}}{\sqrt{\sin^2(\theta) + \gamma_{\mathrm{cant}}^{-2} \cos^2(\theta)}}, \tag{8}$$

where $H_{\mathrm{cant},\perp} = H_{\mathrm{cant}}(90^\circ)$ is the in-plane canting field, $\gamma_{\mathrm{cant}} = H_{\mathrm{cant},\parallel}/H_{\mathrm{cant},\perp}$ its anisotropy parameter, and $H_{\mathrm{cant},\parallel} = H_{\mathrm{cant}}(0^\circ)$ the out-of-plane canting field. This shape of the angular dependence of the transition between the AFM and C-AFM phases in the (H, θ) diagram is represented by the dashed line in Fig. 10(a). It describes the experimental torque data rather well, with the parameters $H_{\mathrm{cant},\perp}(13\ \mathrm{K}) \simeq 0.42(2)$ T and $\gamma_{\mathrm{cant}} \simeq 2.0(2)$. This yields an estimate of the canting field parallel to the c axis $H_{\mathrm{cant},\parallel}(13\ \mathrm{K}) \simeq 0.84(6)$ T.

The low-field torque signal of EuFe$_{1.8}$Co$_{0.2}$As$_2$ at 20 K [Fig. 10(f)] shows a shape typical for an anisotropic paramagnet. However, the anisotropy of the system is quite quickly suppressed with increasing magnetic field, which may indicate a transformation of the paramagnetic state to a short-range ordered state at relatively low field. It might be caused by large fluctuations of the magnetic moments in the vicinity of the transition from a disordered PM state to an ordered

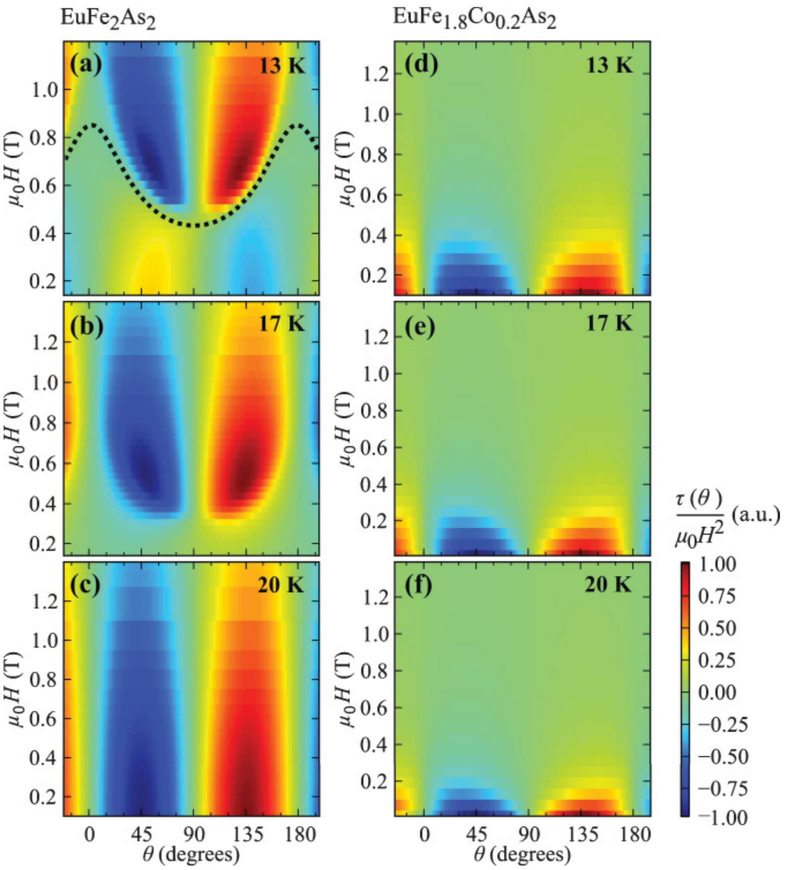

FIG. 10. (Color online) Color map of $\tau/(\mu_0 H^2)$ in arbitrary units (a.u.) for $EuFe_2As_2$ and $EuFe_{1.8}Co_{0.2}As_2$ as a function of angle θ and field H for $T = 13$, 17, and 20 K. The dotted line in (a) is calculated according to Eq. (8). Panels (a), (b), and (c) are the data for $EuFe_2As_2$ at 13, 17, and 20 K, respectively, whereas (d), (e), and (f) are the data for $EuFe_{1.8}Co_{0.2}As_2$ at 13, 17, and 20 K, respectively.

one in $EuFe_{1.8}Co_{0.2}As_2$. Furthermore, at low temperatures, we do not observe any indication of a field-induced transition from the AFM to the C-AFM state [Figs. 10(d) and 10(e)]. Therefore, we conclude that for $EuFe_{1.8}Co_{0.2}As_2$ even at the lowest magnetic field a transition from a PM to a C-AFM state takes place with decreasing temperature, in agreement with the above magnetization data.

IV. DISCUSSION

In Fig. 11, the results of the susceptibility, magnetization, and magnetic torque experiments are summarized. They are discussed in terms of the phase diagram of the Eu^{2+} magnetic sublattice of $EuFe_2As_2$ and $EuFe_{1.8}Co_{0.2}As_2$ for $H \perp c$ and $H \parallel c$.

A. $EuFe_2As_2$

For the parent compound $EuFe_2As_2$, four different magnetic phases were identified [see Figs. 11(a) and 11(b)]: a paramagnetic (PM), an antiferromagnetic (AFM), a canted antiferromagnetic (C-AFM), and a ferromagnetic (FM) phase. The determination of the corresponding transition temperatures and fields is described in Sec. III. The present experiments suggest a C-AFM order of the Eu^{2+} spins in $EuFe_2As_2$ in the temperature range between 17 and 19 K, while below 17 K, an AFM structure is proposed. We suggest that, at low temperatures, the system can be well described with a uniaxial model with easy plane and A-type AFM order. By applying a magnetic field within the AFM phase, a transition from AFM order via a canted configuration to a FM structure is observed. The observed $T_{\mathrm{MM}}(H)$ at which the metamagnetic (MM) transition occurs [open symbols in Fig. 11(a)] is in agreement with the results obtained from the susceptibility for the AFM to C-AFM transition [black filled symbols in Fig. 11(a)]. Thus, we propose that the MM transition corresponds to a spin-flop transition from an AFM to a C-AFM state in $EuFe_2As_2$. The critical magnetic field $H_{\mathrm{cr}}(T)$ at which the magnetic moment in the Eu sublattice saturates was determined at different temperatures. The values of H_{cr} extrapolated to zero temperature were found to be $\mu_0 H_{\mathrm{cr},\perp}(0) \simeq 0.85$ T and $\mu_0 H_{\mathrm{cr},\parallel}(0) \simeq 1.5$ T for $H \perp c$ and $H \parallel c$, respectively. By analyzing the shape of the angular dependence of $H_{\mathrm{cr}}(\theta)$ shown in Fig. 10(a), we may conclude that the in-plane component of the magnetic field is responsible for the canting of the spins.

The magnetic ordering of the Eu^{2+} moments at low temperatures is consistent with the magnetic structure established by neutron diffraction at 2.5 K.[5] Note that, in previous reports,[20,21] a possible C-AFM state in the temperature range $17\ \mathrm{K} \leqslant T \leqslant 19$ K was not discussed. To our knowledge, no neutron data for the magnetic configuration of the Eu sublattice in this temperature range are available.

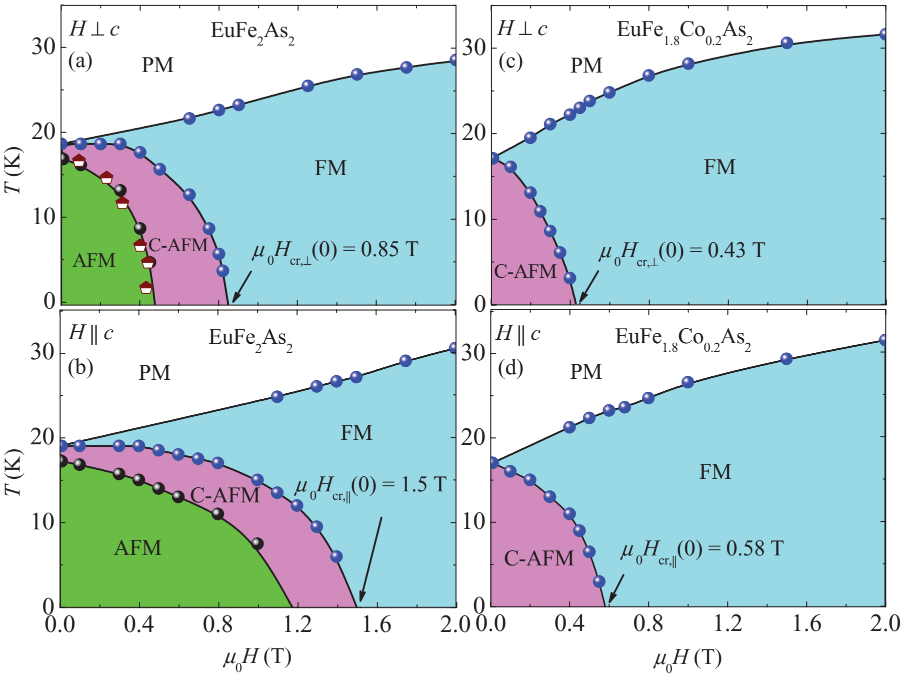

FIG. 11. (Color online) Magnetic phase diagrams of single-crystal $EuFe_2As_2$ [(a) and (b)] and single-crystal $EuFe_{1.8}Co_{0.2}As_2$ [(c)and (d)] for $H \perp c$ and for $H \parallel c$. The various phases in the phase diagrams are denoted as follows: paramagnetic (PM), antiferromagnetic (AFM), canted antiferromagnetic (C-AFM), and ferromagnetic (FM). The filled and open symbols are from the susceptibility and field-dependent magnetization measurements, respectively. The solid lines are guides to the eyes.

B. $EuFe_{1.8}Co_{0.2}As_2$

The corresponding magnetic phase diagrams for Co-doped $EuFe_{1.8}Co_{0.2}As_2$ are shown in Figs. 11(c) and 11(d). The magnetic ordering temperature of $\simeq$17 K is only about 2 K lower as compared to the parent compound. However, in the Co-doped $EuFe_{1.8}Co_{0.2}As_2$, no signatures of a low-field and low-temperature AFM state of the Eu^{2+} moments were found. Only a C-AFM phase (with a FM component in the *ab* plane) is present at low fields and low temperatures. The ordering temperature $T_{\text{C-AFM}}$ decreases with increasing magnetic field, similar to the parent compound [see Figs. 11(a) and 11(b)]. The critical magnetic field H_{cr} at which the Eu magnetic ordering is saturated was determined for different temperatures, and the extrapolated zero-temperature values were found to be $\mu_0 H_{\text{cr},\perp}(0) \simeq 0.43$ T and $\mu_0 H_{\text{cr},\parallel}(0) \simeq 0.58$ T for $H \perp c$ and $H \parallel c$, respectively. These values of $\mu_0 H_{\text{cr}}$ are much smaller than those obtained for the parent compound. Moreover, the magnetic anisotropy $\gamma_{\text{cr}} = H_{\text{cr},\parallel}(0)/H_{\text{cr},\perp}(0) \simeq 1.35$ of Co-doped $EuFe_{1.8}Co_{0.2}As_2$ is also smaller than $\gamma_{\text{cr}} \simeq 1.76$ of the parent compound.

It was concluded from different experiments[21,27,29–31] that there is a strong coupling between the localized Eu^{2+} spins and the conduction electrons of the two-dimensional (2D) Fe_2As_2 layers. Recently, direct experimental evidence for a strong interlayer coupling was obtained by means of ^{75}As NMR,[31] revealing a magnetic exchange interaction between the localized Eu $4f$ moments, which is mediated by the itinerant Fe $3d$ electrons. However, the direct interaction of the Eu moments and the magnetic moments in Fe sublattice can not be neglected. Only a combination of both interactions can further elucidate the C-AFM ground state observed in the parent compound $EuFe_2As_2$ as well as in the Co-doped system $EuFe_{1.8}Co_{0.2}As_2$ (see Fig. 11).

Note that the present results for $EuFe_{1.8}Co_{0.2}As_2$, exhibiting a SDW ground state below 60 K,[30] reveal a C-AFM structure of the Eu spins with a FM component in the *ab* plane. This finding confirms previous assumptions that, for materials in which the Fe ions are in the SDW ground state (such as $EuFe_2As_2$), the direction of the Eu magnetic moments is in the *ab* plane.[5,32] On the other hand, in the case of nonmagnetic Fe ground states, like in superconducting $EuFe_{2-x}Co_xAs_2$ compounds, where the SDW magnetic state is totally suppressed, the direction of the Eu magnetic moments is parallel to the *c* axis.[33–36]

V. CONCLUSIONS

The magnetic properties of single crystals of $EuFe_2As_2$ and $EuFe_{1.8}Co_{0.2}As_2$ were studied by means of susceptibility, magnetization, and magnetic torque investigations. The susceptibility and magnetization experiments performed for various temperatures and magnetic fields along the crystallographic axes provided information on the magnetic structure of the studied crystals. In addition, the evolution of the magnetic structure as a function of the tilting angle of the field and the crystallographic axes is studied by magnetic torque experiments. The phase diagrams for the ordering of the Eu^{2+} magnetic sublattice with respect to temperature, magnetic field, and the angle between the magnetic field and the crystallographic c axis in $EuFe_{2-x}Co_xAs_2$ are determined and discussed. The present investigations reveal a complex and sophisticated interplay of magnetic phases in $EuFe_{2-x}Co_xAs_2$. The magnetic ordering temperature of the Eu^{2+} moments remains nearly unchanged upon Co doping. However, unlike the parent compound, in which the Eu^{2+} moments order antiferromagnetically at low temperatures, the Co-doped system $EuFe_{1.8}Co_{0.2}As_2$ exhibits a C-AFM state with a FM component in the ab plane. The magnetic anisotropy γ_{cr} becomes smaller as a result of Co doping. This implies that the magnetic configuration of the Eu moments is strongly influenced by the magnetic moments of the Fe sublattice, where superconductivity takes place for a certain range of Co doping. A detailed knowledge of the interplay between the Eu^{2+} moments and magnetism of the Fe sublattice is important to understand the role of magnetism of the localized Eu^{2+} moments for the occurrence of superconductivity in $EuFe_{2-x}Co_xAs_2$.

ACKNOWLEDGMENT

This work was supported by the Swiss National Science Foundation, the SCOPES Grant No. IZ73Z0_128242, the NCCR Project MaNEP, the EU Project CoMePhS, and the Georgian National Science Foundation Grant No. GNSF/ST08/4-416.

---

[*] zurabgug@physik.uzh.ch

[†] Current address: Institute of Low Temperature and Structure Research, Polish Academy of Sciences, 50-422 Wroclaw, Poland.

[1] Y. Kamihara, T. Watanabe, M. Hirano, and H. Hosono, J. Am. Chem. Soc. **130**, 3296 (2008).

[2] X. H. Chen, T. Wu, G. Wu, R. H. Liu, H. Chen, and D. F. Fang, Nature (London) **453**, 761 (2008).

[3] M. Rotter, M. Tegel, and D. Johrendt, Phys. Rev. Lett. **101**, 107006 (2008).

[4] F.-C. Hsu, J.-Y. Luo, K.-W. Yeh, T.-K. Chen, T.-W. Huang, P. M. Wu, Y.-C. Lee, Y.-L. Huang, Y.-Y. Chu, D.-C. Yan, and M.-K. Wu, Proc. Natl. Acad. Sci. USA **105**, 14262 (2008).

[5] Y. Xiao, Y. Su, M. Meven, R. Mittal, C. M. N. Kumar, T. Chatterji, S. Price, J. Persson, N. Kumar, S. K. Dhar, A. Thamizhavel, and Th. Brueckel, Phys. Rev. B **80**, 174424 (2009).

[6] M. S. Torikachvili, S. L. Bud'ko, N. Ni, and P. C. Canfield, Phys. Rev. Lett. **101**, 057006 (2008).

[7] Liling Sun, Jing Guo, Genfu Chen, Xianhui Chen, Xiaoli Dong, Wei Lu, Chao Zhang, Zheng Jiang, Yang Zou, Suo Zhang, Yuying Huang, Qi Wu, Xi Dai, Yuanchun Li, Jing Liu, and Zhongxian Zhao, Phys. Rev. B **82**, 134509 (2010).

[8] H. Lee, E. Park, T. Park, V. A. Sidorov, F. Ronning, E. D. Bauer, and J. D. Thompson, Phys. Rev. B **80**, 024519 (2009).

[9] P. L. Alireza, Y. T. C. Ko, J. Gillett, C. M. Petrone, J. M. Cole, G. G. Lonzarich, and S. E. Sebastian, J. Phys. Condens. Matter **21**, 012208 (2009).

[10] K. Igawa, H. Okada, H. Takahashi, S. Matsuishi, Y. Kamihara, M. Hirano, H. Hosono, K. Matsubayashi, and Y. Uwatoko, J. Phys. Soc. Jpn. **78**, 025001 (2009).

[11] H. Fukazawa, N. Takeshita, T. Yamazaki, K. Kondo, K. Hirayama, Y. Kohori, K. Miyazawa, H. Kito, H. Eisaki, and A. Iyo, J. Phys. Soc. Jpn. **77**, 105004 (2008).

[12] W. J. Duncan, O. P. Welzel, C. Harrison, X. F. Wang, X. H. Chen, F. M. Grosche, and P. G. Niklowitz, J. Phys. Condens. Matter **22**, 052201 (2010).

[13] A. Mani, N. Ghosh, S. Paulraj, A. Bharathi, and C. S. Sundar, Europhys. Lett. **87**, 17004 (2009).

[14] T. Terashima, M. Kimata, H. Satsukawa, A. Harada, K. Hazama, S. Uji, H. S. Suzuki, T. Matsumoto, and K. Murata, J. Phys. Soc. Jpn. **78**, 083701 (2009).

[15] C. F. Miclea, M. Nicklas, H. S. Jeevan, D. Kasinathan, Z. Hossain, H. Rosner, P. Gegenwart, C. Geibel, and F. Steglich, Phys. Rev. B **79**, 212509 (2009).

[16] Z. A. Ren, W. Lu, J. Yang, W. Yi, X. L. Shen, Z. C. Li, G. C. Che, X. L. Dong, L. L. Sun, F. Zhou, and Z. X. Zhao, Chin. Phys. Lett. **25**, 2215 (2008).

[17] S. Matsuishi, Y. Inoue, T. Nomura, M. Hirano, and H. Hosono, J. Phys. Soc. Jpn. **77**, 113709 (2008).

[18] J. Zhao, Q. Huang, C. de la Cruz, S. Li, J. W. Lynn, Y. Chen, M. A. Green, G. F. Chen, G. Li, Z. Li, J. L. Luo, N. L. Wang, and P. Dai, Nat. Mater. **7**, 953 (2008).

[19] H. Raffius, E. Mörsen, B. D. Mosel, W. Müller-Warmuth, W. Jeitschko, L. Terbüchte, and T. Vomhof, J. Phys. Chem. Solids **54**, 135 (1993).

[20] Z. Ren, Z. W. Zhu, S. Jiang, X. F. Xu, Q. Tao, C. Wang, C. M. Feng, G. H. Cao, and Z. A. Xu, Phys. Rev. B **78**, 052501 (2008).

[21] S. Jiang, Y. K. Luo, Z. Ren, Z. W. Zhu, C. Wang, X. F. Xu, Q. Tao, G. H. Cao, and Z. A. Xu, New J. Phys. **11**, 025007 (2009).

[22] S. Blundell, *Magnetism in Condensed Matter* (Oxford University Press, New York, 2006).

[23] Y. Xiao, Y. Su, W. Schmidt, K. Schmalzl, C. M. N. Kumar, S. Price, T. Chatterji, R. Mittal, L. J. Chang, S. Nandi, N. Kumar, S. K. Dhar, A. Thamizhavel, and Th. Brueckel, Phys. Rev. B **81**, 220406 (2010).

[24] Shuai Jiang, Hui Xing, Guofang Xuan, Zhi Ren, Cao Wang, Zhu-an Xu, and Guanghan Cao, Phys. Rev. B **80**, 184514 (2009).

[25] Y. He, T. Wu, G. Wu, Q. J. Zheng, Y. Z. Liu, H. Chen, J. J. Ying, R. H. Liu, X. F. Wang, Y. L. Xie, Y. J. Yan, J. K. Dong, S. Y. Li, and X. H. Chen, J. Phys. Condens. Matter **22**, 235701 (2010).

[26] H. S. Jeevan, Deepa Kasinathan, H. Rosner, and P. Gegenwart, Phys. Rev. B **83**, 054511 (2011).

[27] Zhi Ren, Xiao Lin, Qian Tao, Shuai Jiang, Zengwei Zhu, Cao Wang, Guanghan Cao, and Zhu'an Xu, Phys. Rev. B **79**, 094426 (2009).

[28] L. J. Li, Y. K. Luo, Q. B. Wang, H. Chen, Z. Ren, Q. Tao, Y. K. Li, X. Lin, M. He, Z. W. Zhu, G. H. Cao, and Z. A. Xu, New J. Phys. **11**, 025008 (2009).

[29] E. Dengler, J. Deisenhofer, H. A. Krug von Nidda, Seunghyun Khim, J. S. Kim, Kee Hoon Kim, F. Casper, C. Felser, and A. Loidl, Phys. Rev. B **81**, 024406 (2010).

[30] J. J. Ying, T. Wu, Q. J. Zheng, Y. He, G. Wu, Q. J. Li, Y. J. Yan, Y. L. Xie, R. H. Liu, X. F. Wang, and X. H. Chen, Phys. Rev. B **81**, 052503 (2010).

[31] Z. Guguchia, J. Roos, A. Shengelaya, S. Katrych, Z. Bukowski, S. Weyeneth, F. Murányi, S. Strässle, A. Maisuradze, J. Karpinski, and H. Keller, Phys. Rev. B **83**, 144516 (2011).

[32] I. Nowik and I. Felner, Hyperfine Interact. **28**, 959 (1986).

[33] I. Nowik and I. Felner, Physica C **469**, 485 (2009).

[34] C. Feng, Z. Ren, S. Xu, S. Jiang, Z. Xu, G. Cao, I. Nowik, I. Felner, K. Matsubayashi, and Y. Uwatoko, Phys. Rev. B **82**, 094426 (2010).
[35] I. Nowik, I. Felner, Z. Ren, G. H. Cao, and Z. A. Xu, J. Phys. Condens. Matter **23**, 065701 (2011).
[36] I. Nowik, I. Felner, Z. Ren, G. H. Cao, and Z. A. Xu, New J. Phys. **13**, 023033 (2011).
[37] S. Kohout, J. Roos, and H. Keller, Rev. Sci. Instrum. **78**, 013903 (2007).
[38] J. L. Luo, N. L. Wang, G. T. Liu, D. Wu, X. N. Jing, F. Hu, and T. Xiang, Phys. Rev. Lett. **93**, 187203 (2004).
[39] R. S. Perry, L. M. Galvin, S. A. Grigera, L. Capogna, A. J. Schofield, A. P. Mackenzie, M. Chiao, S. R. Julian, S. I. Ikeda, S. Nakatsuji, Y. Maeno, and C. Pfleiderer, Phys. Rev. Lett. **86**, 2661 (2001).
[40] T. Kimura and Y. Tokura, Ann. Rev. Mater. Sci. **30**, 451 (2000).
[41] S. Weyeneth, P. J. W. Moll, R. Puzniak, K. Ninios, F. F. Balakirev, R. D. McDonald, H. B. Chan, N. D. Zhigadlo, S. Katrych, Z. Bukowski, J. Karpinski, H. Keller, B. Batlogg, and L. Balicas, Phys. Rev. B **83**, 134503 (2011)
[42] H. Tanaka, T. Kato, K. Iio, and K. Nagata, J. Phys. Soc. Jpn. **61**, 3292 (1992).
[43] T. Sasaki, H. Uozaki, S. Endo, and N. Toyota, Synth. Metals **120**, 759 (2001).
[44] G. Blatter, M. V. Feigel'man, V. B. Geshkenbein, A. I. Larkin, and V. M. Vinokur, Rev. Mod. Phys. **66**, 1125 (1994).

General conclusion

This thesis reports torque magnetometry investigations of novel high-temperature superconductors and related magnetic materials. The torque technique gives access to the superconductor diamagnetic moment, which in turn yields the anisotropy and the magnetic penetration depth. It also measures any anisotropic magnetic signal coming from an impurity phase, a coexisting order, or a self-standing magnetic order.

In the temperature range $0.87\,T_{\mathrm{c}}$ to T_{c}, the in-plane anisotropy of the cuprate high-temperature superconductor $\mathrm{YBa_2Cu_3O_{7-\delta}}$ is constant, but the out-of-plane anisotropy increases by more than 10% with decreasing temperature. No field dependence was observed. These results are independent of the model (London or Hao-Clem) used for the analysis. The temperature dependence of the anisotropy indicates the presence of two energy scales in the superconducting behavior, which can come from multigap superconductivity or one-gap superconductivity with a pseudogap.

The lock-in transition observed in $\mathrm{YBa_2Cu_3O_{7-\delta}}$ at the 2D to 3D crossover qualitatively follows the theoretical prediction. A quantitative agreement over the full angular range is difficult to prove; even though analytic formulas can be derived for the torque in different angular domains, the necessary approximations make the mathematical connections between those domains problematic. As expected for a behavior originating from vortex pinning, the lock-in is weaker at high temperatures. Surprisingly, the lock-in angular domain also seems to increase with the magnetic field. This surprising behavior might come from the low anisotropy of the compound, which prevents it from having a conventional two dimensional behavior, even at low temperatures.

The anisotropy of the iron-based high-temperature superconductor $\mathrm{Rb}_x\mathrm{Fe}_{2-y}\mathrm{Se}_2$ strongly depends on the magnetic field between 0 T and 1.4 T, and is temperature independent in the range $[T_{\mathrm{c}}/2,\, T_{\mathrm{c}}]$. This is quite different from what happens in other iron-based superconductors, consistent with the singular coexistence of magnetic order and superconductivity in this system. The effective magnetic penetration depth, which takes into account the increase in penetration due to the massive presence of non-superconducting regions distributed in the sample, is around 1.8 μm at 0 K. Additionally, annealing $\mathrm{Rb}_x\mathrm{Fe}_{2-y}\mathrm{Se}_2$ just at the phase separation temperature drastically improves the superconducting properties, whereas annealing far from this temperature has only small or detrimental effects. The influence of the thermal treatment may be related to the spatial distribution of the superconducting and magnetic phases.

The phase diagram for the Eu^{+} sublattice magnetic state in $\mathrm{EuFe_2As_2}$ obtained by SQUID measurements was confirmed by torque. Cobalt doping on the Fe site is known to have an effect on superconductivity. In this study, it is also shown to have an effect on the magnetic ordering of the Eu moments. The antiferromagnetic state at low temperatures and low fields in $\mathrm{EuFe_2As_2}$ disappears with Co doping. This shows the strong interplay between the FeAs layer, where superconductivity takes place, and the strongly magnetic Eu layer.

In order to explore superconductors in a wider temperature and field range, we developed a new torque magnetometer compatible with a commercial cryostat equipped with a high field superconducting magnet. Fields up to 9 T and temperatures down to 2 K can be reached with the new setup. Considering the sophisticated interplay between magnetism and superconductivity, high-quality torque measurements in new parts of the superconducting phase diagram will certainly help the general investigation of superconductivity. In the direct continuity of this work, it would be interesting to test how large the lock-in domain of $\mathrm{YBa_2Cu_3O_{7-\delta}}$ and the anisotropy of $\mathrm{Rb}_x\mathrm{Fe}_{2-y}\mathrm{Se}_2$ can grow under higher magnetic fields. It is unlikely that these parameters' growth is unlimited; their eventual saturation or decrease should correspond to a remarkable point in the phase diagram. Since the record critical temperature is realized in a high anisotropy material, the emergence and disappearance of highly anisotropic behaviors in moderately anisotropic materials is sure to be relevant to the understanding of superconductivity.

Appendix A

Hardware details

- Stepper motor
  Danaher CTP12ELF10MMA00 NEMA 17 dual shaft motor
  Configured for 400 steps/revolution
- Stepper drive
  Danaher P70530, 20-75 VDC, 5A DC current, 1 axis
  Manual switches OFF, P70000 tools configuration: enabled microstepping, dynamic smoothing, current reduction, stall detection OFF
  Power source 20 V DC, holding current 0.18 A, operating current 0.22 A
- Stepper controller
  National Instruments Motion controller PCI-7332 Low Cost 2-axis stepper only controller
- Interface between motion controller and stepper drive
  National Instruments Universal Motion Interface UMI-7764 (20 Mhz encoders) 4-axis
  One analog input used for potentiometer feedback
- Controller to UMI connection
  SH68-C68-S 68 pin VHDCI to 68 pin .050 series D-type cable
- UMI to drive connection
  D-Subs to leads cable
- Optionnal drive programming connection for use with the P7000 tools software Serial programming cable (RS 232)

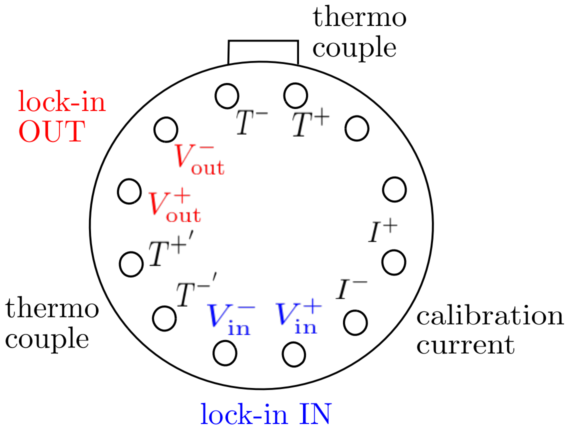

Figure A.1: Connection map of the bottom puck of the inset [item (g) in Fig 2.8]. These connections go trough the PPMS user bridge output.

Appendix B

Magnetic background calculation

This appendix details the calculation of the magnetic torque signal when the magnetization is anisotropic and linear in field. This is used for example when taking into account the magnetic background of a superconducting sample. For simplicity, we assume in the following that the material is uniaxial. The signs of the vectors projections along the principal axes a and c correspond to the configuration represented in Fig. B.1.

$$\begin{aligned}\frac{\vec{\tau}}{\mu_0 V} &= \vec{M} \times \vec{H} \\ &= \vec{M}_c \times \vec{H} + \vec{M}_a \times \vec{H} \\ \left|\frac{\vec{\tau}}{\mu_0 V}\right| &= M_c H \sin(\theta) + M_a H \sin(-(\frac{\pi}{2} - \theta))\end{aligned}$$

Using $\vec{M} = \chi \vec{H}$, where χ is the susceptibility matrix ($M_i = \chi_i H_i$ for any i in $[a, b, c]$), and projecting $\vec{H}$ along the axes, we get:

$$\begin{aligned}\frac{\tau}{\mu_0 V} &= \chi_c H_c H \sin(\theta) - \chi_a H_a H \cos(\theta) \\ &= H^2 \sin(\theta)\cos(\theta)(\chi_c - \chi_a)\end{aligned}$$

Finally:

$$\tau = \mu_0 V \frac{H^2}{2}(\chi_c - \chi_a)\sin(2\theta) \tag{B.1}$$

This general dependence of the torque on magnetic susceptibility appears in paramagnetic and antiferromagnetic materials, where M is proportional to H, but not for example in saturated ferromagnets. The configuration used here corresponds to a paramagnet with an easy direction along the c-axis. The sign of the torque can be reversed depending on the relative position of $\vec{M}$ and $\vec{H}$, and depending on which axis coresponds to the easy direction.

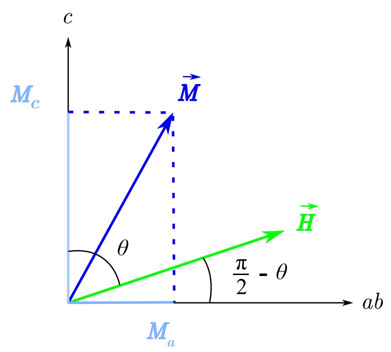

Figure B.1: Schematic representation of the field and magnetization vectors.

Bibliography

[1] H. K. Onnes, *The resistance of pure mercury at helium temperatures*, Commun. Phys. Lab. Univ. Leiden **12**, 120 (1911). (Cited on page 3.)

[2] W. Meissner and R. Ochsenfeld, *Ein neuer Effekt bei Eintritt der Supraleitfähigkeit*, Naturwissenschaften **21**, 787 (1933). (Cited on page 3.)

[3] F. London and H. London, *The Electromagnetic Equations of the Supraconductor*, Proc. R. Soc. A **149**, 71 (1935). (Cited on pages 3 and 7.)

[4] J. Bardeen, L. N. Cooper, and J. R. Schrieffer, *Theory of Superconductivity*, Phys. Rev. **108**, 1175 (1957). (Cited on page 3.)

[5] C. A. Reynolds, B. Serin, W. H. Wright, and L. B. Nesbitt, *Superconductivity of Isotopes of Mercury*, Phys. Rev. **78**, 487 (1950). (Cited on page 3.)

[6] E. Maxwell, *Isotope Effect in the Superconductivity of Mercury*, Phys. Rev. **78**, 477 (1950). (Cited on page 3.)

[7] J. G. Bednorz and K. A. Müller, *Possible high-T_c superconductivity in the Ba-La-Cu-O system*, Z. Phys. B **64**, 189 (1986). (Cited on page 3.)

[8] A. Schilling, M. Cantoni, J. Guo, and H. Ott, *Superconductivity above 130 K in the Hg-Ba-Ca-Cu-O system*, Nature **363**, 56 (1993). (Cited on page 3.)

[9] Y. Kamihara, H. Hiramatsu, M. Hirano, R. Kawamura, H. Yanagi, T. Kamiya, and H. Hosono, *Iron-Based Layered Superconductor: LaOFeP*, J. Am. Chem. Soc. **128**, 10012 (2006). (Cited on page 3.)

[10] G. F. Hardy and J. K. Hulm, *Superconducting Silicides and Germanides*, Phys. Rev. **89**, 884 (1953). (Cited on page 3.)

[11] G.-I. Oya and E. J. Saur, *Preparation of Nb_3Ge films by chemical transport reaction and their critical properties*, J. Low Temp. Phys. **34**, 569 (1979). (Cited on page 3.)

[12] F. Steglich, J. Aarts, C. D. Bredl, W. Lieke, D. Meschede, W. Franz, and H. Schäfer, *Superconductivity in the Presence of Strong Pauli Paramagnetism: $CeCu_2Si_2$*, Phys. Rev. Lett. **43**, 1892 (1979). (Cited on page 3.)

[13] C. Petrovic, P. G. Pagliuso, M. F. Hundley, R. Movshovich, J. L. Sarrao, J. D. Thompson, Z. Fisk, and P. Monthoux, *Heavy-fermion superconductivity in $CeCoIn_5$ at 2.3 K*, J. Phys.: Cond. Mat. **13**, L337 (2001). (Cited on page 3.)

[14] K. Bechgaard, K. Carneiro, M. Olsen, F. B. Rasmussen, and C. S. Jacobsen, *Zero-Pressure Organic Superconductor: Di-(Tetramethyltetraselenafulvalenium)-Perchlorate ($TMTSF_2ClO_4$)*, Phys. Rev. Lett. **46**, 852 (1981). (Cited on page 3.)

[15] A. Hebard, M. Rosseinsky, R. Haddon, D. Murphy, S. Glarum, T. Palstra, A. Ramirez, and A. Kortan, *Superconductivity at 18 K in potassium-doped C-60*, Nature **350**, 600 (1991). (Cited on page 3.)

[16] K. Tanigaki, T. W. Ebbesen, S. Saito, J. Mizuki, J. S. Tsai, Y. Kubo, and S. Kuroshima, *Superconductivity at 33 K in* $Cs_xRb_yC_{60}$, Nature **352**, 222 (1991). (Cited on page 3.)

[17] J. Nagamatsu, N. Nakagawa, T. Muranaka, Y. Zenitani, and J. Akimitsu, *Superconductivity at 39 K in magnesium diboride*, Nature **410**, 63 (2001). (Cited on page 3.)

[18] Z. K. Tang, L. Zhang, N. Wang, X. X. Zhang, G. H. Wen, G. D. Li, J. N. Wang, C. T. Chan, and P. Sheng, *Superconductivity in 4 Angstrom Single-Walled Carbon Nanotubes*, Science **292**, 2462 (2001). (Cited on page 3.)

[19] V. L. Ginzburg and L. D. Landau, *To the Theory of Superconductivity*, Zh. Eksp. Teor. Fiz. **20**, 1064 (1950). (Cited on pages 3, 5 and 27.)

[20] L. P. Gor'kov, *Microscopic derivation of the Ginzburg-Landau equations in the theory of superconductivity*, Sov. Phys. JETP **9**, 1364 (1959). (Cited on page 3.)

[21] L. Landau, *Theory of phase transformations I*, Zh. Eksp. Teor. Fiz. **7**, 19 (1937). (Cited on page 5.)

[22] M. Tinkham, *Introduction to superconductivity*, McGraw-Hill, 1996. (Cited on pages 6 and 27.)

[23] V. G. Kogan, *On neutron diffraction from vortices in uniaxial superconductors*, Physics Letters A **85**, 298 (1981). (Cited on page 7.)

[24] L. J. Campbell, M. M. Doria, and V. G. Kogan, *Vortex lattice structures in uniaxial superconductors*, Phys. Rev. B **38**, 2439 (1988). (Cited on page 7.)

[25] V. G. Kogan, *Free Energy and Torque for Superconductors with Different Anisotropies of* H_{c2} *and* λ, Phys. Rev. Lett. **89**, 237005 (2002). (Cited on pages 7 and 32.)

[26] D. E. Farrell, J. P. Rice, D. M. Ginsberg, and J. Z. Liu, *Experimental Evidence of a Dimensional Crossover in* $Y_1Ba_2Cu_3O_{7-\delta}$, Phys. Rev. Lett. **64**, 1573 (1990). (Cited on pages 7, 27 and 34.)

[27] M. Willemin, C. Rossel, J. Hofer, H. Keller, and A. Revcolevschi, *Test Anisotropy scaling close to the ab plane in* $La_{1.9}Sr_{0.1}CuO_4$ *by torque magnetometry*, Phys. Rev. B **59**, R717 (1999). (Cited on pages 7 and 12.)

[28] T. Nojima, H. Nagano, A. Ochiai, H. Aoki, B. Kang, and S.-I. Lee, *Anomalous field dependence of anisotropy observed in* MgB_2 *single crystals with a torque method*, Physica C **445-448**, 42 (2006). (Cited on page 7.)

[29] K. Tokiwa, T. Koganezawa, S. Mikusu, T. Watanabe, A. Iyo, and Y. Tanaka, *Anisotropy of multilayered* $(Cu,C)Ba_2Ca_3Cu_4O_y$ *superconductors studied by torque magnetometry*, Int. J. Mod. Phys. B **21**, 3285 (2007). (Cited on page 7.)

[30] D. Kubota, K. Nanba, T. Wolf, C. Meingast, and T. Ishida, *Magnetic torque analysis including vortex core contributions for* $Ba(Fe,Co)_2As_2$ *single crystal*, Physica C **471**, 781 (2011). (Cited on page 7.)

[31] T. Hu, H. Xiao, P. Gyawali, H. H. Wen, and C. C. Almasan, *Superconductivity in the pseudogap region of* $Bi_2Sr_{1.4}La_{0.6}CuO_{6+\delta}$ *from angular-dependent torque measurements*, Phys. Rev. B **85**, 134516 (2012). (Cited on page 7.)

[32] R. C. Jaklevic, J. Lambe, A. H. Silver, and J. E. Mercereau, *Quantum Interference Effects in Josephson Tunneling*, Phys. Rev. Lett. **12**, 159 (1964). (Cited on page 9.)

[33] S. Kohout, J. Roos, and H. Keller, *Novel sensor design for torque magnetometry*, Rev. Sci. Instrum. **78**, 013903 (2007). (Cited on page 10.)

[34] E. H. Brandt and G. P. Mikitik, *Why an ac Magnetic Field Shifts the Irreversibility Line in Type-II Superconductors*, Phys. Rev. Lett. **89**, 027002 (2002). (Cited on page 12.)

[35] M. Willemin, C. Rossel, J. Hofer, H. Keller, A. Erb, and E. Walker, *Strong shift of the irreversibility line in high-*T_c *superconductors upon vortex shaking with an oscillating magnetic field*, Phys. Rev. B **58**, R5940 (1998). (Cited on page 12.)

[36] M. Angst, R. Puzniak, A. Wisniewski, J. Jun, S. M. Kazakov, J. Karpinski, J. Roos, and H. Keller, *Temperature and Field Dependence of the Anisotropy of* MgB_2, Phys. Rev. Lett. **88**, 167004 (2002). (Cited on pages 12, 32 and 54.)

[37] M. Angst, *Studies of magnetic properties of novel supercondctors by means of SQUID and torque magnetometry*, PhD thesis, ETHZ, 2003. (Cited on pages 12 and 35.)

[38] N. R. Werthamer, E. Helfand, and P. C. Hohenberg, *Temperature and Purity Dependence of the Superconducting Critical Field,* Hc_2*. III. Electron Spin and Spin-Orbit Effects*, Phys. Rev. **147**, 295 (1966). (Cited on page 12.)

[39] S. Weyeneth, R. Puzniak, N. Zhigadlo, S. Katrych, Z. Bukowski, J. Karpinski, and H. Keller, *Evidence for Two Distinct Anisotropies in the Oxypnictide Superconductors* $SmFeAsO_{0.8}F_{0.2}$ *and* $NdFeAsO_{0.8}F_{0.2}$, J. Supercond. Nov. Magn. **22**, 347 (2009). (Cited on pages 12, 32 and 54.)

[40] *Quantum Design torque patent # 5798641*, 1998. (Cited on page 13.)

[41] M. Lutz, *Programming Python, 4th Edition*, O'Reilly Media, 2010. (Cited on page 14.)

[42] Comsol, *Introduction to COMSOL multiphysics*, Comsol AB, 2010. (Cited on page 14.)

[43] M. Shiralkar, *LabVIEW Graphical Programming Course*, Rice University, Houston, Texas, 2007. (Cited on page 19.)

[44] M. K. Wu, J. R. Ashburn, C. J. Torng, P. H. Hor, R. L. Meng, L. Gao, Z. J. Huang, Y. Q. Wang, and C. W. Chu, *Superconductivity at 93 K in a new mixed-phase Y-Ba-Cu-O compound system at ambient pressure*, Phys. Rev. Lett. **58**, 908 (1987). (Cited on page 27.)

[45] A. Erb et al., *Experimental evidence for fast cluster formation of chain oxygen vacancies in* $YBa_2Cu_3O_{7-\delta}$ *as the origin of the fishtail anomaly*, Solid State Commun. **112**, 245 (1999). (Cited on page 27.)

[46] Z. Hao and J. R. Clem, *Reversible magnetization and torques in anisotropic high-*κ *type-II superconductors*, Phys. Rev. B **43**, 7622 (1991). (Cited on pages 27 and 28.)

[47] Z. Hao, J. R. Clem, M. W. McElfresh, L. Civale, A. P. Malozemoff, and F. Holtzberg, *Model for the reversible magnetization of high-*κ *type-II superconductors: Application to high-*T_c *superconductors*, Phys. Rev. B **43**, 2844 (1991). (Cited on pages 27 and 28.)

[48] Z. Hao and J. R. Clem, *Limitations of the London model for the reversible magnetization of type-II superconductors*, Phys. Rev. Lett. **67**, 2371 (1991). (Cited on pages 27 and 28.)

[49] W. K. Kwok, U. Welp, V. M. Vinokur, S. Fleshler, J. Downey, and G. W. Crabtree, *Direct observation of intrinsic pinning by layered structure in single-crystal* $YBa_2Cu_3O_{7-\delta}$, Phys. Rev. Lett. **67**, 390 (1991). (Cited on pages 27, 33 and 34.)

[50] R. A. Doyle, A. M. Campbell, and R. E. Somekh, *Direct observation of intrinsic pinning in YBCO thin films*, Phys. Rev. Lett. **71**, 4241 (1993). (Cited on pages 27 and 34.)

[51] S. N. Gordeev, A. A. Zhukov, P. A. J. de Groot, A. G. M. Jansen, R. Gagnon, and L. Taillefer, *Oscillatory Melting Temperature of the Vortex Smectic Phase in Layered Superconductors*, Phys. Rev. Lett. **85**, 4594 (2000). (Cited on pages 27 and 34.)

[52] A. Kortyka, R. Puzniak, A. Wisniewski, M. Zehetmayer, H. W. Weber, Y. Q. Cai, and X. Yao, *Anisotropy of the superconducting state parameters and intrinsic pinning in low-level Pr-doped YBaCuO single crystals*, Supercond. Sci. Tech. **23**, 065001 (2010). (Cited on pages 27, 32, 34 and 35.)

[53] D. Feinberg and C. Villard, *Intrinsic pinning and lock-in transition of flux lines in layered type-II superconductors*, Phys. Rev. Lett. **65**, 919 (1990). (Cited on pages 27, 33 and 35.)

[54] M. Zehetmayer, *A review of two-band superconductivity: materials and effects on the thermodynamic and reversible mixed-state properties*, Supercond. Sci. and Tech. **26**, 043001 (2013). (Cited on page 29.)

[55] A. Bussmann-Holder, R. Micnas, and A. Bishop, *Enhancements of the superconducting transition temperature within the two-band model*, Eur. Phys. J. B **37**, 345 (2003). (Cited on page 29.)

[56] A. Kortyka, R. Puzniak, A. Wisniewski, M. Zehetmayer, H. W. Weber, C. Y. Tang, X. Yao, and K. Conder, *Evidence for a temperature dependent anisotropy of the superconducting state parameters in underdoped* $SmBa_2Cu_3O_x$, Phys. Rev. B **82**, 054510 (2010). (Cited on pages 29 and 32.)

[57] D. Feinberg and A. M. Ettouhami, *The lock in transition of vortices in layered superconductors*, Int. J. Mod. Phys. B **7**, 2085 (1993). (Cited on pages 30, 33, 34, 35 and 37.)

[58] J. Hofer, T. Schneider, J. M. Singer, M. Willemin, H. Keller, T. Sasagawa, K. Kishio, K. Conder, and J. Karpinski, *Torque magnetometry on single-crystal high-temperature superconductors near the critical temperature: A scaling approach*, Phys. Rev. B **62**, 631 (2000). (Cited on page 30.)

[59] V. G. Kogan, *Uniaxial superconducting particle in intermediate magnetic fields*, Phys. Rev. B **38**, 7049 (1988). (Cited on page 30.)

[60] D. Zech, J. Hofer, H. Keller, C. Rossel, P. Bauer, and J. Karpinski, *Effective mass anisotropy of* $HgBa_2Ca_3Cu_4O_{10}$ *measured on a microcrystal by means of miniaturized torque magnetometry*, Phys. Rev. B **53**, R6026 (1996). (Cited on page 32.)

[61] S. Weyeneth, R. Puzniak, U. Mosele, N. D. Zhigadlo, S. Katrych, Z. Bukowski, J. Karpinski, S. Kohout, J. Roos, and H. Keller, *Anisotropy of Superconducting Single Crystal* $SmFeAsO_{0.8}F_{0.2}$ *Studied by Torque Magnetometry*, J. Supercond. Nov. Magn **22**, 325 (2009). (Cited on pages 32 and 54.)

[62] R. Khasanov, S. Strässle, D. Di Castro, T. Masui, S. Miyasaka, S. Tajima, A. Bussmann-Holder, and H. Keller, *Multiple gap symmetries for the order parameter of cuprate superconductors from penetration depth measurements*, Phys. Rev. Lett. **99**, 237601 (2007). (Cited on page 32.)

[63] W. E. Lawrence and S. Doniach, *Theory of Layer Structure Superconductors,* in *Proceedings of the Twelth International Conference on Low Temperature Physics*, Academic Press of Japan, Kyoto, 1971. (Cited on page 32.)

[64] B. Josephson, *Possible new effects in superconductive tunnelling*, Phys. Lett. **1**, 251 (1962). (Cited on page 33.)

[65] G. Blatter, M. V. Feigel'man, V. B. Geshkenbein, A. I. Larkin, and V. M. Vinokur, *Vortices in high-temperature superconductors*, Rev. Mod. Phys. **66**, 1125 (p. 1286) (1994). (Cited on pages 33 and 34.)

[66] U. Welp, W. K. Kwok, G. W. Crabtree, K. G. Vandervoort, and J. Z. Liu, *Magnetic measurements of the upper critical field of* $YBa_2Cu_3O_{7-\delta}$ *single crystals*, Phys. Rev. Lett. **62**, 1908 (1989). (Cited on page 33.)

[67] S. Bosma, S. Weyeneth, R. Puzniak, A. Erb, A. Schilling, and H. Keller, *Magnetic torque study of the temperature-dependent anisotropy parameter in overdoped superconducting single-crystal* $YBa_2Cu_3O_7$, Phys. Rev. B **84**, 024514 (2011). (Cited on pages 33 and 52.)

[68] D. Feinberg, *Theory of the tilted vortex lattice in Josephson-coupled layered superconductors*, Physica C **194**, 126 (1992). (Cited on page 33.)

[69] F. Steinmeyer, R. Kleiner, P. Müller, H. Müller, and K. Winzer, *Observation of the Flux Line Lock-In Transition in Layered Superconductors*, Europhys. Lett. **25**, 459 (1994). (Cited on page 33.)

[70] B. Janossy, A. de Graaf, P. H. Kes, V. N. Kopylov, and T. G. Togonidze, *Observation of the lock-in transition in* $Tl_2Ba_2Ca_1Cu_2O_x$, Physica C **246**, 277 (1995). (Cited on page 33.)

[71] G. S. Okram, H. Aoki, M. Xu, and D. G. Hinks, *Vortex lock-in transition in* $Tl_2Ba_2CuO_6$ *superconductor and vortex phase diagram*, Physica C **355**, 65 (2001). (Cited on page 33.)

[72] S. Koleśnik, T. Skośkiewicz, J. Igalson, and Z. Tarnawski, *Experimental observation of the lock-in transition in a* $Bi_2Sr_2CaCu_2O_{8+\delta}$ *crystal near the lower critical field*, Phys. Rev. B **54**, 13319 (1996). (Cited on page 34.)

[73] M. Zehetmayer, M. Eisterer, S. Sponar, H. Weber, A. Wisniewski, R. Puzniak, P. Panta, S. Kazakov, and J. Karpinski, *Magnetic properties of superconducting* $HgBa_2CuO_{4+\delta}$ *single crystals in the overdoped state before and after particle irradiation*, Physica C **418**, 73 (2005). (Cited on pages 34 and 35.)

[74] A. Vermeer, D. de Groot, N. Koeman, R. Griessen, and C. van Haesendonck, *Lock-in transition of flux-lines in layered superconductors*, Physica C **185**, 2345 (1991). (Cited on page 34.)

[75] P. A. Mansky, P. M. Chaikin, and R. C. Haddon, *Vortex lock-in state in a layered superconductor*, Phys. Rev. Lett. **70**, 1323 (1993). (Cited on page 34.)

[76] Y. V. Bugoslavsky, A. A. Zhukov, G. K. Perkins, A. D. Caplin, H. Kojima, and I. Tanaka, *Flux-line lock-in to CuO planes in a* $La_{1.9}Sr_{0.1}CuO_4$ *single crystal*, Phys. Rev. B **56**, 5610 (1997). (Cited on page 34.)

[77] S. Khene, *Experimental evidence of the lock-in transition of vortices in* $La_{1.85}Sr_{0.85}CuO_4$ *single crystal by SQUID measurements*, Physica B **349**, 227 (2004). (Cited on page 34.)

[78] S. Kohout, T. Schneider, J. Roos, H. Keller, T. Sasagawa, and H. Takagi, *Vortex states and magnetic anisotropy in single-crystal* $La_{2-x}Sr_xCuO_4$ *studied by torque magnetometry*, Phys. Rev. B **76**, 064513 (2007). (Cited on page 34.)

[79] M. A. Avila, L. Civale, A. V. Silhanek, R. A. Ribeiro, O. F. de Lima, and H. Lanza, *Irreversible magnetization under rotating fields and lock-in effect on a* $ErBa_2Cu_3O_{7-\delta}$ *single crystal with columnar defects*, Phys. Rev. B **64**, 144502 (2001). (Cited on page 34.)

[80] L. N. Bulaevskii, *Anomalous behavior of torque at high angles in high-temperature superconductors*, Phys. Rev. B **44**, 910 (1991). (Cited on pages 34 and 35.)

[81] D. Zech, C. Rossel, L. Lesne, H. Keller, S. L. Lee, and J. Karpinski, *Angle-dependent reversible and irreversible magnetic torque in single-crystalline* $Y_2Ba_4Cu_8O_{16}$, Phys. Rev. B **54**, 12535 (1996). (Cited on pages 34 and 35.)

[82] C. Rossel, P. Bauer, D. Zech, J. Hofer, M. Willemin, and H. Keller, *Active microlevers as miniature torque magnetometers*, J. App. Phys. **79**, 8166 (1996). (Cited on page 35.)

[83] T. Ishida, K. Kitamura, K. Okuda, and H. Asaoka, *Intrinsic Pinning does not Influence the Vortex Melting Transition of* $YBa_2Cu_3O_{6.94}$ *in* $H \perp c$ *Configuration*, J. Phys. Soc. Jpn. **70**, 2110 (2001). (Cited on page 35.)

[84] V. Vulcanescu, G. Collin, H. Kojima, I. Tanaka, and L. Fruchter, *Locked-unlocked transition of the flux-line-lattice configuration for a* $(La_{1-x}Sr_x)_2CuO_4$ $(x = 0.075)$ *single crystal with a small demagnetizing factor*, Phys. Rev. B **50**, 4139 (1994). (Cited on page 35.)

[85] Y. Kamihara, T. Watanabe, M. Hirano, and H. Hosono, *Iron-based layered superconductor* $La[O_{1-x}F_x]FeAs$ $(x = 0.05\text{-}0.12)$ *with* $T_c = 26$ K, J. Am. Chem. Soc. **130**, 3296 (2008). (Cited on page 51.)

[86] J. Guo, S. Jin, G. Wang, S. Wang, K. Zhu, T. Zhou, M. He, and X. Chen, *Superconductivity in the iron selenide* $K_xFe_2Se_2$ $(0 \leq x \leq 1.0)$, Phys. Rev. B **82**, 180520 (2010). (Cited on page 51.)

[87] A. Krzton-Maziopa, Z. Shermadini, E. Pomjakushina, V. Pomjakushin, M. Bendele, A. Amato, R. Khasanov, H. Luetkens, and K. Conder, *Synthesis and crystal growth of* $Cs_{0.8}(FeSe_{0.98})_2$*: a new iron-based superconductor with* $T_c = 27$ K, J. Phys.: Condens. Matt. **23**, 052203 (2011). (Cited on pages 51 and 55.)

[88] C.-H. Li, B. Shen, F. Han, X. Zhu, and H.-H. Wen, *Transport properties and anisotropy of* $Rb_{1-x}Fe_{2-y}Se_2$ *single crystals*, Phys. Rev. B **83**, 184521 (2011). (Cited on page 51.)

[89] Z. Shermadini, A. Krzton-Maziopa, M. Bendele, R. Khasanov, H. Luetkens, K. Conder, E. Pomjakushina, S. Weyeneth, V. Pomjakushin, O. Bossen, and A. Amato, *Coexistence of Magnetism and Superconductivity in the Iron-Based Compound* $Cs_{0.8}(FeSe_{0.98})_2$, Phys. Rev. Lett. **106**, 117602 (2011). (Cited on pages 51 and 52.)

[90] A. Weidinger, C. Niedermayer, H. Gluckler, A. Golnik, G. Nowitzke, E. Recknagel, H. Eickenbusch, W. Paulus, R. Schollhorn, and J.-I. Budnick, *Local magnetism in superconducting* $YBa_2Cu_3O_{6+X}$, Hyperfine Interact. **63**, 147 (1990). (Cited on page 51.)

[91] W. Bao, Q. Huang, G. F. Chen, M. A. Green, D. M. Wang, J. B. He, X. Q. Wang, and Y. Qiu, *A Novel Large Moment Antiferromagnetic Order in* $K_{0.8}Fe_{1.6}Se_2$ *Superconductor*, Chin. Phys. Lett. **28**, 086104 (2011). (Cited on pages 51 and 52.)

[92] Y. Zhang et al., *Nodeless superconducting gap in* $A_xFe_2Se_2$ *(A = K, Cs) revealed by angle-resolved photoemission spectroscopy*, Nat. Mater. **10**, 273 (2011). (Cited on page 51.)

[93] I. I. Mazin, D. J. Singh, M. D. Johannes, and M. H. Du, *Unconventional Superconductivity with a Sign Reversal in the Order Parameter of* $LaFeAsO_{1-x}F_x$, Phys. Rev. Lett. **101**, 057003 (2008). (Cited on page 51.)

[94] K. Kuroki, S. Onari, R. Arita, H. Usui, Y. Tanaka, H. Kontani, and H. Aoki, *Unconventional Pairing Originating from the Disconnected Fermi Surfaces of Superconducting* $LaFeAsO_{1-x}F_x$, Phys. Rev. Lett. **101**, 087004 (2008). (Cited on page 51.)

[95] A. L. Ivanovskii, *New ternary* $ThCr_2Si_2$*-type iron-selenide superconducting materials: Synthesis, properties and simulations*, Physica C **471**, 409 (2011). (Cited on page 51.)

[96] A. Ricci, N. Poccia, G. Campi, B. Joseph, G. Arrighetti, L. Barba, M. Reynolds, M. Burghammer, H. Takeya, Y. Mizuguchi, Y. Takano, M. Colapietro, N. L. Saini, and A. Bianconi, *Nanoscale phase separation in the iron chalcogenide superconductor* $K_{0.8}Fe_{1.6}Se_2$ *as seen via scanning nanofocused x-ray diffraction*, Phys. Rev. B **84**, 060511 (2011). (Cited on pages 51 and 52.)

[97] B. Shen, B. Zeng, G. F. Chen, J. B. He, D. M. Wang, H. Yang, and H. H. Wen, *Intrinsic percolative superconductivity in* $K_xFe_{2-y}Se_2$ *single crystals*, Europhys. Lett. **96**, 37010 (2011). (Cited on page 51.)

[98] V. Ksenofontov, G. Wortmann, S. A. Medvedev, V. Tsurkan, J. Deisenhofer, A. Loidl, and C. Felser, *Phase separation in superconducting and antiferromagnetic* $Rb_{0.8}Fe_{1.6}Se_2$ *probed by Mössbauer spectroscopy*, Phys. Rev. B **84**, 180508 (2011). (Cited on page 51.)

[99] Z. Wang, Y. J. Song, H. L. Shi, Z. W. Wang, Z. Chen, H. F. Tian, G. F. Chen, J. G. Guo, H. X. Yang, and J. Q. Li, *Microstructure and ordering of iron vacancies in the superconductor system* $K_yFe_xSe_2$ *as seen via transmission electron microscopy*, Phys. Rev. B **83**, 140505 (2011). (Cited on pages 51 and 54.)

[100] W. Li, H. Ding, P. Deng, K. Chang, C. Song, K. He, L. Wang, X. Ma, J.-P. Hu, X. Chen, and Q.-K. Xue, *Phase separation and magnetic order in K-doped iron selenide superconductor*, Nat. Phys. **8**, 126 (2011). (Cited on page 51.)

[101] D. P. Shoemaker, D. Y. Chung, H. Claus, M. C. Francisco, S. Avci, A. Llobet, and M. G. Kanatzidis, *Phase relations in* $K_xFe_{2-y}Se_2$ *and the structure of superconducting* $K_xFe_2Se_2$ *via high-resolution synchrotron diffraction*, Phys. Rev. B **86**, 184511 (2012). (Cited on page 51.)

[102] H. Lei and C. Petrovic, *Anisotropy in transport and magnetic properties of* $K_{0.64}Fe_{1.44}Se_2$, Phys. Rev. B **83**, 184504 (2011). (Cited on pages 52 and 53.)

[103] M. I. Tsindlekht, I. Felner, M. Zhang, A. F. Wang, and X. H. Chen, *Superconducting critical fields of single-crystalline* $K_{0.73}Fe_{1.68}Se_2$, Phys. Rev. B **84**, 052503 (2011). (Cited on page 52.)

[104] R. A. Klemm and J. R. Clem, *Lower critical field of an anisotropic type-II superconductor*, Phys. Rev. B **21**, 1868 (1980). (Cited on page 52.)

[105] D. A. Torchetti, M. Fu, D. C. Christensen, K. J. Nelson, T. Imai, H. C. Lei, and C. Petrovic, *^{77}Se NMR investigation of the $K_xFe_{2-y}Se_2$ high-T_c superconductor ($T_c = 33$ K)*, Phys. Rev. B **83**, 104508 (2011). (Cited on pages 52 and 53.)

[106] E. D. Mun, M. M. Altarawneh, C. H. Mielke, V. S. Zapf, R. Hu, S. L. Bud'ko, and P. C. Canfield, *Anisotropic H_{c2} of $K_{0.8}Fe_{1.76}Se_2$ determined up to 60 T*, Phys. Rev. B **83**, 100514(R) (2011). (Cited on page 52.)

[107] V. Tsurkan, J. Deisenhofer, A. Günther, H.-A. Krug von Nidda, S. Widmann, and A. Loidl, *Anisotropic magnetism, superconductivity, and the phase diagram of $Rb_{1-x}Fe_{2-y}Se_2$*, Phys. Rev. B **84**, 144520 (2011). (Cited on page 52.)

[108] M. Willemin, A. Schilling, H. Keller, C. Rossel, J. Hofer, U. Welp, W. K. Kwok, R. J. Olsson, and G. W. Crabtree, *First-Order Vortex-Lattice Melting Transition in $YBa_2Cu_3O_{7-\delta}$ near the Critical Temperature Detected by Magnetic Torque*, Phys. Rev. Lett. **81**, 4236 (1998). (Cited on page 53.)

[109] Z. Shermadini, H. Luetkens, R. Khasanov, A. Krzton-Maziopa, K. Conder, E. Pomjakushina, H.-H. Klauss, and A. Amato, *Superconducting properties of single-crystalline $A_xFe_{2-y}Se_2$ (A = Rb, K) studied using muon spin spectroscopy*, Phys. Rev. B **85**, 100501 (2012). (Cited on pages 53, 56 and 57.)

[110] M. Bendele, S. Weyeneth, R. Puzniak, A. Maisuradze, E. Pomjakushina, K. Conder, V. Pomjakushin, H. Luetkens, S. Katrych, A. Wisniewski, R. Khasanov, and H. Keller, *Anisotropic superconducting properties of single-crystalline $FeSe_{0.5}Te_{0.5}$*, Phys. Rev. B **81**, 224520 (2010). (Cited on page 53.)

[111] J. R. Clem, M. W. Coffey, and Z. Hao, *Lower critical field of a Josephson-coupled layer model of high-T_c superconductors*, Phys. Rev. B **44**, 2732 (1991). (Cited on page 53.)

[112] M. Angst and R. Puzniak, *Focus on Superconductivity Research*, chapter 1, pages 1–49, arXiv: cond–mat/0305048, Nova Science Publishers, New York, 2004. (Cited on page 54.)

[113] J. D. Fletcher, A. Carrington, O. J. Taylor, S. M. Kazakov, and J. Karpinski, *Temperature-Dependent Anisotropy of the Penetration Depth and Coherence Length of MgB_2*, Phys. Rev. Lett. **95**, 097005 (2005). (Cited on page 54.)

[114] J. Jaroszynski, F. Hunte, L. Balicas, Y.-j. Jo, I. Raičević, A. Gurevich, D. C. Larbalestier, F. F. Balakirev, L. Fang, P. Cheng, Y. Jia, and H. H. Wen, *Upper critical fields and thermally-activated transport of $NdFeAsO_{0.7}F_{0.3}$ single crystal*, Phys. Rev. B **78**, 174523 (2008). (Cited on page 54.)

[115] F. Hunte, J. Jaroszynski, A. Gurevich, D. C. Larbalestier, R. Jin, A. S. Sefat, M. A. McGuire, B. C. Sales, D. K. Christen, and D. Mandrus, *Two-band superconductivity in $LaFeAsO_{0.89}F_{0.11}$ at very high magnetic fields*, Nature **453**, 903 (2008). (Cited on page 54.)

[116] L. Malone, J. D. Fletcher, A. Serafin, A. Carrington, N. D. Zhigadlo, Z. Bukowski, S. Katrych, and J. Karpinski, *Magnetic penetration depth of single-crystalline $SmFeAsO_{1-x}F_y$*, Phys. Rev. B **79**, 140501 (2009). (Cited on page 54.)

[117] I. A. Nekrasov and M. V. Sadovskii, *Electronic structure, topological phase transitions and superconductivity in $(K,Cs)_xFe_2Se_2$*, JETP Letters **93**, 166 (2011). (Cited on page 54.)

[118] I. R. Shein and A. L. Ivanovskii, *Electronic structure and Fermi surface of new K intercalated iron selenide superconductor* $K_xFe_2Se_2$, Phys. Lett. A **375**, 1028 (2011). (Cited on page 54.)

[119] C. Cao and J. Dai, *Electronic Structure of* KFe_2Se_2 *from First Principles Calculations*, Chin. Phys. Lett. **28**, 057402 (2011). (Cited on page 54.)

[120] D. Mou et al., *Distinct Fermi Surface Topology and Nodeless Superconducting Gap in a* $Tl_{0.58}Rb_{0.42}Fe_{1.72}Se_2$ *Superconductor*, Phys. Rev. Lett. **106**, 107001 (2011). (Cited on page 54.)

[121] R. H. Liu, X. G. Luo, M. Zhang, A. F. Wang, J. J. Ying, X. F. Wang, Y. J. Yan, Z. J. Xiang, P. Cheng, G. J. Ye, Z. Y. Li, and X. H. Chen, *Coexistence of superconductivity and antiferromagnetism in single crystals* $A_{0.8}Fe_{2-y}Se_2$ *(A = K, Rb, Cs, Tl/K and Tl/Rb): Evidence from magnetization and resistivity*, Europhys. Lett. **94**, 27008 (2011). (Cited on page 55.)

[122] Y. Mizuguchi, Y. Hara, K. Deguchi, S. Tsuda, T. Yamaguchi, K. Takeda, H. Kotegawa, H. Tou, and Y. Takano, *Anion height dependence of* T_c *for the Fe-based superconductor*, Supercond. Sci. Tech. **23**, 054013 (2010). (Cited on page 55.)

[123] H. Lei and C. Petrovic, *Giant increase in critical current density of* $K_xFe_{2-y}Se_2$ *single crystals*, Phys. Rev. B **84**, 212502 (2011). (Cited on page 55.)

[124] T. Ozaki, H. Takeya, H. Okazaki, K. Deguchi, S. Demura, Y. Kawasaki, H. Hara, T. Watanabe, T. Yamaguchi, and Y. Takano, *One-step synthesis of* $K_xFe_{2-y}Se_2$ *single crystal for high critical current density*, Europhys. Lett. **98**, 27002 (2012). (Cited on page 55.)

[125] H. Ryu, H. Lei, A. I. Frenkel, and C. Petrovic, *Local structural disorder and superconductivity in* $K_xFe_{2-y}Se_2$, Phys. Rev. B **85**, 224515 (2012). (Cited on page 55.)

[126] S. Weyeneth, M. Bendele, F. von Rohr, P. Dluzewski, R. Puzniak, A. Krzton-Maziopa, S. Bosma, Z. Guguchia, R. Khasanov, Z. Shermadini, A. Amato, E. Pomjakushina, K. Conder, A. Schilling, and H. Keller, *Superconductivity and magnetism in* $Rb_xFe_{2-y}Se_2$*: Impact of thermal treatment on mesoscopic phase separation*, Phys. Rev. B **86**, 134530 (2012). (Cited on pages 55, 56 and 57.)

[127] A. Wittlin, P. Aleshkevych, H. Przybylińska, D. J. Gawryluk, P. Dłużewski, M. Berkowski, R. Puźniak, M. U. Gutowska, and A. Wiśniewski, *Microstructural magnetic phases in superconducting* $FeTe_{0.65}Se_{0.35}$, Sup. Sci. and Technol. **25**, 065019 (2012). (Cited on page 56.)

[128] Z. Ren, Z. Zhu, S. Jiang, X. Xu, Q. Tao, C. Wang, C. Feng, G. Cao, and Z. Xu, *Antiferromagnetic transition in* $EuFe_2As_2$*: A possible parent compound for superconductors*, Phys. Rev. B **78**, 052501 (2008). (Cited on page 77.)

[129] Y. Xiao, Y. Su, M. Meven, R. Mittal, C. M. N. Kumar, T. Chatterji, S. Price, J. Persson, N. Kumar, S. K. Dhar, A. Thamizhavel, and T. Brueckel, *Magnetic structure of* $EuFe_2As_2$ *determined by single-crystal neutron diffraction*, Phys. Rev. B **80**, 174424 (2009). (Cited on page 77.)

[130] T. Terashima, M. Kimata, H. Satsukawa, A. Harada, K. Hazama, S. Uji, H. S. Suzuki, T. Matsumoto, and K. Murata, $EuFe_2As_2$ *under High Pressure: An Antiferromagnetic Bulk Superconductor*, J. Phys. Soc. Jpn. **78**, 083701 (2009). (Cited on page 77.)

[131] Z. Guguchia, J. Roos, A. Shengelaya, S. Katrych, Z. Bukowski, S. Weyeneth, F. Murányi, S. Strässle, A. Maisuradze, J. Karpinski, and H. Keller, *Strong coupling between Eu*$^{2+}$ *spins and* Fe_2As_2 *layers in* $EuFe_{1.9}Co_{0.1}As_2$ *observed with NMR*, Phys. Rev. B **83**, 144516 (2011). (Cited on page 77.)

[132] Z. Guguchia, S. Bosma, S. Weyeneth, A. Shengelaya, R. Puzniak, Z. Bukowski, J. Karpinski, and H. Keller, *Anisotropic magnetic order of the Eu sublattice in single crystals of* $EuFe_{2-x}Co_xAs_2$ *(*$x = 0, 0.2$*) studied by means of magnetization and magnetic torque*, Phys. Rev. B **84**, 144506 (2011). (Cited on pages 78 and 81.)

[133] E. Dengler, J. Deisenhofer, H.-A. Krug von Nidda, S. Khim, J. S. Kim, K. H. Kim, F. Casper, C. Felser, and A. Loidl, *Strong reduction of the Korringa relaxation in the spin-density wave regime of* $EuFe_2As_2$ *observed by electron spin resonance*, Phys. Rev. B **81**, 024406 (2010). (Cited on page 78.)

Acknowledgments

I sincerely thank Prof. Dr. Hugo Keller for giving me the opportunity to do a Ph.D. in his group at the University of Zürich. His guidance in physics, article writing, and scientific methods has been invaluable.

I also thank the other group members, for ideas exchanges in or out of group meetings. Among these, I give special thanks to Dr. Stephen Weyeneth, who taught me all about torque experiments, and whose help made experimental physics go much smoother. I learned a lot about torque, SQUID, various lab techniques, data analysis, and magnetometry literature.

I would also like to thank Prof. Dr. Roman Puzniak from the Polish Institute of Physics, who always had insightful ideas about data interpretation, and who consistently improved our articles. I thank Prof. Dr. Schilling for the fruitful collaboration on the Hao-Clem analysis.

For building the new torque inset for the PPMS, I thank Kurt Bösiger and Reto Maier from the University Mechanical Workshop. Thanks as well to Dr. Achim Vollhardt, Peter Soland, and Daniel Florin of the Electronics Workshop, for the inset sensor holder design, shaking amplifier, and useful insights on the electronic devices involved in our new setup.

I thank Dr. Joseph Roos, who got me started on the new torque inset and introduced me to many important points of experimental physics. I also thank Dr. Peter Robmann, for his support with the praktikum, and for measurements of the shaking coils prototypes.

I give thanks to all the other PhD students from our group, and to the members of Prof. Dr. Schilling's group as well. In particular Zurab Guguchia was always ready to help in the lab and share interesting Georgian foods; Dr. Markus Bendele fostered a nice working atmosphere for which I was especially grateful during μSR beamtimes; Olaf Bossen helped a lot in all things related to the PPMS. I also give thanks to Dr. Alexander Maisuradze, Dr. Ludovic Howald, Evelyn Stilp, Fabian Von Rohr, Henrik Grundmann, and Dr. Simon Strässle.

I am grateful to the PSI Laboratory for Developments and Methods team: Dr. Anna Krzton-Maziopa, Dr. Ekaterina Pomjakushina, and Prof. Dr. Kazimierz Conder provided me with cutting-edge iron-selenides superconductors. I also thank Dr. Andreas Erb for the top-quality $\mathrm{YBa_2Cu_3O_{7-\delta}}$ crystals, Dr. Zbigniev Bukowski for the $\mathrm{EuFe_2As_2}$ crystals, and Dr. Nikolai Zhigadlo for the iron-pnictides.

Finally, I would like to thank my friends and family, and especially my partner Raphaël Marinier, for constant support throughout my PhD.

Curriculum Vitae

Saskia Bosma, born in Sèvres (France) on October 17th, 1985.

2003	Scientific Baccalauréat Géneral at Lycée N. D. de la Providence (Vincennes, France)
2003-2006	Classes préparatoires MPSI-MP* at Lycée Charlemagne (Paris, France)
2006-2009	Engineering studies at Supélec (Ecole Supérieure d'Electricité), joint program in Fundamental Physics at Paris Sud XI University (Gif-sur-Yvette and Orsay, France) Main topics: Signal Analysis, Solid State Physics, Electromagnetism, Programming, Automatics, Computer Architecture, Information Systems Diplôme Ingénieur Supélec and Master in Solid State Physics
2007	Internship at Radio France (Paris, France) Audio Tranfer Service
2008	Internship at CERN (Geneva, Switzerland) Automated detection of abnormal signals in ATLAS-LAr calorimeter cells using a clustering algorithm (C++, ROOT)
2009	Internship at SPEC (Saclay, France) Electronic transport measurements on spin transfer systems; study of the influence of magnetic vortex configurations on the magnetoresistance
2009-2013	PhD student at the University of Zurich, Keller group (Zurich, Switzerland) Superconductivity and magnetism; torque magnetometry studies of the superconducting anisotropy in various materials, developement of a new torque setup

Publications list

- *Magnetic torque study of the temperature-dependent anisotropy parameter in overdoped superconducting single-crystal* $YBa_2Cu_3O_{7-\delta}$
  S. Bosma, S. Weyeneth, R. Puzniak, A. Erb, A. Schilling, and H. Keller
  Physical Review B **84**, 024514 (2011)

- *Anisotropic magnetic order of the Eu sublattice in single crystals of* $EuFe_{2-x}Co_xAs_2$ *(*$x = 0, 0.2$*) studied by means of magnetization and magnetic torque*
  Z. Guguchia, S. Bosma, S. Weyeneth, A. Shengelaya, R. Puzniak, Z. Bukowski, J. Karpinski, and H. Keller
  Physical Review B **84**, 144506 (2011)

- *Mixed state of* $La_{1.83}Sr_{0.17}CuO_4$ *studied by means of muon-spin rotation and magnetization experiments in a low magnetic field*
  B. M. Wojek, S. Weyeneth, S. Bosma, E. Pomjakushina, and R. Puzniak
  Physical Review B **84**, 144521 (2011)

- *Magnetic-field tuned anisotropy in superconducting* $Rb_xFe_{2-y}Se_2$
  S. Bosma, R. Puzniak, A. Krzton-Maziopa, M. Bendele, E. Pomjakushina, K. Conder, H. Keller, and S. Weyeneth
  Physical Review B **85**, 064509 (2012)

- *Superconductivity and magnetism in* $Rb_xFe_{2-y}Se_2$*: Impact of thermal treatment on mesoscopic phase separation*
  S. Weyeneth, M. Bendele, F. von Rohr, P. Dluzewski, R. Puzniak, A. Krzton-Maziopa, S. Bosma, Z. Guguchia, R. Khasanov, Z. Shermadini, A. Amato, E. Pomjakushina, K. Conder, A. Schilling, and H. Keller
  Physical Review B **86**, 134530 (2012)

- *Vortex lock-in transition coinciding with the 3D to 2D crossover in* $YBa_2Cu_3O_{7-\delta}$
  S. Bosma, S. Weyeneth, R. Puzniak, A. Erb, and H. Keller
  Physical Review B **86**, 174502 (2012)

- *High-pressure flux growth, structural, and superconducting properties of LnFeAsO (Ln = Pr, Nd, Sm) single crystals* N. D. Zhigadlo, S. Weyeneth, S. Katrych, P. J. W. Moll, K. Rogacki, S. Bosma, R. Puzniak, J. Karpinski, and B. Batlogg
  Physical Review B **86**, 214509 (2012)